SYSTEM-WIDE ADVANCES IN PHOTON-COUNTING CT: CORRECTIONS, SIMULATIONS, AND IMAGE ANALYSIS

Matthew Getzin

Submitted in Partial Fullfillment of the Requirements
for the Degree of

DOCTOR OF PHILOSOPHY

Approved by:
Ge Wang, Chair
Xavier Intes
Leo Wan
Rongjie Lai
Roman Fleysher

Department of Biomedical Engineering
Rensselaer Polytechnic Institute
Troy, New York

[May 2019]
Submitted April 2019

© Copyright 2019
by
Matthew Getzin
All Rights Reserved

Contents

List of Tables . . . viii

List of Figures . . . ix

Acknowledgement . . . xvii

Abstract . . . xviii

1. Introduction . . . 1
    1.1 X-ray Overview . . . 1
        1.1.1 Setting the Stage: Light . . . 1
        1.1.2 Physical Phenomena of Radiation . . . 2
            1.1.2.1 A German Nobel . . . 2
            1.1.2.2 The French-Polish Nobels . . . 3
            1.1.2.3 Physical Interactions: X-ray and Matter . . . 4
            1.1.2.4 Dose Units . . . 9
        1.1.3 Measuring Irradiance and Power . . . 11
        1.1.4 Energy-integrating Detectors . . . 11
        1.1.5 Photon-counting Detectors . . . 13
            1.1.5.1 Spatio-energetic Crosstalk . . . 15
            1.1.5.2 Medipix3R Charge-summing Mode . . . 17
    1.2 System Geometries . . . 17
        1.2.1 2D Parallel Beam . . . 19
        1.2.2 2D Fanbeam . . . 19
        1.2.3 3D Cone-beam . . . 20
    1.3 Reconstruction . . . 20
        1.3.1 The Central Slice Theorem . . . 22
        1.3.2 Filtered Backprojection . . . 22
        1.3.3 Algebraic Reconstruction . . . 24
        1.3.4 Statistical Reconstruction . . . 24
        1.3.5 Spectral Reconstruction . . . 25
        1.3.6 Image Domain Material Decomposition . . . 26
    1.4 System Metrics . . . 29
    1.5 Thesis Outline . . . 31

2. Photon-counting CT Simulation in MATLAB . . . 33
2.1 Introduction . . . 33
2.1.1 Motivation . . . 33
2.2 Using the GUI . . . 34
2.2.1 Location . . . 34
2.2.2 First Glance . . . 37
2.2.3 Setting a Save Directory . . . 38
2.2.4 Loading X-ray Spectra and Material Attenuation Coefficients . . . 38
2.2.4.1 X-ray Spectra . . . 38
2.2.4.2 Material Attenuation Coefficients . . . 39
2.2.5 Filtering the X-ray Spectra . . . 40
2.2.6 Setting Geometry Parameters . . . 41
2.2.7 Phantom Design . . . 43
2.2.8 Setting Detector Energy Thresholds . . . 46
2.3 Scanning Geometry and Forward Projection . . . 47
2.3.1 The MARS Scanner . . . 47
2.3.2 `circular_geometry_w_phantom_ASTRA_v7.m` . . . 48
2.3.3 Calculating the Basis Sinograms . . . 50
2.3.3.1 Siddon's Method . . . 52
2.3.3.2 ASTRA Toolbox Forward-projection . . . 52
2.3.4 Viewing the Material Basis Sinograms . . . 53
2.4 Implementing the PcTK . . . 54
2.4.1 `Convert Basis Sinograms to PC Sinograms -- Callback` . . . 54
2.4.2 Viewing the Photon-counting Sinograms . . . 55
2.5 Reconstruction . . . 56
2.5.1 Mapping to the "Ideal" Detector . . . 56
2.5.2 Filling in the Gaps – 3D Analytic Reconstruction (FBP) . . . 57
2.5.3 Circular Cone-beam Reconstruction (ASTRA's FDK) . . . 61
2.5.4 Masking the Projection Matrix – Algebraic Reconstruction (ASTRA's SIRT) 62
2.6 Running in Bulk . . . 62
2.7 Working Example(s) . . . 65
2.7.1 Single Chip Detector . . . 65
2.7.2 Three Chip Detector . . . 67
2.8 Future Improvements . . . 69
2.9 Conclusion . . . 69

3. Correcting Counts . . . 73
3.1 Introduction . . . 73
3.2 Methods . . . 74
3.2.1 Spatial Non-uniformity Response Modeling . . . 74
3.2.2 Determination of the Linear Range . . . 75
3.2.3 Correction Method in the Linear Range . . . 75
3.3 Experimental Results . . . 76
3.4 Discussion . . . 77
3.4.1 Empirical Correction Method in the Linear Range . . . 77
3.4.2 Empirical Correction Method in the Nonlinear Range . . . 78
3.4.3 Conclusion . . . 79
4. Enhancing Spectral CT with Aperture Encoding . . . 80
4.1 Introduction . . . 80
4.2 Materials and Methods . . . 82
4.2.1 Aperture Design . . . 82
4.2.2 MCNP6.1 Simulation Environment . . . 82
4.2.3 Experimental Design . . . 84
4.3 Numerical and Experimental Results . . . 86
4.3.1 MCNP6.1 Results . . . 86
4.3.2 Projection Results . . . 87
4.4 Discussion and Conclusions . . . 89
4.5 Acknowledgements . . . 91
5. Increasing Separability of K-edge NPs with FDA . . . 92
5.1 Introduction . . . 92
5.2 Materials and Methods . . . 96
5.2.1 Phantom Preparation . . . 96
5.2.2 MARS Spectral Imaging . . . 96
5.2.3 Pre-processing Pipeline . . . 98
5.2.4 Univariate Analysis . . . 99
5.2.5 Multivariate Analysis . . . 100
5.2.6 Fisher's Discriminant Analysis . . . 100
5.2.7 Color-mapping . . . 101
5.3 Results . . . 102
5.3.1 Iodine Contrast . . . 102

5.3.2 Pure Lanthanide Nanoparticles . . . 103
5.3.3 Mixed Lanthanide Nanoparticles . . . 105
5.3.4 FDA Analysis of Contrast . . . 107
5.3.5 Color-mapping . . . 109
5.4 Discussion and Conclusion . . . 110
5.5 Acknowledgements . . . 111
6. Non-linear Material Segmentation and Quantification . . . 116
6.1 Introduction . . . 116
6.2 Materials and Methods . . . 117
6.2.1 Real Data . . . 117
6.2.2 Simulated Data . . . 118
6.2.3 Data Handling . . . 121
6.2.4 Data Polarization . . . 121
6.2.5 Bin Gradient . . . 122
6.2.6 Kernel Fisher Discriminat Analysis . . . 122
6.2.7 Parameter Selection with k-fold Cross-validation . . . 123
6.2.8 Image Segmentation and Material Quantification . . . 123
6.3 Results . . . 124
6.3.1 Visualizing the Data Space . . . 124
6.3.2 MARS HA-I Phantom . . . 124
6.3.3 MARS K-edge Phantom . . . 128
6.3.4 Simulated K-edge Phantom . . . 129
6.4 Discussion and Conclusion . . . 130
6.5 Acknowledgements . . . 134
7. Material Decomposition with a Convolutional Neural Network (MD-CNN) . . . 135
7.1 Introduction . . . 135
7.2 Methods . . . 136
7.2.1 Simulation . . . 136
7.2.2 Network Architecture . . . 138
7.2.3 Loss Function, Hyperparameters, and Training . . . 140
7.3 Results . . . 141
7.3.1 Training . . . 141
7.3.2 Decomposition . . . 141
7.4 Discussion and Conclusion . . . 143

8. Summary 147
8.1 Contributions and Future Work 147
References 151
Appendices
A. Supplemental Figures: Material Segmentation 170

List of Tables

1.1 $\mathbb{R}$ and $\mathbb{N}$ refer to real number and natural number sets, respectively. The dimensions are length (L), mass (M), time (T), temperature (K), current (A), and 1 for unitless quantities. 5

1.2 The dimensions are length (L), mass (M), time (T), temperature (K), current (A), and 1 for unitless quantities. 10

3.1 Parameters looking up table for nonlinear range correction. 79

5.1 Iodine constructs and lanthanide dopants of $NaYF_4$ nanoparticles tested as contrast. . 96

5.2 Imaging, energy binning, and reconstruction parameters. 97

5.3 Sample combinations for FDA models. 109

6.1 Imaging, energy binning, and reconstruction parameters. 119

7.1 Simulation geometry, energy binning, and reconstruction parameters. 137

List of Figures

1.1 The Electromagnetic Spectrum [1]. 2

1.2 This is the first roentgenogram (*i.e.* X-ray projection image) taken of Wilhelm Röntgen's wife's hand around 1895 [2]. 3

1.3 The Bohr model representation of an arbitrary atom with labelled electron shells and vacancies. 6

1.4 The four major light-matter interactions in the 0.1-1.02 MeV energy range are depicted along with a populated Bohr model atom. 6

1.5 A simplified representation of a divergent radiation source emitting in all directions with an intensity of I_0. The intensity flux of such sources decrease as one moves away from the source as per the inverse square law. 7

1.6 For a given cubic volume of space that is occupied by matter i or j the irradiance of the light Φ_0 will decrease according to Eq. 1.8. 8

1.7 Simplified diagram showing the Compton scattering interaction of material M. The image was adapted from [3]. 8

1.8 (a) The normalized spectra shapes of a tungsten source with 2 kVp and 2 filtration settings: (red) 80 kVp, 2 mm glass filter; (green) 120 kVp, 2 mm glass filter; (blue) 120 kVp, 2 mm glass + 2 mm copper filter. (b) A dual layer detector inherently filters the incident spectrum into low (red) and high (blue) energy measurement sets. 13

1.9 A simplified illustration of a photon-counting detector. 14

1.10 The nonlinear counting behaviors seen in PCDs result in spatio-energetic crosstalk between nearby pixels. These behaviors include charge-sharing, fluorescence escape, long-distance fluorescence, and pulse pileup (shown left-to-right, top-to-bottom). . . 16

1.11 Basic parametric geometries: (a) circle, (b) polar coordinates, and (c) circular helix. . 18

1.12 (a) The parallel beam geometry and (b) fanbeam geometries are the most common 2D tomographic geometries for non-diffracting sources. (c) Derivation of the filtered backprojection algorithm in the fanbeam geometry from the parallel beam equations require the definition of the additional angular quantities α and β as well as the distance measures D, s, and t. (d) The cone-beam geometry has one additional angle parameter γ which is used in the cosine approximation (shown as the green fan) for use with the fanbeam analytical reconstruction methods. Images were adapted from [31], [32]. 21

1.13 (a) CNN-based implementation of the PRISM algorithm. (b) Sparsity constraining arm. (c) Low-rank constraining arm. Final implementations of the encoder-decoder portions of the networks are still being discussed. 27

2.1 When opened in MATLAB's GUIDE, each element of `spectral_geometry_simulation_v7_GPU.fig` can be adjusted. This includes the Callback functions (*i.e.* what happens when you press a given button). 35

2.2 The opening state of the GUI contains five (5) top buttons, four (4) panels (two of which contain tables), and one (1) axes. 37

2.3 The view of the GUI after the X-ray spectra `.csv` has been loaded. 39

2.4 The view of the GUI after the material properties `.csv` has been loaded. 40

2.5 The key geometries which constrain the phantom size are depicted. 44

2.6 This figure shows an `Automated Ellipsoids` output containing up to 10 ellipsoids in a 141x141x141 voxel matrix. The materials, concentrations, sizes, and placements of the mixture ovals are randomly selected from the subset of materials specified by the user. 47

2.7 This figure shows the central slice of material basis phantom as created by the `Automated Ellipsoids` selection. The voxel intensities are equal to the percent (by weight) of the materials in a given voxel. A second figure showing orthogonal views of the 3D phantom is also shown. 48

2.8 This image shows the original spectrum, filtered spectrum, and energy thresholds as defined by the user. 49

2.9 When running the `Calc. Basis Sinograms`, a pop-up figure shows the source/ideal detector trajectories and provides a single view represented by a 3D surface plot. Additionally, the command window prints the data acquisition progress. 51

2.10 Viewing the material basis sinograms in the GUI for a 3x1 detector array over a single translation. 53

2.11 Command window output after running the `Convert Basis Sinograms to PC Sinograms Callback`. 55

2.12 Viewing the photon-counting sinograms in the GUI for a 3x1 detector array over a single translation. 56

2.13 A slice of the ideal detector sinogram with 360 views in the cone beam (pseudo-fan at central ideal slice) and after running `FAN2PARA_custom.m`. The white regions represent ideal detector pixels for which no data was collected due to gaps or offsets in the detector positions. In cases where sufficient data has been collected in the conebeam trajectory and the gaps have been correctly offset, the parallel-beam transformation of the data results in a continuous sinogram which can be used for analytic reconstruction via FBP. 59

2.14 The key geometric relationships for an accurate fanbeam-to-parallel beam rebinning. . 60

2.15 The feathering process of filling in the data for parallel beam (θ, t)s with the available fanbeam angles (β_1, α_1) and (β_2, α_2). The gap neighbors are weighted with a linear bias toward the fanbeam angle which supplies the gaps data. 60

2.16 Single chip – Phantom_001 reconstruction outputs. 66

2.17 Single chip – Phantom_002 reconstruction outputs. 66

2.18 Single chip – Phantom_003 reconstruction outputs. 67

2.19 Single chip – Phantom_004 reconstruction outputs. 67

2.20 Single chip – Phantom_005 reconstruction outputs. 68

2.21 Three chip – Phantom_001 reconstruction outputs from energy bin 1. 70

2.22 Three chip – Phantom_002 reconstruction outputs from energy bin 1. 71

2.23 Three chip – Phantom_003 reconstruction outputs from energy bin 1. 72

3.1 (a) Measured counts vs. tube current is plotted for each of the PCD channels which operate in charge-summing mode. The dashed line is the "ideal" response for Ch 8. (b) The calculated (Eq. 3.4) mean detector offset for Ch 8 across all pixels where I_1 and I_2 are sequentially sampled current pairs (e.g. 15, 20, 25, 30, 35μA, etc.). The linear range is encompassed by the first 5 current pairs (0-40 μA). 77

3.2 (a) SSTD for open-beam data as a function of linear range tube currents. (b) The uncorrected (top) and corrected (bottom) sinograms for 1440 angle projections around a wire phantom. 78

3.3 (a) The temporal distributions of the PcTK output pixels are Poisson-counting with the same mean. (b) Uncorrected MARS detector pixels are Poisson-counting, yet their mean values are widely distributed. (c) Corrected MARS detector pixels are Poisson-counting with the same mean (provided they occupy the same monolith/chip). 78

4.1 Typical encoded aperture designs. (a) The design for 2X resolution enhancement in 2D tomography, (b) the design for 3X resolution enhancement in 2D tomography, and (c) the design for 2X resolution enhancement in 3D tomography. 83

4.2 This MCNP geometry rendering shows the aperture encoding configurations used in the simulations. The gold filter, seen in aperture configurations 1 and 2 as yellow, was placed flush with the CZT detector (shown as dark blue). Spacing of elements is not to scale and the FIR tally only used the planar grid of the CZT detector face for its measurement. 85

4.3 X-ray micro-imaging platform. (a) The full single-projection setup included a Hamamatsu microfocus x-ray source; a QRM Micro-CT-BarPattern resolution phantom; a Microworks 28keV, G0 absorption grating with 50.26 μm period; and a Rayence model 1215MCB flat panel detector; (b) The G0 absorption grating has four 15 mm x 15 mm grating areas with various periods. The 50.26 μm grating is the top right grating area; and (c) In this setup, the G0 grating would ideally lie within detector plane in order to match the pitch and period between detector and grating, respectively. Our hardware, however, limited how close we could bring these two elements ($\sim$0.5-1 cm). This and the mismatch between detector pitch and grating period, are possible sources of enhancement error. 86

4.4 Comparison of simulated phantom image resolution. (a) ART-TV reconstructed image of the phantom without aperture configuration. (b) ART-TV reconstructed image of the encoded aperture combined matrix. (c) Zoomed-in image for phantom without aperture showing 200, 100, 75, and 50 μm circles. (d) Zoomed-in image for phantom with encoded aperture. 88

4.5 Comparison of projection images from the experiment. (a) Single-view projection of the QRM MicroCT-BarPattern (5 mm X 5 mm) phantom without the encoded aperture. (b) Single-view projection of the phantom with the encoded aperture in front of the detector. (c-d) Zoom window of the 5, 10, 15, 20, 25, and 30 μm line pairs. No filter was applied to these images. (e-f) The same zoom window, but with a median spatial filter (radius = 1) applied. 90

4.6 The modulation transfer function curves for each of the projection images demonstrate a slight increase in contrast for the low frequency spatial patterns with aperture encoding. A much more significant increase in contrast can be seen at the higher frequency spatial patterns. Adding a median spatial filter decreases the overall modulation depth of both the encoded aperture (AP) and no aperture (NA) images. 91

5.1 The 48-mm diameter acrylic phantom can hold up to 12 liquid mixtures. The larger diameter tubes hold $\sim$2 mL while the smaller tubes hold $\sim$500 μL. 97

5.2 The mass attenuation coefficients for the contrast materials used in this study are shown in the context of the MARS spectral detector threshold placements. These thresholds were determined by equally distributing total detector counts across all bins. 98

5.3 The pairwise comparison results for iodine samples demonstrate how strong the contrast between iodine-based molecules at these concentrations and low-contrast solutions as the values of the significant T^2 test statistics have values $\sim$180. None of the contrast materials can be distinguished from any of the other contrast materials (HB-adjusted α^* = 0.0126, α^{**} = 0.0014). 103

5.4 The pairwise comparison results for the iodine samples with 5 energy bins look very similar to the conventional comparison results. The only change in the significance of the pair-wise comparisons is in the ability to differentiate water from oil, although formamide can no longer be discerned from oil (HB-adjusted α^* = 0.0038, α^{**} = 0.0013). It should be noted, however, that the significant T^2 statistics are now $\sim$450, nearly 3X greater than in the univariate comparison. 104

5.5 The pairwise comparison results for the pLn NP samples show that despite the contrast materials ability to be distinguished from oil, they cannot (with the exception of Ta and Eu) be distinguished from water. In this image, the significant T^2 statistics have values $\sim$40. This reflects the difficulty of telling many of these materials apart from one another (even qualitatively). None of the contrast materials can be distinguished from any of the other contrast materials (HB-adjusted α* = 0.0016, α** = 0.00044). . 105

5.6 The pairwise comparison results for all samples show much greater separability can be achieved between the Ta- and Eu- nanoparticles and water. Additionally, several of the nanoparticles can even be distinguished from one another (HB-adjusted α* = 0.0049, α** = 0.00048). The significant T^2 values are $\sim$80, which is 2X greater than in the univariate comparison. 106

5.7 The pairwise comparison results for all mLn NPs suggest that none of the materials could be used as contrast at concentrations even as high as 27 $mgNP/mL$ in an energy-integrating system (HB-adjusted α* = 0.011, α** = 0.00054). The T^2 values for these samples hover well below 10. 107

5.8 The pairwise comparison results for the mLn NPs with 5 energy bins suggest that a few of the formulations, namely Gd/Eu, can be distinguished from the other low-contrast materials. (HB-adjusted α* = 0.0025 and α** = 0.0011). Its T^2 value when compared to one of the water samples was $\sim$30. 108

5.9 The top row shows the weights for all the 126 four-sample combinations for the pLn phantom which were used to calculate 3 LC FDA models. The middle row shows a scatter plot of T^2 scores for each combination as well as the α* and α** values which shown as blue and green horizontal lines, respectively. The bottom row is the total number of significant T^2 statistics as compared to α* and α** values. 112

5.10 The top row shows the weights for all the 126 four-sample combinations for the mLn phantom which were used to calculate 3 LC FDA models. The middle row shows a scatter plot of T^2 scores for each combination as well as the α* and α** values which are shown as blue and green horizontal lines, respectively. The bottom row is the total number of significant T^2 statistics as compared to α* and α** values. 113

5.11 FDA models mapped into multiple color spaces demonstrate the combination-dependence of the 3D FDA models that can be used to further separate different contrast materials. 114

5.12 FDA models mapped into multiple color spaces demonstrate the combination-dependence of the 3D FDA models that can be used to further separate different contrast materials. Some of these color combinations also seem to highlight the image artifacts introduced from system aspects that are outside the scope of this study (*i.e.* miscalibration, spatial non-uniformities, etc.). equally 115

6.1 (a) A model spectrum for a tungsten source operated at 120 kVp is depicted alongside NIST material attenuation profiles of those materials present in the MARS K-edge material phantom. The vertical lines represent the energy thresholds. (b) A model spectrum for a tungsten target operated at 80 kVp is depicted alongside the NIST material attenuation curves of those materials contained in the hydroxyapatite-iodine phantom. This phantom could be used to train a kFDA segmentation model for applications such as plaque characterization. (c) Again, the model 120 kVp tungsten source spectra is depicted alongside the K-edge material attenuation profiles of those materials contained in the simulated phantom. 120

6.2 Projecting each of the 14 V dimensions into a 3D subspace to allow for some basic understanding regarding relationship of mulitiple concentrations of HA, I, water, oil, and air in the expanded spectral dataspace. 124

6.3 Projecting each of the 14 V dimensions into a 3D subspace to allow for some basic understanding regarding relationship of the single concentrations of Gd, Lu, Ta, Eu, Yb, water, oil, and air in the expanded spectral dataspace. 125

6.4 Projecting each of the 14 V dimensions into a 3D subspace to allow for some basic understanding regarding relationship of multiple concentrations of cortical bone (HA), I, Au, Ag, Ta, Gd, and water in the expanded spectral dataspace. 125

6.5 (a-d) The first four eigenvectors of the kFDA mapped HA-I data show how the various materials are separated in the mapped dataspace. 2D plots of these eigenvector representations of the data are included in Appendix A. (e-f) Lines are fit to the two materials for which multiple concentrations are available in the phantom: (e) hydroxyapatite and (f) iodine. Each of fitted lines are used to quantify the material concentration in a labelled pixel and the final concentration is computed as the average of all computations. 126

6.6 (a) The reconstructed image from the first energy bin for the HA-I phantom. (b) The kFDA labeled image. (c) The linear fit concentration map for samples labeled as HA or as I. The HA sample concentrations should be multiplied by a factor of 100. 127

6.7 (a) The reconstructed image from the first energy bin for plaque sample 1. (b) The kFDA labeled image (center). (c) The linear fit concentration map for samples labeled as HA or as I. The HA sample concentrations should be multiplied by a factor of 100. (d) The reconstructed image from the first energy bin for plaque sample 2. (e) The kFDA labeled image. (f) The linear fit concentration map for samples labeled as HA or as I. The HA sample concentrations should be multiplied by a factor of 100. 127

6.8 (a-g) The first seven eigenvectors of the kFDA mapped MARS K-edge data show how the various materials are separated in the mapped dataspace. The first five eigenvectors do the most to distinguish the various materials. 2D plots of these eigenvector representations of the data are included in Appendix A. 129

6.9 (a) The reconstructed image from the first energy bin for the real K-edge phantom. (b) The kFDA labeled image. 130

6.10 (a-f) The first six eigenvectors of the kFDA mapped MARS K-edge data show how the various materials are separated in the mapped dataspace. 2D plots of these eigenvector representations of the data are included in Appendix A. (g-k) The linear fits for the concentrations found in the reconstructed material basis phantom produced by the simulation. The final concentration is an average of the calculated value from the 6 lines fit to the energy bin measurements. 131

6.11 (a) The reconstructed image from the first energy bin for simulated K-edge calibration phantom (left). The kFDA labeled image (center). The linear fit concentration map for samples labeled as a K-edge material (right). (b) The reconstructed image from the first energy bin for the mixed K-edge phantom (left). The kFDA labeled image (center). The linear fit concentration map for samples labeled as a K-edge material (right). 132

7.1 The left image sets are one slice from the reconstructed simulation outputs for 3 of the test phantoms, and the right image sets are the material basis ground-truth (reconstructed from material basis sinograms during simulation). Each of the 100 simulated phantoms had 63 usable slices. The phantoms were randomly split into training (80), validation (10), and testing (10) sets. 49 patches of size (32x32) were extracted from the training and validation slices with a pixel stride of 16. Testing was done on full-size images. 139

7.2 The proposed CNN for material decomposition. 140

7.3 The training and validation curves for (a) MSE and (b) wMSE over 100 epochs for the networks trained using Loss1 and Loss2 functions. 141

7.4 (a) MSE and (b) wMSE total cost across all 63 slices of the test phantoms. MSE levels differ by less than an order of magnitude between the network trained with Loss1 vs. Loss2. On the other hand, wMSE is reduced by over an order of magnitude for half of the phantoms when the network is trained with Loss2. Only phantom 8 shows a deviation from reduced wMSE when trained with Loss2. 142

7.5 The material basis ground-truth's for test phantom 4, slice 31 are shown next to the outputs from MD-CNN-Loss1 and MD-CNN-Loss2. Both loss functions do a good job at learning the high concentration material bases: air, water, and bone. MD-CNN-Loss2, however, is much better at distinguishing the K-edge material bases from the input image set. 143

7.6 The material basis ground-truth's for test phantom 5, slice 31 are shown next to the outputs from MD-CNN-Loss1 and MD-CNN-Loss2. Both loss functions do a good job at learning the high concentration material bases: air, water, and bone. MD-CNN-Loss2, however, is much better at distinguishing the K-edge material bases from the input image set. 144

7.7 The material basis ground-truth's for test phantom 8, slice 31 are shown next to the outputs from MD-CNN-Loss1 and MD-CNN-Loss2. Both loss functions do a good job at learning the high concentration material bases: air, water, and bone. The ground-truth concentrations for this phantom were particularly hard for the model to accurately predict. 144

7.8 Plot profiles across the central row of pixels of 5 of the 10 test phantoms (including those shown in previous figures) – ground-truth (blue), Loss1 (yellow), Loss2 (green). 145

8.1 The MARS scanning pipeline. The red hexagons represent start and endpoints in the user experience with the micro-CT scanner. The blue rectangles represent points along the pipeline which require human interaction, while the green rectangles are automated processes. The yellow diamonds are decision forks which dictate the workflow and the purple rectangles contain user-defined parameters. 148

A.1 2D plots of the materials in the eigenvector space made with the MARS HA I phantom. 170

A.2 2D plots of the materials in the eigenvector space made with the simulated 7 material phantom. 171

A.3 2D plots of the materials in the eigenvector space made with the simulated 7 material phantom (continued). 172

A.4 2D plots of the materials in the eigenvector space made with the mars K-edge phantom. 173

A.5 2D plots of the materials in the eigenvector space made with the mars K-edge phantom (continued). 174

Acknowledgement

Many thanks go out to the numerous people who have seen me grow throughout the nearly 7 years that I spent at RPI. To keep the list short, I focus here on those people who have seen me through the ups and downs of the past year.

First, to my wife – Juliana – I want to thank you for being my anchor to the earth when I, all-too-often, got lost in my head with no means of coming out of it by myself. You were patient and loving with me, which I desperately needed since the critic inside was busy being cruel and unforgiving. I could not have finished the work without you by my side.

To my parents – Eric and Paula – I want to thank you for gifting me with insatiable curiosity, a more-than-adequate intellect, as well as social graces. I would not be able to navigate this world without your guidance and support.

To my sisters – Casey, Annie, and Maggie – I want to thank you for reminding me to come home and to have fun. You are all very special to me and have been constant sources of love and support.

I want to thank my advisor – Dr. Ge Wang – for working with me over the past 6+ years. Our high risks did not reap the high rewards, although I have been rewarded in experience. Your guidance has been invaluable for my continued growth as a researcher and scientist.

Thank you to all those lab members and collaborators that have helped me along the way, namely – David Rundle, Dr. Manos Gkikas, Dr. Guang Li, Dr. Lars Gjesteby, Dr. Qingsong Yang, Dr. Wenxiang Cong, Mengzhou Li, Fenglei Fan, and Qing Lyu.

I'd like to thank my committee members – Drs. Intes, Wan, Lai, and Fleysher for their important feedback which helped to fill in any holes that I may have left in the original thesis draft.

Finally, I want to thank the Biomedical Engineering Department at RPI for providing my opportunities and funding to continue my doctoral education, the core facility directors at CBIS including Drs. Scott McCallum and Brigitte Arduini, and CBIS director Dr. Jason Davis.

Abstract

Imaging plays a major role in biomedicine with X-ray computed tomography (CT) as a primary example. X-ray CT becomes increasingly popular since its invention in the 1970's, now reaching over 100 million scans yearly worldwide. Advances in CT techniques and algorithms have been recently made, enabled by high-performance computing power and novel system hardware. State-of-the-art research CT prototypes have now begun to incorporate dynamic source filters and photo-counting detectors to measure spectral information for low dose, high resolution, and material decomposition. Less than two years ago, the Biomedical Imaging Center group at RPI obtained one of the best preclinical micro-CT scanners – the MARS micro-CT (MARS Bioimaging Ltd., Christchurch, NZ). Equipped with a Medipix3RX cadmium-zinc-telluride (CZT) photon-counting detector, the scanner is capable of simultaneously recording data in 5 distinct energy bins. This thesis provides solid results and physical insights for improving the current photon-counting imaging performance provided by this MARS system through (1) pre-reconstruction, spatial non-uniformity corrections, (2) hardware mechanisms to increase spatial resolution, and (3) post-reconstruction methods for analyzing image regions which contain varying levels of contrast materials. During this research project, a full-scale system simulator was developed in MATLAB as the "ideal" photon-counting detector/system model, which is a significant portion of the thesis. Our major goal is to provide a base for future development of a seamless imaging pipeline, which is from acquisition and pre-processing to reconstruction and post-processing, analysis, as well as material decomposition in a unified deep learning framework.

Chapter 1
Introduction

1.1 X-ray Overview

To be trained as a biomedical engineer is to be trained at the interface of many different technologies, each of which is evolving and changing on its own separate trajectory. The job of the biomedical engineer, therefore, is a task of wrangling-in these technologies and applying them effectively to a human- or health-related issue. While biomedical technologies have existed since the dawn of human civilization (*e.g.* a peg-leg, wooden dentures, etc.), it wasn't until the dawn of the industrial revolution that the current state of "devices" and "imaging" could be achieved.

The discovery of X-ray, as well as other forms of "invisible" radiations, in the late 19th/early 20th centuries gave birth to many of the marvels of modern medicine – tomographic imaging, radiation therapies, etc. These technologies and techniques have evolved over time through (1) the advancement of algorithms for image reconstruction from projection data, (2) the development of novel hardware configurations, and (3) advances in hardware technology (i.e. sources and detectors). The bleeding edges of today's X-ray (and particle physics) imaging technologies are a direct result of advances of radiation source(s) and detector(s). In between, advances in nanomaterials promise to expand our current concepts of conventional (grayscale) X-ray-based imaging into the world of digital color (3-channels, *e.g.* RGB) and beyond (much of the work presented here was done with a Medipix-3R camera capable of 5 energy channels, *i.e.* hyperspectral). Additionally, nanomaterials have shown promise for applications such as drug delivery and tissue ablation. The following introduction puts the current state of X-ray imaging in historical, theoretical, and practical context.

1.1.1 Setting the Stage: Light

Prior to the discovery of infrared (IR) light in 1800 and ultraviolet radiation in 1801, light was narrowly defined as those electromagnetic radiations in the visible part of the EM spectrum. As early as 1590, Dutch spectacle makers had begun experimenting with lenses which led to the development the first telescopes and microscopes. Lens technology evolved throughout the 16th, 17th, and 18th centuries by combining lenses of varying convexity/concavity and through the development of achromatic lenses. Isaac Newton is said to have built the first flat reflective surface in

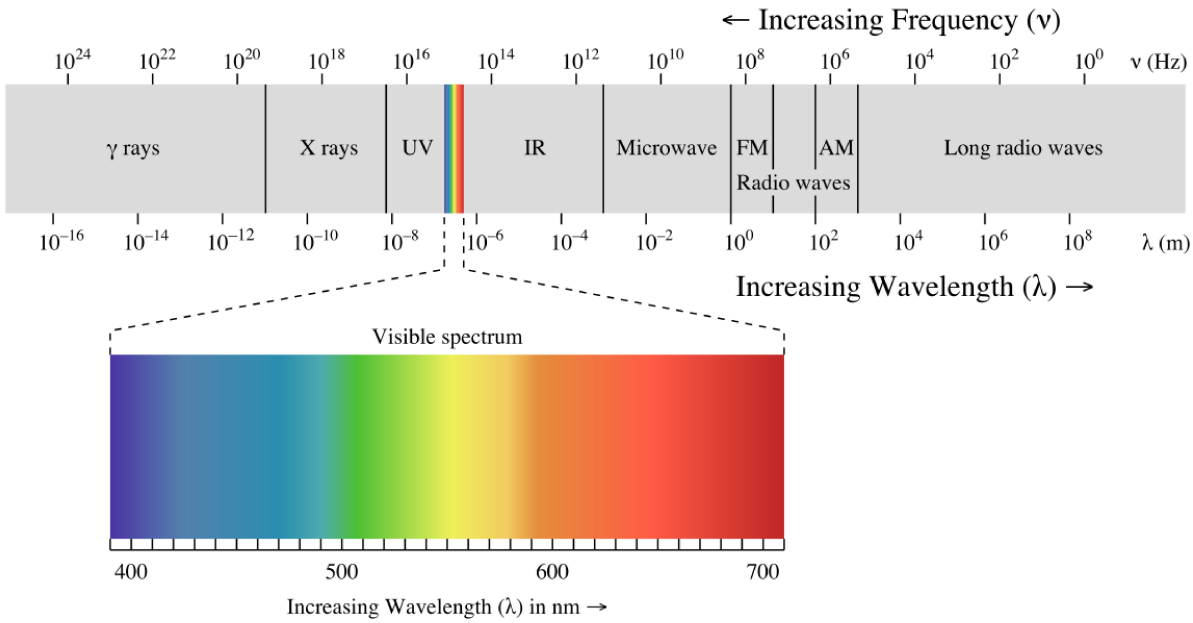

Fig. 1.1: The Electromagnetic Spectrum [1].

1668 which led to developments in mirror technology by changing the mirror geometry in 1721 and developing techniques for silvering (1857) and aluminizing (1932) the mirror surfaces to achieve greater reflectivity. Although visible light imaging (*i.e.* optical imaging) techniques are continually being developed for biomedical applications, these techniques followed several decades after the definition of light expanded to include both the visible spectrum as well as ionizing radiations, IR, microwaves (c.1920), and radio-frequency (RF, c.1888).

1.1.2 Physical Phenomena of Radiation

1.1.2.1 A German Nobel

In 1901, Wilhelm Conrad Röntgen was awarded the very first Nobel Prize in Physics for his 1895 discovery of the high energy (0.1-10000 keV) electromagnetic oscillations called, in his native German – röntgenstrahlung. Better known today as X-ray, these light photons are emitted from cathode ray tubes (CRT) and are considered "invisible" to the human eye. Despite their invisibility, Röntgen discovered them due to a curious interaction between a covered CRT and a distant screen coated in barium platinocyanide. Despite both the CRT covering and the distance between the CRT and the screen, when the tube had current (and therefore a voltage), the screen would fluoresce. Röntgen performed many of these experiments placing objects with differing

Fig. 1.2: This is the first roentgenogram (*i.e.* X-ray projection image) taken of Wilhelm Röntgen's wife's hand around 1895 [2].

thicknesses in between the source and detector, all the while characterizing the behavior of these mysterious rays. The quintessential image from this time period (c.1895) is indeed the birth of today's medical imaging industry which saw its first action in 1896 battlefields, where physicians used the technology to find embedded bullets. X-ray use for industrial imaging began in 1913 when the CRTs were upgraded by the Coolidge high vacuum X-ray tubes which could operate at 100 kilovolts (kVp). X-ray tubes upgraded in terms of operating voltage two more times before 1932.

1.1.2.2 The French-Polish Nobels

In 1903, Antione Henri Becquerel, Pierre Curie, and Maria Sklodowska-Curie also became Nobel Laureates for their discovery and work with natural forms of radiation, a.k.a. radioactivity. This phenomenon is seen as a release of γ-photons, β particles (electrons/positrons), free neutrons, and/or α nuclei from naturally occurring elements with unstable atomic structures. The lack of stability results in a natural decay in which these elements lose part of their mass in great release of energy the result of which is a more atomically stable element. Again, this discovery was aided by chance during Becquerel's ongoing study of sunlight induced fluorescence in naturally occurring materials. On a cloudy day in 1896, Becquerel placed some uranium in a bag with covered

photographic plates. When he later developed the films, he discovered that there had been an exposure that could not have been accounted for by the sun. He hypothesized (and proved with the help of Curies' 1898 discovery of polonium and radium) that the element itself was the source of the exposure he had captured on the plates. With the energy of the emitted γ-rays and other radiation being $10^0 - 10^3\times$ the energy of industrial X-rays produced by the best vacuum tubes of the day, radium-sources were quickly adapted for industrial radiography, allowing for imaging of high atomic number (high$-Z$) material objects >30 cm thick. Shortly after 1946, natural radium sources were quickly replaced by man-made cobalt and iridium sources which were both more radioactive and cheaper.

1.1.2.3 Physical Interactions: X-ray and Matter

A photon is a perturbation of an electromagnetic field. Put another way, it is one form of a fundamental quanta of energy, specifically of electromagnetic radiation (*i.e.* light) which carries an energy that is proportional to its wavelength. Each photon (light and ionizing radiation alike) travels in straight lines through vacuous space-time, from its source with initial power I_0 to its destination(s). The illuminance of the light source (*i.e.* the number of photons travelling through a given plane at any given time) can be expressed as a function in Cartesian space-time, dependent on the linear attenuation coefficient μ and density ρ of the materials which occupy the space of interest. μ is a function of space-time, λ_{eV}, and the atomic number Z in space. ρ is a function of space-time, temperature T, and the atomic number Z.

$$\Phi(x,\ y, z, t, \mu, \rho) \tag{1.1}$$

$$\mu(x,\ y, z, t, \lambda_{eV}, Z) \tag{1.2}$$

$$\rho(x,\ y, z, t, T, Z) \tag{1.3}$$

In many imaging scenarios, μ and ρ are considered constant in space and time (*i.e.* the object being imaged does not move across space-time during the window of time needed to capture an image). The most extreme contradictions to the previous statement include the specific research areas of cardiac imaging, motion correction, and angiography.

Unlike the low energy varieties of light (*e.g.* visible) which are reflected with mirrors, refracted with lenses, and randomly scattered in several materials (such as tissue), ionizing radiation can interact with the matter in one of the four ways represented in Fig. 1.4:

Table 1.1: $\mathbb{R}$ **and** $\mathbb{N}$ **refer to real number and natural number sets, respectively. The dimensions are length (L), mass (M), time (T), temperature (K), current (A), and 1 for unitless quantities.**

Quantity	Symbol	Base Units	Symbols	Dimension
Position ($\mathbb{R}^3$)	$F(X), X \leftarrow \langle x,\, y,\, z \rangle$	meter	$mm, pixel(\mathbb{N})$	L
Length	$\int F(X)dX$	meter	Å, nm, mm	L
Area	$\int\int F(X)\delta x\ \delta y$	square meter	mm^2, μm^2	L^2
Volume	$\int\int\int F(X)\delta x\ \delta y\ \delta z$	cubic meter	$\mu m^3, cm^3 \equiv mL$	L^3
Mass	m	kilograms	kg	M
Time	t	seconds	s	T
Wavelength	λ	meter	nm	L
Linear Atten. Coef.	μ	meters^{-1}	cm^{-1}	L^{-1}
Density	ρ	kg·meter^{-3}	$mg \cdot cm^{-3}$	$M{\cdot}L^{-3}$
Temperature	T	Kelvin	K	K
Plane angle	θ, ϕ, ψ	radian	rad	1
Solid angle	$d\Omega$	steradian	sr	1
Force	F	newton	$N \equiv kg \cdot m \cdot s^{-2}$	$M{\cdot}L{\cdot}T^{-2}$
Energy (heat)	E	joule	$J \equiv N \cdot m$	$M{\cdot}L^2T^{-2}$
Energy (of photon)	$\frac{hc}{\lambda} \equiv \lambda_{eV}$	electron-volts	$eV \equiv 1.602 \times 10^{-19} J$	$M{\cdot}L^2T^{-2}$
Speed of light	c	2.998×10^6	$m \cdot s^{-2}$	$L{\cdot}T^{-2}$
Planck's constant	h	6.626×10^{-34}	$J \cdot s$	$M{\cdot}L^2T^{-1}$
Power (energy flux)	I	watt	$W \equiv J \cdot s^{-1}$	$M{\cdot}L^2T^{-3}$
Irrandiance	Φ	watt· meter^{-2}	$W \cdot m^{-2}$	$M{\cdot}T^{-3}$
Radiance	$\Phi_{d\Omega}$	$W{\cdot}m^{-2}{\cdot}sr^{-1}$	$W \cdot m^{-2} \cdot sr^{-1}$	$M{\cdot}T^{-3}$

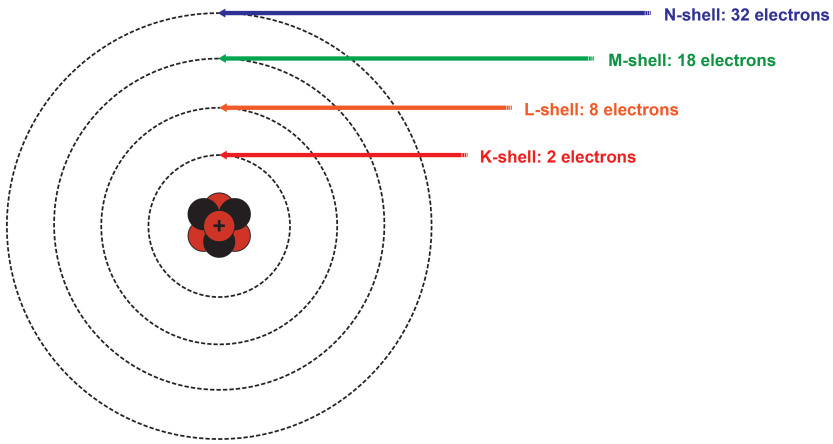

Fig. 1.3: The Bohr model representation of an arbitrary atom with labelled electron shells and vacancies.

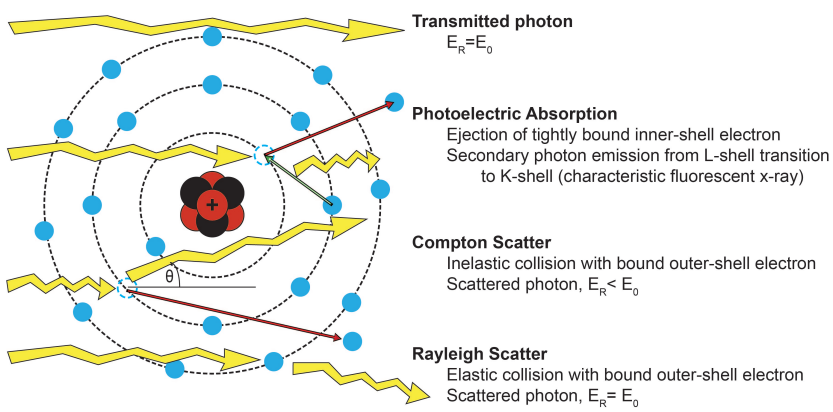

Fig. 1.4: The four major light-matter interactions in the 0.1-1.02 MeV energy range are depicted along with a populated Bohr model atom.

1. **Transmission:** Light continues its straight-line trajectory through matter without loss of power.

$$\frac{dI_r}{dr} = 0 \tag{1.4}$$

where I_r is the intensity along a single ray, dr is the distance traveled in space along a line defined by $\overrightarrow{r}$ such that

$$\overrightarrow{r} = \langle x_{,0}\,, y_0, z_0 \rangle + \Upsilon \langle dx, dy, dz \rangle \tag{1.5}$$

Υ is the parametric constant that determines the line's slope in the 3 linear dimensions. Irra-

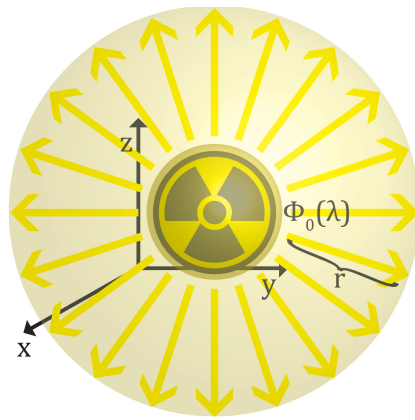

Fig. 1.5: A simplified representation of a divergent radiation source emitting in all directions with an intensity of I_0. The intensity flux of such sources decrease as one moves away from the source as per the inverse square law.

diance through the xy-plane is defined as

$$I_{x,y} = \int\int \Phi \; dx \, dy. \tag{1.6}$$

Irradiance measured through a fixed area of a spherical plane that is at a distance of r from a divergent source decreases as distance from the source increases as per the Inverse Square Law:

$$\Phi_r = \frac{\Phi_0}{4\pi r^2} \tag{1.7}$$

2. **Absorbance (photoelectric effect):** The energy carried by the absorbed photon is completely transferred to an electron which is ejected from its orbital when the energy transferred is large enough. The loss of an electron results in the absorbing matter taking on an "ion"-ized state. The point in space where this energy transfer occurs is stochastic in nature, yet the probability of a photoelectric event occurring in space-time increases with increasing atomic number Z^3, density ρ, and irradiance Φ. The probability of absorption *generally* decreases with increasing photon energy λ_{eV}. When applied to 3D macro-environments, the ease at which a material is penetrated by radiation is quantified by the material absorption coefficient μ_{abs}. The total irradiance from a source through a material i decreases according to the following, where $\mu_i(\lambda_{eV})$ is the material absorption coefficient as function of photon energy

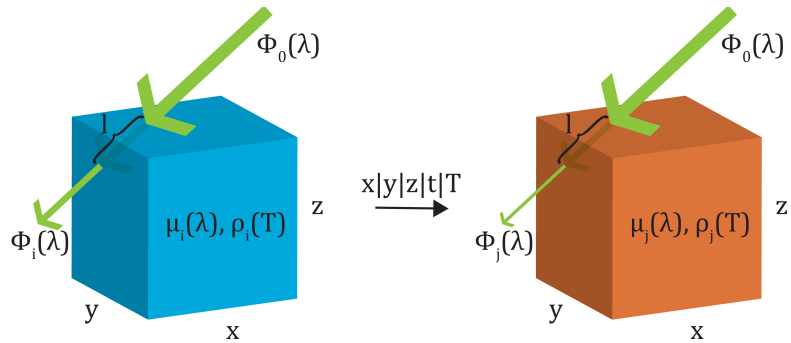

Fig. 1.6: For a given cubic volume of space that is occupied by matter i or j the irradiance of the light Φ_0 will decrease according to Eq. 1.8.

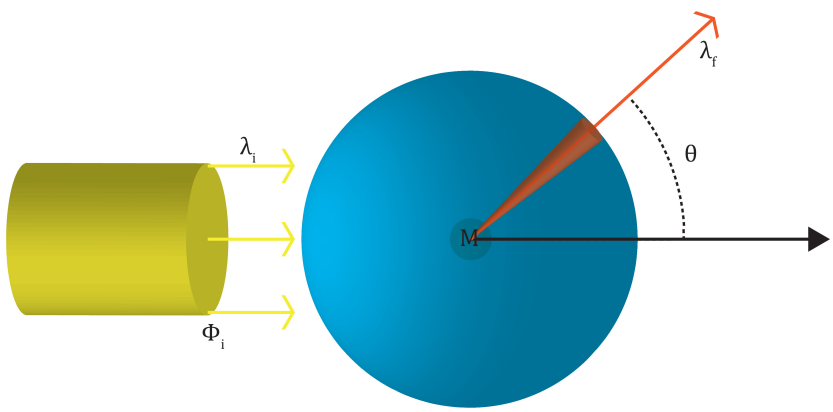

Fig. 1.7: Simplified diagram showing the Compton scattering interaction of material M. The image was adapted from [3].

and $\int \cdot dl$ is the length traveled through the material.

$$\Phi_i(\lambda) = \Phi_0(\lambda_{eV})\, e^{-\int \mu_i(\lambda_{eV})\, dl} \tag{1.8}$$

3. **Compton scatter:** The matter partially absorbs the energy of the incident photon λ_i resulting in a scattered photon whose vector is at an angle θ relative to the angle of incidence [3].

$$\lambda_{sc} = \lambda_i \frac{1}{1 + \epsilon(1 - \cos\theta)}, \tag{1.9}$$

where λ_{sc} is the energy of the scattered photons, $\epsilon = \lambda_i / m_e c^2$, m_e is the mass of an electron, and c is the speed of light.

4. **Pair production:** The creation of a quantum entangled electron-positron pair. For this to

occur, the photon's energy must meet or exceed the threshold equivalent to the total resting mass energy of the particle-pair or 1.02 MeV. The probability of this interaction occurring increases with λ_{eV} and atomic number Z^2.

The combination the linear absorption coefficient, the Compton cross-section, and pair-production cross-section for a given material at a given energy is the material's attenuation. Of these three *high-energy* photon-matter interactions, medical imaging is situated in the part of the spectrum that is dominated by photoelectric effect and Compton scattering. X-ray crystallography makes use of the Compton signal of atoms, whereas X-ray CT is primarily focused on the absorption properties of its sample.

1.1.2.4 Dose Units

Since many biomedical applications of radiation (*i.e.* X-ray CT, SPECT, PET, radiotherapy, etc.) require a human patient to be exposed to the ionizing energy, a system of measures has also been put into place in order to quantify the dose to which the patient is exposed in a given procedure. Table 1.2 expands on the quantities of Table 1.1 for this purpose.

Due to the stochastic nature of energy deposition from radiation in matter, several quantities are defined including exposure, absorbed dose, absorbed dose rate, and absorbed dose equivalent. Each quantity has its own units (and/or set of units) and its own history of use which has evolved over time.

Exposure is defined as the electric charge freed in the air of a specified volume by a source of radiation per unit mass of that air. The most widely used units of exposure today are $C \cdot kg^{-1}$ which replaced the units roentgen (R). For quantifying radiation damage, exposure has largely been replaced with the quantity absorbed dose (D). D describes the amount of energy deposited in material by ionizing radiation. The most commonly used units for absorbed dose are grays $\left(Gy\right)$ and rads (rad). A Gy is defined as one joule per kilogram of matter. The rate at which energy is deposited in matter ($\frac{\delta D}{\delta t}$) is defined as the absorbed dose rate. Finally, the quantity of absorbed dose equivalent ($D_{\equiv}$) accounts for the quality of the radiation and the sensitivity of the specific biological tissues being exposed in its calculation of damaging energy deposition. It has units of sieverts (Sv). The following equality demonstrates the relationship of each of these dose quantities and units.

$$(1\ J/kg = 1\ Gy = 100\ rad) \triangleq (1\ Sv = 100\ rem) \triangleq (114\ R = 0.02942\ C/kg) \tag{1.10}$$

Table 1.2: The dimensions are length (L), mass (M), time (T), temperature (K), current (A), and 1 for unitless quantities.

Quantity	Symbol	Base Units	Example Symbols to Scale	Dimension
Current	A	ampere	A	A
Charge	C	coulomb	$C \equiv s \cdot A$	T·A
Voltage	V	volt	$V \equiv W \cdot A^{-1} \equiv J \cdot C^{-1}$	$\mathrm{M{\cdot}L^2{\cdot}T^{-3}{\cdot}A^{-1}}$
Radioactivity	R	becquerel	Bq	$\mathrm{T^{-1}}$
Irradiance	Φ	watt· meter^{-2}	$W \cdot m^{-2}$	$\mathrm{M{\cdot}T^{-3}}$
Absorbed dose	D	gray, rad	$Gy \equiv J \cdot kg^{-1} \equiv 100\ rad$	$\mathrm{M^2{\cdot}T^{-2}}$
Absorbed dose rate	$\frac{\delta D}{\delta t}$	gray·s^{-1}	$Gy \cdot s^{-1}$	$\mathrm{L^2{\cdot}T^{-3}}$
Absorbed dose equiv.	$D_{\equiv}$	sievert, rem	$Sv \equiv J \cdot kg^{-1} \equiv 100\ rem$	$\mathrm{L^2{\cdot}T^{-2}}$
Exposure	X	roentgen	$R \equiv 2.58 \times 10^{-4}\ C \cdot kg^{-1}$	$\mathrm{M^{-1}{\cdot}T{\cdot}A}$

1.1.3 Measuring Irradiance and Power

The story of Röentgen's and Becquerel's discoveries of X- and γ-rays allude to the first generation of radiation detectors. In both cases, radiographic films (comprising of paper coated in metal emulsions) were used to capture the emissions from the CRTs and radioactive uranium. During his initial experimentation with X-rays, Röentgen's original platinocyanide-coated screen was replaced with a photographic plate made of glass covered in an emulsion of silver salts. Both plates and films require a secondary processing step called "development" to show the exposure of the surface to the radiation. This process, which is analog in nature, is depicted in Fig. 1.2.

The evolution of X-ray detectors from analog to digital follows the evolution of photography. First, the films and plates evolved into a combination of scintillating materials, lenses, amplifiers, photodiodes, and/or visible-light cameras. Scintillating materials are materials which when irradiated by X-ray give off a visible light fluorescence. To this day, the fastest scanners produced by the major CT manufacturers (*e.g.* GE, Phillips, and Siemens) are using a combination of scintillators and photodiodes. Various scintillating materials have been developed throughout the years which can differ in properties such as conversion efficiency and afterglow (*i.e.* the time after photon absorption during which the scintillator is giving off light) (see [4] for a detailed review). More recently flat-panel detectors made from direct-conversion semiconductors such as silicon have been developed. The evolution of more advanced semiconductor crystal growth has finally led to direct-conversion detectors which respond proportionally to the incoming photon's energy [5]. Combining these crystals (*e.g.* cadmium-telluride - CdTe; cadmium-zinc-telluride - CZT) with application-specific integrated circuits (ASICs), the individual electron cloud responses can be counted and binned through comparison to set analog signal thresholds. These detectors have been deemed "photon-counting detectors" (PCDs) and promise to allow for advanced imaging applications including "true-color" and molecular CT aided by advances in material science and nanomedicine.

1.1.4 Energy-integrating Detectors

The term "energy-integrating" refers to the behavior of detectors whereby any two incident monochromatic X-ray beams with differing energy and equal flux are registered equally by the detector. Said another way, X-ray photons produce a detector response in a flux-dependent, energy-independent manner in energy-integrating detectors (EIDs). EIDs are used in all forms of conventional radiography and CT. They are even used in several "dual-energy" spectral configurations.

Modern EIDs mostly take the form of scintillation detectors as the current materials used in the direct-conversion EIDs suffer from low charge yields, residual signal due to charge trapping, and gain spread from pixel-to-pixel at high dose rates [5]. In general, EIDs suffer from electronic noise sources (*i.e.* dark-field counts), Swank (s*i.e.* shot) noise, as well as the Poisson noise associated with detection of random processes.

While scintillating EIDs can achieve very fast acquisitions, their final images can suffer greatly from "beam-hardening". Beam-hardening artefacts arise from the fact that materials become increasingly transparent to photons with increasing energy. Therefore, more low energy photons are absorbed by the patient/object than high energy photons. When dense materials are present (*i.e.* bone or metal), most low-energy photons are absorbed, but the high energy photons move through the patient. Then at the level of detector, the photons are detected with weight proportional to the energetic flux the incident photons. Since the high energy part of source-spectrum will have higher flux levels, the overall signal is disproportionate and the reconstruction result will contain streaks around the dense area [6], [7]. Many methods have been developed to reduce these artefacts, specifically metal artifacts, as reviewed by Gjesteby *et al.* [8].

One major hardware-based solution (although software measures are needed to process the data) to beam hardening is through dual-energy acquisitions. Although there are many ways of achieving the dual-energy spectral measurements, they all involve (re)shaping the source beam such that most of the counts incident on the EID(s) are of low or high energy. The three major ways of achieving these separate spectral shapes are through (1) fast kVp switching, (2) source beam filtration, and (3) dual-layer EIDs. The fast kVp switching approach has been adopted by GE Healthcare in their Gemstone ™ Spectral Imaging (GSI) and makes use of the spectral shape change resulting from varying the voltage on the source tube as seen in the Fig. 1.8a where the red spectrum is a tungsten source operated at 80 kVp and the green spectrum is a tungsten source operated at 120 kVp. Alternatively, the spectrum shape can be altered by placing varying thicknesses of metals in the beam path (*e.g.* 2 mm glass, 1.96 mm aluminum, 2 mm copper, 0.375 mm brass, 4 mm titanium). This method has been adopted by some scanners produced by Siemens. The green and blue spectra in Fig. 1.8a depict the shape differences between a tungsten source filtered by 2 mm glass and 2 mm copper, respectively. The dual-layer detector approach takes on a similar logic as the pre-sample source filtration method of beam shaping. The key difference, however, is that the detector itself is filtering the incident photons with the top layer of the detector absorbing the low-energy photons but being largely transparent to the high-energy photons [9]. The dual-

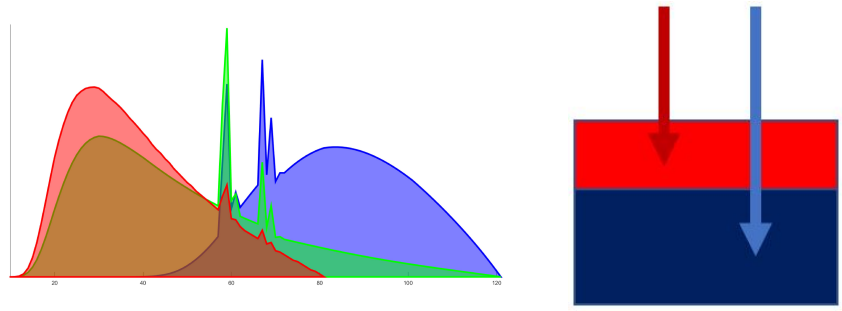

(a) (b)

Fig. 1.8: (a) The normalized spectra shapes of a tungsten source with 2 kVp and 2 filtration settings: (red) 80 kVp, 2 mm glass filter; (green) 120 kVp, 2 mm glass filter; (blue) 120 kVp, 2 mm glass + 2 mm copper filter. (b) A dual layer detector inherently filters the incident spectrum into low (red) and high (blue) energy measurement sets.

layer detectors can be found in the Philips IQon scanners. Fig. 1.8b shows a simple illustration of the dual layer approach where the red and blue arrows represent low and high energy photons, respectively. After acquiring the dual spectral responses, specialized analysis can allow for computation of "monochromatic" images or effective Z measurements that can eliminate beam-hardening artefacts [10] (more details in Section 1.3.6).

1.1.5 Photon-counting Detectors

In contrast to EIDs, photon-counting detectors directly convert single photon absorption events to measurable electrical signal [11],[12]. By coupling these direct-conversion pixels to specialized ASICs, the signals (which are proportional to the photon's energy), can be counted with respect to set signal thresholds which bound ranges of photon energy (*i.e.* energy bins). In this way, the spectra of photons that is incident on the detector is separated into multiple energy "channels". These detectors offer several advantages when compared to EIDs including low electronic noise (eliminated by noise-floor thresholding), no source of Swank noise, and small pixel sizes [5],[11]. Additionally, the ability to expand the number of spectral measurements promises to have applications toward new contrast agents and molecular imaging capabilities with X-ray [13]–[17]. Due to their single-photon sensitivity, PCDs have an inherently high SNR, however, they also have comparatively low count rates and are operated with levels of flux that are orders of magnitude lower than typical clinical scanners. While this is a dose reduction, low flux levels from the source can quickly result in count-starvation at the detector as the patient/sample size increases [18],[19]. For this reason, coupled with the expense and complicated manufacturing process involved in growing

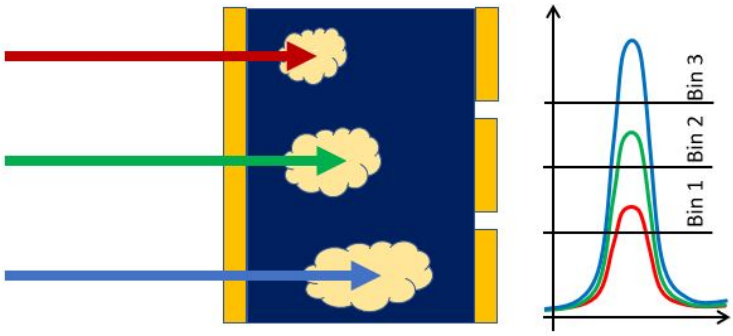

Fig. 1.9: A simplified illustration of a photon-counting detector.

the ceramic semiconductors used in PCDs, they have yet to find their way into the clinic.

The beam-hardening artefacts seen in EIDs are inherently handled by PCDs due to two physical mechanisms: (1) each photon is counted individually (as opposed to flux proportional signal) and therefore equally weighted over the energy bin [20]; (2) the energy bins over-which photons are counted cover a much smaller range than EIDs. In fact, in multi-energy bin PCD imaging, beam-hardening is still present in the low energy bins, but it is certainly reduced. Advanced reconstruction techniques may be able to eliminate these artifacts altogether in multi-energy spectral imaging.

Fig. 1.9 shows a simplified illustration of a photon-counting detector discriminating the energy of the incoming photons (*i.e.* red arrow is low energy, green arrow is higher energy, and blue arrow is highest energy). After photon absorption, an electron cloud is generated in the semiconducting crystal. A bias voltage is placed on the crystal causing the electron cloud to migrate through the detector and be collected at the cathode electrode pixels. The collected electrons are amplified and compared to set thresholds with the associated count added to the appropriate channel. Both simulation and experiments have shown that the size of the electron cloud increases with increasing migration distance and increasing photon energy [21], [22]. On one hand, higher energy photons penetrate deeper into the detector before being absorbed; on other, low energy photon-induced electron clouds must travel further in the detector crystal to reach the counting electrode. Given these opposing sources of electron cloud size, the most recent detector simulations consider the size of electron clouds as a constant with respect to both incoming energy and distance traveled in the detector [23]. Often, PCD detector simulations assume that the electron cloud travels in a perpendicular vector to the charge collection surface. This assumption, however, is an oversimplification as the direction of travel for the charges follows field lines in the crystal (which can vary

with incident flux) [24].

1.1.5.1 Spatio-energetic Crosstalk

Despite the advantages that PCDs offer, there are detector behaviors that occur in PCDs which can degrade the spectral fidelity of the measured photons. Each of these behaviors has a relationship with flux-rate and/or pixel surface area and is born out of the fundamental X-ray/matter interactions described in Sec. 1.1.2.3. Their individual and combined effects cause non-linear counting to occur within the detector.

- **Charge-sharing** arises from the post-absorption electron cloud spilling over pixel boundaries (depicted in top left of Fig. 1.10). This causes a registration of two or more photon counts in a neighborhood of pixels. Each of the counts has registered energy that is proportional to the amount of the original cloud that was collected by the respective pixel. This behavior increases linearly with flux, but has an inverse, non-linear relationship with pixel size.

- **Fluorescence Escape** arises from the secondary X-ray photon that is emitted after the vacancy left by the original absorbed photon ejects a photoelectron (depicted in the top right of Fig. 1.10). At some probability the secondary photon altogether escapes the detector. The escape probability is linked to the secondary photons energy (*i.e.* Kα/Kβ fluorescence of the detector material), the distance from the emission point to the surface/edge of the detector (the depth is linked to the primary photon's energy), and the direction of the emission (all directions are equally likely). In the event of the escaped fluorescence, the measured photon energy is equal to the incident energy minus the energy of the fluorescence photon. This phenomenon has a linear relationship with flux, but no relationship with pixel surface size.

- **Long-distance Fluorescence Reabsorption** has the same beginnings as escaped fluorescence, but rather than the fluorescence photon escaping the detector, it is reabsorbed by a neighboring (*i.e.* within a certain radius) pixel (depicted in the bottom left of Fig. 1.10). Like with charge-sharing, the result is the registration of multiple counts. The total energy registered will be equal to the incident photon, but with one of the multiple counts having the energy of the fluorescence photon. This phenomenon will have a linear relationship with flux and an inverse, nonlinear relationship with the pixel size.

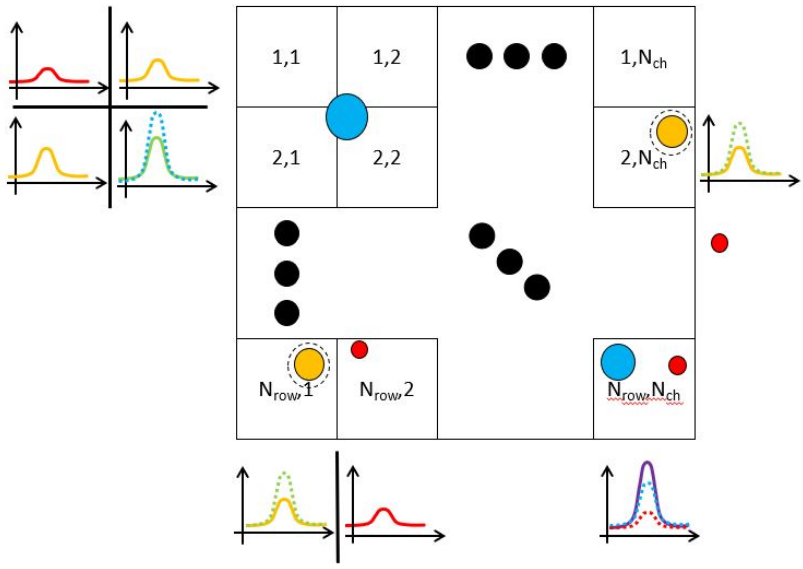

Fig. 1.10: The nonlinear counting behaviors seen in PCDs result in spatio-energetic crosstalk between nearby pixels. These behaviors include charge-sharing, fluorescence escape, long-distance fluorescence, and pulse pileup (shown left-to-right, top-to-bottom).

- **Pulse-pileup** is the result of two or more photons coincident on a single pixel (depicted in the bottom right of Fig. 1.10). The count responses will superimpose, resulting in a single count whose energy is the sum of all the coincident photon energies. This behavior has nonlinear relationship with both the pixel size and flux rate [25].

Though listed separately, each of these effects is always occurring across all pixels and therefore can interact (*i.e.* a fluorescence photon can be split, or a pulse-pileup charge can be minus fluorescence energy). Several groups have made attempts to model these cross-talk phenomena (minus pulse-pileup) and their efforts have culminated in proprietary software known as the Photon-counting Toolkit (PcTK) [23], [26]. The software, which is used in the simulation framework outlined in Chapter 2, uses a spatio-energetic probabilistic model to (re)distribute the simulated photons incident on a central pixel in a 3x3 neighborhood. The model has tunable parameters, such as charge cloud radius, pixel size, and spectral spread standard deviation (called "electronic noise"), which effect the spectral response function (SRF) of the model. After count redistribution, different noise models (Gaussian vs. Poisson) can be utilized to add noise to the n-tuple or 2-tuple counts, respectively. n-tuple here is referring to how many counts occur as the result of single incident photon due to charge-sharing with more than 1-pixel, multiple fluorescence events, etc.

1.1.5.2 Medipix3R Charge-summing Mode

MARS Bioimaging has incorporated the Medipix3R CZT detector (developed at CERN) into their commercially available microCT [27]–[29]. This detector module has built in circuitry which aims to, all but, eliminate the nonlinear counting behavior associated with charge-sharing and long-distance fluorescence. The charge-summing mode (CSM) is describe in detail by Pennicard [30]. Briefly, when a photon is absorbed by a pixel, the eight neighbors are momentarily arrested (*i.e.* kept from counting) and queried for any instances of simultaneous counts. When found, the charge in the 2x2 neighborhood in which these simultaneous counts occur is pooled and attributed to the pixel with the maximum registered energy (winner takes all). At low flux rates, the circuit is an effective solution to the count and spectral distortions attributable to the charge-sharing and *most* long-distance fluorescence. Increased flux rates can overwhelm this circuitry, leading to further degradation of counting behaviors (*e.g.* general loss or non-registration of counts).

The Medipix3R, however, has a combination of material and pixel size which keep the CSM from eliminating the distortions introduced by long-distance fluorescence. Specifically, the cadmium (Cd) atoms of the detector crystal have Kα and Kβ fluorescence with 23.17 and 26.09 keV, respectively. Both energies are just below the Cd K-edge (26.73 keV) resulting in relatively long mean-free paths (*i.e.* average distance travelled before an absorption event), specifically 114.6 μm and 159.5 μm, respectively. Since the Medipix3R was built with 110 μm^2 pixels there is a significant portion (30%) of the reabsorbed fluorescence photons which escape the 2x2 neighborhood over which the charge-summing circuitry.

1.2 System Geometries

Figs. 1.5-1.7 have clear indications regarding the important geometries that one must be familiar with when working in CT (e.g. circles, helices, right triangles, fans, cones, solid angles, squares, and cubes). Briefly, the parametric equation of a circle is

$$\frac{(x-c_x)^2}{R^2} + \frac{(y-c_y)^2}{R^2} = 1 \tag{1.11}$$

where (c_x, c_y) are the coordinates for the circle center and R is the circle radius. Related to the equation of a circle is the idea of polar coordinates. Using Pythagorean theorem and given a set of

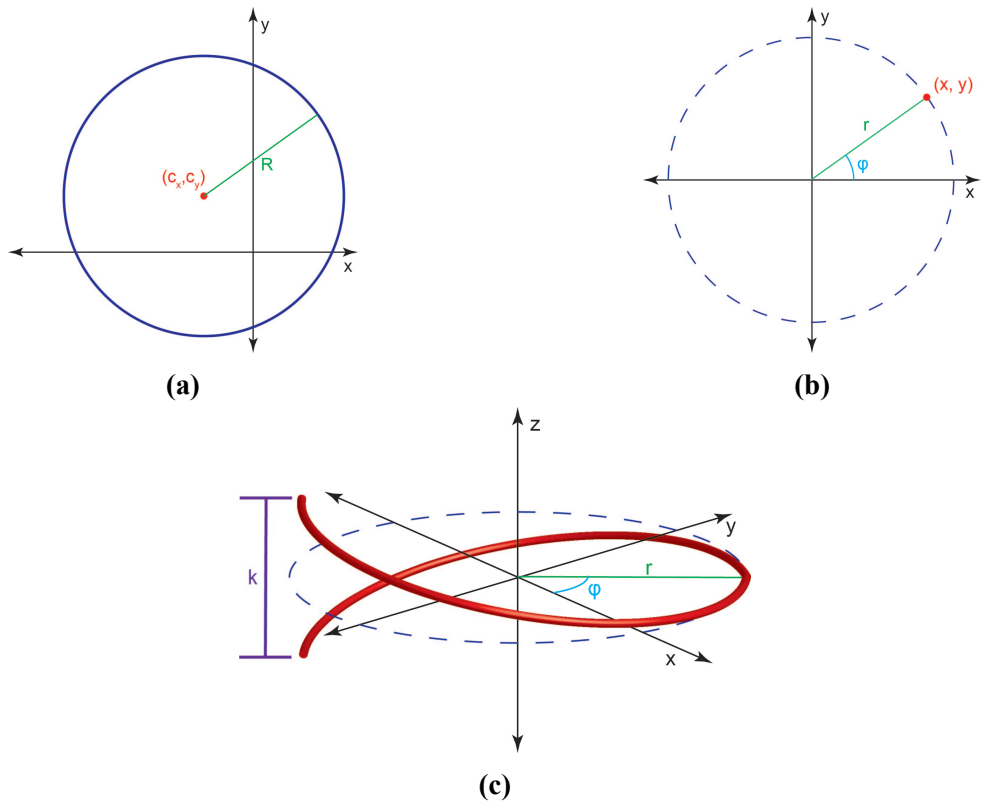

Fig. 1.11: Basic parametric geometries: (a) circle, (b) polar coordinates, and (c) circular helix.

polar coordinates (r, ϕ), the corresponding Cartesian coordinates can be calculated as

$$(x = r\ \cos\phi,\ \ y = r\ \sin\phi). \tag{1.12}$$

Extending polar coordinates into three dimensions, the parametric equations for a helix can be written as

$$(x = r\ \cos\phi,\ \ y = r\ \sin\phi,\ \ z = \frac{k\,\phi}{2\pi}) \tag{1.13}$$

where k is the helix pitch. $\theta \in [0 : \frac{2\pi}{n} : 2\pi)$ would provide n points over one full rotation of the helix which translates k in the z-direction. Fig. 1.11 depicts these basic parametric geometries.

These geometries and coordinate transformations serve as the basis for defining X-ray source and detector trajectories during computed tomography data collection. Many geometric and mathematical frameworks have been developed over the years to allow for accurate 2D and 3D data reconstruction from corresponding 1D and 2D projection images, respectively. Each of these methods builds on the previous and will be briefly introduced in the following subsections. Kak *et al.* [31] should be consulted for a detailed derivation of the methods introduced below as many of the equa-

tions presented here are adapted from that resource.

1.2.1 2D Parallel Beam

The simplest 2D tomography geometry, parallel beam, is a direct corollary from the Radon transform. For a given object, defined here as $f(x,\, y)$, placed in a global $x,\, y$-coordinate system, the projection through the object at a line defined by $t = x\ \cos\theta + y\ \sin\theta$ is [31]

$$\begin{aligned} P_\theta(t) &= \int_{(\theta,t)line} f(x,\, y)\ dl \\ &= \int_{-\infty}^{\infty}\int_{-\infty}^{\infty} f(x,\, y)\delta(x\ \cos\theta + y\ \sin\theta - t)\ dx\ dy \end{aligned} \tag{1.14}$$

where $P_\theta(t)$ is the Radon transform of $f(x,\, y)$. This type of projection geometry can be achieved by translating a single source and detector (*i.e.* pixel) in parallel across the sample at a set angle. Once enough line integrals have been collected to span the object a projection has been made; and the process can be repeated over several angles so that multiple projection views are collected around the sample. Notably, the views collected along any line (θ, t) and its conjugate ray $(\theta + \pi, -t)$ will be equivalent. Therefore, collecting views from $[0, \pi)$ is enough for image reconstruction in the parallel beam geometry. Fig. 1.12a depicts a parallel beam projection at a single angle.

1.2.2 2D Fanbeam

Another 2D scanning geometry can be defined based a single source point from which many rays emanate in a fan. The fanbeam geometry can be equiangular by choosing an arc detector or by arranging a linear array such that the spacing of the pixels collect rays at equally-spaced angles (*i.e.* the outer detector pixels cover larger areas). Alternatively, the fanbeam detector can consist of a linear arrangement of equally-spaced detector pixels. Fig. 1.12b depicts a fanbeam projection at a single angle. For the sake of brevity, only the backprojection equations for the equally-spaced linear detector will be provided. To simplify the derivation of these equations from the parallel beam equations, an imaginary linear array is often defined going through the origin. With this imaginary detector array, a few extra angular and distance quantities are defined for the purpose of extending the parallel beam analytical reconstruction algorithms for fanbeam reconstructions. The angle of the central beam of the fan with the vertical image axis is defined as β and the angle that any outer beam makes with the central beam is defined as α. The perpendicular distance from an outer beam to the central beam is defined as t and the angle that this vector makes to the horizontal image axis

is θ. Finally, the distance from the source to the imaginary detector is D. These quantities have the following relationships to the parallel beam geometries [31]:

$$\begin{aligned} t &= s\ \cos\alpha \qquad \theta = \beta + \alpha \\ t &= \tfrac{sD}{\sqrt{D^2+s^2}} \quad \theta = \beta + \arctan\tfrac{s}{D} \end{aligned} \tag{1.15}$$

The projection from the source to the imaginary detector is defined here as [31]

$$R_\beta(s) = \int_{(\beta,s)line} f(x,\, y)\ dl \tag{1.16}$$

1.2.3 3D Cone-beam

Through the extension of the 1D linear detector array to a 2D planar array, the 2D fanbeam geometry naturally extends to a 3D conebeam geometry. The center plane made by the central line of detector pixels (wrt. the source point) will be a true fanbeam geometry while each of the off-center lines of pixels will have an angle γ with the center plane. If the source has a circular trajectory, the data collected will not be sufficient for a stable 3D reconstruction (*i.e.* it does not satisfy Tuy's condition). Methods such as the Feldkamp-Davis-Kress method have been developed to approximate a stable 3D reconstruction. When needed in this thesis, a simpler alternative, cosine correction, is used to approximate fanbeam data at the off-center detector lines. That is [31]

$$\hat{R}_{\beta,\gamma}(s) = R_{\beta,\gamma}(s)\ \cos\gamma. \tag{1.17}$$

The true power of the conebeam geometry is exploited through its coupling with the helical source/detector trajectory. The equations and methods needed to reconstruct the data collected in this manner are beyond the scope of this thesis.

1.3 Reconstruction

An informative, albeit general, overview of various reconstruction models can be found in the recently published tutorial by McCann and Unser [33]. Descriptions of specific algorithms can be found for: fanbeam [34], cone-beam [35]–[37], algebraic [38], [39], energy-selective [40], dictionary learning [41], parallelization/CUDA implementations [42], spectral reconstruction [43]–[53], neural network-based approaches [37], [54]. This list is far from exhaustive, but they will certainly

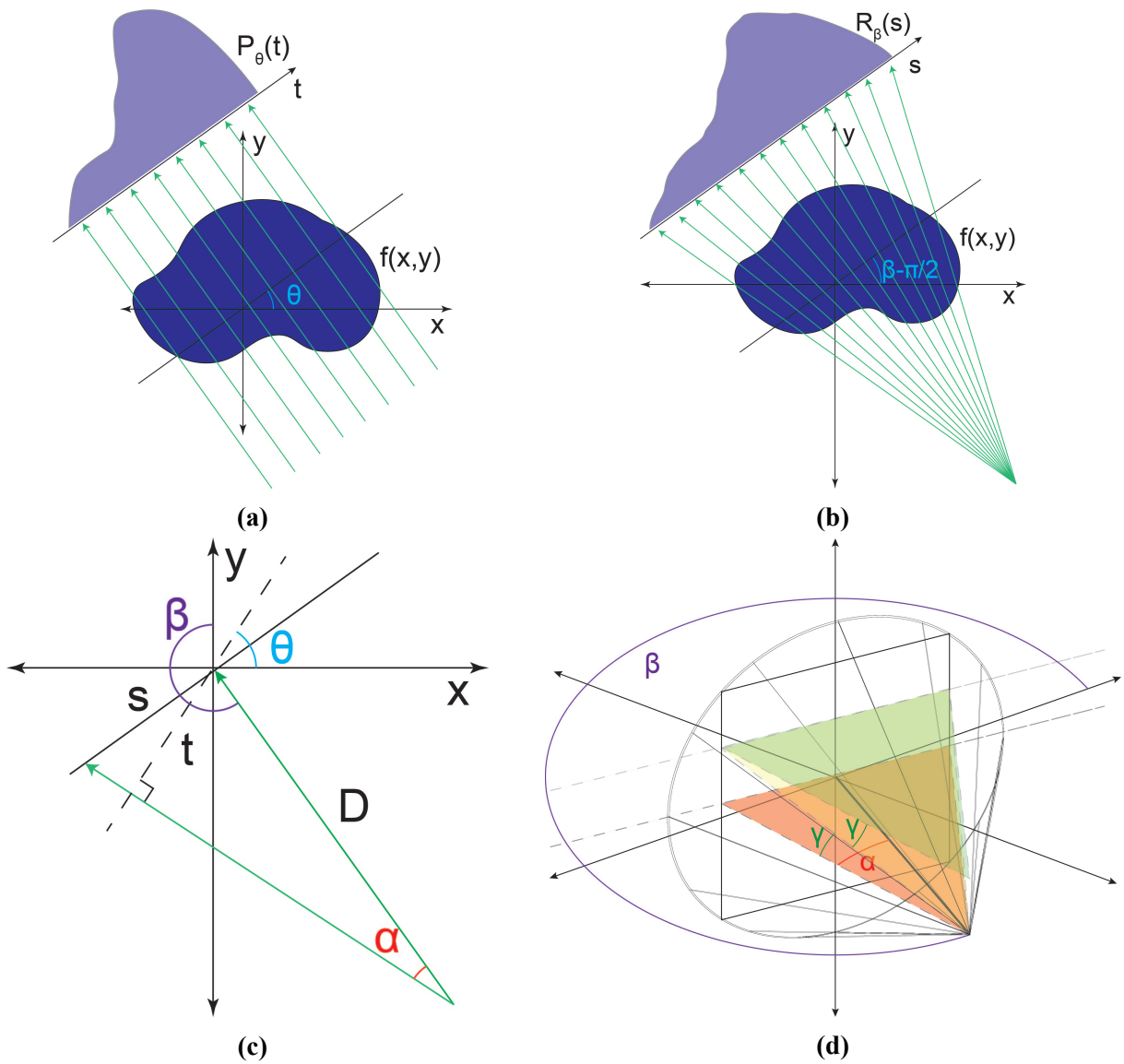

Fig. 1.12: (a) The parallel beam geometry and (b) fanbeam geometries are the most common 2D tomographic geometries for non-diffracting sources. (c) Derivation of the filtered backprojection algorithm in the fanbeam geometry from the parallel beam equations require the definition of the additional angular quantities α and β as well as the distance measures D, s, and t. (d) The cone-beam geometry has one additional angle parameter γ which is used in the cosine approximation (shown as the green fan) for use with the fanbeam analytical reconstruction methods. Images were adapted from [31], [32].

provide a framework from which to pull ideas and inspiration regarding future reconstruction implementations. Several references in this list will be further explored in later sections. First, however, the bed-rock of image reconstruction, its analytical framework (wrt to imaging geometry), is presented.

1.3.1 The Central Slice Theorem

A key concept and theorem for reconstructing collected projection data is the Central Slice Theorem (CST; a.k.a Fourier Slice Theorem). In lieu of a full derivation of the theorem a few key equivalencies are defined to get a full understanding of the implications of CST. First, the 2D Fourier transform of $f(x,\, y)$ is defined as [31]

$$F(u,\, v) = \int_{-\infty}^{\infty} \int_{-\infty}^{\infty} f(x,\, y) e^{-j2\pi(ux+vy)}\, dx\, dy. \tag{1.18}$$

Second, the projection at angle θ ($P_\theta(t)$) and its 1D Fourier transform is defined as

$$S_\theta(w) = \int_{-\infty}^{\infty} P_\theta(t) e^{-j2\pi wt}\, dt \tag{1.19}$$

The key equation of CST then is an equivalency between the 1D Fourier transform of the projection at angle θ and the line of the object's 2D Fourier transform that is subtended by the same angle [31]:

$$\begin{aligned} S_\theta(w) &= \int_{-\infty}^{\infty} \int_{-\infty}^{\infty} f(x,\, y) e^{-j2\pi w(x\, \cos\theta + y\, \sin\theta)}\, dx\, dy \\ &= F(w\, \cos\theta,\ w\, \sin\theta) \\ &= F(w,\ \theta) \end{aligned} \tag{1.20}$$

Therefore, by taking 1D Fourier transforms on a set of finite projection angles, the values of $F(u,\, v)$ along the same collection of angles can be determined. The inverse Fourier transform can be used to recover the object if $F(u,\, v)$ is known.

1.3.2 Filtered Backprojection

Although CFT provides the theoretical basis for using the inverse Fourier transform to reconstruct the object image, in practice it requires the whole of the object's 2D Fourier transform to be known (*i.e.* an infinite number of projection angles). Since taking infinite measurements is not conducive to real-world applications, other algorithms are needed for accurate image reconstruction

from a finite number of measurements. Filtered backprojection (FBP) represents the most basic of the analytical algorithms which address this need.

The parallel beam FBP algorithm takes the following form [31]:

$$f(x,\, y) = \int_0^{\pi} Q_\theta(x\ \cos\theta + y\ \sin\theta)\ d\theta \tag{1.21}$$

where

$$\begin{aligned} Q_\theta(t) &= \int_{-\infty}^{\infty} S_\theta(w) H(w) e^{j2\pi wt}\ dw, \\ &= \int_{-\infty}^{\infty} P_\theta(t')\, h(t-t')\ dt', \end{aligned} \tag{1.22}$$

$$H(w) = |w|\, b_w(w), \quad b_w(w) = \begin{cases} 1, & |w| < W \\ 0, & otherwise \end{cases}, \tag{1.23}$$

and

$$h(t) = \int_{-\infty}^{\infty} H(w) e^{j2\pi wt}\ dw \tag{1.24}$$

Eq. 1.22 represents the filtering operation in "filtered" backprojection. The first line of this equation is the Fourier domain operation where the 1D Fourier transform of an angular projection is multiplied times the filtration kernel $H(w)$ where W is the cut-off frequency of the filter. The second line is the convolutional representation of the filtration operation.

The fanbeam geometry's FBP algorithm can be directly derived from the parallel beam equations and the relationships outlined in the Section 1.2.2. Its final representation takes the following convolutional form with the image given in polar coordinate system (*i.e.* (r, ϕ) vs (x, y)) [31]:

$$f(r,\, \phi) = \int_0^{2\pi} \frac{D}{D + r\sin(\beta - \phi)} \int_{-\infty}^{\infty} R_\beta(s) g(s' - s) \frac{D}{\sqrt{D^2 + s^2}}\ ds\ d\beta \tag{1.25}$$

where

$$g(s) = \frac{1}{2} h(s) \tag{1.26}$$

The equations presented above are continuous function representations of the filtered backprojection algorithmic basis. In practice, these equations need to be discretized due to the limited number of detector pixels, projection views, and the digital nature of the reconstructed images. The discretization, though non-trivial, can be found in the Kak chapter [31]. No further discussion of these

analytical (or direct conversion) reconstruction algorithms will be had, but rather other formulations of the reconstruction problem will be presented in the following sections.

1.3.3 Algebraic Reconstruction

The remaining algorithms to be presented here make use of the linear system model

$$Ax = b. \tag{1.27}$$

For the reconstruction problem, A represents a system matrix which describes the imaging process (*i.e.* intersections of ray projections and image voxels over all acquired angles for a given source-detector configuration), b is the collected sinogram, and x is the image to be reconstructed. Solving the inverse problem can be achieved with iterative, algebraic methods [38], [39] with the iterative equation

$$x^{k+1} = x^k + \lambda_k \frac{b_i - \langle a_i, x^k \rangle}{\|a_i\|^2} a_i^T \tag{1.28}$$

where x^k is the kth iteration of the image reconstruction, λ is the relaxation parameter, b_i is the ith component of the vector b, a_i is the ith row of the system matrix A, $\langle u, v \rangle$ gives the inner product of u and v, $||u||^2$ gives the square magnitude of u, and u^T denotes the transpose of the vector u. The algebraic formulation presented can incorporate prior information to improve the reconstruction result.

1.3.4 Statistical Reconstruction

Building on the algebraic method, statistical image reconstruction uses a similar linear model can be expanded to include a noise term ϵ,

$$Ax + \epsilon = b. \tag{1.29}$$

With ϵ taking a known form (*e.g.* Gaussian or Poisson), the inverse problem can now take on the following form:

$$\underset{x}{\operatorname{argmin}} \frac{1}{2}\|b - Ax\|_2^2 + \sum_r \lambda_r R_r(\cdot) \tag{1.30}$$

where the mean-square error term represents the data fidelity and the $R_r(\cdot)$ functions are the regularizing functions. These functions are weighted by λ_r which is used to balance the regularization and data fidelity. This function is derived from the max *a posteriori* (MAP) estimator according

to Bayesian law. Regularization can be applied directly to x or, depending on the method used for solving this minimization, to the auxiliary variables needed for solving the method. The solution of the minimization problem presented here will be the reconstructed image. Many regularization functions which represent prior information or assumptions about the image space have been researched. These include spatially independent and Markov random field model-based priors, compressed-sensing (*e.g.* L_1, $L_p(0 < p < 1)$, and L_0 norms), nonlinear neighborhood filter-based, patch-based, dictionary-learning [41], and prior image regularizations [55]. After the formulation of the final objective function, iterative schemes are employed to solve the problem when a closed-form solution is unattainable. These methods tend to be relatively slow (compared to FBP) and a major challenge for these methods is hyperparameter (λ_r) tuning. Machine learning and neural network approaches have been adopted to "LEARN" the necessary parameters [37], [56].

1.3.5 Spectral Reconstruction

The problem of reconstructing spectral CT data is not different from the conventional problem in terms of geometry or system modeling, but rather it differs by expanding b and x from rank-n tensors to rank-$n+1$ tensors (*i.e.* matrices to volumes in 2D reconstruction and volumes to hyper-volumes in 3D reconstructions). The simplest way of tackling this dimension increase is to sequentially reconstruct the energy volumes as if they are independent image sets. It is a rather naive approach given the large correlation between energy bins. Several methods have been proposed which expand the methods of regularization into the spectral dimension [43]–[53].

One such method - prior rank, intensity, and sparsity model (PRISM) - was proposed by our group [57]. This model is based on the idea that overall spectral image (X) is the combination of a low rank sample "background" (X_L) and the channel specific sparse signals(X_S). Mathematically, that can be represented as

$$X = X_L + X_S \tag{1.31}$$

with the objective function following as

$$(X_L, X_S) = \underset{X_L, X_S}{\operatorname{argmin}} \|A(X_L + X_S) - Y\|^2 + R(X_L, X_S). \tag{1.32}$$

The regularizations that are enforced in this model are meant to ensure low-rank, sparsity,

and overall image smoothness/contrast as follows

$$R(X_L, X_S) = \lambda_* \|T_L(X_L)\|_* + \lambda_1 \|T_S(X_S)\|_1 + \lambda_t \|X\| \tag{1.33}$$

where $\|\cdot\|_*$ is the nuclear norm, $\|\cdot\|_1$ is the L_1 norm, and $\|\cdot\|$ is a regularizing norm. Each regularization term is multiplied by a respective relaxation term (λ_*, λ_1, λ_t). The functions $T_S(\cdot)$ and $T_L(\cdot)$ are tight framelet (TF) transforms which are used to strengthen the respective rank/sparsity regularizations. Two different TF models are used in the 2011 paper but suffice it to say that both are static convolutions across the respective X tensor. This type of transform lends itself well to be learned using a supervised CNN. This type of approach can also learn the respective relaxation parameters which are notoriously hard to determine. Future work in this area may look to merge the ideas put forth in the LEARN network [56] with the PRSIM model. Fig. 1.13 shows a potential framework for developing a neural network implementation of the PRISM reconstruction algorithm.

1.3.6 Image Domain Material Decomposition

The expansion of the spectral data dimension afforded by spectral photon-counting detectors also allows for the linear attenuation model used in conventional CT images to be expanded into other linear combination models that have been deemed "material decomposition". More specifically, the linear attenuation values measured in each energy bin (image domain) can be modeled by none other than the previously given linear combination model (Eq. 1.27). For the linear material decomposition (MD) model, the variables b, A, and x represent the approximated linear attenuation coefficients (from the reconstruction), a model matrix, and basis images, respectively. Intuitively, the number of material bases that the linear MD model can separate is limited by the number of measurements, else the problem becomes ill-posed. With noise present in the images, like the noisy model shown in Eq. 1.29, even systems which have equal measurements and unknowns can be ill-posed.

The model that one chooses to apply to the MD problem can differ based on application and data. Three are mentioned below. The first is a purely physical model which can be used for dual energy data. The two linear attenuation coefficients are decomposed into a photoelectric absorption

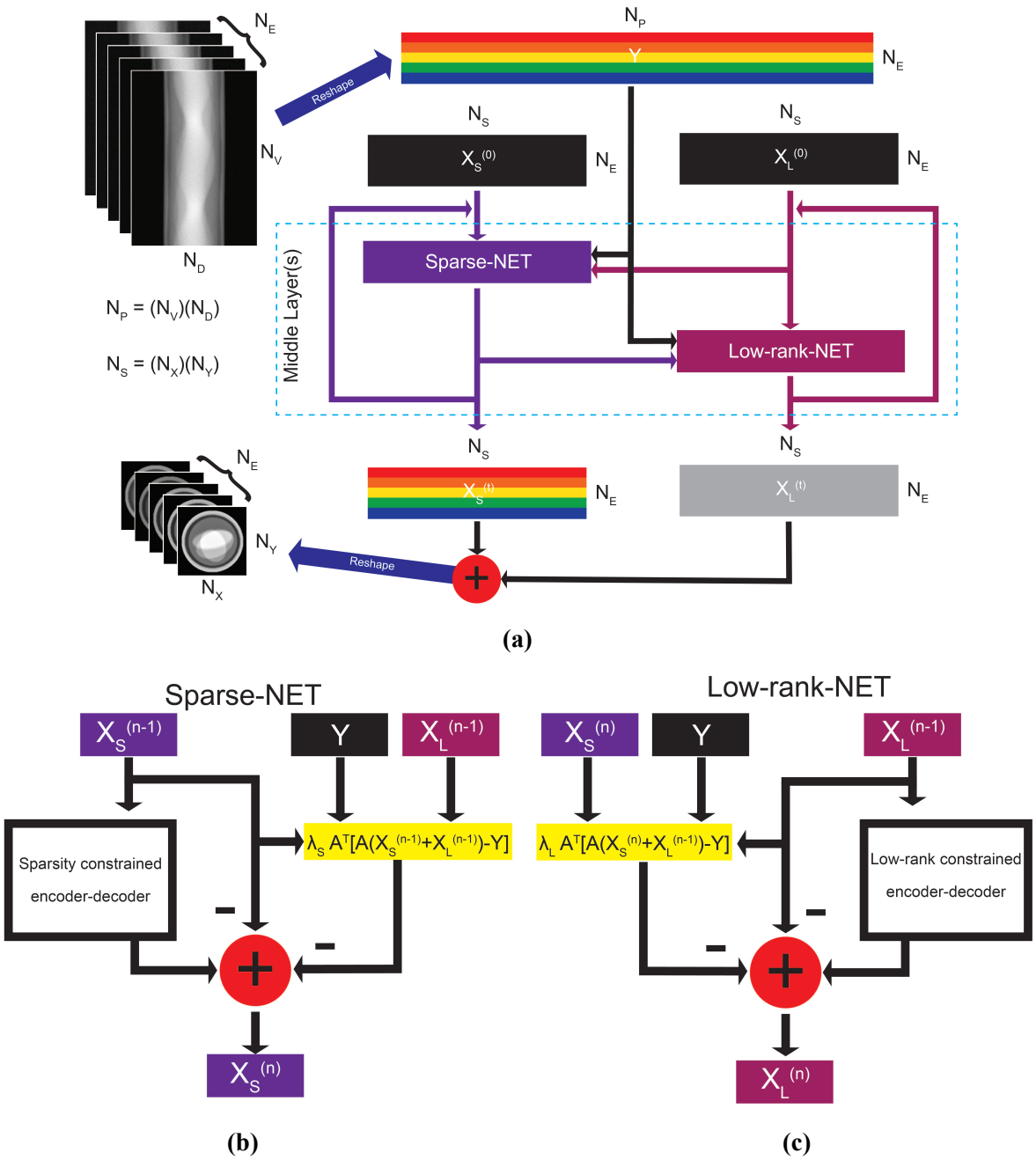

Fig. 1.13: (a) CNN-based implementation of the PRISM algorithm. (b) Sparsity constraining arm. (c) Low-rank constraining arm. Final implementations of the encoder-decoder portions of the networks are still being discussed.

and Compton scatter component [58], [59].

$$\mu(E,x) = \underbrace{a_{ph}(x)\frac{1}{E^3}}_{\text{Photoelectric}} + \underbrace{a_{Co}(x) f_{KN}\left(\frac{E}{E_e}\right)}_{\text{Compton Scatter}} \tag{1.34}$$

In this model, there are two physical interaction components rather than "material components". The fraction in the photoelectric term and the Klein-Nishina function ($f_{KN}\left(\frac{E}{E_e}\right)$) can be pre-computed and arranged in an A model matrix. From there the same inversion methods used in reconstruction or a simpler linear least square (LLS; nonnegative liner least square, NNLLS) [60] may be used to solve for the basis images a_{ph} and a_{Co}. It is from this type of model that Z-equivalent and monochromatic image estimates can be estimated [61].

When the detectors can measure more than two energy bins, the physical model can be expanded to include more physical phenomena (namely K-edge discontinuities) [58], [59].

$$\mu(E,x) = \underbrace{a_{ph}(x)\frac{1}{E^3}}_{\text{Photoelectric}} + \underbrace{a_{Co}(x) f_{KN}\left(\frac{E}{E_e}\right)}_{\text{Compton Scatter}} + \underbrace{\sum_k a_k(x) f_k(E)}_{\text{K-edge}} \tag{1.35}$$

Several publications have used this model coupled with LLS or NNLLS to approximate the basis images for K-edge containing contrast materials (*i.e.* iodine, gadolinium, gold) [16], [62], [63].

The final model that has been described in several papers is a volumetric density model. In this model the approximated linear attenuation coefficients (b) are decomposed into material basis images containing volumetric density approximations (x) using a model matrix (A) which contains candidate material mass attenuation coefficients.

$$\begin{bmatrix} \mu_1(x) \\ \mu_2(x) \\ \vdots \\ \mu_n(x) \end{bmatrix} = \begin{bmatrix} \frac{\mu_{1,1}}{\rho_1} & \frac{\mu_{1,2}}{\rho_2} & \cdots & \frac{\mu_{1,m}}{\rho_m} \\ \frac{\mu_{2,1}}{\rho_1} & \frac{\mu_{2,2}}{\rho_2} & \cdots & \frac{\mu_{2,m}}{\rho_m} \\ \vdots & \vdots & \ddots & \vdots \\ \frac{\mu_{n,1}}{\rho_1} & \frac{\mu_{n,2}}{\rho_2} & \cdots & \frac{\mu_{n,m}}{\rho_m} \end{bmatrix} \begin{bmatrix} \rho_{V1}(x) \\ \rho_{V2}(x) \\ \vdots \\ \rho_{Vm}(x) \end{bmatrix} \tag{1.36}$$

This model is used by the MARS Bioimaging team and is coupled with some other heuristic approaches (*e.g.* segmentation or angular rejection) [13], [64], [65]. This model has also been adopted for more advanced inversion methods [66], [67] as well as machine learning approaches to solving the problem [68], [69].

While the formal approach to MD requires solving the inverse problem, a few publications have also found segmentation-based approaches to be effective in identifying and quantifying materials in the image domain [64], [70].

It is worth mentioning that the dual energy model and approach to MD is highly effective for most modern clinical imaging procedures. In fact, the use of contrast today in CT is limited to iodine injection and the increased contrast from the relatively high-density material is easily identifiable in patients. For some applications, such as plaque characterization, there may be some confusion between the calcium signal and that of the iodine. The onset of PCDs promises further advances in areas such as nanomedicine, semiconductor science, and pharmacological targeting since it will be through these mechanisms that new K-edge containing contrast materials can be used in a clinical setting with the "holy grail" being multiplexed, molecular X-ray CT.

1.4 System Metrics

A recent series papers published by the Pelc group as Stanford between 2015-2018 [18], [19], [71]–[73], have linked the problem spaces of materials decomposition, denoising, detector physics, and the quality metrics that have been used for years to quantify performance of conventional systems. Rajbhandary *et al.* found by using simulations that the material basis estimation bias has nonlinear relationships with aspects of the imaging systems; specifically, bias increased with any change to the system or imaging parameters that reduced the number of photons measured by a given energy bin (*i.e.* low flux, wide spectrum, more bins, and projections per dose level) [18]. Then, Persson *et al.* provided a statistical framework with which bias and variance are shown to be on either end of an image artifact balancing point. Through denoising of images using anticorrelated noise models, reduced image variance is seen but at the expense of areas of extreme bias (*i.e.* high frequency portions of the image) [19]. This led to a linear systems theory which gives a statistical framework for performance characterization of PCDs that is a direct generalization of those used for conventional detector performance [71]–[73] . Thus, the following is a quick overview of imaging metrics/statistics [74], [75].

It is pertinent to first define the statistical quantities of image mean and image variance.

$$\mu_{image} = \frac{1}{n}\sum_{n} f(n), \quad \sigma^2_{image} = \frac{1}{n-1}\sum_{n}\left(f(n) - \mu_{image}\right)^2 \tag{1.37}$$

$f(n)$ is the reconstructed image or detector frame. Image noise (*i.e.* image standard deviation) is

defined as

$$\sigma_{image} = \sqrt{\sigma_{image}^2}. \tag{1.38}$$

The above quantities are considered over all pixels n in an image or detector frame. These could also be defined over a subregion(s) of the image/detector (*i.e.* region-of-interest; ROI). In the case that the image/frame is not a flat level of signal (*i.e.* many regions in the frame), the calculation of image noise will be best calculated over one subregion, otherwise the varying signal levels will artificially inflate the calculated noise.

With image noise properly calculated, signal-to-noise ratio (SNR) is defined as [74], [75]

$$SNR = \frac{\mu_{ROI}}{\sigma_{image}}. \tag{1.39}$$

Alternatively, we can calculate difference (*i.e.* contrast) between two subregions using the contrast-to-noise (CNR) as [74], [75]

$$CNR = \frac{\mu_{ROI1} - \mu_{ROI2}}{\sigma_{image}}. \tag{1.40}$$

System resolution can be quantified through calculation of modulation transfer function (MTF). Proper calculation of this metric involves frame capture of either (1) a source point (*e.g.* from a pinhole camera) or (2) a line phantom which contains several sets of line pairs of varying spreads and thicknesses. Upon acquisition of the corresponding frames, a 1D Fourier transform can be calculated over a line of pixels containing the source point or line pairs ($I(u) = FFT[f(n)]$). The output of this function will provide a measure of contrast amplitude with respect to spatial frequency.

A similar system metric, noise power spectrum (NPS), measures the variation of the contrast amplitude with respect to spatial frequency [76].

$$NPS(u) = \frac{1}{k}\sum_{l=1}^{k}\frac{1}{N_l} \tag{1.41}$$

where k is the number of rays through the image region and N_l is the average number of detected photons.

Signal-to-noise ratio can be alternatively defined in terms of MTF and NPS such that [74],[75]

$$SNR_{out}(u) = \frac{MTF(u)}{\sqrt{NPS(u)}} \tag{1.42}$$

This definition can then be used to further quantify system noise with respect to the individual quanta that the detector measures by defining the quantity called noise equivalent quanta (NEQ) such that [71], [74], [75]

$$\begin{aligned} NEQ(u) &= SNR_{out}(u)^2 \\ &= \left(\frac{N}{\sqrt{N}}\right)^2 \\ &= \frac{q_0^2 G^2 MTF^2(u)}{NPS(u)} \quad \text{(EID)} \\ NEQ(u,E,E') &= \sum_k \sum_{k'} q_0(E) H_k(u,E) * [W_{d+}^{-1}]_{k,k'}(-u) * H_{k'}(u,E') q_0(E') \\ &\qquad \text{(PCD)} \end{aligned} \tag{1.43}$$

where N is the number of incident quanta on a Poisson counting detector ($counts \sim P(\lambda)$) which give the same output SNR as on a non-ideal detector, q_0 is the mean incident flux, and G is the detector gain. In the PCD equation, H_k is the signal transfer function, W_{d+} is the noise cross spectral density matrix, E is energy, and k, k' are energy bins. Finally, detective quantum efficiency (DQE) which measures how effectively the incoming photons are used in generating signal is defined as [71]

$$\begin{aligned} DQE(u) &= \frac{SNR_{out}(u)^2}{SNR_{in}(u)^2} \\ &= \frac{NEQ(u)}{N} \\ &= \frac{NEQ(u)}{q_0} \quad \text{(EID)} \\ DQE(u,E,E') &= q_0(E)^{-1/2} NEQ(u,E,E') q_0(E')^{-1/2} \quad \text{(PCD)} \end{aligned} \tag{1.44}$$

1.5 Thesis Outline

The remaining chapters of this thesis expand on the concepts, methods, and ideas presented in this introduction. Each of the chapters tackles a different challenge facing the current state of the MARS imaging pipeline (see Fig. 8.1). Chapter 2 outlines the layout, key algorithms/functions, and use cases for the spectral CT simulation package which was developed through the combination proprietary and open-source MATLAB packages: PcTK, ASTRA toolbox, and TomoPhantom. Working examples of phantoms generated and reconstructed in this simulation framework are

shared.

Chapter 3 demonstrates the detector-level, empirical count correction algorithm that was developed and implemented on real MARS scanner detector data. The data shown represents the linear range correction, and an expansion of the method into the nonlinear range is discussed. The PcTK simulation is used in this chapter as an "ideal model" reference.

Chapter 4 describes a hardware solution for enhancing resolution. The configuration is modeled in the Monte Carlo environment MCNP6.1 and real data is shown which demonstrate modest spatial resolution enhancement through the aperture encoding method described.

The final three chapters deal in the material decomposition space, though each of them has a unique take on the problem. Chapter 5 begins approaching the MD problem by first demonstrating the inherent separation potential between known K-edge materials when imaged with PCDs. This chapter focuses on statistical hypothesis testing and linear dimension reduction methods to analyze the data. Chapter 6 expands on the linear methods by kernelizing the known subgroups and developing a segmentation and quantification method. The utility of this method is demonstrated using both simulated and real datasets where in either case the method can identify more unique materials than energy bin measurements (under key assumptions). Chapter 7 describes the ability of a simple 8-layer convolutional neural network (CNN) to decompose simulated phantoms with up to 8 material combinations and only 5 energy measurements. The results in this chapter show great promise for the future of MD using neural networks.

Chapter 8 summarizes the work described in this thesis, putting it all in context of the MARS scanning pipeline.

Chapter 2
Photon-counting CT Simulation in MATLAB

2.1 Introduction

This chapter describes the graphical user interface (GUI) that was built to mimic the geometry and photon-counting detector of the MARS spectral micro-CT. This software combines the well-documented and supported ASTRA toolbox, TomoPhantom toolbox, and photon-counting toolkit (PcTK). The ASTRA toolbox comes equipped with GPU-compatible forward-projection, back-projection, and algebraic reconstruction algorithms for 2D and 3D geometries. The TomoPhantom toolbox allows for quick generation of custom 3D phantoms. The PcTK models the output signal of a 2D CdTe detector array for a given X-ray spectrum, material attenuation coefficients, detector parameters (*e.g.* pixels size, detector thickness, etc.), and material basis sinograms. This chapter describes (1) the datasets that are necessary to prepare prior to using this spectral scanner simulator, (2) how phantoms are generated, (3) how data is generated for a desired scanner geometry, (4) what algorithms are used to map multiple detector chip data streams to a single ”ideal detector”, and (5) the rebinning and reconstruction methods. that are available to reconstruct the output data.

2.1.1 Motivation

This GUI can be utilized as a teaching tool or as an experimental interface for direct comparison with real photon-counting detector data or for the development of algorithms (*i.e.* count corrections, reconstruction, and/or material decomposition). In fact, the simulation GUI is capable of “scanning” random samples in bulk which can allow for efficient generation of the data needed to train machine learning and deep neural network architectures that can begin to address the challenges associated with photon-counting systems including non-linear counting behaviors, image denoising, and material decomposition. Finally, the simulator was built from a set of open-source (*i.e.* ASTRA and TomoPhantom toolboxes) and proprietary (*i.e.* PcTK) software packages which encouraged a modular structure to the code. This plug-and-play framework should allow for flexible implementations of the simulation to be developed that parallel updates to the software or specific experimental conditions including scanning geometry, phantom generation, detector models, and reconstruction algorithms.

As a teaching tool, the simulator requires inputs that emulate the physics (or are directly

measured) from the numerous aspects of the spectral CT imaging system. The fact that it is a graphical user interface allows for direct interaction and manipulation of the system physics that can foster a deep understanding of the system that a book or command-line code may not offer beginning students. Indeed, the tool has already been deployed to teach undergraduate and young graduate student researchers the basic physics underlying the spectral CT imaging system. The underlying physics used for conventional CT are the same (up to the detector physics) as those presented in the spectral CT simulator. Therefore, this simulator can be used to teach the fundamentals of CT in general, from source filtering and sample attenuation to the effects of simple and complex detector geometries.

Since the simulation provides a framework for modeling the whole scanning system, its utility need not be limited to the development of detector level corrections or reconstruction algorithms alone. As an example, the simulation has already been used to (1) justify assumptions in empirical count correction schemes (Chapter 3, (2) verify the PRISM reconstruction framework (not reported), (3) train neural network architectures for non-linear behavior and Poisson-noise denoising (not reported), and (4) develop segmentation algorithms and train neural network architectures for use in material decomposition applications (Chapters 6 and 7).

2.2 Using the GUI

2.2.1 Location

The most recent implementation of the spectral micro-CT simulator can be found in

getzim@gewang-deepreconserver.bme.rpi.edu:
\home\getzim\MATLAB\spectral_geometry_simulation_v7_GPU.m

The figure itself was developed in MATLAB's Graphical User Interface Developer's Environment (GUIDE) and can be found in

getzim@gewang-deepreconserver.bme.rpi.edu:
\home\getzim\MATLAB\spectral_geometry_simulation_v7_GPU.fig

By right-clicking on the above filename in the `Current Folder` section of the MATLAB interface and selecting `Open in GUIDE` each element (*i.e.* text, push button, axes, table, etc.) can be

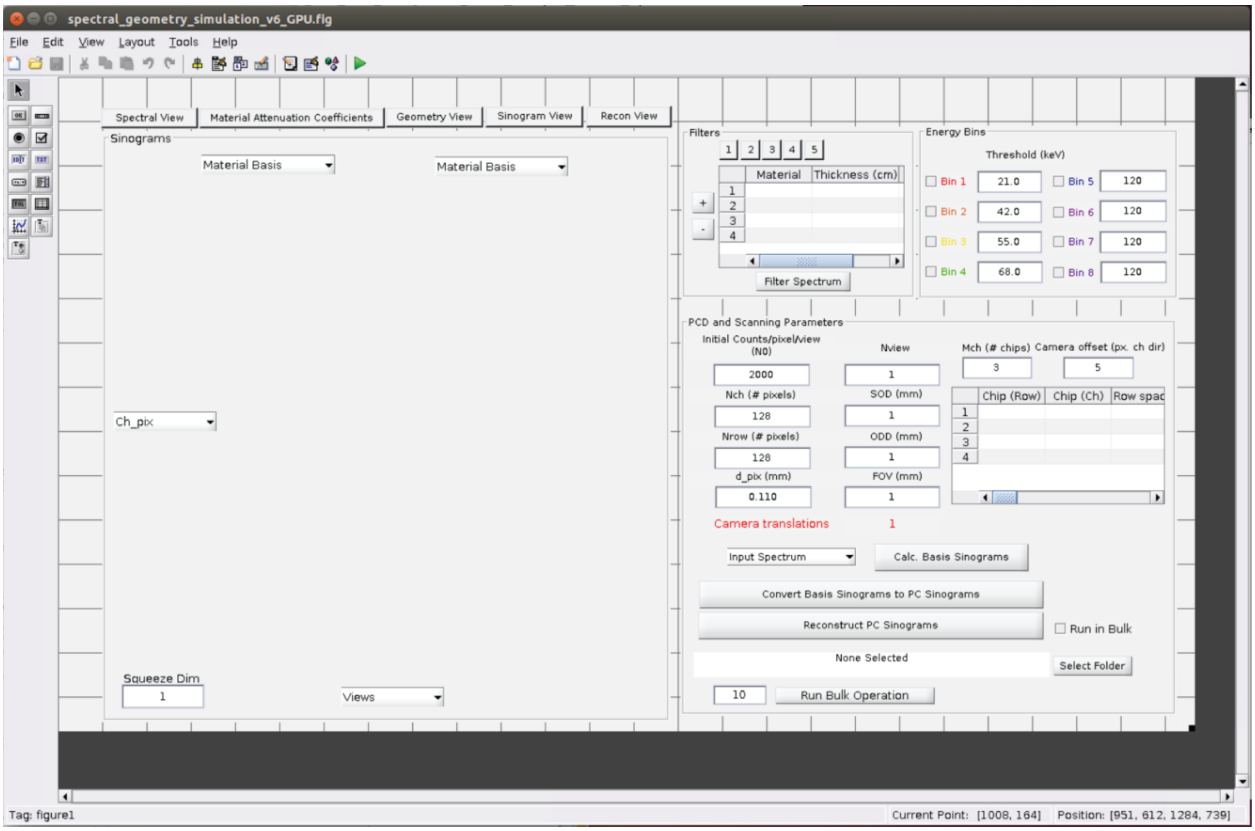

Fig. 2.1: When opened in MATLAB's GUIDE, each element of `spectral_geometry_simulation_v7_GPU.fig` can be adjusted. This includes the Callback functions (*i.e.* what happens when you press a given button).

customized and the Callback functions can be defined and adjusted. Figure 2.1 shows the GUI figure opened in the developer's environment. By interfacing with the GUI in the GUIDE mode, a detailed understanding for each button's functionality can be attained by beginning users. Indeed, in the case that new functions are desired or old functions need debugging, it is a good idea to start here in order to navigate through the various functions and files called by the buttons/fields.

In addition to the `.mat` and `.fig` files mentioned above, the following `.m` files are called by various buttons in the form of `Callback` functions and should be included in the working directory (or path) of the main GUI codes:

- `generatePhantom.m` : function which creates a random 2D head phantom consisting of several ellipses of random sizes consisting of random water + contrast material mixtures given GUI-defined input parameters. It is called a head phantom due to the outside ellipse containing bone.

- `generatePhantom3D.m` : function which uses `TomoPhantom`'s function, `TomoP3DObject`,

to create a random 3D head phantom consisting of several ellipsoids of random sizes consisting of water + contrast material mixtures at random concentrations [34], [77]. The contrast materials are a user-defined input parameter.

- `generateMatCalPhantom3D.m` : function which uses `TomoPhantom`'s function, `TomoP3DObject`, to create a 3D head phantom consisting of several ellipsoids of fixed sizes consisting of fixed concentrations of water + contrast material mixtures [34], [77]. The contrast materials are user-defined input parameters.

- `circular_geometry_w_phantom_ASTRA_v7.m` : script that compiles GUI-defined input parameters which define the geometry and trajectories of the source, each detector chip, and the ideal detector.

- `planar_array_ideal.m` : function called inside `circular_geometry_w_phantom_ASTRA_v7.m`, this function provides the pixel coordinates of the ideal detector.

- `planar_array_ASTRA_FP.m` : function called inside `circular_geometry_w_phantom_ASTRA_v7.m`, this function outputs the forward projection value as well as the pixel coordinates for the detector chip specified as input. ASTRA toolbox functions `astra_create_proj_geom`, `astra_mex_data_3d`, and `astra_create_sino3d_cuda(_mg)*` are called in this function [78], [79]. *The `_mg` extension is an altered code to allow for GPU specification.

- `ideal_det_trans.m` : function called inside `circular_geometry_w_phantom_ASTRA_v7.m`, this function uses the ideal detector and individual chip coordinates to map the sinogram data from the individual chips to the ideal detector with proper use of bilinear interpolation.

- `translate_proj_to_ideal.m` : script which translates the photon-counting data for each detector chip and maps them to the ideal detector using the maps output by `ideal_det_trans.m`.

- `FAN2PARA_custom.m` : function called during the reconstruction of the photon-counting data. Used to convert the central vector of the ideal detector pixels from pseudo-fanbeam geometry (pseudo because in a conebeam geometry is used in forward projection) to parallel

beam so that analytic methods of reconstruction such as filtered backprojection (FBP) can be used.

Further explanation of these codes as well as their underlying geometries and algorithms will be discussed in the order that they are encountered during a typical run of the simulator.

2.2.2 First Glance

The GUI can be loaded by simply typing the filename (a.k.a. the function name) into the MATLAB command line and pressing `ENTER` or by clicking the green triangle in the top of the GUIDE window. Figure 2.2 is a screen capture taken directly after running the function. The following top buttons can be seen upon opening the GUI (indicated by the red box and arrows seen in Figure 2.2):

- **Spectral View** (`push button`) : This button controls the appearance of any loaded spectra as well as the Spectral Panel.

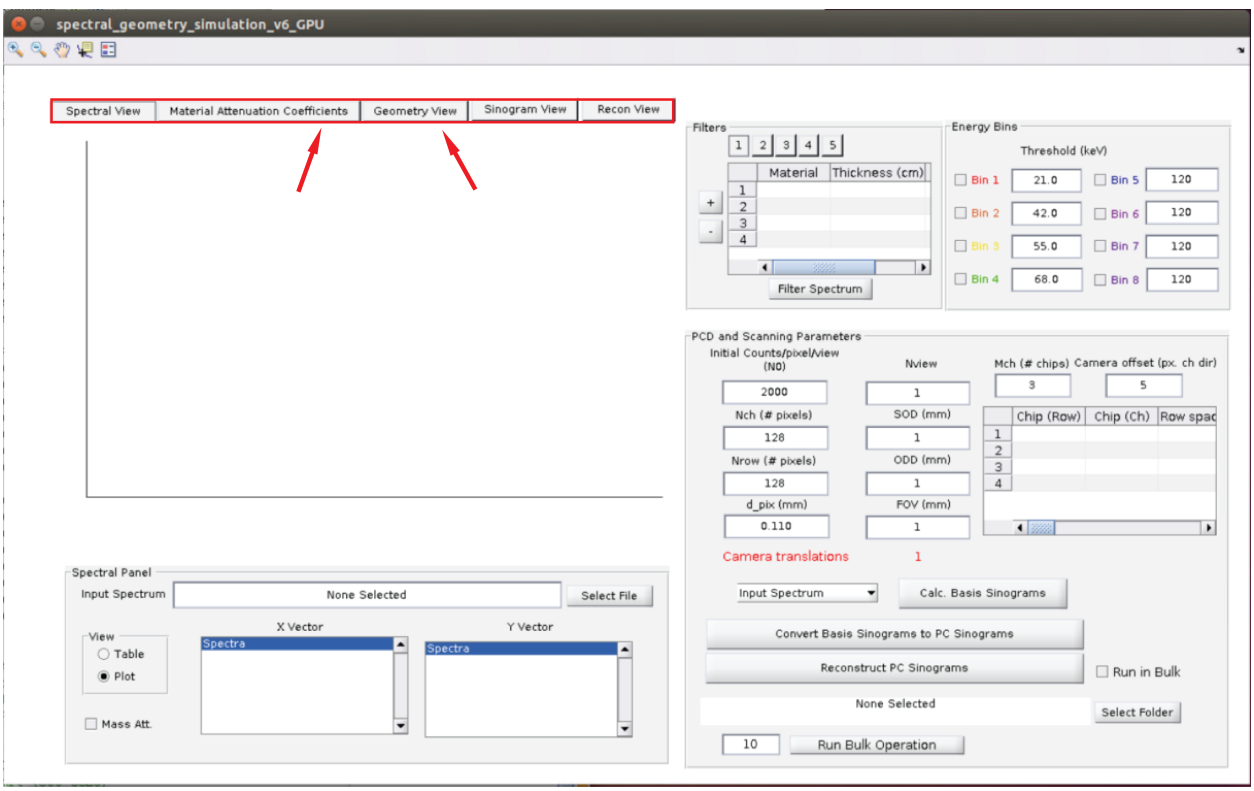

Fig. 2.2: The opening state of the GUI contains five (5) top buttons, four (4) panels (two of which contain tables), and one (1) axes.

- **Material Attenuation Coefficients** (`push button`) : This button switches the axes to show the loaded table of material-specific densities and linear attenuation coefficients. It also replaces the Spectral Panel with a Material Panel.
- **Geometry View** (`push button`) : This button again changes the axes to show a single slice of the phantom geometry. When pressed, the area currently occupied by the Spectral Panel is replaced by a `listbox` containing phantom creation options and a `push button` which resets the phantom slice.
- **Sinogram View** (`push button`) : This button changes the axes to display any calculated sinograms (either material basis or simulated photon-counting results).
- **Recon View** (`push button`) : *This button has no current function, although it should serve the purpose of displaying any reconstruction results on the axes.*

In addition to the top buttons, an axis and several panels are also visible. These will be addressed individually as we proceed through the process of simulating a scan.

2.2.3 Setting a Save Directory

Press the `Select Folder` button in the bottom right corner of the `PCD and Scanning Parameters` panel to select a save directory. `.mat` files are added to this folder after the automated creation of a material phantom, calculation of the material-basis sinograms, the completion of the PcTK data conversion, and reconstruction of the photon-counting sinograms. *Errors will be thrown during the creation of phantoms or any subsequent action if this directory is not specified.*

2.2.4 Loading X-ray Spectra and Material Attenuation Coefficients

After setting the output directory, the user should load the `.csv` files which contain the source spectra and material properties of interest. The following directions assume a fresh start of the GUI, however, the `push buttons` described in the previous section can be pressed in any order and/or can be resubmitted if a new spectra or material file is desired.

2.2.4.1 X-ray Spectra

In the `Spectral Panel`, press the `Select File` button to open a file browser. Select the `.csv` which contains one column of X-ray energy levels (*e.g.* 1-120keV in 1 keV increments) and

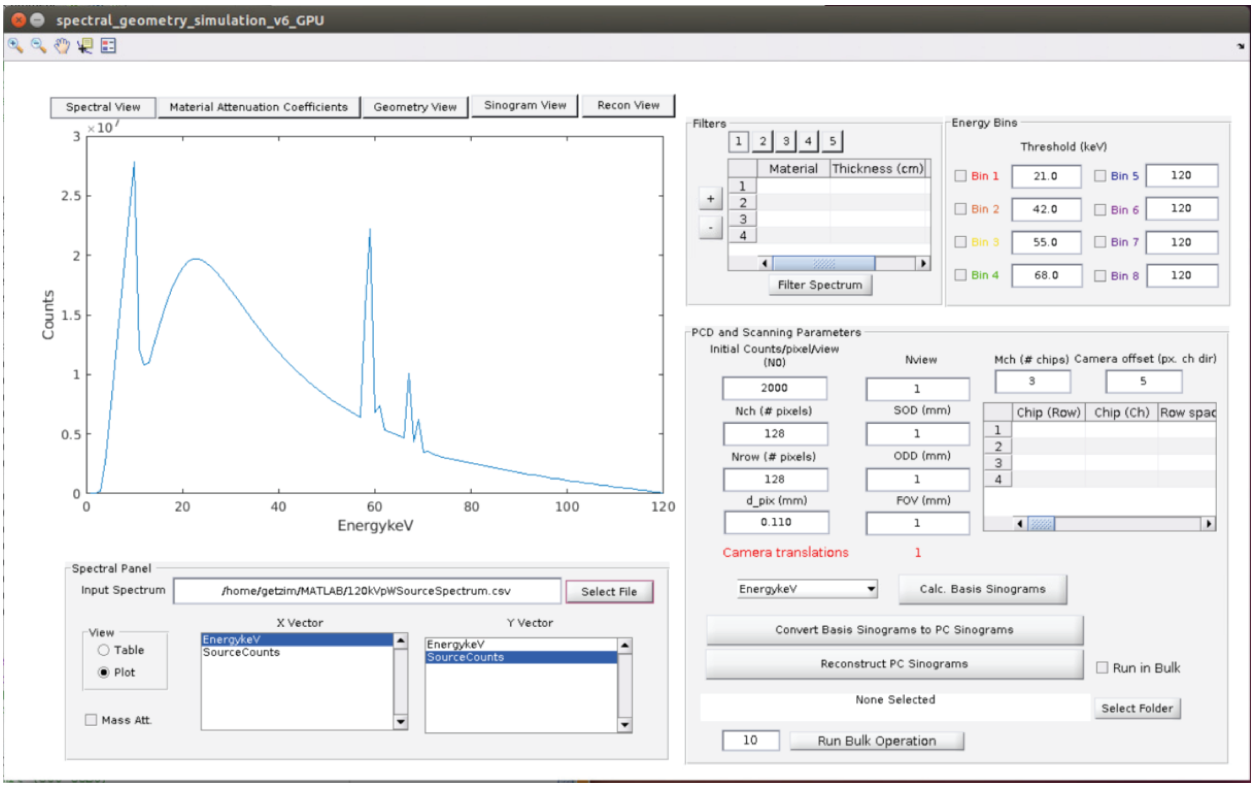

Fig. 2.3: The view of the GUI after the X-ray spectra `.csv` has been loaded.

one column of relative counts at each energy level for a given X-ray tube (*e.g.* tungsten anode). Currently, this function will only load a single spectrum, however, the Callback can be easily adjusted to accommodate multiple.

Once loaded, the contents of the edit box next to the `Select File` button will now contain the path to the spectra `.csv` and both listboxes will contain the vectors which can be plotted against each other in the axes. The default selection of these listboxes places Energy (keV) on the X-axis and Counts on the Y-axis. Figure 2.3 shows the immediate result after loading the spectra file. To toggle between the table and plot views of the spectra vectors, the radio buttons in the `View` subpanel can be selected.

2.2.4.2 Material Attenuation Coefficients

To load the table of material properties, first select the top button labeled `Material Attenuation Coefficients`. This will result in the displayed spectral plot to be replaced by a blank table and the `Spectral Panel` to be replaced by the `Material Panel`. Again, the `Select File` button can be pressed to open a file browser. Select a `.csv` file** which contains a row of material

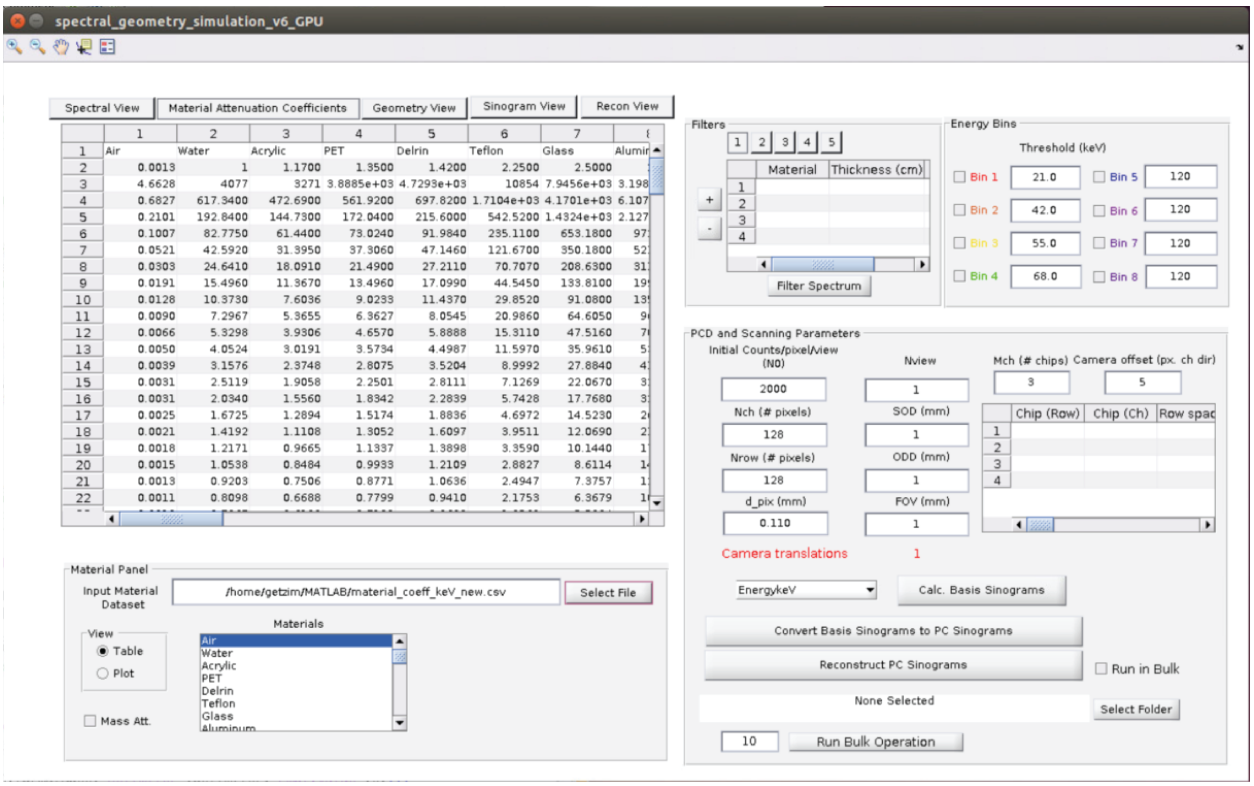

Fig. 2.4: The view of the GUI after the material properties `.csv` has been loaded.

names, a row of material densities, and several rows containing the material-specific linear attenuation coefficients over the same energy range as the loaded X-ray spectrum. Each column should contain a different material.

Figure 2.4 shows the table view of the loaded material properties. Again, to toggle this view between the table and a plot, use the radio buttons in the `View` subpanel. Several materials can be displayed in the plot view by holding down `Ctrl` or `Shift` while selecting the materials of interest from the `Materials` listbox.

***The callback for the `Select File` button* (`select_input_spectrum_Callback`) *must be adjusted for any new material table as the number and titles of the incoming materials are hard-coded in the current software implementation.*

2.2.5 Filtering the X-ray Spectra

Once the original spectrum and materials tables are loaded, the `Filters` panel can be used to adjust the spectra counts based on a given set of material filters (*e.g.* 2mm Glass + 1.96mm

Aluminum). Up to five (5) different filters can be created, each being applied separately to the original input spectra. To toggle between filters, select the corresponding numeral button from the top of the panel.

Select the `minus` (−) button. This will bring up a pop-up list containing all the materials in the filter. Prior to making any filters, no materials will be in the list, however, choose the `Select All` button and press `OK`. Then select the plus (+) button. Again, a popup list will appear, but this time all the loaded materials will be in the list. Select as many materials as needed and press `OK`. Materials can be added and subtracted in this fashion at any time during the simulation but note that if the filter is changed the PcTK output will change, so the conversion process will need to be re-run before the effects of the new spectra are reflected in the data.

The `Filter` table will populate with the material name in the first column, a blank space in the second column, and the `Material` table's column number of the selected material in the third and final column. Enter the desired thickness (in cm) for each of the materials in the table and press `Filter Spectrum`**. Figure 2.8 shows the `Plot` view of the original and filtered spectra.

***If an error is thrown, toggle the* `Table` *and* `Plot` *views once while in the* `Material Panel`*. Select* `Filter Spectrum` *again.*

2.2.6 Setting Geometry Parameters

The major scanning parameters (besides source offsets**) each have an edit box whose value is used in calculating the basis sinograms after the `Calc. Basis Sinograms` button is pressed. The currently editable parameters are:

- **N0** : The ***total*** number of incident photons on each pixel per view (required to run PcTK).
- **Nch** : The number of pixels in the "channel" direction of the detector array. *Used to determine the image size (*i.e. *phantom dimensions).*
- **Nrow** : The number of pixels in the "row" direction of the detector array (Nrow $>= 3$).
- **Nview** : The number of views per rotation (360 degrees).
- $\mathbf{d}_{pix}$: The distance spanned by one side of square detector pixel in millimeters (mm). *Used to determine the image size (*i.e. *phantom dimensions).*

- **SOD** : The distance from the source to the center of the object (*i.e.* center of rotation) in millimeters (mm). *Used to determine the image size (*i.e. *phantom dimensions).*
- **ODD** : The distance from the center of the object (*i.e.* center of rotation) to the center of the detector array in millimeters (mm). *Used to determine the image size (*i.e. *phantom dimensions).*
- **FOV** : The distance which spans the diagonal of the 3D phantom in millimeters (mm). *Used to determine the image size (*i.e. *phantom dimensions).*
- **Mch** : The number of detector chips in the channel direction. Setting this parameter will populate the Chip Offset Parameter table. *Used to determine the image size (*i.e. *phantom dimensions).*
- **Camera offset** : The number of pixels in the "channel" direction that ALL chips (*i.e.* the camera) are offset. This parameter is important to consider when there are several chips in the camera and the chips have gaps between them.
- **Chip Offset Parameters** :
  - **Chip (Row)** : uneditable column indicating the "row" number of the chip. The current implementation forces all chips to be within the same row.
  - **Chip (Ch)** : uneditable column indicating the "channel" number of the chip.
  - **Row spacing** : editable column whose value will be multiplied by the span of the chip in the "row" dimension ($\mathbf{Nrow}*\mathbf{d}_{pix}$) and added as a "row" dimension offset to the corresponding chip. (Default: 0)
  - **Row spacing offset** : editable column whose value will be multiplied by the pixel dimension ($\mathbf{d}_{pix}$) and added as a "row" dimension offset to the corresponding chip. (Default: 0)
  - **Ch spacing** : editable column whose value will be multiplied by the span of the chip in the "channel" dimension ($\mathbf{Nch}*\mathbf{d}_{pix}$) and added as a "channel" dimension offset to the corresponding chip. (Default: ((**Mch**/2)+0.5) - (chip #))
  - **Ch spacing offset** : editable column whose value will be multiplied by the pixel dimension ($\mathbf{d}_{pix}$) and added as a "channel" dimension offset to the corresponding chip.

This parameter is responsible for putting gaps between the chips as they are found in the MARS camera. Chips with negative **Ch spacing** should also have negative offsets. (Default: 0)

- **Axial offset** : editable column whose value will be multiplied by the pixel dimension ($\mathbf{d}_{pix}$) and added to the **ODD** of the corresponding chip.
- **Tangential offset** : editable column whose value will be multiplied by the pixel dimension ($\mathbf{d}_{pix}$) and added as a "channel" dimension offset to the corresponding chip. This parameter is a slight redundancy of the **Ch spacing offset** parameter.
- **Radial offset** : editable column whose value will be added as a z-dimension offset in millimeters (mm). This parameter is relevant in spiral geometries.

In addition to these editable parameters, the number of camera translations needed to cover the user-defined FOV is calculated and shown in red below the edit boxes. Any changes to the editable parameters that alter the translation(s) are reflected immediately. Finally, the source spectrum should also be selected from the drop-down menu below the `Calc. Basis Sinograms` button.

***To add source offsets, the* `circular_geometry_w_phantom_ASTRA_v7.m` *file should be edited directly.*

2.2.7 Phantom Design

To begin designing a phantom which contains any combination of the previously loaded materials and/or aqueous mixtures of the given materials, select the `Geometry View` button on the top of the GUI. This will eliminate either the `Spectral Panel` or the `Material Panel` and make available a pop-down menu and a phantom reset button. Select the `Reset Phantom` button to initialize an image matrix whose size is automatically calculated as a function of the parameters highlighted above as follows. System magnification (mag) is defined as

$$mag = \frac{SOD + ODD}{SOD}. \tag{2.1}$$

Magnification is then used to determine in minimum pixel size of the reconstruction image in a real system. It also dictates the minimum pixel size of the phantom (p_{pix}) in the simulation, such that

$$p_{pix} = \frac{d_{pix}}{mag}. \tag{2.2}$$

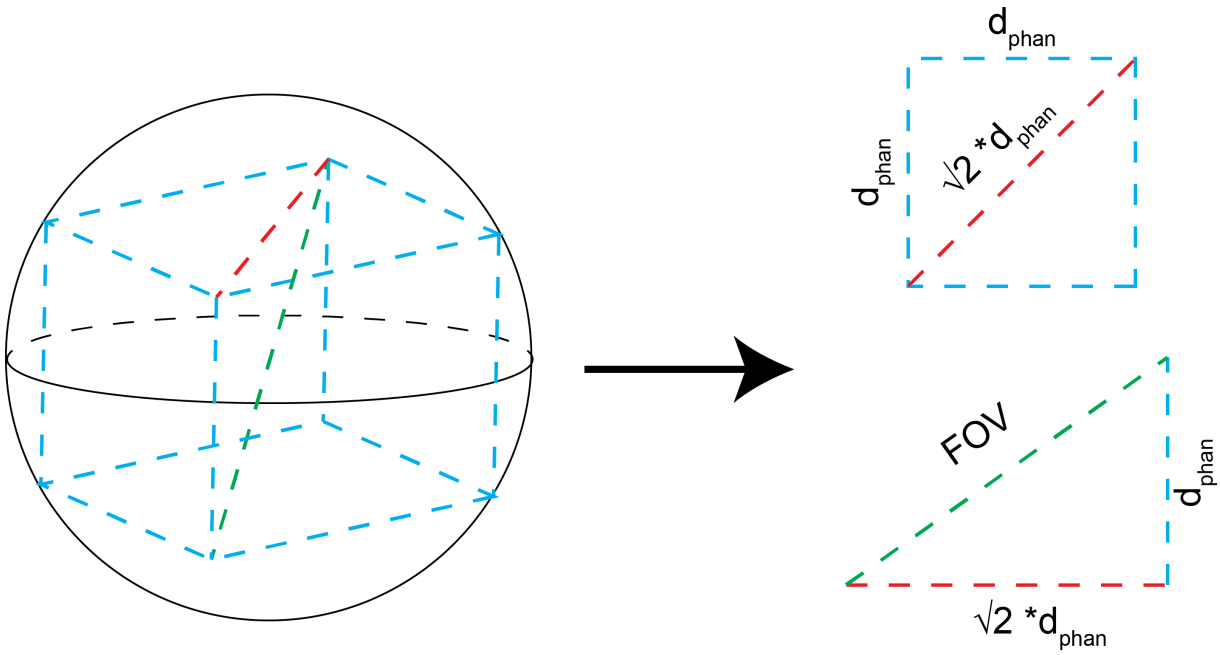

Fig. 2.5: The key geometries which constrain the phantom size are depicted.

Using the geometric relationships shown in Figure 2.5, the side length of the cubic phantom can be calculated using the Pythagorean theorem such that

$$d_{phan} = \frac{FOV}{\sqrt{3}}. \tag{2.3}$$

Finally, the number of pixels in each of the three cubic dimensions of the phantom can be calculated as follows.

$$Nphan = ceil\left(\frac{d_{phan}}{p_{pix}}\right) \tag{2.4}$$

Phantoms are generated through the selection of one of the following options:

- **Circle** : This selection will open a `Circle` panel that allows for the placement of a circle with a given radius, center point, and material basis to be added to a 2D image slice. Press the `Submit` button after defining the necessary parameters (all in pixel units).

- **Rectangle** : This selection will open a `Rectangle` panel that allows for the placement of a rectangle with a given length, width, center point, skew angle, and material basis to be added to a 2D image slice. Press the `Submit` button after defining the necessary parameters (all in

pixel units).

- **Oval** : This selection will open a `Oval` panel that allows for the placement of an oval with a given vertical radius, horizontal radius, center point, skew angle, and material basis to be added to a 2D image slice. Press the `Submit` button after defining the necessary parameters (all in pixel units).

- **Automated Ovals** : This selection will open an `Automated Oval` panel that allows for the definition of a new image size, a maximum number of ovals, and a set of materials which are randomly selected to be mixed with water at random concentrations and placed in the 2D image slice as a new material basis through the use of the `generatePhantom.m` function. This function is meant to emulate a human head by first making a large outer oval that contains cortical bone and an inner oval that contains water (similar attenuation to brain). The mixture ovals are randomly placed within this water region. After pressing submit, the image displayed in the GUI is a summation image of each of the material basis slices (where the voxel value corresponds to the material column in the material table). A separate pop-up figure will appear showing each of the ovals in a unique image slice where the voxel values are equal to the percent mass concentration that the corresponding material occupies within the voxel. This material basis phantom, as well as a cell array containing the names and attenuation properties of each material, is saved into the output directory as .\weighted_phantom.mat.

- **Automated Ellipsoids (3D)** : This selection will open the `Automated Oval` panel as above. Rather than defining random 2D ovals, this function defines 3D phantoms containing random ellipsoids using the function `generatePhantom3D.m`. This function, too, is meant to emulate a human head by first making a large outer ellipsoid that contains cortical bone and an inner ellipsoid that contains water (similar attenuation to brain). The mixture ellipsoids are randomly placed within this water region. After pressing submit, the image displayed in the GUI is a summation image of the central slice of each of the material basis slices (where the voxel value corresponds to the material column in the material table). Two separate pop-up figures will appear one showing the central slice of each of the ellipsoids in a unique image where the voxel values are equal to the percent (by mass) that the corresponding material occupies and the other showing three, orthogonal views of the 3D phantom (summed material bases). The material basis phantom, as well as a cell array containing the names of each material, is saved into the output directory as .\weighted_phantom.mat.

- **Material Calibration (3D)** : This selection will open the `Automated Oval` panel as above. Rather than defining random 2D ovals or 3D ellipsoids, this function defines 3D phantoms containing fixed size/placement/concentration ellipsoids using the function `generateMat-CalPhantom3D.m`. Again, this phantom is modeled after a human head, *i.e.* a large outer ellipsoid containing cortical bone and an inner ellipsoid containing water. Depending on the number of materials chosen to constitute the mixtures, the sets of 4 ellipsoids of fixed size and concentrations will be placed around the center of the inner water ellipsoid. The size, placement, and concentrations currently employed are hard-coded into the `generateMat-CalPhantom3D.m` file and were chosen to provide sufficient data to train robust nonlinear classification schemes (*e.g.* kernelized Fisher's Discriminant Analysis). After pressing submit, the image displayed in the GUI is a summation image of the central slice of each of the material basis slices (where the voxel value corresponds to the material column in the material table). Two separate pop-up figures will appear one showing the central slice of each of the ellipsoids in a unique image where the voxel values are equal to the percent (by mass) that the corresponding material occupies and the other showing three, orthogonal views of the 3D phantom (summed material bases). The material basis phantom, as well as a cell array containing the names of each material, is saved into the output directory as .\weighted_phantom.mat.

The `Automated Oval`, `Automated Ellipsoids (3D)`, and `Material Calibration (3D)` selections are the only two which create aqueous mixtures of the materials selected with random concentrations. The final phantom will contain an image for each selected material (plus bone and water) where the voxel value is equal to the mass percentage of the respective material contained within the voxel bounds. Figure 2.6 shows the GUI after submitting an `Automated Ellipsoids` selection. Figure 2.7 show the separate pop-up figures.

2.2.8 Setting Detector Energy Thresholds

The energy thresholds, and resulting energy windows, are set in the `Energy Bins` panel. Simply select the checkbox next to each Bin (a.k.a. lower threshold) which is desired and enter the value of the threshold energy. If less than 8 bins are required, start with Bin 1 and select them in order. Figure 2.8 shows each of the thresholds in the `Spectral View` plot.

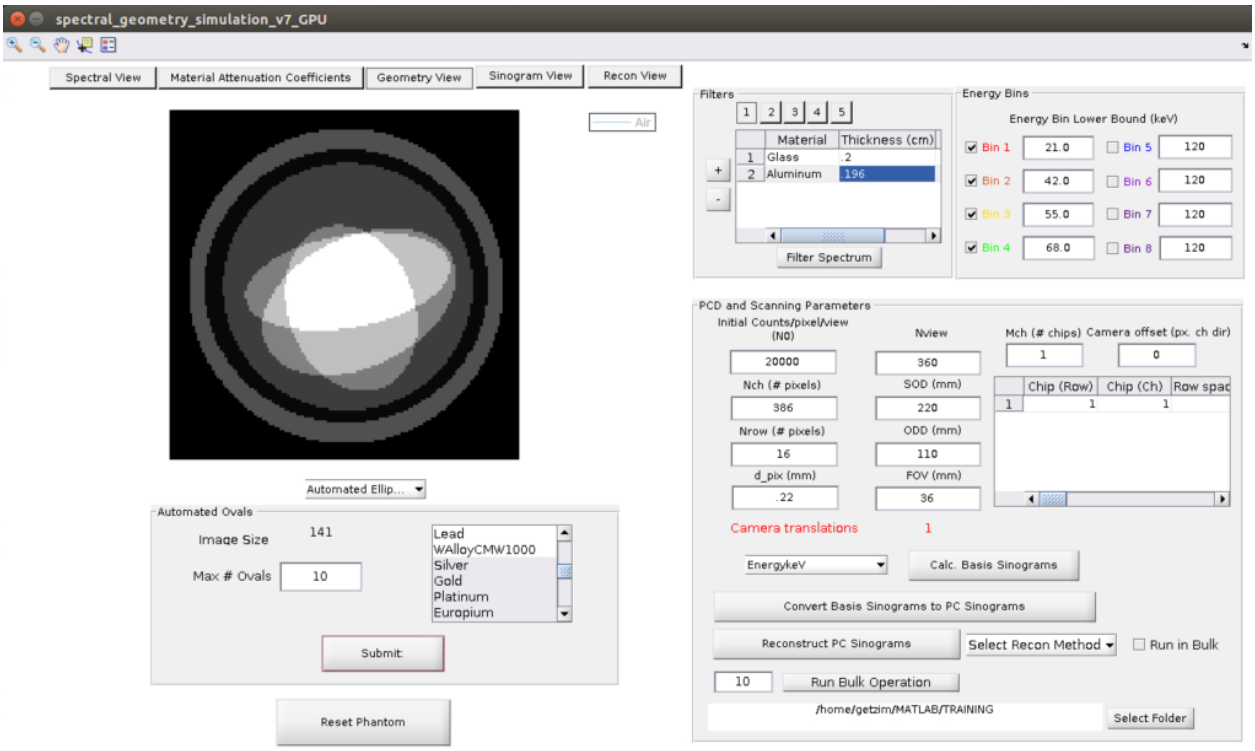

Fig. 2.6: This figure shows an `Automated Ellipsoids` output containing up to 10 ellipsoids in a 141x141x141 voxel matrix. The materials, concentrations, sizes, and placements of the mixture ovals are randomly selected from the subset of materials specified by the user.

2.3 Scanning Geometry and Forward Projection

2.3.1 The MARS Scanner

The simulated scanner has a flexible geometry which allows for any number of detector chips to be arranged in a single row. Each chip's individual offsets can be manually adjusted to test real-world detector configurations and geometries, such as that of the MARS micro-CT scanner located in the Bioimaging Center (BIC) at the Center for Biotechnology and Interdisciplinary Studies (CBIS) on the campus of Rensselaer Polytechnic Institute (RPI) in Troy, NY. The real-world MARS scanner is currently equipped with a Medipix3RX detector module which comprises of three (3) 128x128 pixel CZT detector chips. Each pixel is 110 μm^2 which give an active area of 14x14mm^2 for each chip. In this camera the chips have radial offsets, gaps (channel spacing offsets), and axial offsets. The scanner contains a 120 kVp tungsten (W) source with variable filtering options.

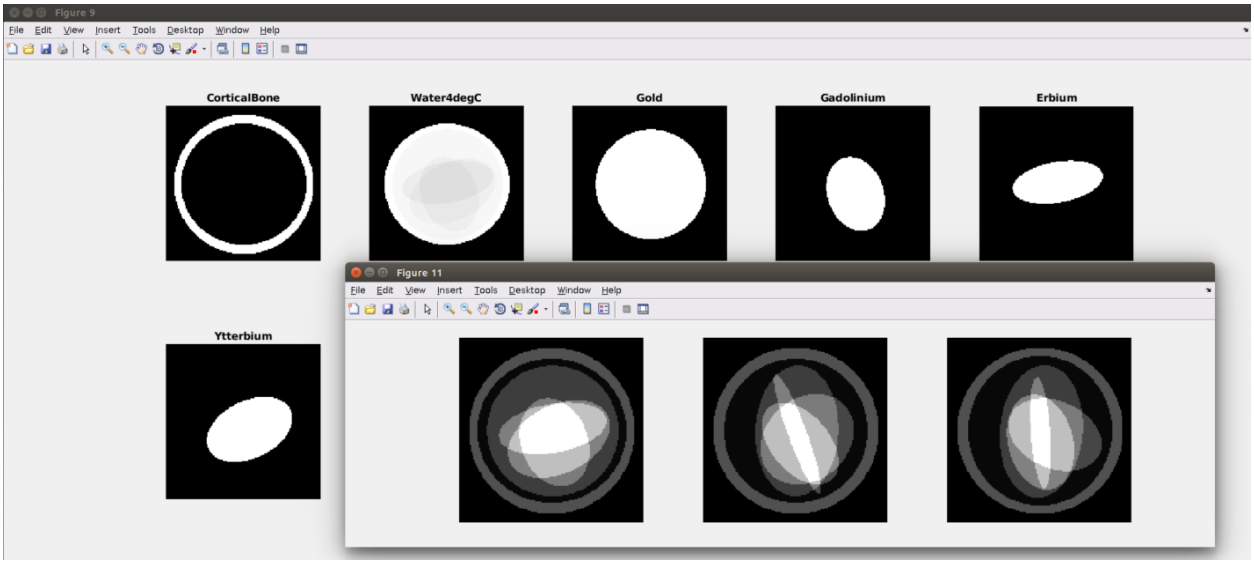

Fig. 2.7: This figure shows the central slice of material basis phantom as created by the `Automated Ellipsoids` selection. The voxel intensities are equal to the percent (by weight) of the materials in a given voxel. A second figure showing orthogonal views of the 3D phantom is also shown.

2.3.2 `circular_geometry_w_phantom_ASTRA_v7.m`

The simulation models the source as a single point with coordinates in 3 spatial dimensions (s_x, s_y, s_z) which are defined as follows:

$$s_x = SOD\sin(\theta) + \Delta_{tan_s}\cos(\theta + \pi) \tag{2.5}$$

$$s_y = SOD\cos(\theta) - \Delta_{tan_s}\sin(\theta + \pi) \tag{2.6}$$

$$s_z = \Psi\left(\frac{\theta + \pi}{2\pi}\right) + \Delta_{axial_s} \tag{2.7}$$

where SOD is the source-to-object (*i.e.* source-to-center-of-rotation, source-to-origin) distance, θ is the rotation angle, Δ_{tan_s} is the source's tangential offset, Δ_{axial_s}, is the source's axial offset, and Ψ is the helical pitch for 3D scans. In its simplest, circular geometry implementation, the offset variables and pitch can be set to 0 (current implementation is hard-coded for this geometry).

To allow for user flexibility in defining the detector geometry, are allocated. One is used to collect the individual data streams (*i.e.* projection matrices) from each of the specified detector chips at each angle and translation position (see Algorithm 1 for details regarding the translation determination). The second cell array represents a single "ideal" detector which spans the area covered by all the chips and their translations. A third structure contains the mapping information

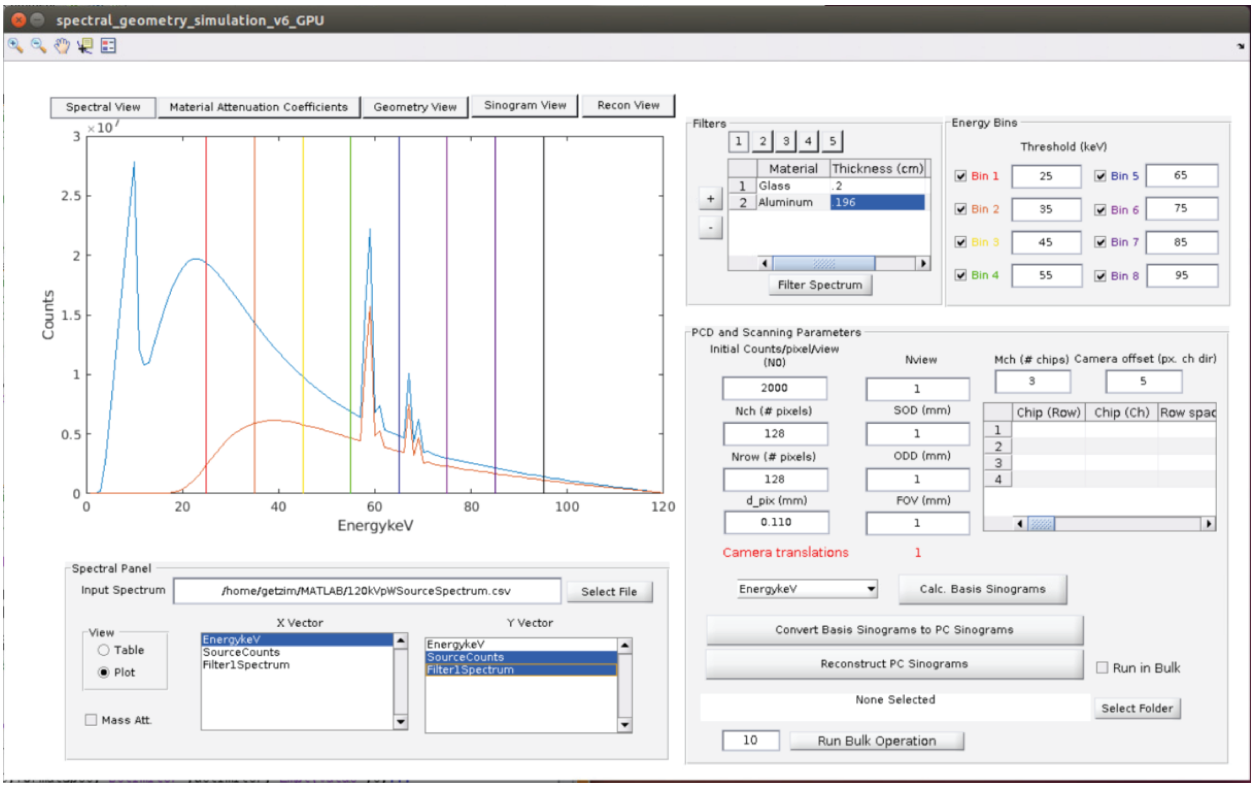

Fig. 2.8: This image shows the original spectrum, filtered spectrum, and energy thresholds as defined by the user.

from each of the individual chips to the ideal detector pixels (see Algorithm 3 for details regarding this mapping).

The ideal and individual detector chips are defined by a set of detector related coordinates as follows:

$$d_{\perp x} = ODD\sin(\theta) = d_{ideal,x} \tag{2.8}$$

$$d_{\perp y} = ODD\cos(\theta) = d_{ideal,y} \tag{2.9}$$

$$d_{\perp z} = \Psi\left(\frac{\theta}{2\pi}\right) = d_{ideal,z} \tag{2.10}$$

$$d_{ix} = \left(ODD + \Delta_{radial_{d_i}}\right)\sin(\theta) + \left[\Phi_{ij} + \Delta_{tan_{d_i}} + (t(k) * FOV_{camera})\right]\cos(\theta) \tag{2.11}$$

$$d_{iy} = \left(ODD + \Delta_{radial_{d_i}}\right)\cos(\theta) - \left[\Phi_{ij} + \Delta_{tan_{d_i}} + (t(k) * FOV_{camera})\right]\sin(\theta) \tag{2.12}$$

$$d_{iz} = \Psi\left(\frac{\theta}{2\pi}\right) + \Delta_{axial_{d_i}} \tag{2.13}$$

$d_{\perp}$ is the point used in defining the orthonormal vector to the source point, d_i is the center point for chip i, and d_{ideal} is the center point of the ideal detector. ODD is the object-to-detector (*i.e.* center-

of-rotation-to-detector) distance, $\Delta_{radial_{d_i}}$ is detector chip i's radial offset, $\Delta_{tan_{d_i}}$ is detector chip i's tangential offset, $\Delta_{axial_{d_i}}$ is chip i's axial offset, Φ_{ij} is the spacing between the center points of detector chips i and j, FOV_{camera} is the field-of-view spanned by all chips, d_{pix} is the pixel dimension, and $t(k)$ is the detector module shift defined using the following algorithm:

Algorithm 1 Determining Detector Module Shift

```
procedure SHIFT(FOV_camera)                                   ▷ Calculating the module shift
    FOV_camera ← d_pix * Nch * Mch + Σ_{i,j} Φ_ij             ▷ Calculate span of camera
    exact_shift ← (mag*FOV) / FOV_camera
                                  ▷ Calculate the ratio of magnified FOV and the span of camera
    if exact_shift > 1 then
        translation ← ceil(exact_shift)
        t ← [ −((exact_shift−1)/2) : (exact_shift−1)/(translation−1) : ((exact_shift−1)/2) ]
    else
        translation ← 1
        t ← 0
    end if
    return t                                                  ▷ The vector of shifts is t
end procedure
```

Algorithm 1 was written to emulate the behavior of the real-world scanner when FOVs which are greater than that spanned by all three chips is defined by the user. The translation(s) are stored in the first dimension of the 5D sinogram output data.

Once the source points, orthonormal points, and chip centers are defined, sets of planar grids are defined about the individual detector centers as in Algorithm 2. The pixel centers (along with the source positions) are used as vectors which define the X-ray ray-traces. These ray vectors are fed into either a Siddon's method algorithm or one of the ASTRA toolbox's forward projection functions to calculate the material-basis projection data through the phantom for each detector, material, and view separately. The material-basis phantom slices that are used in this calculation are the masks shown in Figure 2.7. Each mask is binary except the water mask, which is adjusted to a grayscale image whose voxel values are equal to the percent by weight of water contained in each voxel. This process can be parallelized to increase speed.

2.3.3 Calculating the Basis Sinograms

Although the latest version of this simulation exclusively uses the ASTRA toolbox, earlier versions relied on Siddon's method for calculating the projection data. Both are briefly described

Algorithm 2 Calculating Detector Pixel Coordinates as implemented by `planar_array_ideal.m` and `planar_array_ASTRA_FP.m`

procedure FINDGRIDCOORD($s_{xyz}, d_{ixyz}, d_{pix}, d_{\perp xyz}, N_{ch}, N_{row}$) ▷ Calculate detector i pixel center coordinates
  $d_{L\times W} \leftarrow \left[d_{pix} * N_{ch}, d_{pix} * N_{row}\right]^T$ ▷ Calculate detector dimensions
  $[Q, P] \leftarrow \texttt{meshgrid}\left(\frac{-d_L}{2} : d_{pix} : \frac{d_L}{2}, \frac{-d_W}{2} : d_{pix} : \frac{d_W}{2}\right)$
  ▷ Calculate equally spaced pixel edges centered at (0,0)
  $u_{xyz} \leftarrow \left[0, 0, s_z\right]^T - \left[d_{\perp x}, d_{\perp y}, d_{\perp z}\right]^T$
  ▷ Define orthonormal vector on detector from source
  $[v_{xyz}, w_{xyz}] \leftarrow \texttt{null}(u)$
  ▷ Calculate two orthonormal vectors to u_{xyz} that lie in the detector plane
  $X_{edge} \leftarrow d_{ix} + v_x * P + w_x * Q$
  $Y_{edge} \leftarrow d_{iy} + v_y * P + w_y * Q$
  $Z_{edge} \leftarrow d_{iz} + v_z * P + w_z * Q$ ▷ Calculate coordinates for pixel edges
  for $jj = 1 : \texttt{size}(X_{edge}, 1) - 1$ **do** ▷ Loop through detector rows and columns
    for $kk = 1 : \texttt{size}(X_{edge}, 2) - 1$ **do**
      $X_i \leftarrow mean(mean(X(jj : jj+1, kk : kk+1)))$
      $Y_i \leftarrow mean(mean(Y(jj : jj+1, kk : kk+1)))$
      $Z_i \leftarrow mean(mean(Z(jj : jj+1, kk : kk+1)))$
      ▷ Calculate coordinate for pixel centers
    end for
  end for
  return $D_i \leftarrow \texttt{cat}(3, X_i, Y_i, Z_i)$ ▷ coordinates for detector i are concatenated into D_i
end procedure

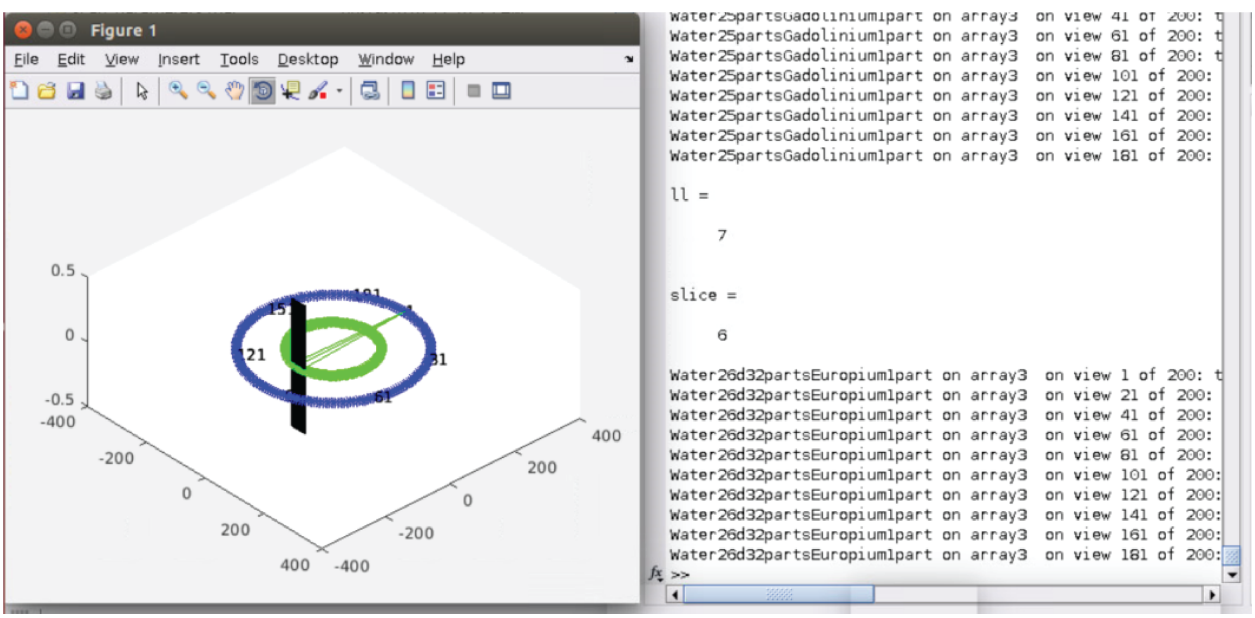

Fig. 2.9: When running the `Calc. Basis Sinograms`, a pop-up figure shows the source/ideal detector trajectories and provides a single view represented by a 3D surface plot. Additionally, the command window prints the data acquisition progress.

in this section with their differences highlighted. In both cases, previously built code (`Siddon9.m` or `astra_create_sino3d_cuda.m`) are adapted with wrapper-code that feeds the source position, detector centers, orthonormal vector, and phantom as inputs. Both wrappers output material-basis projection data. The wrappers can be run by pressing the `Calc. Basis Sinograms` button. During the evaluation of the `Callback` function, a pop-up figure will appear which plots the trajectories of the source and ideal detector, as well as a 3D surface of the detector chips at a single viewing angle. Additionally, the progress is printed in the `Command Window`. Figure 2.9 shows these outputs.

Upon completion of this step of the simulation, each detector will have been independently modelled according to the scanning geometry with each of rays from the source to each pixel position (both with a phantom and in open-beam). This results in $2 * \texttt{Mch}$ sets of material-basis projections. Additionally, an ideal detector geometry is also defined and used to map the individual chip data to this ideal detector plane. More information regarding this mapping algorithm can be found in the reconstruction section of this manual (specifically Algorithm 4).

2.3.3.1 Siddon's Method

In order to employ Siddon's method, the center of each pixel must be defined. Algorithm 2 is used to obtain the pixel center coordinates. These are then used as inputs to `Siddon9.m` which outputs the image pixel positions and weights (*i.e.* length through image pixel) through which the ray traces and which need be applied to the input phantom to obtain the line integral for the projection data [80].

2.3.3.2 ASTRA Toolbox Forward-projection

Algorithm 2 is also used to define the detector array inputs for the ASTRA toolbox forward-projection. However, one major difference can be found between the Siddon's method and ASTRA toolbox. Rather than taking each pixel center as an input, the ASTRA forward-projection algorithms only require vectors which define the two directions (starting from the top-left pixel) of the detector array. The current implementation of the ASTRA forward-projection uses the `` `cone_vec' `` setting, which is a cone beam method where each view is coded as a vector of 12 source/detector parameters. More information regarding the various methods available can be found in the ASTRA Toolbox documentation [78], [79].

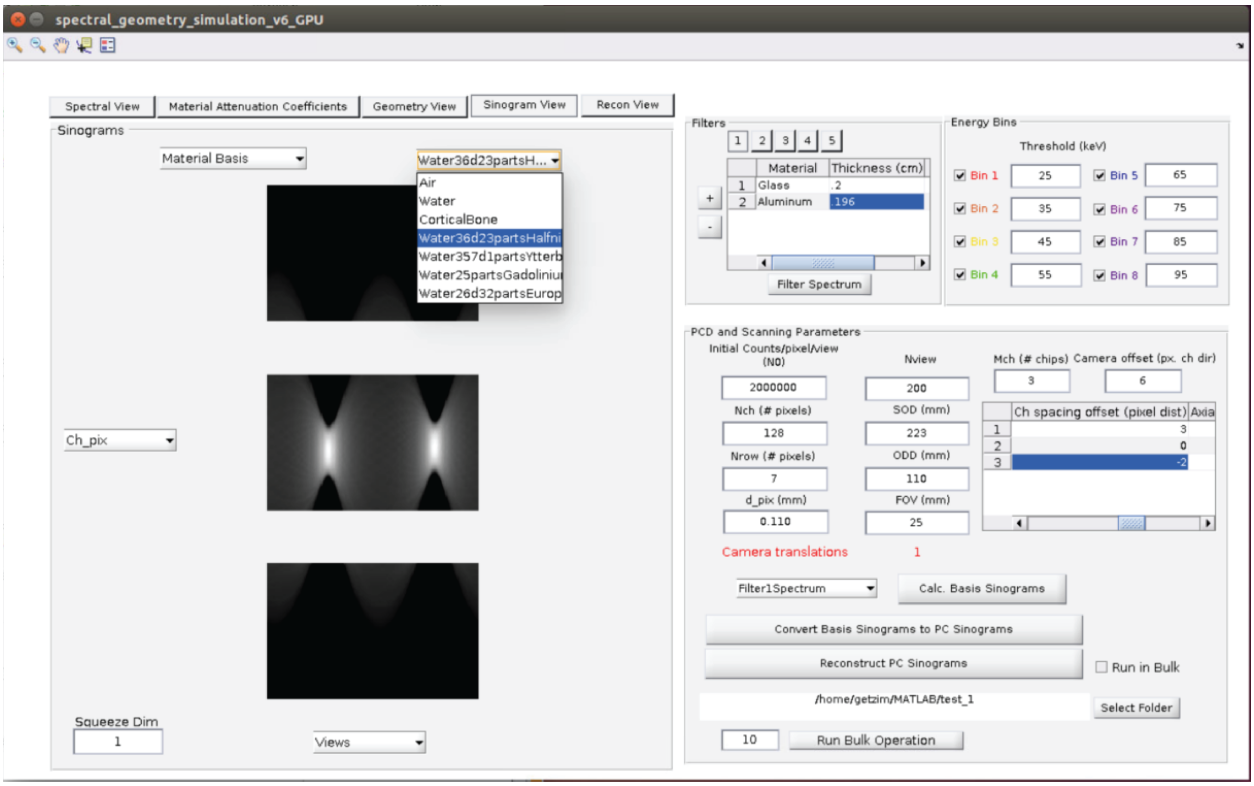

Fig. 2.10: Viewing the material basis sinograms in the GUI for a 3x1 detector array over a single translation.

2.3.4 Viewing the Material Basis Sinograms

After the completion of the `Calc. Basis Sinograms Callback` functions, the `Sinogram View` button can be pressed to display the material basis data measured at each detector chip. To select the material basis sinograms, click on the top left pull-down menu in the `Sinogram` panel and select `Material Basis`. This will initiate the plot and display the `Air` basis sinogram (Ch vs Viewing angle, 1st row). The other material bases can be selected by using the top right pull-down menu in the `Sinogram` panel. Figure 2.10 demonstrates how this functionality can be used to examine the material basis sinograms. Users can also view the other dimensions of the data or other rows by adjusting the lower pull-down menus and the edit box in the bottom left corner of the `Sinogram` panel. The views in these other dimensions are not guaranteed to line-up or be arranged in a coherent manner. One last note, if a value larger than the that contained by the `Squeeze Dim`, an error will be thrown in the `Command Window`, but no major changes will be seen at the level of the GUI.

2.4 Implementing the PcTK

2.4.1 `Convert Basis Sinograms to PC Sinograms -- Callback`

Implementation of the photon-counting toolkit (PcTK) was adapted from `script_workflow_PcTK.m` and `gen_nCovE.m` which are both provided as part of the license agreement with the creators of the PcTK. These are two of only three `.m` files provided with this license, whereas every other code provided is `.p` (*i.e.* proprietary code) and cannot be opened or explored [23], [26]. Many of the parameters needed to run the PcTK are hard-coded into the simulator and have to do with the detector material properties, physics models, and noise profiles. At this time, only CdTe detectors are modeled by this toolkit. Despite this material difference to our real-world detector (*i.e.* CdTe vs CZT), the simulator should still provide a decent representation of the signal generated by the MARS scanner when operated.

There are a few PcTK parameters which are user defined in the simulator, namely the input source spectrum, the material properties of the filters and phantom, and the energy thresholds. These parameters can be adjusted according to the directions outlined in Section 2.2. Outside of these parameters, the other major inputs to this step of the simulation are the material-basis projection matrices which were produced by the codes and algorithms outlined in Section 2.3. At the level of the real-world detector, each of the chip's data streams are independent at the time of measurement, therefore the PcTK is run separately for each of the chips. To convert the material-basis sinograms to photon-counting data using the PcTK, press the `Convert Basis Sinograms to PC Sinograms` button. Figure 2.11 shows the output one should expect after pressing the `Convert Basis Sinograms to PC Sinograms` button.

It should be noted that the PcTK, as per the documentation, is a 2D detector model which uses a 3x3 neighborhood at each pixel to model the complex detector physics (*e.g.* charge sharing). Therefore, even in situations where 2D reconstructions are desired and 1D detector vectors should be sufficient for measuring the necessary projection data for recon, the detector model must have at least 3 rows to run the PcTK. Upon completion of the PcTK, four datasets per chip (i) are output – `pc`i`_mean`, `ob`i`_mean`, `pc`i`_noisy`, and `ob`i`_noisy`, where the `pc` sinograms are with the sample in the beam and the `ob` sinograms are the open-beam data used for count normalization. The current software implementation takes advantage of MATLAB's built-in `parfor` functionality for parallelizing the analysis by running the toolkit on each viewing angle separately/in parallel.

```
 on view 180 of 200: time = 12:3:23 (hour:min:sec)
 on view 200 of 200: time = 12:3:24 (hour:min:sec)
CHIP 3 of 3
 on view 2 of 200: time = 12:3:34 (hour:min:sec)
 on view 4 of 200: time = 12:3:34 (hour:min:sec)
 on view 6 of 200: time = 12:3:34 (hour:min:sec)
 on view 9 of 200: time = 12:3:34 (hour:min:sec)
 on view 14 of 200: time = 12:3:34 (hour:min:sec)
 on view 21 of 200: time = 12:3:34 (hour:min:sec)
 on view 32 of 200: time = 12:3:34 (hour:min:sec)
 on view 45 of 200: time = 12:3:34 (hour:min:sec)
 on view 3 of 200: time = 12:3:42 (hour:min:sec)
 on view 5 of 200: time = 12:3:41 (hour:min:sec)
 on view 20 of 200: time = 12:3:41 (hour:min:sec)
 on view 44 of 200: time = 12:3:42 (hour:min:sec)
 on view 1 of 200: time = 12:3:42 (hour:min:sec)
 on view 13 of 200: time = 12:3:42 (hour:min:sec)
fx >>
```

Fig. 2.11: Command window output after running the `Convert Basis Sinograms to PC Sinograms Callback`.

2.4.2 Viewing the Photon-counting Sinograms

After the completion of the `Convert Basis Sinograms to PC Sinograms Callback` functions, the `Sinogram View` button can be pressed to display the photon-counting data measured at each detector chip. To select the photon-counting sinograms, click on the top left pull-down menu in the `Sinogram` panel and select the `PC Mean` or the `PC Noisy` options. This will initiate the plot and display the `Energy Bin 1` sinogram (Ch vs Viewing angle, 1st row) with or without noise. The other energy bins can be selected by using the top right pull-down menu in the `Sinogram` panel. Figure 2.12 demonstrates how this functionality can be used to examine the photon-counting sinograms. Users can also view the other dimensions of the data or other rows by adjusting the lower pull-down menus and the edit box in the bottom left corner of the `Sinogram` panel. The views in these other dimensions are not guaranteed to line-up or be arranged in a coherent manner. One last note, if a value larger than the that contained by the `Squeeze Dim` is input into the edit box, an error will be thrown in the `Command Window`, but no major changes will be seen at the level of the GUI.

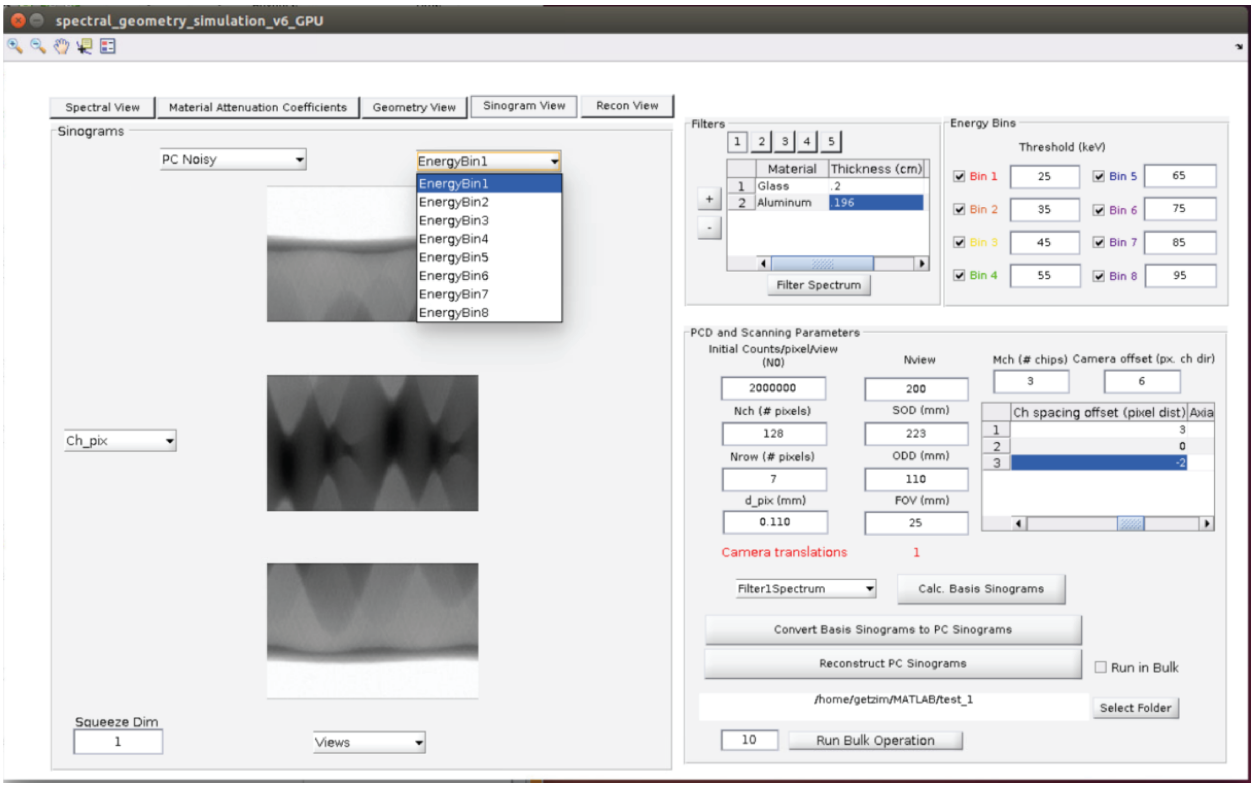

Fig. 2.12: Viewing the photon-counting sinograms in the GUI for a 3x1 detector array over a single translation.

2.5 Reconstruction

The last part of the simulator is the reconstruction of the sinogram data into a full 3D image and a single 2D slice (central slice of the ideal detector). Just as in the simulation's sinograms generation steps, multiple methods can be (and are) used to convert the "raw" photon-counting projection data into 3D image sets. A 2D analytical reconstruction using filtered backprojection (FBP) and a 3D, GPU-compatible algebraic reconstruction (ASTRA-SIRT) are implemented. For both reconstruction algorithms, mapping and consolidation of the separate chips' data to a single, "ideal" detector plane is the first step.

2.5.1 Mapping to the "Ideal" Detector

The current implementation of the mapping algorithm starts by normalizing the spectral "counts" by the open-beam data with the following equation:

$$I_n = -\log_{10}\left(\frac{I}{I_0}\right) \tag{2.14}$$

where I is the "raw" sinogram data in counts and I_0 is the open-beam sinogram data also in counts. Then the mapping calculated with Algorithm 3 is used to interpolate the spectral data at the individual chips to the ideal detector. Geometric functions used in Algorithm 3 are part of the `geom3d` library available for download on the MATLAB File Exchange. The main function of the algorithm is to establish the relationship between the individual pixels of the "ideal" detector and those of the detector chips (at their multiple translational positions). The output of Algorithm 3 is 3-channel cell array whose two dimensions are equal to the size of the ideal detector. The first channel contains an $n \times 3$ matrix whose rows contain the row, column, and relative weight of the n pixels that were determined to be closest to the point of intersection of the ray from the source through the center of the ideal detector pixel. The second channel contains the chip ID number and the third channel contains the translation number. It should be noted that the mapping done with Algorithm 3 is done during the sinogram generation (`ideal_det_trans.m`), but the actual translation of this mapping into an "ideal" sinogram is done during the reconstruction part of the program (`translate_proj-_to_ideal.m`).

The translation itself simply consists of two `for` loops which loop over the rows and columns of pixels from the "ideal" detector. If there are data from the $fcells$, $matID$, and $translation$ stored in a pixel, it performs a linear combination of the relevant pixels according to the weight calculated and stored in Algorithm 3.

2.5.2 Filling in the Gaps – 3D Analytic Reconstruction (FBP)

3D Feldkamp-type analytic reconstructions and approximations from conebeam data have been discussed by our group at some length [35], [36]. A quick approximation of the usual point-by-point cone-angle correction is to correct a whole row of data (at angle γ to the central axis) using a $\cos\gamma$ multiplier. This weighted approximation allows for quick 3D approximations. In future implementations, a more accurate 3D reconstruction based on [36] will be incorporated.

Inevitably with geometries containing multiple independent detector chips, there are gaps on the "ideal" detector where no data has been collected. This is unacceptable for analytical reconstruction algorithms. In general, an overall camera offset may be introduced in order to ensure that the gaps do not line-up with the gaps of the detector located opposite (refer to Section 2.2.6). Figure 2.13 displays one row of the conebeam sinogram. This view (if the center row of the ideal detector) can be used as a pseudo-fanbeam geometry for a fan-to-parallel beam rebinning [31]. The result of this rebinning can also be seen. When properly sampled with enough views and with the

Algorithm 3 Geometric Mapping of Chips to the "Ideal" Detector

procedure MapChips2Ideal($D_{ideal}, D_0, s_{xyz}, d_{pix}, chipID$) ▷ Map/interpolate chip data to ideal detector
  $i_Xv \leftarrow D_{ideal,x}(:)$
  $i_Yv \leftarrow D_{ideal,y}(:)$
  $i_Zv \leftarrow D_{ideal,z}(:)$ ▷ Vectorize the ideal detector center coordinates
  $plane0 \leftarrow \texttt{createPlane}\big(\left[D_0(1,1,:)^T, D_0(1,2,:)^T, D_0(2,1,:)^T\right]\big)$ ▷ Input: three points in 3×3 array
  for $ii = 1 : \texttt{length}(i_Xv)$ **do**
    $line \leftarrow \texttt{createLine}(s_{xyz}, [i_Xv(ii), i_Yv(ii), i_Zv(ii)])$ ▷ Input: source and ideal pixel ii coords.
    $p0 \leftarrow \texttt{intersectLinePlane}(line, plane0)$ ▷ Calculate intersection point of X-ray line with detector chip
    $fcells \leftarrow \texttt{cell}(\texttt{size}(i_Xv))$ ▷ Allocate cell array for mapping library
    $matID \leftarrow \texttt{zeros}(\texttt{size}(i_Xv))$ ▷ Allocate of matrix to contain ID for the chip whose data to search
    if $p0 >= \texttt{min}(\texttt{min}(D_0))$ & $p0 <= \texttt{max}(\texttt{max}(D_0))$ **then** ▷ $p0$ is within bounds of chip 0
      $gx \leftarrow (D_0(:,:,1) - p0(1))^2$
      $gy \leftarrow (D_0(:,:,2) - p0(2))^2$
      $gz \leftarrow (D_0(:,:,3) - p0(3))^2$ ▷ Calculate square difference in x, y, and z
      $distI \leftarrow \sqrt{gx + gy + gz}$ ▷ Calculate image containing Euclidean distance of pixel center to p0
      $distIn \leftarrow \frac{|d_{pix} - distI|}{d_{pix}} \odot distI <= d_{pix}$ ▷ Elementwise multiplication of $1 - \frac{distI}{d_{pix}}$ and $distI <= d_{pix}$ ▷ $distIn$ is an image where $<= 4$ pixels contain the value of $1 - \frac{distI}{d_{pix}}$
      $distInorm \leftarrow \frac{distIn}{\texttt{sum}(\texttt{sum}(distIn))}$ ▷ Compute weight of remaining pixels in $distIn$
      $[row, col, v] \leftarrow \texttt{find}(distInorm)$ ▷ Find row, column and value of non-zero pixels in $distInorm$
      $fcells\{ii\} = \texttt{cat}(2, row, col, v)$ ▷ Save mapping in cell array
      $matID(ii) \leftarrow chipID$ ▷ Save array of chip IDs
    end if
  end for
  return $fcells,\ matID$
  ▷ These arrays are later combined with the translation info into a single, 3-channel cell array
end procedure

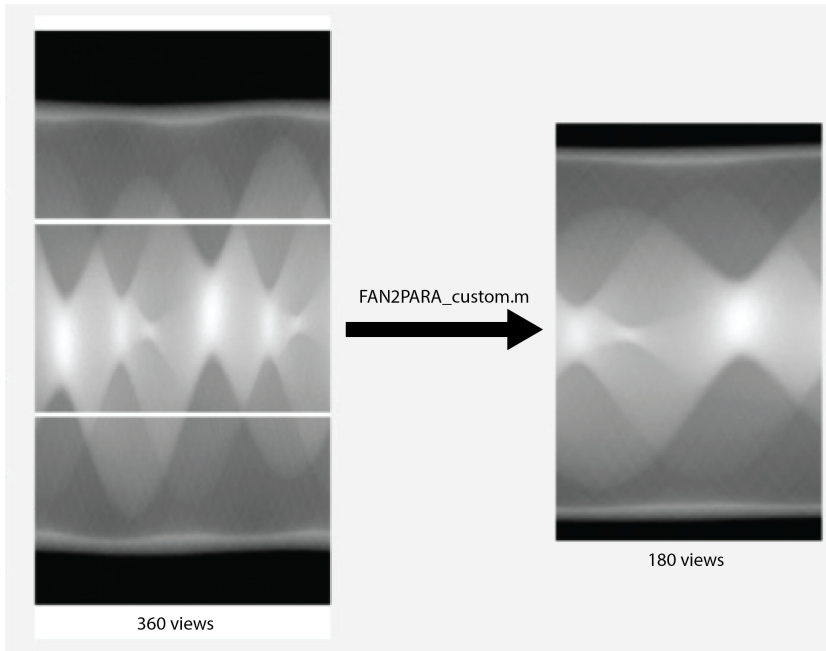

Fig. 2.13: A slice of the ideal detector sinogram with 360 views in the cone beam (pseudo-fan at central ideal slice) and after running `FAN2PARA_custom.m`. The white regions represent ideal detector pixels for which no data was collected due to gaps or offsets in the detector positions. In cases where sufficient data has been collected in the conebeam trajectory and the gaps have been correctly offset, the parallel-beam transformation of the data results in a continuous sinogram which can be used for analytic reconstruction via FBP.

correct camera offset. The gaps between chips in the conebeam/fanbeam configuration are filled in after rebinning to the parallel case. Figure 2.14 shows the key geometric relationships that are needed to calculate the appropriate data remapping from fan (β, α) to (θ, t). Finally, Algorithm 4 shows the simplified steps for searching for the closest sampled αs and βs. Once found, 2D interpolation in the neighborhood around the nearest point is done to find the (θ, t) value for both (β_1, α_1) and (β_2, α_2). For most (θ, t)s, both (β_1, α_1) and (β_2, α_2) have data to use in the rebinning, but in the gaps, only (β_1, α_1) or (β_2, α_2) has data to fill the gap. In order to ensure no severe discontinuities, the neighborhood around pixels are linearly weighted toward the (θ, t) pixel where only one of (β_1, α_1) or (β_2, α_2) contributes data randomly weights the data from the two contributors. This is called feathering and it is demonstrated in Figure 2.15.

The output of Algorithm 4 can be fed directly into MATLAB's `iradon` or more sophisticated FBP implementations for reconstruction.

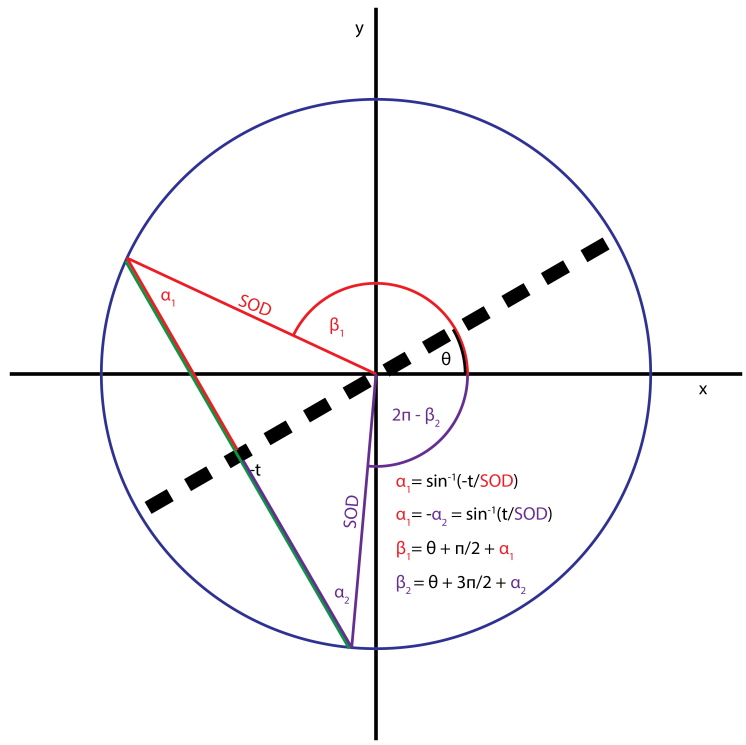

Fig. 2.14: The key geometric relationships for an accurate fanbeam-to-parallel beam rebinning.

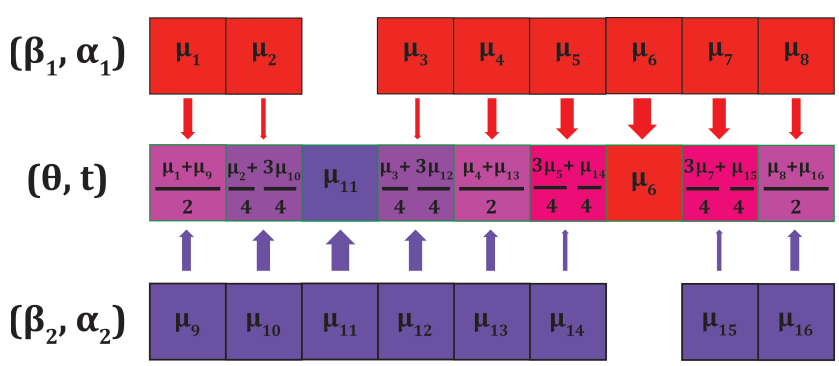

Fig. 2.15: The feathering process of filling in the data for parallel beam (θ, t)s with the available fanbeam angles (β_1, α_1) and (β_2, α_2). The gap neighbors are weighted with a linear bias toward the fanbeam angle which supplies the gaps data.

Algorithm 4 Customize fanbeam to parallel beam re-binning

procedure FAN2PARA_CUSTOM($nDet_{para}, fanDat, SOD, ODD, d_{pix,fan}, FOV$)
  Initialize $paraDat, paraDat_t1, paraDat_t2$
  $paraDat, paraDat_t1, paraDat_t2 \leftarrow \texttt{zeros}(nDet_{para}, 180)$
  $d_{pix,para}$
  $\theta s \leftarrow \texttt{repmat}([0:179], [1, \texttt{size}(paraDat, 1)])$
  $Ts \leftarrow \texttt{repmat}(-([1:nDet_{para}]' - \frac{nDet_{para}+1}{2}), [1, \texttt{size}(paraDat, 2)])$
  $\alpha s \leftarrow \texttt{repmat}\left(\arctan\left(-\frac{[1:\texttt{size}(fanDat,1)]' - \frac{\texttt{size}(fanDat,1)+1}{2} * d_{pix,fan}}{SOD+ODD}\right), [1, \texttt{size}(fanDat, 2)]\right)$
  $\beta s \leftarrow \texttt{repmat}\left([0 : \frac{360}{\texttt{size}(fanDat,2)} : 360 - \frac{360}{\texttt{size}(fanDat,2)}], [\texttt{size}(fanDat, 1), 1]\right)$
  for all pixel rows and columns of the ideal detector (ii, jj) **do**
    $\alpha_1 \leftarrow \arcsin\left(\frac{Ts(ii,jj) * d_{pix,para}}{SOD}\right)$
    $\alpha_2 \leftarrow -\alpha_1$
    $\beta_1 \leftarrow \theta s(ii, jj) + \alpha_1 + \frac{\pi}{2}$
    if $\beta_1 >= 359$ **then**
      $\beta_1 \leftarrow \beta_1 - 360$
    end if
    $\beta_2 \leftarrow \theta s(ii, jj) + \alpha_2 + \frac{3\pi}{2}$
    if $\beta_2 >= 359$ **then**
      $\beta_2 \leftarrow \beta_2 - 360$
    end if
    Find closest sampled points in $fanDat$ – (b_1, a_1) and (b_2, a_2) to (β_1, α_1) and (β_2, α_2), respectively
    $paraDat_t1(ii, jj) \leftarrow \texttt{interp2}(fanDat(b_1, a_1), \alpha s(b_1, a_1), \beta s(b_1, a_1), \alpha_1, \beta_1)$
    $paraDat_t2(ii, jj) \leftarrow \texttt{interp2}(fanDat(b_1, a_1), \alpha s(b_1, a_1), \beta s(b_1, a_1), \alpha_2, \beta_2)$
  end for
  $paraDat \leftarrow \texttt{featherCombine}(paraDat_t1, paraDat_t2)$ ▷ See Figure 2.15
end procedure

2.5.3 Circular Cone-beam Reconstruction (ASTRA's FDK)

For 3D, circular cone-beam trajectories and single chip detectors, the ASTRA toolbox provides a CUDA implementation of the Feldkamp-Davis-Kress reconstruction algorithm. The inputs to this method include the sinogram and the projection geometry as specified by the parameters d_{pix}, Nch, $Nrow$, SOD, ODD, and a vector of projection angles in radians [78],[79]. This method cannot handle missing data due to gaps between chips, so for multichip detector configurations the algebraic method should be utilized (see Sec. 2.5.4)

2.5.4 Masking the Projection Matrix – Algebraic Reconstruction (ASTRA's SIRT)

For 3D algebraic reconstructions, the gaps found between chips are less of an issue and the input sinogram can be coupled with a binary mask that indicates which pixels to use for the reconstruction. The output of the chip-to-ideal detector mapping scheme plus the mask of this sinogram can be used directly as inputs into the ASTRA toolbox's SIRT algorithm along with vectors which contain source and detector position parameters [78], [79].

2.6 Running in Bulk

If large datasets are desired, the user can choose to run the simulation in bulk. To do so, set-up the simulation as if to run a single scan – load spectra and material CSV's, filter and select the desired input spectra, set thresholds and scan geometry. Once this is done, open the geometry view and select the automated phantom creator of your choice, but DO NOT submit. In the edit box next to the `Run Bulk Operation` button, specify how many random phantoms to scan. If reconstructions of the scanned data are desired, select the `Run in Bulk` checkbox next to the `Reconstruct PC Sinograms` button, otherwise when the `Run Bulk Operation` button is selected, the `Callback` functions for the phantom creation, basis sinogram calculation, and basis-to-photon-counting conversion will be run. Outputs will be placed in numbered {OUTPUT_DIRECTORY}\Phantom-_xxxx folders. The following files are output:

- weighted_phantom.mat
  - `spectra` – (1×2) cell array containing the names of the energy scale and spectrum used as input for the scan.
  - `counts` – $(M \times 2)$ cell array containing the energy increments and counts per increment of the input spectrum used for the scan.
  - `materials` – $(1 \times N + 1)$ cell array containing the names of the N materials in the phantoms. The extra column contains the title for energy spectrum.
  - `mat_coeffs` – $(K + 1 \times N + 1)$ cell array containing the density and linear attenuation coefficients for the N materials in the phantoms. K is the number of energy increments of the energy-dependent coefficients.
  - `thresh` – $(1 \times L)$ vector containing the threshold values for the L energy bins (the maximum L gives the upper threshold (*i.e.* no bin above).

  - `phan` – $(P_{size} \times P_{size} \times P_{size} \times N)$ matrix where each of the N 3D volumes contains the placement of material N. The non-zero voxels of each volume represent the % by weight of that voxel that is material N.

- scan_parameters.mat
  - `FOV` – (1×1) floating-point value which dictates the length of the in-plane diagonal of the phantom.
  - `ODD` – (1×1) floating-point value which dictates the distance between the center-of-rotation (*i.e.* the center-of-the-object) and the ideal detector plane.
  - `SOD` – (1×1) floating-point value which dictates the distance between the source and the center-of-rotation (*i.e.* the center-of-the-object).
  - `nViews` – (1×1) integer indicating the number of views per rotation.
  - `num_pix_ch` – (1×1) integer indicating the number of detector columns (*i.e.* channels).
  - `num_pix_row` – (1×1) integer indicating the number of detector rows.
  - `pix_dist` – (1×1) floating-point value which dictates the distance spanned by 1 dimension of the square detector pixels.
  - `chips` – $(1 \times C_n)$ structure array containing the following fields:
    * `spacing_row` – (1×1) floating-point value which indicates the real-world position of the chip center wrt its row position.
    * `spacing_ch` – (1×1) floating-point value which indicates the real-world position of the chip center wrt its channel position.
    * `axial_offset` – (1×1) floating-point value which indicates the real-world dimension of the chip's axial (*i.e.* z-axis or row direction) offset.
    * `tangential_offset` – (1×1) floating-point value which indicates the real-world dimension of the chip's tangential (*i.e.* channel direction) offset.
    * `radial_offset` – (1×1) floating-point value which indicates the real-world dimension of the chip's radial (*i.e.* ODD) offset.
    * `camera_tan_offset` – (1×1) floating-point value which indicates the real-world dimension of the camera's (*i.e.* all the chip's) uniform tangential offset.

- ..\2_PcTK_outputdata* – This folder contains the PcTK output for each individual chip and translation where the three types of output are mean, noisy (Poisson noise), and ground truth (`gt`). These outputs are made for the sample scan (`m4`) as well as the open beam (`ob`) scans.

- rawData.mat

  - `chips` – ($1 \times C_n$) structure array containing the following fields:

    * *Same offset variable and values as listed above*
    * `mat_bas` – (`nViews` $\times N \times$ `num_pix_ch` $\times$ `num_pix_row`) matrix of floating-point values which indicate the line integral at a pixel through material N for a given view.
    * `ob_mat_bas` – (`nViews` $\times 1 \times$ `num_pix_ch` $\times$ `num_pix_row`) matrix of floating-point values which indicate the line integral at a pixel through open air for a given view.
    * `pc_mean (noisy, gt)` – (`nViews` $\times L \times$ `num_pix_ch` $\times$ `num_pix_row`) matrix of floating-point values which indicate the counts at a pixel through all materials for a given view. The `noisy` version has added Poisson noise and the `gt` version is the analytic ground-truth.
    * `ob_mean (noisy, gt)` – (`nViews` $\times L \times$ `num_pix_ch` $\times$ `num_pix_row`) matrix of floating-point values which indicate the counts at a pixel through air for a given view. The `noisy` version has added Poisson noise and the `gt` version is the analytic ground-truth.

- ASTRA_dataset_noisy.mat

  - `proj_dat1` – ($L \times$ `num_pix_row_ideal` $\times$ `nViews` $\times$ `num_pix_ch_ideal`) matrix of floating-point values which indicate the line integral at a pixel through all materials for a given view. A conebeam geometry is used.
  - `mat_dat` – (`num_pix_row_ideal` $\times$ `num_pix_ch_ideal` $\times$ `nViews`) binary matrix where non-zeros indicate which pixels to use for reconstruction with the ASTRA toolbox.

  - `ASTRA_recon` – ($L \times P_{size} \times P_{size} \times$ `num_pix_row`) reconstruction volume of floating-point values which indicate approximate attenuation coefficient at a given voxel after the ASTRA SIRT reconstruction algorithm.

- FBP_dataset_noisy.mat
  - `paraProj2` – (`num_pix_para_det_ch` $\times$ `nViews` $\times$ `num_pix_para_det_ch` $\times L$) matrix of floating-point values which indicate the line integral at a pixel through all materials for a given view. A parallel beam geometry is used.
  - `FBP_recon` – ($L \times P_{size} \times P_{size} \times$ `num_pix_row`) reconstruction volume of floating-point values which indicate approximate attenuation coefficient at a given voxel after the analytic reconstruction algorithm.

2.7 Working Example(s)

2.7.1 Single Chip Detector

Using the `Automated Ellipsoid BULK` mode, (5) 3D, aqueous K-edge material phantoms were generated and stored as outlined above. Each was scanned with the following geometric parameters:

- 1 chip
- `num_pix_ch` $= 128$
- `num_pix_row` $= 5$
- `pix_dist` $= 0.110mm$
- `FOV` $= 7mm$
- `ODD` $= 110mm$
- `SDD` $= 223mm$
- `nViews` $= 360$

Each of the single chip working model phantoms and their reconstructions are shown in Figs. 2.16, 2.17, 2.18, 2.19, and 2.20. Each energy bin is reconstructed separately. As energy increases, the phantoms attenuate fewer photons and have fewer photons to begin with. Therefore,

those channels are dominated by noise. The phantoms shown are merely geometric ground-truths. The contrast shown does not reflect the attenuation in the phantom in any way. If a shape can be seen in the phantom, but not in the reconstructed image, the shape contains a below-detectable concentration of contrast material. Further analysis of the reconstructed photon counting data (*e.g.* denoising, material decomposition, and threshold optimization) can be performed on these outputs.

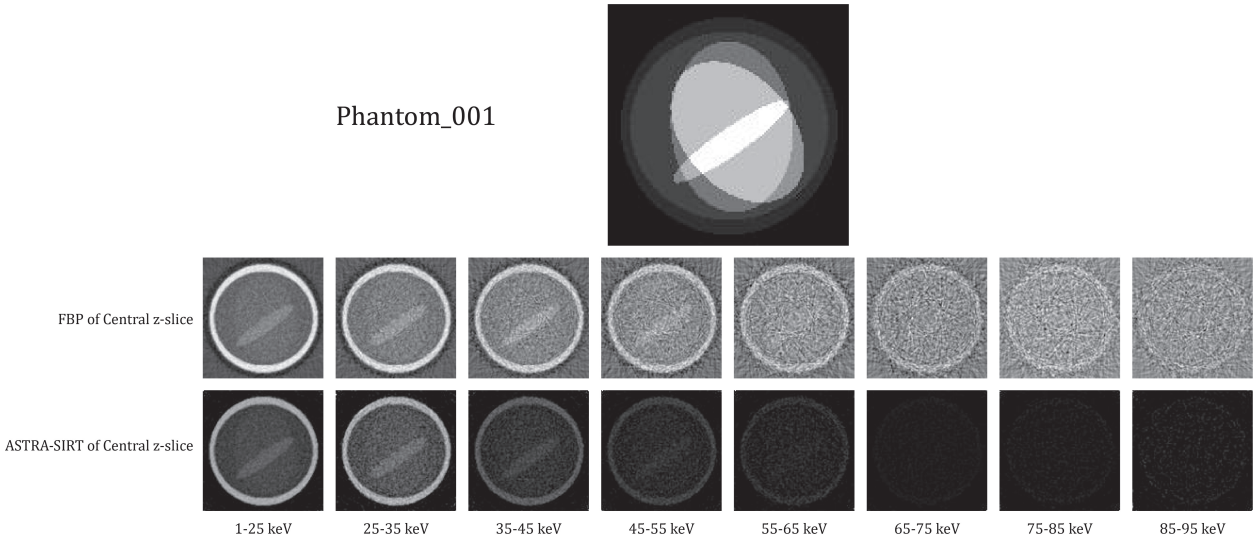

Fig. 2.16: Single chip – Phantom_001 reconstruction outputs.

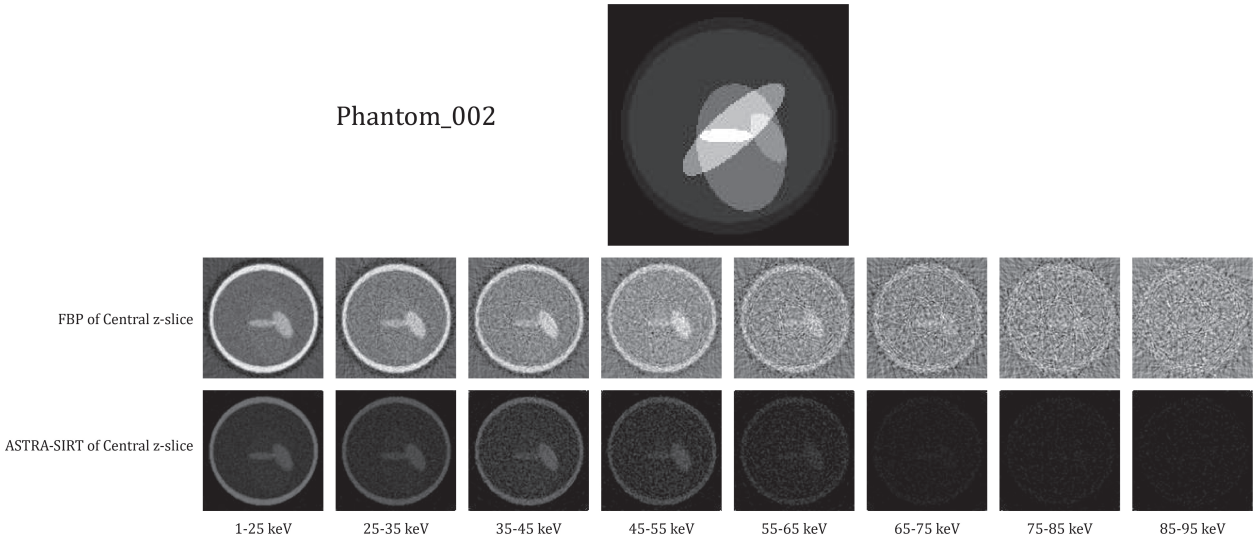

Fig. 2.17: Single chip – Phantom_002 reconstruction outputs.

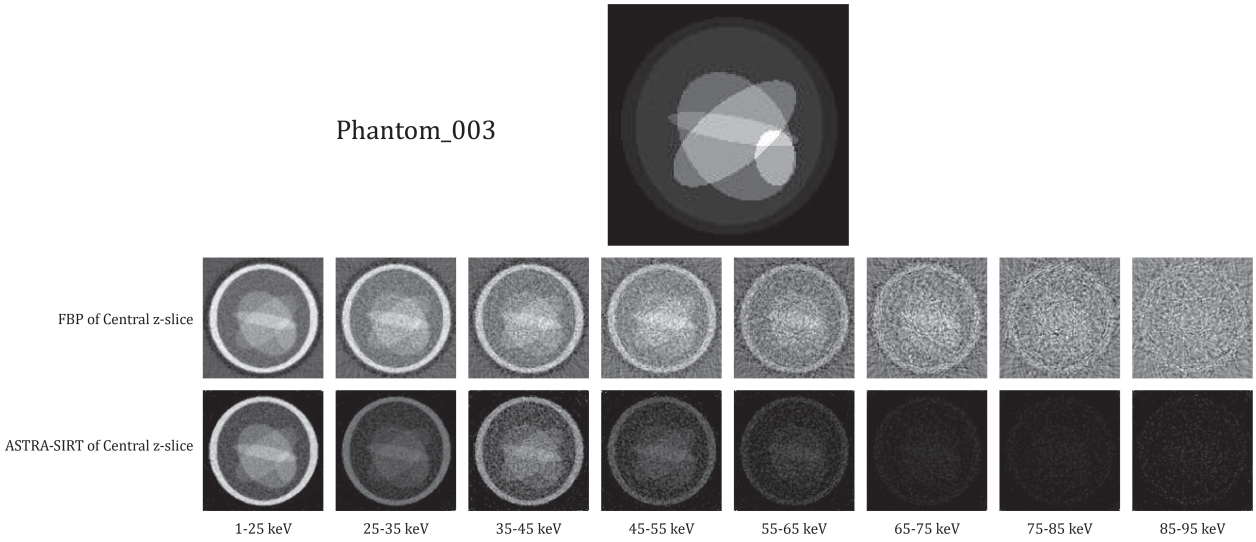

Fig. 2.18: Single chip – Phantom_003 reconstruction outputs.

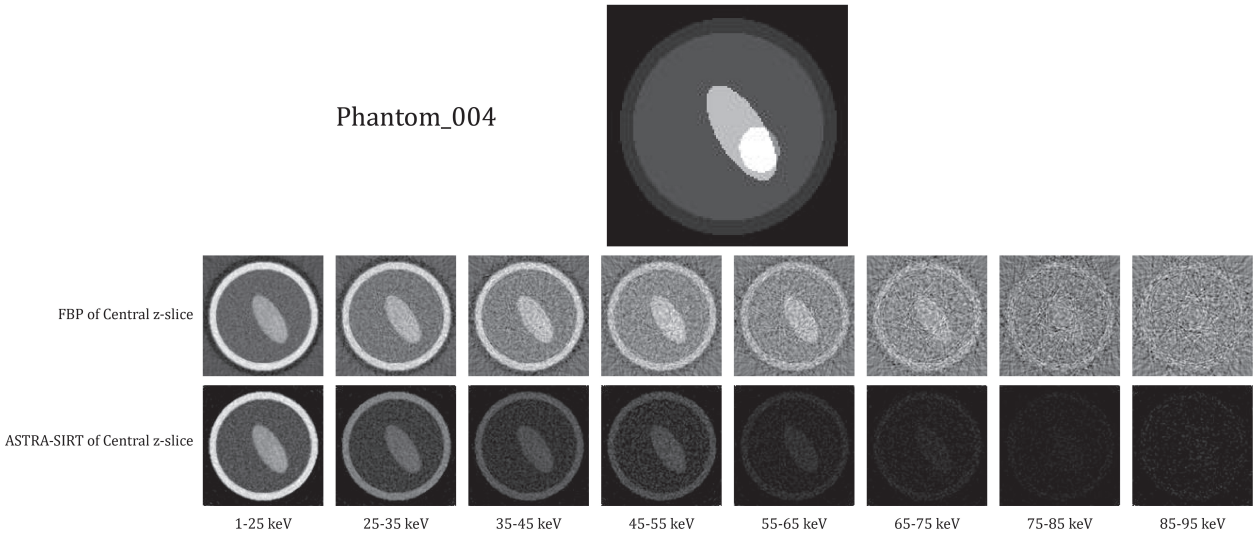

Fig. 2.19: Single chip – Phantom_004 reconstruction outputs.

2.7.2 Three Chip Detector

Using the `Automated Ellipsoid BULK` mode, (3) 3D, aqueous K-edge material phantoms were generated and stored as outlined above. Each was scanned with the following geometric parameters:

- 3 chips
  - Chip 1 offsets – 3-pixel channel spacing, 2-pixel axial offset, 3 mm radial offset

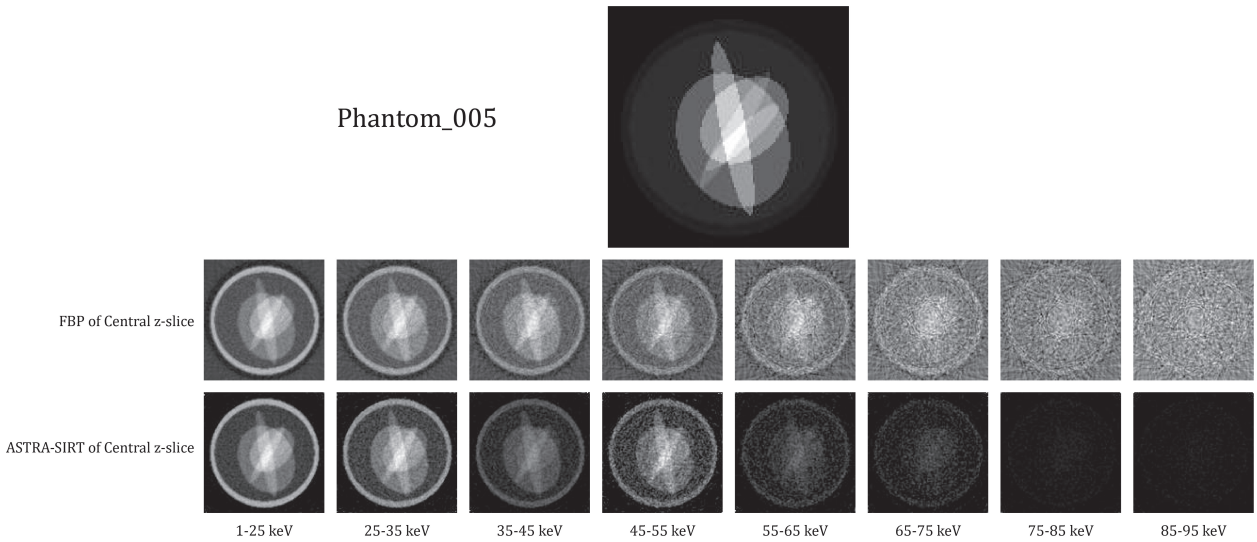

Fig. 2.20: Single chip – Phantom_005 reconstruction outputs.

  - Chip 2 offsets – no offsets
  - Chip 3 offsets – -2-pixel channel spacing , -3-pixel axial offset, -3 mm radial offset

- 8-pixel camera offset
- `num_pix_ch` $= 128$
- `num_pix_row` $= 64$
- `pix_dist` $= 0.110mm$
- `FOV` $= 27mm$
- `ODD` $= 110mm$
- `SDD` $= 223mm$
- `nViews` $= 360$

Each of the three chip working model phantoms and their volumetric reconstructions are shown in Figs. 2.21, 2.22, and 2.23. Only the first energy bin is shown. As with the single chip, the phantoms shown are merely geometric ground-truths. The differences between the FBP 3D approximation and the ASTRA-SIRT 3D reconstruction can be seen. The ASTRA algorithm reconstructs fewer of the slices due to data insufficiency as the slice gets further away from the mid-plane. The

FBP approximation however can reconstruct any row of pixels that contains data with the cosine correction.

2.8 Future Improvements

While the algorithms outline in this manual are sufficient for collecting circular cone-beam scans with several detector arrangements and geometries, some improvements should be made to make the tool a little more flexible and powerful. The following updates are suggested:

- Make **Recon View** (`push button`) functional for quickly viewing the reconstruction output.
- Make multi-selection option for users to decide which reconstruction algorithm to use and on which data (*i.e.* noisy, mean, ground-truth).
- Create user input boxes allowing for the expansion of the geometric functionality to include helical scans. These should include a pitch and length of scan edit box.
- Add GUI section for tuning PcTK parameters including the electron cloud radius, detector thickness, detector density, and electronic noise parameter.

2.9 Conclusion

This chapter outlines the geometry and customized data mapping algorithms used in the spectral CT simulator. The specifics for the available reconstruction algorithms as well as the detector model can be found in the respective user manuals as well as the literature resources for these pieces of software [23],[26],[35],[36],[78],[79]. Specific examples of how the data is used in experiments and algorithm development will be expounded up in later chapters.

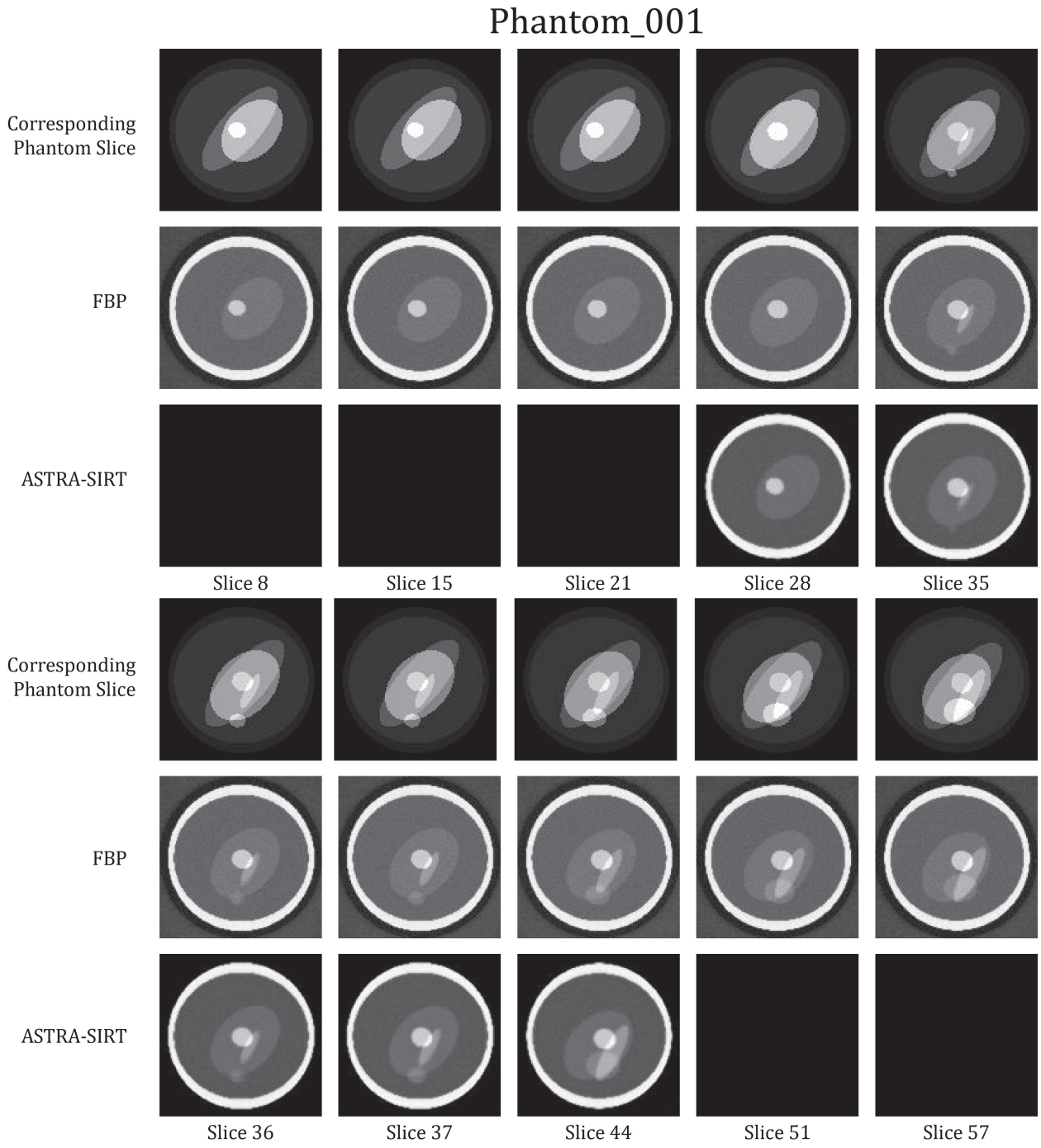

Fig. 2.21: Three chip – Phantom_001 reconstruction outputs from energy bin 1.

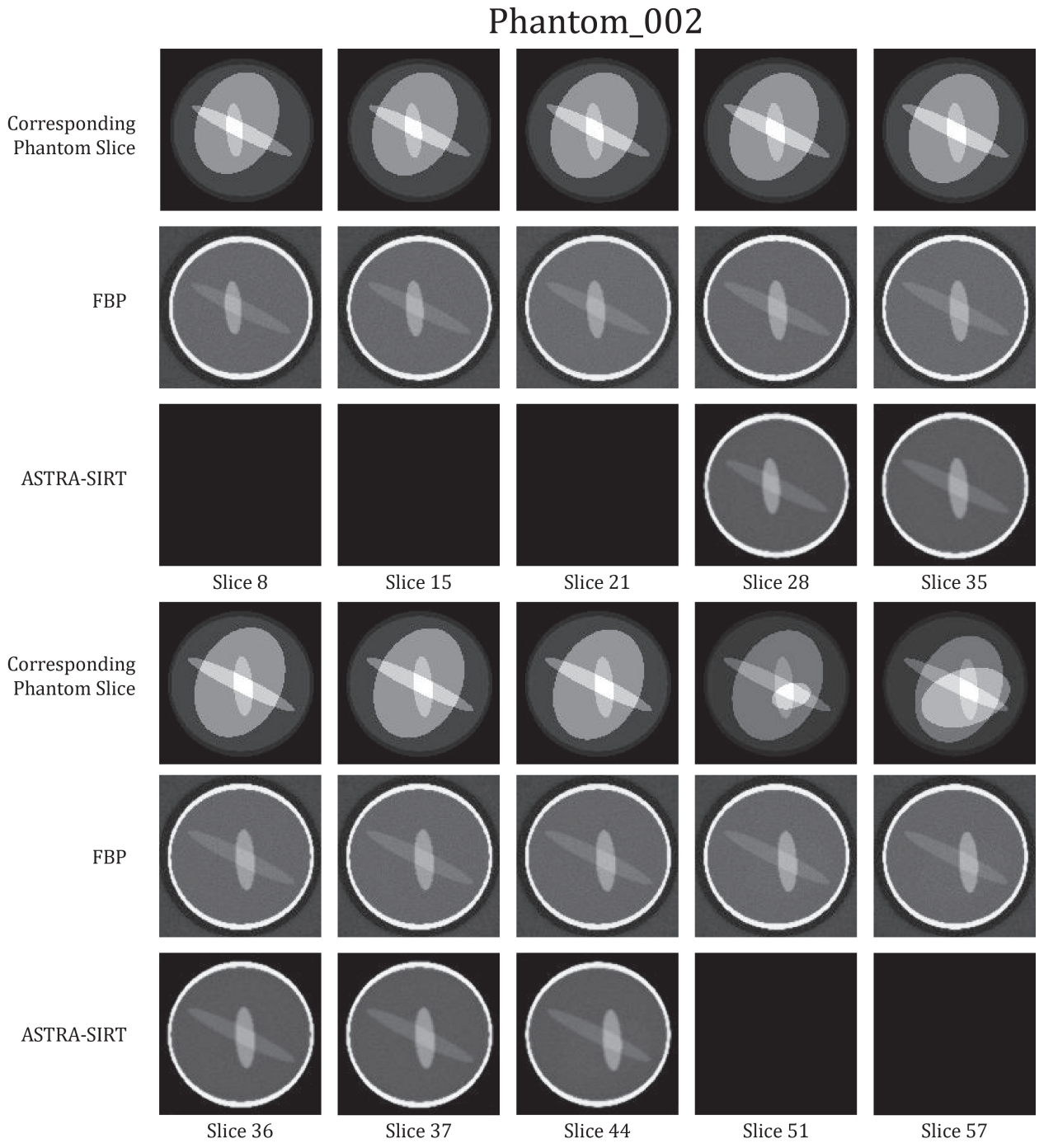

Fig. 2.22: Three chip – Phantom_002 reconstruction outputs from energy bin 1.

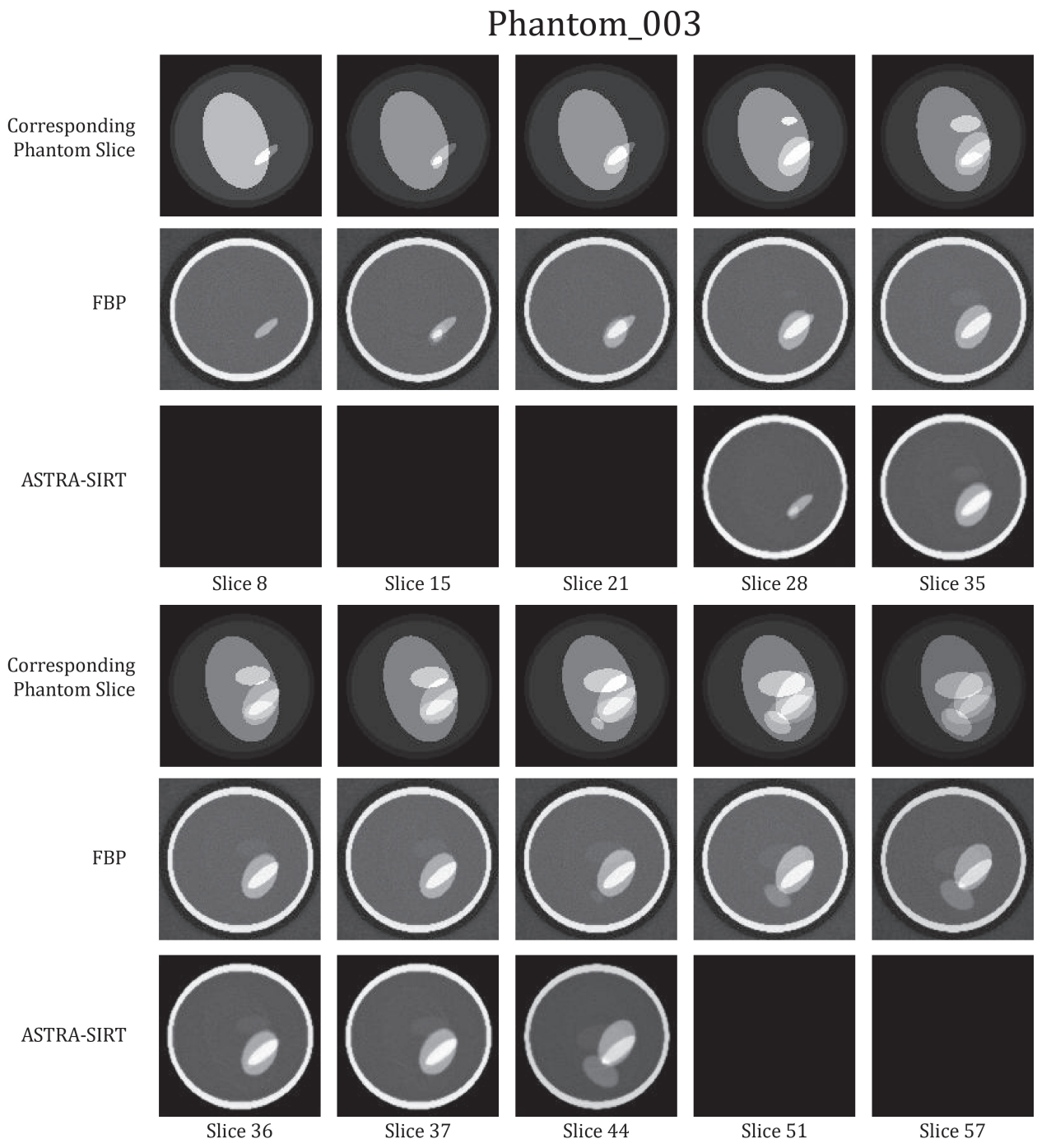

Fig. 2.23: Three chip – Phantom_003 reconstruction outputs from energy bin 1.

Chapter 3
Correcting Counts

3.1 Introduction

After decades of development, X-ray photon-counting detectors (PCDs) become increasingly popular with applications in medical imaging, material science, and other areas [12], [14]. Compared to conventional charge-integrating detectors, PCDs count individual photons, binning them into different energy bins instead of integrating over the whole x-ray energy spectrum. This rids the detector and resulting images of some major problems such as electronic noise and beam hardening. Indeed, PCDs have already shown potentials for better SNR and energy discrimination capabilities [14], [29], [81]. The promising energy-resolved performance of PCDs aids in many in material decomposition and quantitative CT tasks [13], [17], [81]. However, some technical problems remain, such as counting rate limit, spatial non-uniformity and spectrum distortion that compromise practical applications. While the operational counting rate is often less than $10^6 cps/mm^2$, the state-of-the-art semiconductor PCDs offer counting rates higher than $10^7 cps/mm^2$ [82]. An overly high counting rate would distort the energy profile of detected signals. The spectrum distortion is a nonlinearity problem caused by several physical effects: pulse pileup, charge sharing, escape of K-fluorescence x-rays, Compton scattering, charge-steering, etc. [24]. Many researchers have made efforts to solve these problems; for example, proposing different methods to eliminate the pulse pileup and charge sharing induced ring artifacts [13], [13], [24], [25], [82]. Spatial non-uniformity is another cause for image artifacts due to the charge trapping on structural defects which have not been well studied.

Here we explain and implement an open beam correction method aimed at the spatial non-uniformity of pixels based on the first and second moment correction [83]. First, two sets of frame data are collected in the open beam setting with fixed exposure time but at two different fluxes located in the linear range. Then, the datasets are processed by a pixel mask to turn off abnormal pixels (*i.e.* overly noisy, dead, and high counting pixels), and the gain correction factor matrix is calculated to normalize the variances of pixel responses. Finally, a mean correction factor matrix

Portions of this chapter have been submitted for review as: M. Getzin, M. Li, D. S. Rundle, A. P. H. Butler, and G. Wang, "Spatial uniformity correction for MARS photon-counting detectors," at Fully 3D 2019: 15th International Meeting on Fully Three-Dimensional Image Reconstruction, Philadelphia, PA, USA, June 2-6, 2019.

is obtained. All these corrections can be combined to produce pixel responses of the same quasi-poison distribution (*i.e.* normal with mean equal variance).

In addition to the empirical correction methods and experiments, a proposal for correcting non-linear counting behaviors (*e.g.* charge-sharing and pulse pile-up). First, an extension of the two-moment empirical correction for the linear range will be proposed. This method is based on data measurements and requires the arrangement of these data points into a look-up table (LUT). Other methods which incorporate data produced by the PCD simulation described in Chapter 2. In addition to simulation, state-of-the-art neural network approaches are proposed. Discussions of transfer learning from these simulation-trained neural networks to real-world MARS data will also be made.

3.2 Methods

3.2.1 Spatial Non-uniformity Response Modeling

Before the introduction to the model, let us first introduce some notations. Under a given flux and integration time, the counts of the ith pixel of the detector at the jth measurement is denoted as $C_{i,j}$. Reasonably, we assume that each pixel counts Poisson statistics in time, yet different pixels may have different sensitivity due to the structural defects. Thus, for each pixel-specific counting experiment we have

$$C_{i,j} \sim P(\lambda_i) \tag{3.1}$$

On the other hand, it is well known that a too high incoming photon rate will lead to a loss of the measured counts with the loss increasing nonlinearly with respect to the flux as illustrated in Fig. 3.1a. This can be explained with pulse pileup and charge sharing effects that are a function of the flux, leading to a nonlinear distortion of the counting curve. We can model this relationship as

$$\lambda_i = (g_i I + d_i(I))t \tag{3.2}$$

where g_i is the linear gain coefficient depicting the ideal linear relationship between the flux and the counting rate, I stands for the photon flux, t represents the exposure time, and d_i depicts the nonlinear deviation of the real count from the ideal linear output which is a function of I. Different values of g_i and d_i represent the spatial nonuniformity. Inclusion of t outside the brackets indicates that integration time has no influence on the nonlinear effects.

3.2.2 Determination of the Linear Range

If the photon flux is low enough, we can assume that

$$E(C_{i,j}) \propto I \text{ when } I < I_L \tag{3.3}$$

where $\propto$ means a linear relationship, and the interval $[0,\ I_L]$ is sufficiently narrow. In other words, d_i can be zero or, at most, an approximately constant offset. Suppose that we collect two sets of data, $C_{i,j}^{(1)}$ and $C_{i,j}^{(2)}$, with a given exposure time t_0 under fluxes of I_1 and I_2 respectively in the interval $[0,\ I_L]$. Using the two sets of time measurements for each pixel, we can calculate g_i and d_i according to the model given as Eq. 3.2,

$$g_i = (\lambda_i^{(1)} - \lambda_i^{(2)})/(I_2 - I_1)t_0,\ d_i = (\lambda_i^{(1)} I_2 - \lambda_i^{(2)} I_1)/(I_2 - I_1)t_0 \tag{3.4}$$

where $\lambda_i^{(.)}$ is calculated from the average of $C_{i,j}^{(.)}$, $j = 1,\ 2,\ \ldots,\ M$. Then, we can calculate the correction for the gain as

$$k_i = \bar{g}_i / g_i, \tag{3.5}$$

where $\bar{g}_i$ is the average of g_i, $i = 1,\ 2,\ \ldots,\ N$.

As we know, for a PCD there is no electronic noise in principle, and the count offsets should be very small in the linear range. Therefore, d_i should remain a very small value when the flux is in the linear range, and d_i calculated from any two flux points should just fluctuate with a very small relative magnitude. But when one of the flux points moves out of the linear range, the calculated di' will increase by a relatively large magnitude,

$$d_i' = (d_i^{(1)} I_2 - d_i^{(2)} I_1)/(I_2 - I_1)t_0 \tag{3.6}$$

Thus, we can pick a series flux points $I_l, l = 1,\ 2,\ \ldots,\ H$; and calculate $d_i^{(l)}$ from two flux points I_l, I_{l+1} until the Lth $d_i^{(L)}$ gets over a pre-specified threshold. Then, we define the linear range as $[0,\ I_L]$.

3.2.3 Correction Method in the Linear Range

We know that for an ideal detector in the open beam, the pixels will count following the same Poisson distribution in the spatial domain. Thus, we would like to correct our open beam frames of

counts $C_{i,m}$ to a spatial norm distribution $N(\bar{g}_i I t_0,\ \bar{g}_i I t_0)$ which is an approximation of a Poisson distribution.

The correction steps are as follows. First, in the open beam situation, we choose two appropriate flux points in the linear range to calculate the matrixes of d_i and k_i with Eqs. 3.4 and 3.5. Then, for the correction of the ith pixel $S_{i,p}$ in our measured P frames, $p = 1,\ 2,\ \ldots,\ P$, we calculate the temporal mean $S_i^{(m)}$ of P measurements of $S_{i,p}$, and according to the maximum likelihood, we may guess $S_{i,p}$ was collected at the flux point where the pixel counts in a Poisson distribution $P(S_i^{(m)})$. According to our linear model (Eq. 3.2), the g_i, d_i, and k_i will remain almost unchanged at different flux points. Thus, we can directly use the d_i and k_i to correct collected data for any flux in the linear range without introducing significant errors. Finally, we conduct the following correcting steps with the d_i and k_i. (1) unbiasing $S'_{i,p} = S_{i,p} - S_i^{(m)}$; (2) variance correction $S'_{i,p} = \sqrt{\bar{g}_i I t_0 / S_i^{(m)}}\, S'_{i,p}$; (3) mean correction $S'_{i,p} = S'_{i,p} + \bar{g}_i I t_0$, where we have $\bar{g}_i I t_0 = (S_i^{(m)} - d_i t_0) k_i$.

3.3 Experimental Results

We conducted three experiments in our MARS system. There are 3 chips in the detector and $128 * 128$ pixels on each chip with a pixel size of $110 * 110 \mu m^2$, and each pixel contain 8 channels (Chs). To determine the flux linear range of the PCD, 24 current points were chosen from $15\mu A$ to $130\mu A$ with an increment of $5\mu A$, and 500 frames of open beam images were collected at each current value with the integration time of $125ms$. The overall mean count value of each channel (discarding 3 Chs that do not have charge sharing correction circuits) is plotted against the set tube current in Fig. 3.1a. Each Ch has a different threshold which means different Chs will receive different level fluxes at the same current. Thus, without loss of generality, Ch 8 (threshold $23.5keV$) was chosen to demonstrate further analysis. As we can see, the curve is nearly linear when current is low, yet it deviates with increasing current and even drops at $130\mu A$ suggesting the presence of severe nonlinear effects at such high currents. Following the method in sec. 3.2.3, the calculated offsets as function of tube current is shown in Fig. 3.1b. The solid line represents the mean of offsets d_i of all pixels, while the bars across the line indicate the variance of d_i at each current, $i = 1,\ 2,\ \ldots,\ 16384$. The increasing mean indicates that the counting process suffers serious nonlinear effects as current increases. The wide-spread variance bars show the nonuniformity between pixels. We can also roughly determine the current linear range as $[0, 40\mu A]$, with the offset mean fluctuating from 30 to 55. To demonstrate the effectiveness of our method in linear range, we calculate the correction parameters from data collected at currents of $15\mu A$ and $40\mu A$, then used the parameters

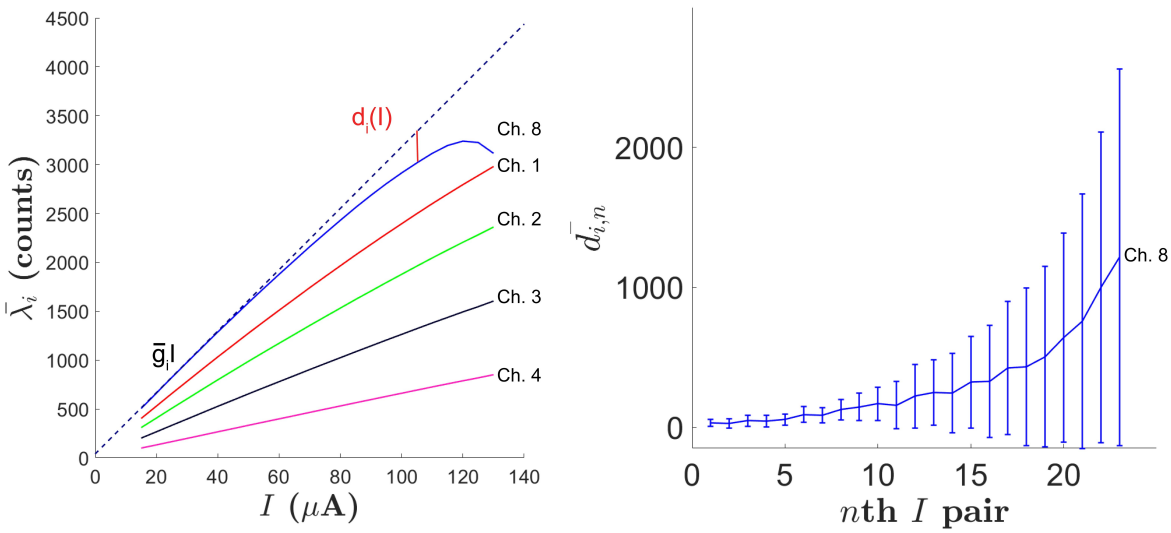

(a) **(b)**

Fig. 3.1: (a) Measured counts vs. tube current is plotted for each of the PCD channels which operate in charge-summing mode. The dashed line is the "ideal" response for Ch 8. (b) The calculated (Eq. 3.4) mean detector offset for Ch 8 across all pixels where I_1 and I_2 are sequentially sampled current pairs (e.g. 15, 20, 25, 30, 35μA, etc.). The linear range is encompassed by the first 5 current pairs (0-40 μA).

to correct the open beam image sets collected between $15\mu A$ and $40\mu A$. The mean of the spatial standard deviations (SSTD) of the 500 images before and after correction are compared as shown in Fig. 3.2a. As we can see the SSTD across the detector in Ch 8 has been decreased by at least 4 folds, indicating reduced non-uniformity.

Finally, we scanned a wire phantom and selected Ch. 8 data from one column of pixels across all three chips. The sinogram from that line of pixels, before (top) and after (bottom) correction, is shown in Fig. 3.2b. After the correction, the line-pattern nonuniformity shown in the raw data has been greatly reduced, and several small line structures which are hard to see in the uncorrected sinogram can be easily discerned.

3.4 Discussion

3.4.1 Empirical Correction Method in the Linear Range

The results presented in the previous section provide strong evidence that the two-moment, empirical correction method is effective in reducing the spatial non-uniformity that is inherent in real-world PCDs. Indeed, each corrected frame is spatially Poisson with the individual pixels counting according to the same Poisson distribtution over time (P>1 frames per view or open beam

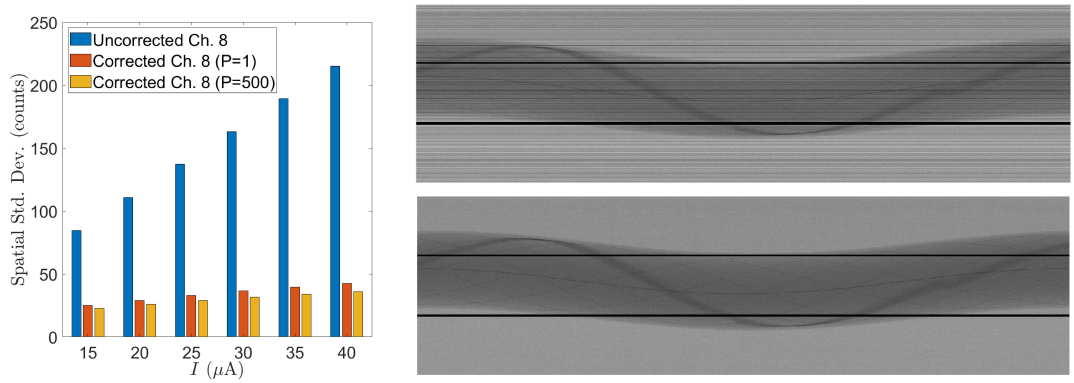

(a) (b)

Fig. 3.2: (a) SSTD for open-beam data as a function of linear range tube currents. (b) The uncorrected (top) and corrected (bottom) sinograms for 1440 angle projections around a wire phantom.

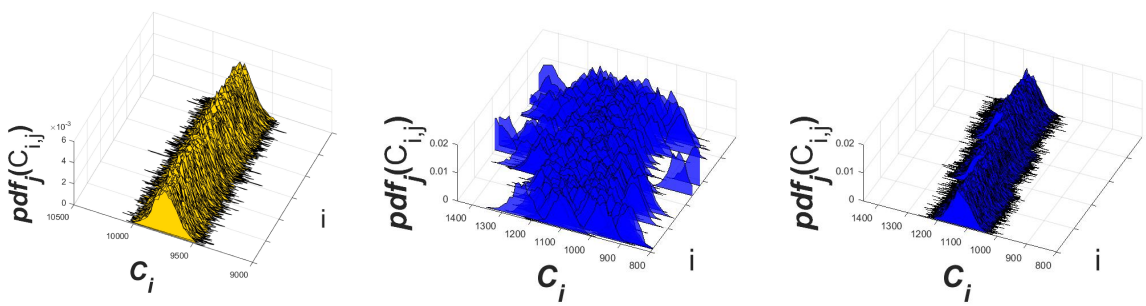

(a) (b) (c)

Fig. 3.3: (a) The temporal distributions of the PcTK output pixels are Poisson-counting with the same mean. (b) Uncorrected MARS detector pixels are Poisson-counting, yet their mean values are widely distributed. (c) Corrected MARS detector pixels are Poisson-counting with the same mean (provided they occupy the same monolith/chip).

frames). Even when only a single view is measured, the effect of correction method on the spatial non-uniformity is drastic. While results were primarily shown for the arbitration counter (Ch. 8), the method is effective in correcting the counts for all measured energy threshold (or bins). Finally, the resulting noise profiles and counting statistics that are achieved after the empirical correction follow the ideal detector's counting behavior as demonstrated by Figure 3.3

3.4.2 Empirical Correction Method in the Nonlinear Range

When the flux is in the nonlinear range, d_i becomes a function of flux due to pulse pileup, charge sharing, etc. Here we assume that the system is time-invariant, which means whenever

Table 3.1: Parameters looking up table for nonlinear range correction.

Flux Points	$i = 1$	$\dots$	$i = N$
I_{L+1}	$(\lambda_1^{L+1},\ \bar{g}_i I_{L+1} t_0)$	$\dots$	$(\lambda_N^{L+1},\ \bar{g}_i I_{L+1} t_0)$
$\dots$	$\dots$	$\dots$	$\dots$
I_G	$(\lambda_1^{G},\ \bar{g}_i I_G t_0)$	$\dots$	$(\lambda_N^{G},\ \bar{g}_i I_G t_0)$

we conduct a measurement on the same pixel with the same flux and exposure time, the count should follow the same Poisson distribution. Thus, it is possible for us to use the precalculated parameters from open beam data to correct the measurement data with a sample in the beam. To keep the linearity of corrected responses, we may still use the reference line $\lambda = \bar{g}_i I t_0$ in the linear range case. In other words, we should still correct our open beam frames of counts $C_{i,m}$ to a spatial normal distribution $N(\bar{g}_i I t_0,\ \bar{g}_i I t_0)$. The correction steps are as follows, (1) choose representative flux points I_l within the usable nonlinear range, $l = L+1,\ L+2,\ \dots,\ G$; (2) measure M open beam frames of counts $C_{i,j}^{(l)}$ at each flux point $I_l, j = 1,\ 2,\ \dots,\ M$, and calculate the corresponding temporal mean $\lambda_i^{(l)}$ and variance $V_i^{(l)} = \lambda_i^{(l)}, i = 1,\ 2,\ \dots,\ N$; (3) use the parameters pairs $(\lambda_i^{(l)},\ V_i^{(l)})$ to form a look up table as shown as Table 3.1; (4) calculate the temporal mean $S_i^{(m)}$ of P frames of measurements $S_{i,p}$ with the sample in the beam, $p = 1,\ 2,\ \dots,\ P$; (5) for the correction of the ith pixel, find $\lambda_i^{(l*)}$ in the ith row that has the closest value to $S_i^{(m)}$; (6) conduct the correction of $S'_{i,p} = \sqrt{\bar{g}_i I^{(l*)} t_0)/(\lambda_i^{(l*)}}(S_{i,p} - \lambda_i^{(l*)}) + \bar{g}_i I_{l*} t_0$. To be mentioned, we can only correct the data where the fluxes are in the interval $[I_L,\ I_{max}]$ and can collect data at as many flux points as we can to get the higher accuracy, but when the flux points are sparse, we can conduct curve fitting to the curve $d'_i(\lambda_i)$ and use $(S_i^{(m)}, S_i^{(m)} - d'_i S_i^{(m)} t_0)$ to implement the correction for every pixels to increase the accuracy, where the fitting data are $(\lambda_i^{(l)},\ d_i'^{(l)} = \lambda_i^{(l)}/t_0 - \bar{g}_i I_l)$.

3.4.3 Conclusion

The Medipix3R detector's counting behavior has been modeled here with a linear count model. By coupling the model with some basic assumptions, the spatial nonuniformity seen with the flux in the linear range has been corrected using a two-moment correction method. The corrected frames more closely resemble the behavior modeled by the ideal detector PcTK model (*i.e.* Poisson counting across space). Corrections performed using several frames per projection (*i.e.* open-beam) result in near perfect counting distributions across the pixels. Even counts corrected with a single frame per projection have a significant reduction in spatial noise, although the spatial variance is slightly greater than the spatial mean (*i.e.* non-Poisson).

Chapter 4
Enhancing Spectral CT with Aperture Encoding

Recent advances in X-ray imaging technologies have paved the way for use of energy-discriminating photon-counting detector arrays. These detectors show promise in clinical and preclinical applications. Multi-energy or spectral CT images can be visualized in multi-colors. Despite the advantages offered by the spectral dimension of acquired data, higher image resolution is still desirable, especially in challenging tasks such as on-site studies of resected pathological tissues. Here we propose to enhance image resolution of a spectral X-ray imaging system by partially blocking each detector element with an absorption grating (for reduced aperture), commonly used for Talbot-Lau interferometry. After acquiring X-ray data at an initial grating-detector configuration, the grating is shifted to expose previously blocked portions so that each measurement contains new information. All the acquired data are then combined into an augmented system matrix and subsequently reconstructed using an iterative algorithm. Our proof of concept simulations are performed with MCNP6.1 code and the experiment was performed using a Hamamatsu microfocus X-ray source, an absorption grating, and an X-ray camera. Our results demonstrate that the gratings commonly used for x-ray phase-contrast imaging have a utility for super-resolution imaging performance.

4.1 Introduction

X-ray detection technology can be categorized into two groups: energy-integrating and photon-counting. The advantages of photon-counting, energy-discriminating detectors are evident relative to energy-integrating detectors [84]. First, energy-discriminating detectors should not have any of the beam hardening bias that is seen in energy-integrating counterparts [85],[86]. Second, the ideal photon-counting detectors have an inherently higher signal-to-noise ratio (SNR) by utilizing spectral information, suppressing electronic and Swank noise [87], and rejecting scattered photons [20]. The SNR improvement for photon-counting detectors can be up to 90% [86]. Third and most importantly, photon-counting detectors can reveal elemental composition of materials and support

This chapter has been presented as: M. Getzin *et al.* , "Enhancing spatial resolution for spectral μCT with aperture encoding," in *Developments in X-Ray Tomography X*, vol. 9967, Sep. 2016. doi:10.1117/12.2237840 [Online]. Available: https://www.spiedigitallibrary.org/conference-proceedings-of-spie/9967/99670W/Enhancing-spatial-resolution-for-spectral-uCT-with-aperture-encoding/10.1117/12.2237840.full?casa_token=vZ8vw5K-JqwAAAAA%3aTYqJ3oFa0uu0rVo8cRc_PFqb6SBiT4C7CM1_iz6D-hjdYJJYr3oE8_E0wAkKhNFJNOKoSw&SSO=1 (Accessed: Apr. 12, 2019).

novel contrast-enhanced studies [59], [88] thus opening new possibilities for functional, cellular and molecular imaging with novel contrast agents such as GNPs [89]–[92]. Although clinical spectral CT remains a challenge due to high detector costs, performance uniformity and stability, and relatively low- incident X-ray flux [29], the challenges are not as relevant in preclinical/pathological scanners. Therefore, many researchers have proposed using new photon-counting detectors and microfocus X-ray sources as the basis for dedicated spectral micro-CT [13], [29], [41], [93]–[96]. The utility of photon-counting detectors was shown in measuring spectra from bremsstrahlung sources [13] as well as increasing contrast-to-noise ratio (CNR) relative to the integrating detectors. High CNR can be achieved with X-ray energy weighting schemes [20], [43], [93], [97]. The newest and most advanced line of photon-counting detectors, Medipix3 (CERN, Geneva, SUI), has also been incorporated into a preclinical scanner where it was demonstrated that the charge summing mode of the detector allowed for charge sharing compensation [28]. In modern biomedical imaging, there is a large technology gap between optical microscopy and micro-CT techniques. This gap on the mesoscopic scale is a result of high scattering and absorption of visible and NIR light and spatial resolution limitations of state-of-the-art CT detectors (PC and integration). Therefore, very few techniques allow for imaging samples that require depths $\sim$1-10 mm and in-plane resolution $\sim$5-50 μm. We propose to fill this gap by taking advantage of geometric magnification for small samples [98], as well as implementing novel x-ray encoded aperture imaging for major resolution enhancement. The notion of using encoded apertures in X-ray imaging has been around since the 1970s, although the scope of the research in this area has been focused on placing at least one set of apertures between the source and an object to be imaged for tomosynthesis [99]–[102] and, more recently, phase contrast [102]–[124] and scatter imaging [105], [116], [125]. In tomosynthesis, encoded apertures are used to allow for multiple x-ray projections to be made simultaneously and subsequently decoded based on the known imaging geometry. This allows for 3D images to be produced using a limited number of projection angles, thereby reducing radiation exposure. In interferometric phase contrast and scatter imaging, multiple sets of apertures (gratings) placed on either side of the object may be used to obtain desired images. Although the structure and materials of the gratings and apertures used in tomosynthesis, phase contrast, and scatter imaging are likely to be the same as those used in resolution enhancement aperture encoding, our techniques differs in both the imaging geometry and the technical purpose. Hardware with both function and placement somehow akin to those proposed by resolution enhancement encoded apertures are anti-scatter grids. These grids, often composed of strips of lead and a radiolucent substance [126], are placed

before the detector to limit the amount of radiation scatter that reaches the detector. These grids were investigated with both standard flat panel and high-resolution CMOS detectors and shown to increase CNR after corrective methods eliminate the grid artifacts in the images [127], [128]. In fact, the similarity in function and placement of our proposed resolution enhancement encoded apertures and anti-scatter grids, may allow for dual-function, anti-scatter/resolution enhancement encoded apertures. The fourth section of this paper will discuss this possibility. In the next section, we describe our simulation environment and experimental design. In the third section, we present our representative results. In the fourth section, we discuss relevant issues, suggest future directions, and conclude the paper.

4.2 Materials and Methods

4.2.1 Aperture Design

Much like the design of the anti-scatter grids, encoded apertures for resolution enhancement must have alternating radiopaque and radiolucent areas. The key to achieving the desired enhancement is to sufficiently block some portion of the detector element while allowing the other section of the element to measure the incoming radiation. Subsequently, the aperture is moved to allow for previously blocked places of the detector to measure the incoming radiation so that new information is collected. This procedure is repeated sufficiently many times to allow for all the subsections of the detector to measure the incoming radiation and for as many views as deemed necessary for tomographic reconstruction.

The most straight-forward design places the encoded aperture flush with the detector array. The size of the radiolucent portion of the encoded aperture will depend on the desired enhancement. Fig. 4.1 gives several example designs. Scan time and radiation dose will increase linearly with the number of sub-elements into which each detector element is divided. Other designs may also be of interest and will be discussed in fourth section of this paper. For the following simulations and experiments, the assumptions and geometries were based on the distance between the encoded aperture and detector being zero.

4.2.2 MCNP6.1 Simulation Environment

The simulations were performed using Monte Carlo N-Particle (MCNP) software as developed by Los Alamos National Laboratory [129]. The purpose of the simulations was to test and extend the resolution enhancement capabilities of the proposed aperture encoding method. The

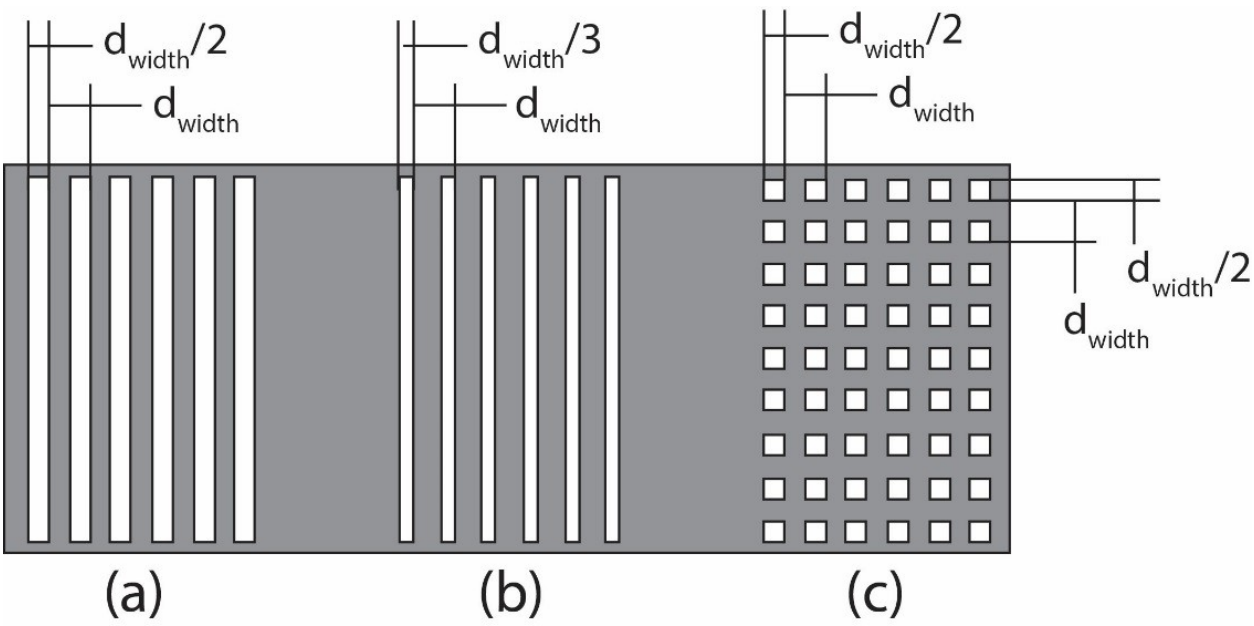

Fig. 4.1: Typical encoded aperture designs. (a) The design for 2X resolution enhancement in 2D tomography, (b) the design for 3X resolution enhancement in 2D tomography, and (c) the design for 2X resolution enhancement in 3D tomography.

FIR5 (transmitted radiographic image projection) tally method was deemed most in this study. Three hardware configurations were simulated each with 180 projection angles. The tallies were later parsed and placed into system matrices for reconstruction. A resolution phantom of 4 mm radius was placed at the origin of the simulation frame. The phantom was filled with water and contained three sets of seven cylinders (radii - 450, 380, 300, 200, 100, 75, and 50 μm) spaced equiangularly around a circle with radius of 3 mm and three sets of four cylinders (radii - 200, 150, 75, and 50 μm) at placed equiangularly on a circle with a radius of 1.5 mm. The inner cylinders were filled with three biologically relevant materials as defined by NIST: silicon, bone, and whole blood. The geometric rendering of this simulation environment is shown in Fig. 4.2.

For the FIR5 tally, the detector was simplified to a grid of detector elements on a planar surface. The grid was defined as 256 x 1 array of 110 μm x 110 μm detector elements. This array was bisected by the XZ-plane and placed at 9.4313 cm from the origin in the Y direction. Only direct x-ray contributions to the flux were used for image reconstruction.

A gold grating was defined as a 512 x 1 x 1 array of 55 μm x 500 μm x 110 μm cells. These cells were alternately filled with gold and dry air. The grating was also centered in the XZ-plane and placed within 0.5 μm from the detector pane. In the control configuration, this grating was removed and replaced with dry air while the two test configurations differed by translating the grating 55 μm

in the X-direction. In both simulations, the source energy was defined as a monochromatic, 100 keV and the source shape was defined as a cone-beam point source located -4.4302 cm from the origin and 13.8615 cm from the detector. Its cone angle was defined to span every element of the X-ray detector array (6° from XZ-plane). Taking into account the source-detector and source-object distances, the effective pixel size was 35.15 μm x 35.15 μm without the grating and 17.58 μm x 35.15 μm with the grating. With the geometric parameters described above, we reconstructed the CT image without the grating via ART-TV method for 10 iterations and the size of reconstructed image is 256x256. The combined aperture sinogram was also reconstructed via ART-TV for 10 iterations. Since the detector element pitch of the encoded aperture CT system is half in the X-direction that of the original detector pitch. The size of reconstructed image is 512x512. Image quality was determined by quantifying modulation depth (MD) between the silicon circles and the surrounding water. Here MD is defined as the ratio between the difference in contrast between the respective areas over the sum of these two contrast values.

4.2.3 Experimental Design

The experimental setup is shown in Fig. 4.3. The x-ray source was made by Hamamatsu Photonics, the model number L10101. The tube voltage was set to 40kV and the x-ray tube current was set 180 μA. The x-ray flat panel detector was made by Rayence, model 1215CF-MP. The pixel pitch is 49 μm, the number of active pixels is 2352x2944, the energy range is 40 to 90 kVp, and the frame rate can be 10 fps. For the initial single projection experiments reported, we used a 28 keV, Talbot order 3 gold absorption grating made by Microworks Precision Structures. The period of the grating, 50.26 μm was chosen since it was the closest period to the pixel pitch that was available in the lab. The gold layer had a height>80 μm on was deposited on a 200 um thick section of silicon. 20 projections and their corresponding reference projections were taken at 2.5 μm translation increments, resulting in 10 pairs of projections which could be combined for resolution enhancement in the X direction. In order to calibrate the geometric parameters of our CT system by x-ray geometric calibration method via locally linear embedding [130], we first scanned the phantom without the grating. The source to detector distance is 148.6 cm, the source to object distance is 126.26 cm. Then we calibrated the detector offset along Y axis and rotation stage center offset with the calibration method, after 5 calibration iterations, the calibrated detector offset along Y axis was -0.7392 cm and the calibrated rotation stage center offset was -0.6170 cm. Images were subject to median filtering for noise reduction, especially for the encoded aperture

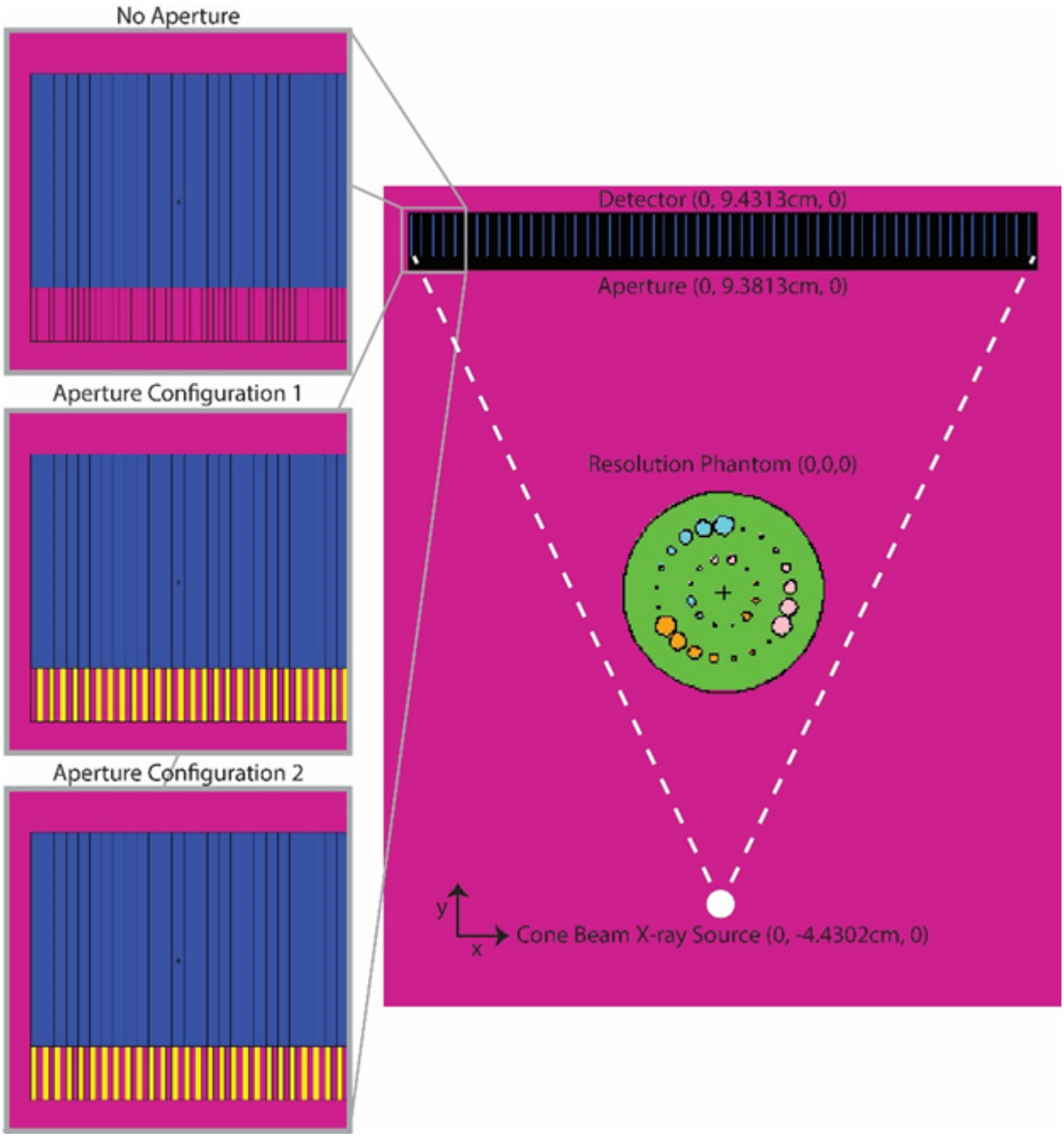

Fig. 4.2: This MCNP geometry rendering shows the aperture encoding configurations used in the simulations. The gold filter, seen in aperture configurations 1 and 2 as yellow, was placed flush with the CZT detector (shown as dark blue). Spacing of elements is not to scale and the FIR tally only used the planar grid of the CZT detector face for its measurement.

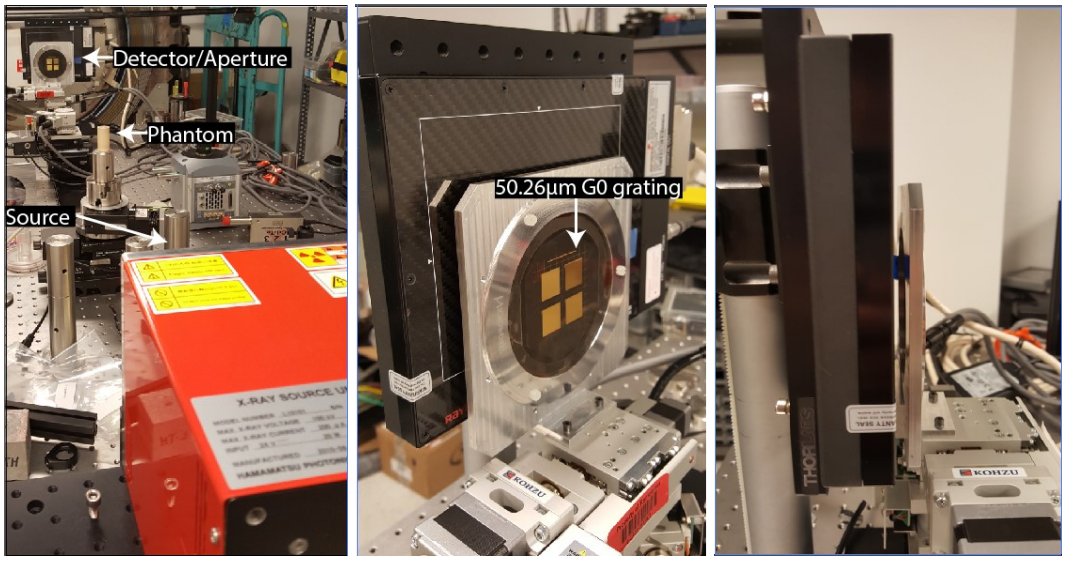

(a) (b) (c)

Fig. 4.3: X-ray micro-imaging platform. (a) The full single-projection setup included a Hamamatsu microfocus x-ray source; a QRM Micro-CT-BarPattern resolution phantom; a Microworks 28keV, G0 absorption grating with 50.26 μm period; and a Rayence model 1215MCB flat panel detector; (b) The G0 absorption grating has four 15 mm x 15 mm grating areas with various periods. The 50.26 μm grating is the top right grating area; and (c) In this setup, the G0 grating would ideally lie within detector plane in order to match the pitch and period between detector and grating, respectively. Our hardware, however, limited how close we could bring these two elements ($\sim$0.5-1 cm). This and the mismatch between detector pitch and grating period, are possible sources of enhancement error.

image. Projection image quality was determined by quantifying modulation depth (MD) of the 30 μm line pairs. Additionally, modulation transfer function curves were created for both unfiltered and median filtered images.

4.3 Numerical and Experimental Results

4.3.1 MCNP6.1 Results

Fig. 4.4a shows the reconstruction results for simulated no aperture configuration. Fig. 4.4b shows the combined aperture reconstruction. Fig. 4.4c shows a zoomed-in frame of the no aperture image which contains the 200, 100, 75, and 50 μm. Fig. 4.4d shows the corresponding zoom frame for the encoded aperture image. It is qualitatively clear that the resolution of encoded aperture image increased relative to the no aperture image. This is quantitatively confirmed by the 176% increase (0.0290 to 0.0801) in MD in the 50 μm circle and the 42% increase (0.1000 to 0.1419) in

MD in the 75 μm circle.

4.3.2 Projection Results

Fig. 4.5a shows the projection image of the QRM (Quality Assurance in Radiology and Medicine, Möhrendorf, Germany) Micro-CT-BarPattern phantom without the encoded aperture. Qualitatively, the image has decent contrast between the bar patterns and the chip. All six sections of line pairs in the box (5, 10, 15, 20, 25, and 30 μm) can be seen, but as the unfiltered zoomed-in image (Figures 7c) shows, the ability to discern the individual lines becomes hard at the 20 μm line pairs. Whatever ability to discern individual bars is seen before application of the filter was lost after image convolution with a median filter (r=1). The mean unfiltered MD over the length of the 30 μm contrast bars was 0.0842. The filtered MD was immeasurable due to the blurring, although it was estimated to be about 0.04 for the MTF curves (shown in Fig. 4.6).

Fig. 4.5b shows one of the combined projection images in an augmented matrix. Due to the design of the grating used for the aperture encoding, the matrix size is only doubled in columns and only offers potential for resolution enhancement in the direction perpendicular to the grating alignment (in this case, horizontal). For visual convenience, the image was scaled to be the same width as the no aperture image. Qualitatively, the image has good contrast; however, a distinct, periodic vertical artifact pattern can be seen throughout the image. Furthermore, the encoded aperture seems to have slightly lower overall contrast compared to the no aperture image which may indicate some aspect of scatter rejection from the aperture. Fig. 4.5d and 4.5f shows the same zoomed-in region of contrast bars as seen for the no aperture image (Fig. 4.5c and 4.5e). The mean unfiltered and filtered MDs over the length of the 30 μm contrast bars for the aperture encoded image were 0.1847 and 0.1001, respectively. Between the results shown in Fig. 4.5 and 4.6, contrast in the 30 μm line pairs was over doubled when comparing the unfiltered results and increased by 25% when comparing the filtered encoded aperture to the unfiltered no aperture image. It should be noted, however, that despite the large increase in MD seen in the unfiltered encoded aperture image, there was significant oscillatory noise in the horizontal direction which can make discerning the resolution bars a challenging task. This is especially true in the areas of high spatial frequency (smaller line pairs). For that reason, a median filter was used in post-processing to clean-up the signal of the encoded aperture image. Convolving this same filter with the no aperture image, however, caused a significant loss the ability to discern bars of even 30 μm width. Fig. 4.6 shows the modulation transfer function curves for the unfiltered and filtered images of both the no aperture and encoded

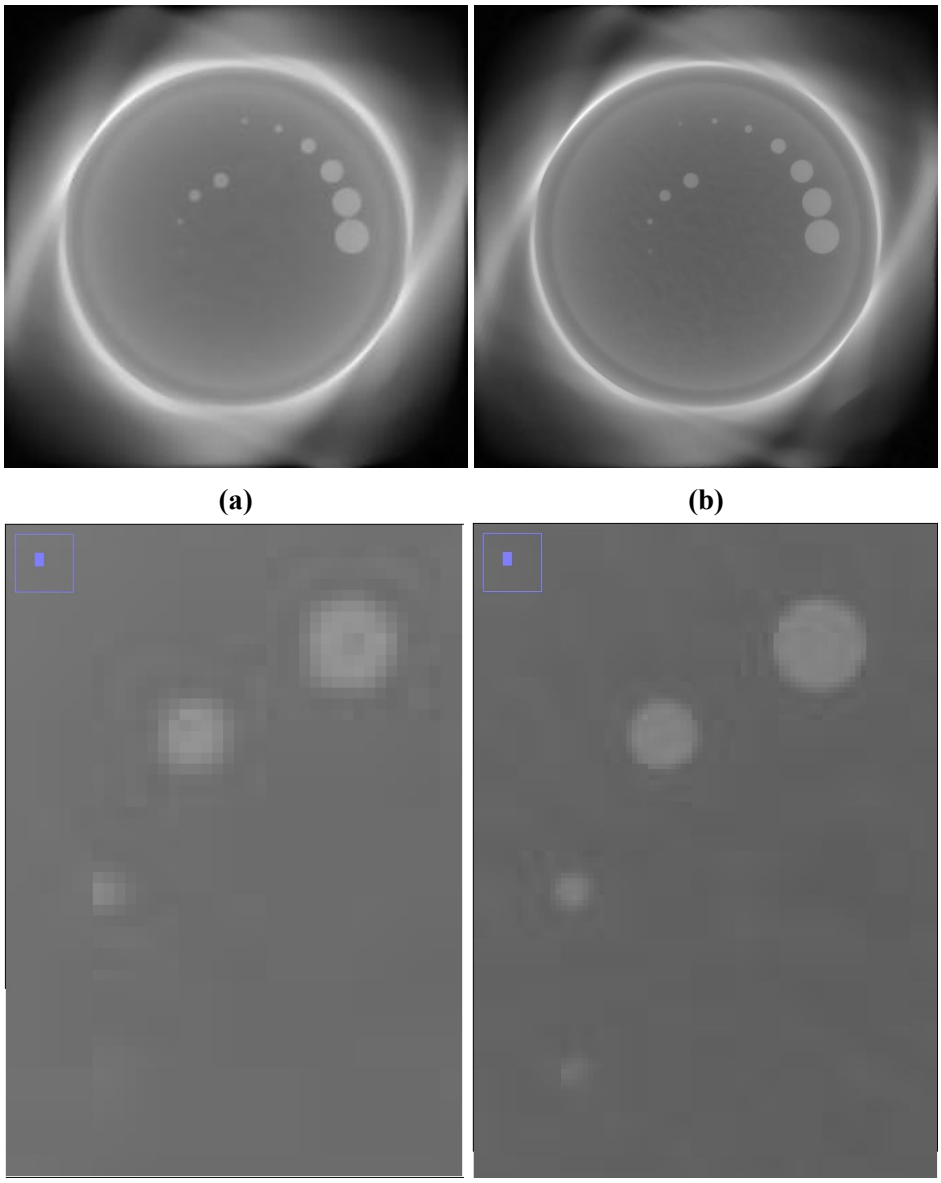

Fig. 4.4: Comparison of simulated phantom image resolution. (a) ART-TV reconstructed image of the phantom without aperture configuration. (b) ART-TV reconstructed image of the encoded aperture combined matrix. (c) Zoomed-in image for phantom without aperture showing 200, 100, 75, and 50 μm circles. (d) Zoomed-in image for phantom with encoded aperture.

aperture configurations.

4.4 Discussion and Conclusions

The results from both our Monte Carlo simulations and experimental data support the hypothesis that encoded apertures placed directly in front of an X-ray detector can enhance the resolution of the reconstructed image. However, there are some hardware optimization and calibration issues that need to be addressed to achieve maximum resolution enhancement. Although the difference between the absorption grating period and the detector element size is only $1\mu m$, the errors propagate and must be managed early on the design process. Therefore, the purchase of custom absorption gratings for our specific detectors is the first major step in optimizing this technique. Additionally, reducing the distance between the grating and detector should also help improve resolution enhancement capabilities. Encoded apertures with periods that are less than the detector element size may also be used for resolution enhancement. For apertures with such disparities, use of geometric magnification will be necessary and, therefore, precise placement of both detector and aperture will be the key to improve resolution. Additional problems and considerations, e.g., shadows due to small angle scattering, may appear with these configurations and need to be further analyzed. Furthermore, varying the grating thickness, geometry, and/or materials may allow us to gain insight into dual-function encoded apertures for resolution enhancement and scatter rejection. While the current simplified Monte Carlo detector model considered flux through a planar grid only, this capability is expected to allow us to use advanced Monte Carlo simulation with the photon-counting properties of the CZT spectral detector in the future. Our results show that this model was sufficient for proof of concept that the grating-based encoded apertures could serve as a hardware solution for resolution enhancement. However, more complex Monte Carlo detector models which model the photon, electron transport and quantum interactions of the spectral detector will be necessary to show the feasibility of applying the encoded apertures to the spectral μCT realm. Experimentally, it is also our plan to show the feasibility of these methods using our new Medipix3.0 spectral detector. In conclusion, we have shown by simulations and experiments that optimized aperture encoding can be utilized to improve spatial resolution of both conventional and spectral μCT through the combination of multiple sets of projection data. Although this approach increases both the scan time and delivered radiation dose to the object, ex vivo biopsy analysis or preclinical animal studies could benefit from the increased spatial resolution. Our results suggest that in-plane resolution enhancement of 2X can be achieved with the optimized absorption grat-

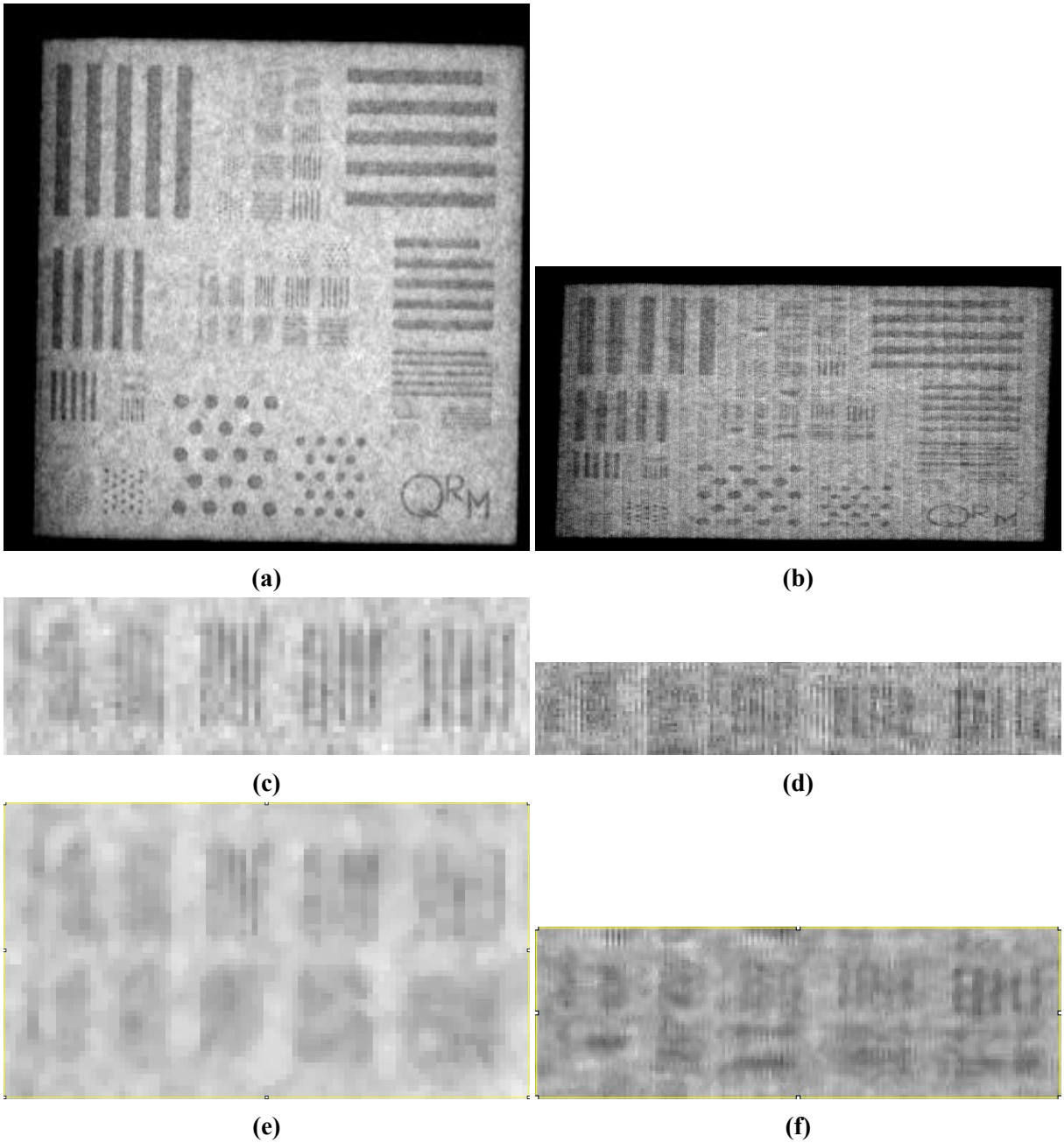

Fig. 4.5: Comparison of projection images from the experiment. (a) Single-view projection of the QRM MicroCT-BarPattern (5 mm X 5 mm) phantom without the encoded aperture. (b) Single-view projection of the phantom with the encoded aperture in front of the detector. (c-d) Zoom window of the 5, 10, 15, 20, 25, and 30 μm line pairs. No filter was applied to these images. (e-f) The same zoom window, but with a median spatial filter (radius = 1) applied.

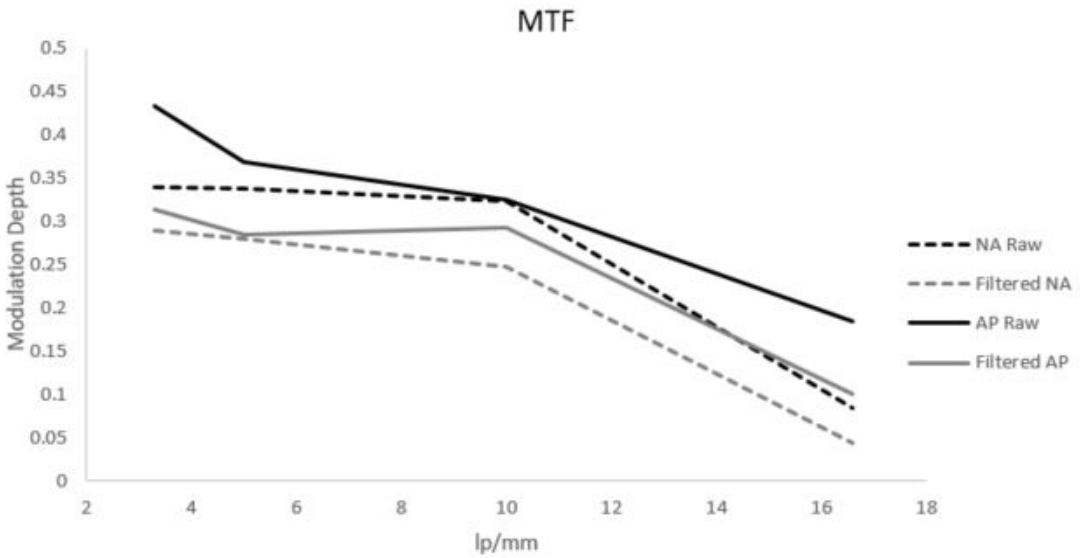

Fig. 4.6: The modulation transfer function curves for each of the projection images demonstrate a slight increase in contrast for the low frequency spatial patterns with aperture encoding. A much more significant increase in contrast can be seen at the higher frequency spatial patterns. Adding a median spatial filter decreases the overall modulation depth of both the encoded aperture (AP) and no aperture (NA) images.

ings. Additionally, the aperture encoded images have also showed large contrast enhancement in both simulation and experimentation. While both the simulations and experiments dealt solely with conventional X-ray detection methods, the encoded aperture technique is expected to be valid for photon counting detectors.

4.5 Acknowledgements

This work was supported by NIH under Grant R01 EB016977.

Chapter 5
Increasing Separability of K-edge NPs with FDA

5.1 Introduction

In the past 10-15 years, the X-ray imaging field has seen a drastic increase in literature concerning "spectral" computed tomography (CT). The term "spectral" has been used to describe any X-ray-based imaging technique which utilizes the energy- *and* material-dependence of photon interactions with matter. This differs from conventional X-ray CT which only utilizes the material-dependence of these interactions. Therefore, a spectral CT data set inherently contains more information about the scanned sample than a conventional CT data set, where the increase in information obtained is directly related to the ability of the spectral technique to differentiate the energy component(s) of the radiation used during the scan. An apt analogy can be found in visible light detection where photons from the broad visible spectrum can be measured by cameras which subsequently bin the photon counts into one (BW) or several (RGB) channels. In the same way that RGB expands the dimension of measured visible photons from a single dimension to three dimensions, spectral CT methods provide the means for expanding of the energy dimension of measured X-ray photons. Several spectral methods are currently available which utilize unique hardware configurations including dual-source [131], [132], fast kVp switching [16], [45], [133]–[136], and photon-counting detectors (PCDs) [15], [26], [58], [59], [137]–[140]. Each of these methods differ in how energy information is obtained and at what resolution (i.e. how many channels or energy bins). The higher the energy resolution (more energy bins), the greater the energetic expansion in the measured data.

Coupled with the spectral expansion of CT imaging data, the adoption of multivariate statistical methods should be used to analyze the information contained in the resulting data sets. Indeed, He *et al.* [140] demonstrated how the spectral data can be compressed without significant data loss through the use of principal component analysis (PCA). This multivariate method extracts the similarities contained within the spectral dimensions of the data set and can be used to improve contrast resolution and signal-to-noise ratio in comparison to each of the original energy images. How-

This chapter previously appeared as: M. Getzin, *et al.* , "Increased separability of K-edge nanoparticles by photon-counting detectors for spectral micro-CT," *J. Xray Sci. Technol.*, vol. 26, pp. 707-726, May 2018, doi: 10.3233/XST-18382.

ever, the purpose of many imaging techniques is centered at material differentiation whether it be between healthy and disease-state tissues or, in the case of dynamic contrast-enhanced (DCE) imaging techniques, between native tissue and the contrast agents (e.g. iodine, gadolinium). Therefore, multivariate statistical methods which extract similarities between energy bins (e.g. PCA) may be ill-suited to achieve material separation at high sensitivities versus methods, such as Fisher's discriminant analysis (FDA), which build models that maximize separation between materials. This is especially true in areas which contain low concentrations of contrast materials or in applications involving a combination of contrast materials. The objective of this paper is to demonstrate the increased ability to differentiate contrast materials through the use of spectral imaging techniques (specifically through photon-counting detectors), multivariate statistics, and linear discriminant methods.

Dual-source and fast kVp switching have been adopted in many clinical scanners produced and developed by the major companies in the area, namely Siemens and GE. These methods utilize source-level variations in the X-ray spectra, while the detectors in these scanners are conventional, energy-integrating detectors. Known differences in the source spectra and the addition of contrast materials (most often iodine-based) have allowed for the first wave of material decomposition (MD) through spectral means. These methods have been used in several clinical applications including diagnosing thyroid disease [134], cardiac scanning [131], and venography [136]. In the end, these methods allow for the expansion of the spectral dimension from a single, energy-weighted dimension into two, energy-weighted dimensions, where the count variations measured in these two channels are directly related to the differences in the source spectra.

In contrast to the dual-energy methods (dual-source and fast kVp switching), photon-counting detector methods of spectral imaging have yet to be incorporated into the clinic. This slow transition may be attributed to the fact that the specialty semiconductor arrays used for X-ray detection work at comparably low-count rates relative to conventional detectors. Additionally, it is quite expensive to manufacture clinically-sized, spectral detector arrays. Despite the current clinical limitations of these detectors, they have been the subject of many simulations [26], [137], [139] and have been incorporated into pre-clinical scanners [27], [29], [88], [140], [141], such as the Medipix All Resolution Scanner (MARS) micro-CT developed by CERN and MARS Bioimaging Ltd. As with the dual-energy methods, expansion of the spectral dimension can be achieved with these detectors; however, instead of an expansion from 1D to 2D, the Medipix 3.0 detector allows for up to 5 dimensions of spectral data to be measured in a single exposure through the use of application-specific

integrated circuits (ASICs). This is achieved by setting energy thresholds which determine the arrangement of 5 differential energy bins. The early studies cited here have focused on utilizing this spectral expansion to demonstrate the ability of photon-counting to increase material separation and decomposition compared to energy-integrating detectors. Up to this point, separation of materials within this spectral framework has been demonstrated through segmentation via linear least squares [64], [65] and the comparison of angular measures between energy-bin pairs of attenuation coefficients [13].

Another major technique for MD which has been discussed is through K-edge imaging. This method places thresholds at the same energies of the discontinuities seen in high Z materials' attenuation curves. Energy bins on either side of a K-edge will have different measured attenuation coefficients (lower in the window below K-edge bin), which has been hypothesized (and shown through simulation) to help differentiate between multiple K-edge materials in an image. These measurements allow for the decomposition of the acquired data into the following basis function model [40], [58], [65]:

$$\mu(E,x) = a_{ph}(x)\frac{1}{E^3} + a_{Co}(x)f_{KN}(E/E_e) + \sum_{m=1}^{M} a_{K_m}(x)f_{K_m}(E) \tag{5.1}$$

where M are the K-edges of the materials in the phantom, a_{ph}, a_{Co}, and a_{K_m} are physical parameter constants of the materials interacting with the X-ray beam which relate to photoelectric absorption, Compton scattering, and K-edge discontinuities, respectively:

$$a_{ph} \approx K_1\frac{\rho}{A}Z^n, n \approx 4 \tag{5.2}$$

$$a_{Co} \approx K_2\frac{\rho}{A}Z \tag{5.3}$$

$$a_{K_m} \approx \rho \tag{5.4}$$

where K_1 and K_2 are constants, ρ is material density, A is atomic weight, and Z is atomic number. The basis functions associated with these parameter constants model the energy dependence of these phenomena. Specifically, $1/E^3$ approximates the energy dependence of absorption, f_{KN} is the Klein-Nishina function, and f_{K_n} is the mass attenuation coefficient ($\frac{\mu(E)}{\rho}$) of the mth K-edge material in the sample. In a system capable of measuring 5 energy bins, up to 3 K-edge material components can be determined. Any more would result in an underdetermined inverse problem.

Despite the bin-width optimization put forth by our group [139], several real-world limitations of the detectors are not considered in such simulations. The optimized bin widths were determined to be $\sim$4 keV, yet bin widths that are this narrow are all-but-impossible to achieve with the current scanners due to count-starvation and pixel-to-pixel energy threshold variations. These variations result in detection errors of up to $\pm$5 keV. Despite this limitation of the current detectors, K-edge information is still very valuable in spectral imaging and the development of novel contrast materials are actively being explored by several groups around the world [16], [135], [142], [143].

Outside of the K-edge model framework, the built-in MARS-MD algorithm uses a three-step heuristic process which culminates in the use of a rejection criteria to settle on an MD solution containing the most likely combination of materials to which the algorithm is calibrated. Calibration is highly sensitive to scan parameter changes as well as changes to the sample materials and concentrations. Retroactive calibration and MD are possible but requires a calibration phantom that contains multiple concentrations of the materials of interest (as well as water and lipid) [65]. The heuristic approach to solving the underdetermined inverse problem divides the problem into multiple sub-problems, solves each sub-problem, and uses rejection criteria to select the "best" sub-solution. Two versions of the algorithm are described, including a linear least squares-based bin segmentation [64]. Multivariate FDA methods (as developed in this paper) have been shown to be very similar to linear least squares method in both theory and practical application [144].

In this paper, aqueous formulations including iodine, tantalum or lanthanide nanomaterials were loaded in an acrylic phantom and scanned using the MARS spectral micro-CT. The energy thresholds were placed irrespective of the materials being imaged. Instead, the thresholds were determined by distributing the total detector counts evenly between each of the energy bins. Multivariate statistical methods were used to demonstrate the enhanced material separability achievable through the spectral expansion afforded by PCDs compared to univariate, energy-integrating detector. Furthermore, Fisher discriminant analysis (FDA) was used to further enhance the statistical separability of materials by maximizing the ratio of between-material and within-material scatter. The FDA models built in this paper reduced the spectral data to 3 dimensions defined by a set linear combinations (LC) of the raw spectral data. These models were then used to map the images into commonly used color spaces (RGB and L*a*b*) whose resulting color maps reflected the material separation achievable by FDA dimensionality reduction.

This paper is organized as follows: Section 2 provides the details regarding phantom preparation, image pre-processing, statistical analysis, and FDA. Section 3 contains the results of these

Table 5.1: Iodine constructs and lanthanide dopants of $NaYF_4$ nanoparticles tested as contrast.

I_3 Constructs	Pure Lanthanide	Mixed Lanthanides (% Wt.)
Diatrizoate Na	Eu	Gd/Eu (50/50)
Iohexol	Gd	Gd/Lu (50/50)
Hydrophobic I_3	Yb	Yb/Eu (98/2)
Diatrizoic acid	Lu	Yb/Er (98/2)
	Ta	Yb/Lu (50/50)

analyses. A brief discussion and concluding remarks are found in Section 4.

5.2 Materials and Methods

5.2.1 Phantom Preparation

530 μL suspensions of K-edge-material-containing nanoparticles (NP) in water were prepared at $\sim 27.0\ mgNP/mL$ where 15% of the mass concentration of the NP is the high Z contrast component. Several lanthanide elements as well as tantalum were tested for contrast-enhancement relative to low-contrast materials (oil, water, and acrylic). Table 5.1 shows all the nanoparticle formulations used in this study. Dispersion of the nanoparticle formulations was ensured by sonication. As comparisons, solutions of four different iodinated molecules (sodium diatrizoate (DiaNa), iohexol (iodinated formulation that is administered to patients orally for CT at 300 mg/mL), hydrophobic iodine (HydrophoI), and diatrizoic acid (DiaAcid)) were also made and tested at concentrations of 18.0 mgI/mL water, 30.0 mgI/mL water, 18.6 mgI/mL formamide, and 19.6 mgI/mL formamide (FA), respectively. Well-dispersed solutions/suspensions were loaded into threaded acrylic tubes such that air bubbles were minimized throughout the samples. The tubes were then arranged in a 50-mm diameter acrylic holder (Figure 5.1). Each scanned phantom arrangement contained at least one sample holder containing oil, water, and air.

5.2.2 MARS Spectral Imaging

The MARS spectral micro-CT scanner was used to acquire projection data and reconstruct the tomographic images. Table 5.2 contains the important imaging protocol and reconstruction parameters used in this study. Tube current was adjusted in order to maintain an open-beam count-rate of <10 counts/msec with an average of ~ 2000 total counts per pixel per projection. The energy thresholds were determined during the protocol design such that the total open-beam counts

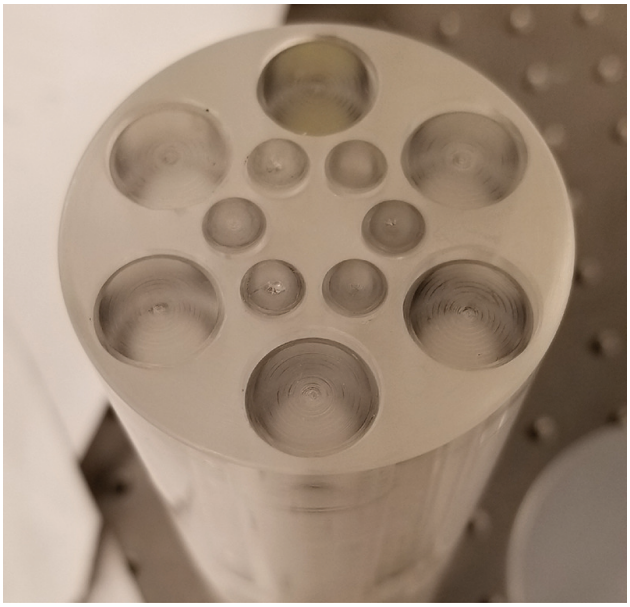

Fig. 5.1: The 48-mm diameter acrylic phantom can hold up to 12 liquid mixtures. The larger diameter tubes hold ∼2 mL while the smaller tubes hold ∼500 μL.

Table 5.2: Imaging, energy binning, and reconstruction parameters.

MARS Imaging Parameters		**Energy Thresholds**	
Tube Voltage	120 kVp	*Energy1*	28.5 keV
Tube Current	22.0 μA	*Energy2*	41.0 keV
Field-of-View	58.0 mm	*Energy3*	53.5 keV
Source-to-Object Dist.	223.1 mm	*Energy4*	65.0 keV
Object-to-Detector Dist.	60.0 mm	**MARS Reconstruction**	
Beam Filtration	1.96 mm Al	*ART Method*	v1.2
Projections/Rotation	720	*Voxel Size*	90 μm
Integration Time	250 msec		

were distributed equally between all 5 energy bins simultaneously for each projection. Figure 5.2 shows the placement of the energy thresholds as well as the linear attenuation curves of the K-edge materials used in this study. The default scanner reconstruction is an iterative, algebraic (ART) cone-beam method - MARS v1.2 - which can take up to 2 hours to reconstruct a scan length of 10 mm [38], [39]. The results of the reconstruction include 5 energy binned volume sets where the voxel values are energy-window-specific linear attenuation coefficient (μ) approximations. Two other algebraic reconstruction algorithms are supplied with the MARS scanner, but further discussion of these algorithms is outside of the scope of this paper.

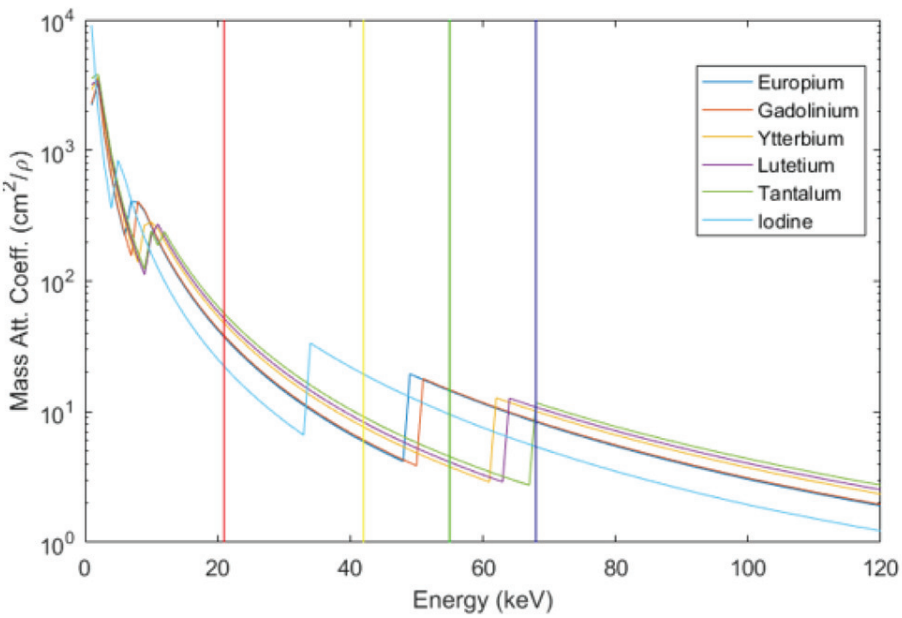

Fig. 5.2: The mass attenuation coefficients for the contrast materials used in this study are shown in the context of the MARS spectral detector threshold placements. These thresholds were determined by equally distributing total detector counts across all bins.

5.2.3 Pre-processing Pipeline

After reconstruction was complete, images were analyzed using a pipeline in MATLAB which found and isolated the inner volumes of the 12 sample tubes. The method (description to follow) is one combination of the many possible computer vision and image segmentation methods that can be utilized to segment the 12 tube phantom. The relative success of the available methods is largely dependent on contrast-to-noise ratio (CNR) or other contrast metrics (T^2) between the sample and the holder. As a major goal of this paper was to quantify the T^2 metric between various sample materials, the task of the pipeline was to quickly and robustly identify the inner contents of all 12 sample holders so that further statistical analysis could be done on the extracted data.

First, the energy bin image volumes were collected into a 4D array whose first three dimensions were determined by the size of field of view (FOV) divided by the voxel size in x, y, and z, respectively. The fourth dimension corresponded to the number of energy bins. A semi-automatic segmentation was developed for material labelling needed to train the FDA models. Each energy bin volume was quantized (i.e. intensity values were revalued between 1 and 6) using Otsu's multithreshold method. The sum of the quantized energy bin volumes, the result of which was a single 3D volume, was analyzed for circles (corresponding to the sample holders) on a z-slice-by-slice ba-

sis. Circles which were common between z-slices were considered as sample holders. These steps alone were capable of consistently identifying 9 of the 12 sample holders, where the missing three corresponded to the large diameter samples containing water and oil (i.e. samples containing low contrast relative to acrylic holder). Luckily, the arrangement of the samples containing air (which were easily identified by the algorithm) was a symmetric representation of these missing samples. Therefore, by reflecting the identified air samples across the axis of symmetry, all 12 sample holders could be identified and used to create a binary, volumetric mask. This mask was used to extract the multivariate data points for each material, which were arranged in an $N \times 6$ matrix where N corresponds to the total number of data points in all samples. The first column of the data matrix contained a material class label (c_i) from 1 to 12 and columns 2 through 6 contained the voxel intensities from the images corresponding to energy bin 1 through energy bin 5, respectively.

5.2.4 Univariate Analysis

In order to determine the utility of the inherent dimensionality expansion achieved by the photon-counting detector (PCD), the multivariate spectral data was first compressed to a univariate space to serve as the energy-integrating comparison. This was done by simply calculating the normalized mean across all bins for each data point. Quantification of contrast in univariate, conventional CT images is often done using metrics such as CNR; however, to our knowledge, no expansion of this contrast metric to multivariate spaces exists. Therefore, normalized sample intensity means were individually compared to one another using the square of the T test statistic as calculated by

$$T_{UV}^2 = \frac{(\bar{x_i} - \bar{x_j})^2}{s_{ij}^2} \tag{5.5}$$

where x_i and x_j are the univariate sample means of the samples being compared and

$$s_{ij}^2 = \frac{(n_{x_i} - 1)s_i^2 + (n_{x_j} - 1)s_j^2}{n_{x_i} + n_{x_j} - 2}. \tag{5.6}$$

s_i^2, s_j^2 are the normalized sample variances; x_i, x_j are the sample means; and n_{x_i}, n_{x_j} are the number of data points for the two samples, respectively. It should be noted that the univariate T ($\sqrt{T^2}$) statistic is linearly correlated to CNR ($R^2 > 0.95$ - analysis not shown). This provides a good basis for the use of the T^2 statistic, which can be extended to multivariate analyses (see below), for quantifying contrast differences between materials. Statistical significance of the univariate test statistics was computed by comparing values to an F distribution with 1 and $> 350,000$ degrees

of freedom (DOF) where 350,000 was determined by the smallest combination of $n_{x_i} + n_{x_j}$ for all material volumes. The α values for determining significance of the comparisons were corrected using the Holm-Bonferroni (HB) method where α* is the 95% confidence threshold equivalent and α** is equivalent to 99% confidence threshold . These corrected values are reported in the figure captions.

5.2.5 Multivariate Analysis

After the univariate case was analyzed, the multivariate energy information, as given by the reconstructed energy bin data and the FDA determined LCs of the energy bin data, were analyzed and compared to the univariate results. The natural multivariate extension of the T^2 test statistic is the Hotelling's T^2 test statistic. The multivariate expansion of Eq. (5.5) and Eq. (5.6) are given as

$$T^2_{MV} = (\bar{X}_i - \bar{X}_j)^T * (\Sigma^2_{ij})^{-1} * (\bar{X}_i - \bar{X_j}) \tag{5.7}$$

and

$$\Sigma^2_{ij} = \frac{(n_{x_i} - 1)\Sigma^2_i + (n_{x_j} - 1)\Sigma^2_j}{n_{x_i} + n_{x_j} - 2}, \tag{5.8}$$

where $\bar{X}_i$ and $\bar{X}_j$ are $M \times 1$ vectors whose elements correspond to the M normalized means of the M energy bin voxel intensities contained in a sample or of the ($M = 3$) LCs of sample voxel intensities being compared. Σ^2_{ij}, Σ^2_i, Σ^2_j are the unbiased correlation combination matrix for samples i and j, the sample i correlation matrix, and sample j correlation matrix, respectively. Each correlation matrix is $M \times M$. Again, n_{x_i} and n_{x_j} are the number of data points for the two samples i and j, respectively. In the M-D multivariate cases, the calculated test statistics were compared to χ^2 distributions with M DOF. Again, the α values used for determining the significance of the comparisons were corrected using the HB method described previously. α* and α** values are reported in the figure captions.

5.2.6 Fisher's Discriminant Analysis

Separability of the various samples were also analyzed after applying Fisher's discriminant analysis (FDA) for dimension reduction. These methods attempt to model the differences between each sample based on a LC of the original variables in an MD data set. The l resulting linear discriminant functions used in the FDA models are determined by analyzing some known combination of segmented and normalized sample means as well as the between-sample, and within-sample cor-

relation matrices of k samples, where $k \geq l + 1$, as follows:

$$\hat{Y_{lD}} = \hat{p}\hat{X} = \begin{bmatrix} p_{1,1}X_1 + \ldots + p_{1,M}X_M \\ \vdots \\ p_{l,1}X_1 + \ldots + p_{l,M}X_M \end{bmatrix} \tag{5.9}$$

Eq. (5.9) shows the linear mapping ($\hat{Y_{lD}}$) of the MD voxel data into l-dimensions through the calculation of the inner product of the $l \times M$ matrix of weights ($\hat{p}$) and the $M \times 1$ vector of energy bin data ($\hat{X}$). The weight matrix is calculated according to the distributions of k samples by maximizing the following objective function:

$$J(\hat{p}) = \frac{\hat{p}^T S_B \hat{p}}{\hat{p}^T S_W \hat{p}} \tag{5.10}$$

where S_B and S_W are the "between-class" and "within-class" scatter matrices, respectively. They are defined as follows:

$$S_B = \sum_k n_k(\bar{X}_k - \bar{X})(\bar{X}_k - \bar{X})^T \tag{5.11}$$

$$S_W = \sum_k \sum_{i \in k} n_k(X_i - \bar{X}_k)(X_i - \bar{X}_k)^T \tag{5.12}$$

where n_k is the number of data points in sample k, X_k is the sample mean, X is the mean across all samples, and X_i is data point i in sample k. The resulting $\hat{p}$ is such that each weight vector is orthonormal to all the others. Once $\hat{p}$ is calculated, the weights are applied to all remaining sample volumes for subsequent calculation of Hotelling's T^2 statistic (to compare the multivariate contrast). The FDA models are also used to map the spectral data into multiple color spaces (see color-mapping below).

5.2.7 Color-mapping

In the case of dimension reduction via FDA from 5 energy bins to 3 LCs of the energy bins, the natural corollary is to map the resulting LCs into one of the common 3-channel color spaces used in digital image processing. The most common of these color spaces is the RGB space, or true-color space, which models the color output of physical devices. Although the mapping of the LCs is straightforward, 6 (3!) different color-mapping combinations are possible from each FDA model. Each colormap may have its own advantages or disadvantages in terms of how a human perceives the information available in the resulting images. Alternative 3-channel color spaces exist, including the L*a*b* space, which is meant to model human visual perception. Again, 6

different L*a*b* combinations of can be made from a single FDA output. In addition to calculating and quantifying the total significant T^2 statistics after applying the FDA models, a "best" models were mapped, both in RGB and L*a*b* color spaces, to allow for qualitative analysis of perceivable differences in image quality and sample discernibility. A subset of these mapping results which demonstrated notable qualitative features are reported.

5.3 Results

5.3.1 Iodine Contrast

The univariate data set was meant to emulate the type of information available to algorithms and humans making decisions using conventional, energy-integrating detectors. High concentrations of common iodinated contrast agents were scanned as a measure of comparison for the later scans containing aqueous mixtures of lanthanide nanomaterials. Figure 5.3 shows an example slice from the image volume whose voxel intensities are the normalized mean for that voxel across all 5 energy bins. Each of the iodinated samples is statistically different from the low-contrast samples (water, oil, and formamide) as seen by the robust T^2 statistics calculated for these comparisons ($T^2 \gg 50$). However, it should be noted that differences between the low-contrast samples are much less pronounced, which resulted in several qualitatively "different" samples that were not statistically different when compared directly (e.g. water vs oil). Similarly, iohexol subjectively has much higher signal than the other iodinated samples due to its relatively higher concentration; however, the T^2 statistic ($\sim$15 in all iodine comparisons) falls just below the adjusted 95% confidence threshold ($\sim$16). The maximum SNR in the univariate image is given as 18.25 dB and corresponds to the iohexol sample.

Given that the univariate analysis alone allows for differentiation between the iodinated and low-contrast samples, it should be expected that little enhancement of these differences can be gained from the dimensionality expansion provided by the photon-counting spectral detector. Figure 5.4 shows the same volume slice shown in Figure 5.3 for each of the 5 energy bin reconstructed images as well as the quantitative effect of the dimension expansion (T^2 comparison grid). Just as in the univariate (energy-integrating) analysis, each of the iodinated samples is readily distinguishable from the low-contrast samples, however this time with even more robust T^2 statistics ($\gg$125). Again, very little statistically distinguishes these iodinated samples from each other, despite the qualitative evidence to the contrary. The spectral expansion does, however, allow for better separation of two of the low-contrast samples, water and oil, whose comparisons are seen to give a

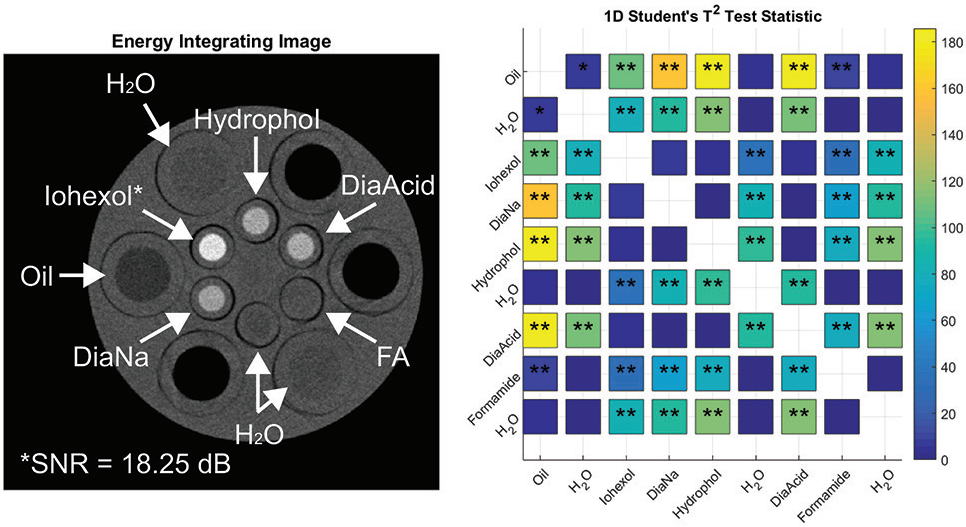

Fig. 5.3: The pairwise comparison results for iodine samples demonstrate how strong the contrast between iodine-based molecules at these concentrations and low-contrast solutions as the values of the significant T^2 test statistics have values $\sim$180. None of the contrast materials can be distinguished from any of the other contrast materials (HB-adjusted α^* = 0.0126, α^{**} = 0.0014).

significant T^2 statistic in each of the available comparisons. Formamide, on the other hand, was significantly different from oil in the univariate case, but is no longer statistically distinguishable from oil after the spectral expansion, as its T^2 statistic falls just short of the α* threshold. The highest SNR is reported for each energy bin image and these values each correspond to the signal seen in the iohexol sample volume.

5.3.2 Pure Lanthanide Nanoparticles

The nanoparticle formulations comprising of single lanthanide (and tantalum) elements were then tested as contrast (second column of Table 5.1). The images and models from these scans are labeled as pLn which stands for "pure lanthanide". The univariate data set was again formulated by averaging the pixel intensities across all 5 energy bins. Figure 5.5 shows results from the univariate T^2 statistics calculated between each sample group. Evidently, oil can be more easily discriminated from the contrast-containing samples than can water. However, oil cannot be distinguished from water. Ta and Eu based contrast agents are the only (of the five tested) in this image set that can be discriminated from water ($T^2 \sim 16$, while all the other (Gd, Yb, and Lu) have test statistics too low to reject the null hypothesis that their means are equal to that of water. Additionally, none of the contrast materials can be discriminated from one another. The maximum SNR found in this image

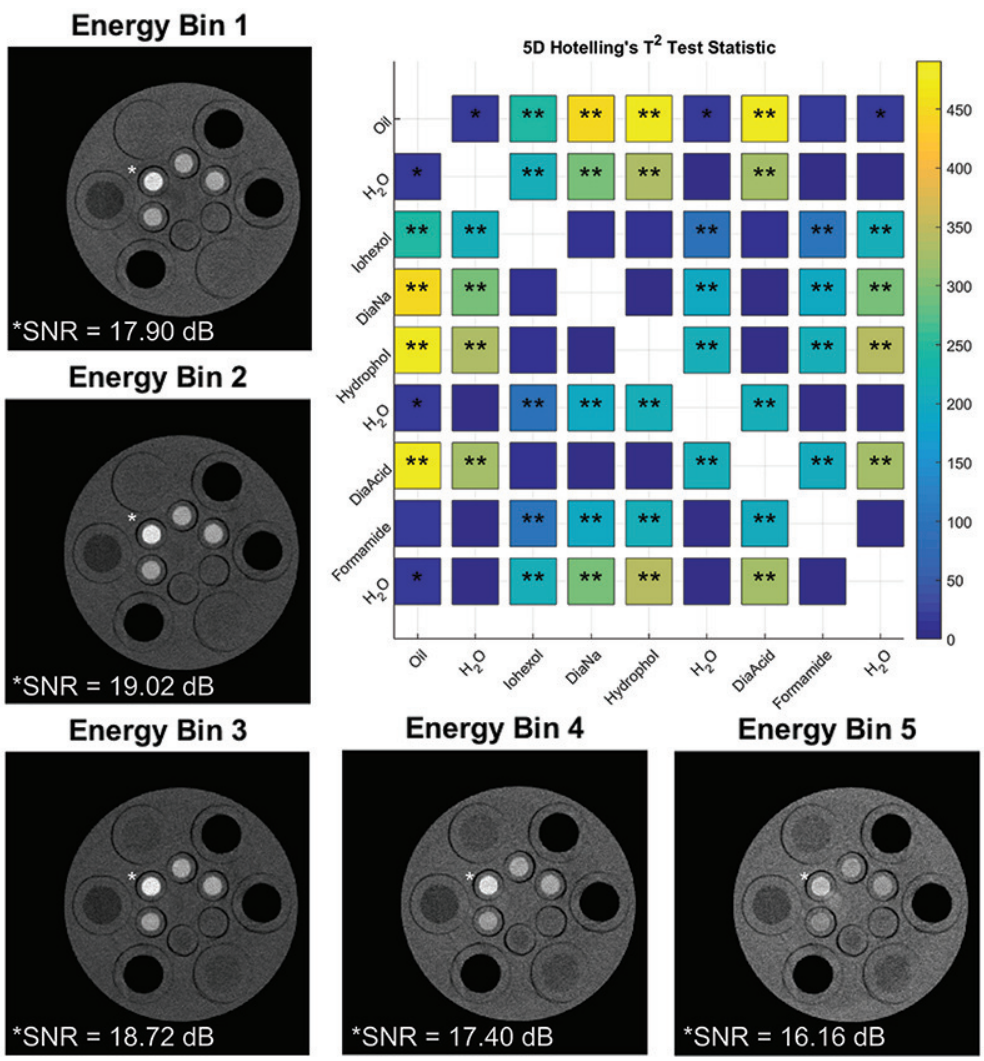

Fig. 5.4: The pairwise comparison results for the iodine samples with 5 energy bins look very similar to the conventional comparison results. The only change in the significance of the pair-wise comparisons is in the ability to differentiate water from oil, although formamide can no longer be discerned from oil (HB-adjusted α^* = 0.0038, α^{**} = 0.0013). It should be noted, however, that the significant T^2 statistics are now ∼450, nearly 3X greater than in the univariate comparison.

is 3.015 dB and it corresponds to the Eu-based nanomaterial.

Despite the inability of the univariate (energy-integrating) data to detect contrast from most of pLn nanomaterials at 27.0 $mgNP/mL$, Figure 5.6 demonstrates how the dimension expansion from the PCD greatly enhances not only the ability to distinguish contrast materials from water, but also the ability to distinguish contrast materials from each other. As seen in the pairwise comparisons, Eu-based materials are easily separable from Yb-, Lu-, and Ta-based materials ($T^2 \sim 40$. Similarly, Ta-based materials can be easily distinguished from Gd- and Eu-based materials. Fur-

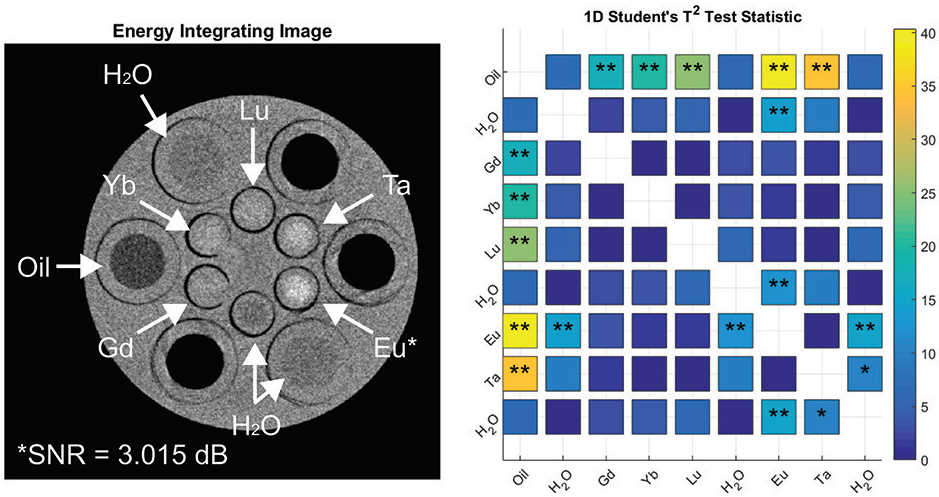

Fig. 5.5: The pairwise comparison results for the pLn NP samples show that despite the contrast materials ability to be distinguished from oil, they cannot (with the exception of Ta and Eu) be distinguished from water. In this image, the significant T^2 statistics have values ∼40. This reflects the difficulty of telling many of these materials apart from one another (even qualitatively). None of the contrast materials can be distinguished from any of the other contrast materials (HB-adjusted α* = 0.0016, α = 0.00044).**

thermore, the Gd-based particles show increased separability from water compared to the univariate data set ($T^2 \sim 25$). The maximum SNR found in each energy bin image corresponds to the Eu-based contrast, yet it is degraded compared to the SNRs measured in the iodinated images.

5.3.3 Mixed Lanthanide Nanoparticles

Several nanoparticle formulations also used mixed lanthanide (mLn) formulations as outlined in the third column of Table 5.1. Figure 5.7 shows the layout of these samples in the phantom as well as the pairwise comparisons for each of the samples as measured by energy-integrating detectors. Mixed lanthanide (mLn) NPs do not demonstrate very strong contrast at 27.0 $mgNP/mL$ when compared to low contrast materials such as water ($T^2 \ll 10$). As a group, they are shown to have different contrast than oil with some consistency ($T^2 \sim 14$), however the Yb/Lu dopants do not show significant contrast when compared to oil. The highest SNR is reported at 15.11 dB, which corresponds to the signal from the Gd/Lu sample.

In the spectral expansion image, a few of the mLn NP formulations are more readily discernible from the low contrast materials. Figure 5.8 shows the results from the multivariate analysis of the raw spectral data. While the strongest contrast comes from Gd/Eu mixture ($T^2 \sim 28$), the

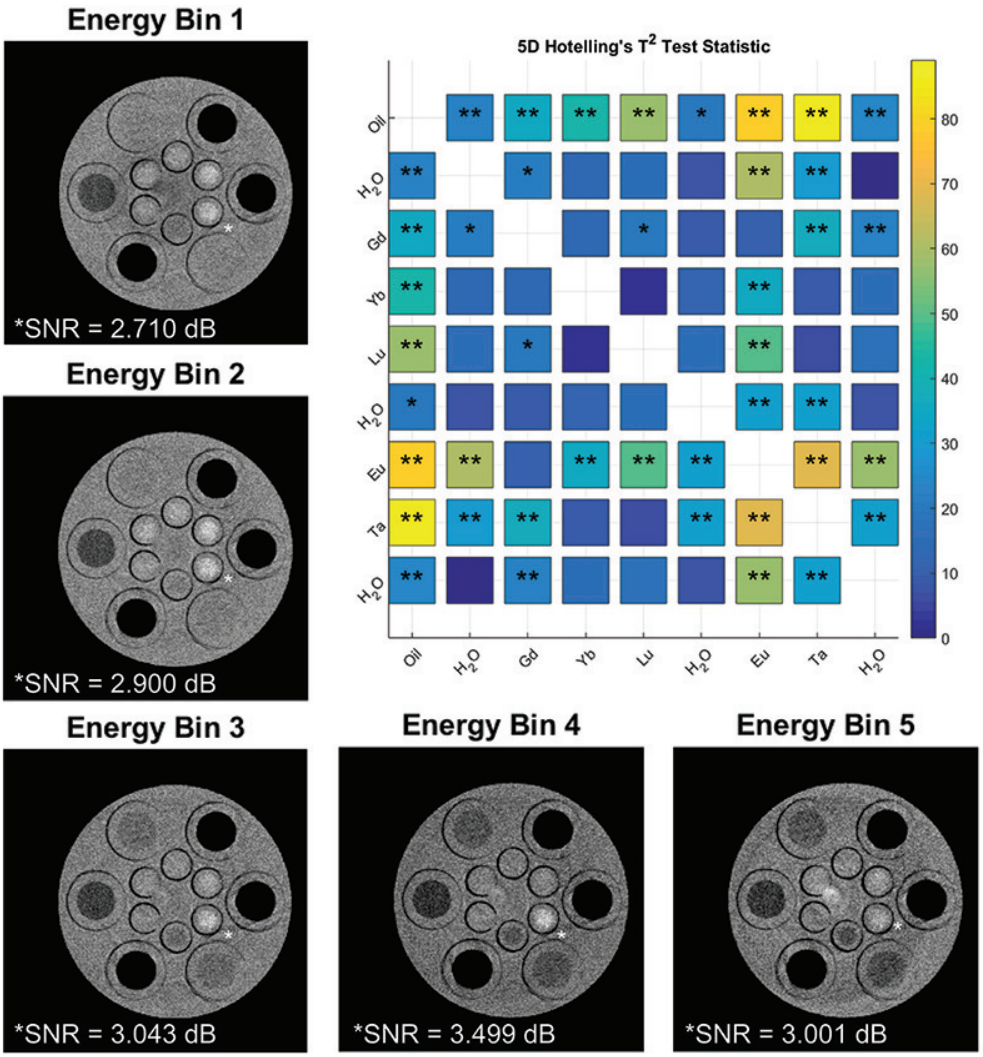

Fig. 5.6: The pairwise comparison results for all samples show much greater separability can be achieved between the Ta- and Eu- nanoparticles and water. Additionally, several of the nanoparticles can even be distinguished from one another (HB-adjusted α* = 0.0049, α = 0.00048). The significant T^2 values are $\sim$80, which is 2X greater than in the univariate comparison.**

mLn materials, in general, do not seem to be as strong of attenuators as the pLn NPs, as indicated by their respective T^2 statistics when compared with water. The inability to discriminate these materials is in spite of restored SNRs $\sim$ 15 dB which are comparable to the SNR levels seen in the iodinated images. All the maximum SNRs correspond to the Gd/Lu sample with the exception of energy bin 1 whose maximum SNR corresponds to the Yb/Er sample.

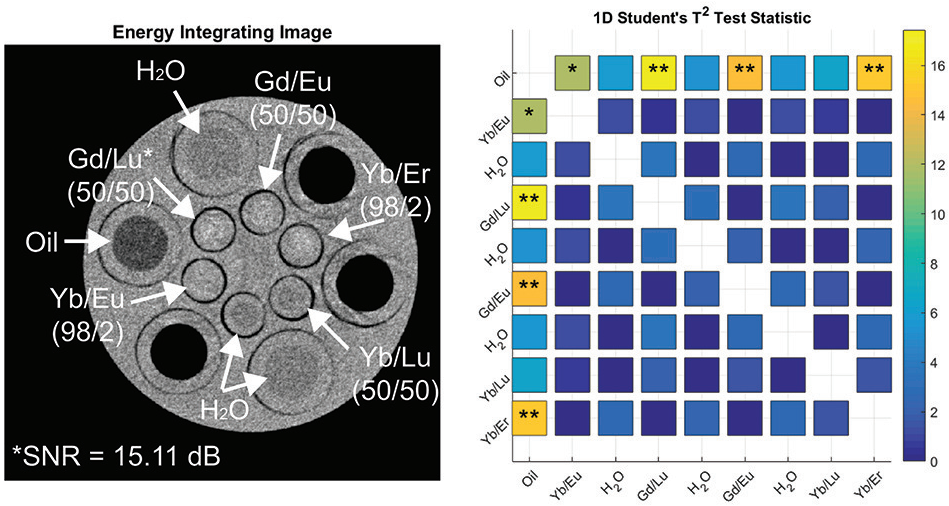

Fig. 5.7: The pairwise comparison results for all mLn NPs suggest that none of the materials could be used as contrast at concentrations even as high as 27 $mgNP/mL$ in an energy-integrating system (HB-adjusted α* = 0.011, α = 0.00054). The T^2 values for these samples hover well below 10.**

5.3.4 FDA Analysis of Contrast

The pairwise T^2 analyses performed for both the univariate and multivariate image sets demonstrate the raw power of dimension expansion attributable to the photon-counting detector. However, there are several multivariate methods available for refining the separation of sample data. One relatively simple example is Fisher's discriminant analysis (FDA). The purpose of this analysis is to reduce data redundancy between the measured variables, in this case - binned X-ray attenuation calculated according to energy threshold placements at the detector level - while simultaneously maximizing the separation between the samples used to develop the model. FDA is also a form of dimension reduction whose resulting model subspace has dimension l which, according to its governing equations (5.10)-(5.12), is equal to the rank of S_B as determined by the $l+1$ samples used to make the model.

Supposing (1) that a data reduction from 5 energy bins to 3 LCs is optimal for the purposes of data visualization (RGB or L*a*b* color-mapping of our images) and (2) that the current phantom arrangements contain nine samples of interest (1 air, 2 water, 1 oil, and 5 contrast samples), 126 combinations of 4 different samples are available per phantom to build an FDA model for further contrast discrimination. All 126 possible combinations were analyzed to determine the combination(s) which built the highest performing FDA models as assessed by the total number of significant T^2 statistics. Figures 5.9 and 5.10 compare the FDA models for all combinations of

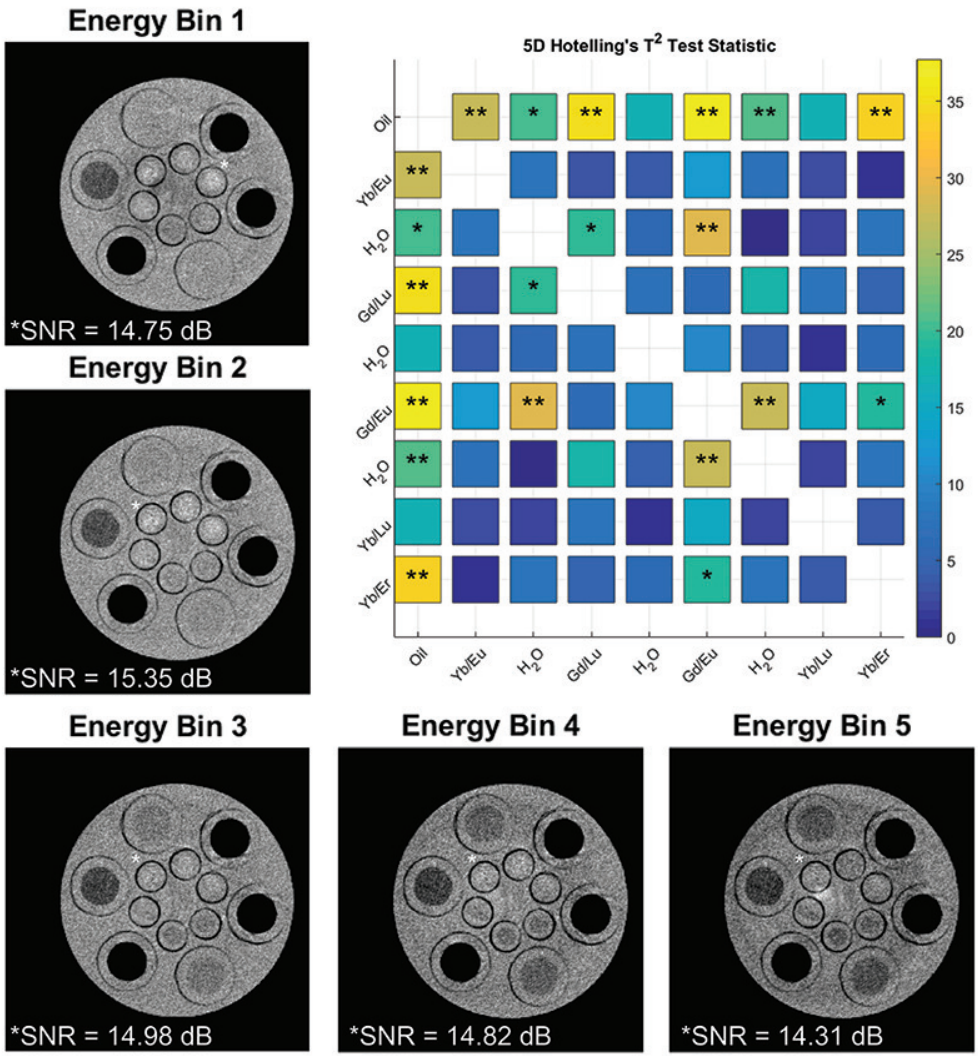

Fig. 5.8: The pairwise comparison results for the mLn NPs with 5 energy bins suggest that a few of the formulations, namely Gd/Eu, can be distinguished from the other low-contrast materials. (HB-adjusted α* = 0.0025 and α = 0.0011). Its T^2 value when compared to one of the water samples was $\sim$30.**

samples in both the pure and mixed lanthanide phantoms, respectively. As was shown in the raw spectral comparisons, more pLn NPs show significant levels of contrast relative to the low-contrast materials as well as to the other contrast-enhancing materials. The FDA models of interest are those which have the maximum number of T^2 scores that are significant ($> \alpha^*, \alpha^{**}$). Table 5.3 shows the combinations of FDA training materials which provided sequentially improved models compared to prior, according to the number significant T^2 scores. Results from combinations 1, 2, 7, and 8 are used for color-mapping and visualization.

Table 5.3: Sample combinations for FDA models.

	pLn Phantom Combinations				mLn Phantom Combinations			
1	Oil	Air	H_2O	Gd	Oil	Air	H_2O	Gd/Lu
2	Oil	Air	Yb	Ta	Oil	Yb/Eu	Gd/Lu	Yb/Lu
3	Oil	H_2O	Gd	Yb	Oil	H_2O	Gd/Lu	Gd/Eu
4	Oil	H_2O	Gd	Lu	Oil	H_2O	Gd/Lu	Yb/Er
5	Oil	H_2O	Yb	Ta	Oil	Gd/Lu	Gd/Eu	Yb/Lu
6	Oil	H_2O	Eu	Ta	Oil	Gd/Lu	Gd/Eu	Yb/Er
7	Oil	Gd	Yb	Ta	Oil	Gd/Lu	Yb/Lu	Yb/Er
8	H_2O	Gd	Yb	Ta	Gd/Lu	Gd/Eu	Yb/Lu	Yb/Er

5.3.5 Color-mapping

Figure 5.11 and Figure 5.12 show example slices from each of the phantom arrangements after mapping via 8 different 3 LC FDA models from 2 different scans (4 from each). Each result is displayed as a single RGB and a single L*a*b* color space image. The color combination chosen for display was the qualitative "best" image – showing the best contrast between those samples whose T^2 values supported their being different colors. Several aspects of these color representations of the spectral data are of note.

- Several of the images show distinct ring artifacts which are especially present toward the center of the images (not necessarily the center of the phantom). In fact, the center artifacts (bright blue in pLn/mLn 8 combinations) are likely a result of a slight geometric miscalibration and are more apparent in the high energy bin images.

- Several of the images show a proclivity for exposing the Gd and Eu containing contrasts. Gd and Eu show up as similar colors in nearly all the images. This is reflected by the lack of differentiation shown in the 5 bin spectral data. Furthermore, K-edge theory and the "equal-counts" threshold placement support this inseparability (see Figure 5.2).

- Several of the images also show a proclivity for exposing Ta, Yb, and Lu. These, too, present themselves as similar colors although a different color than Gd and Eu. Again, this grouping is both reflected by our statistical analyses as well as theory. Interestingly, the color of these were often slight increases in water's intensity/color saturation.

- Although the training materials from the two image sets used to build the FDA models are different, their results were often very similar (e.g. pLn1 vs mLn1, pLn2 vs mLn2, & pLn8

vs mLn8). This shows both that the models presented are not subject to over-fitting and that these may be used as robust classifiers in future MD problems.

- The oil sample is consistently darker than both the acrylic phantom and the water samples. However, areas of both the water and acrylic show strong effects of noise. This is especially true in the FDA models which do not train on water or oil. It should be noted that training for water was done with one of the three available water samples in the phantom and the ability to discern some of the Ta/Yb/Lu samples was often affected by which water sample was used in the training of the FDA model.

- When applied to the phantom containing iodine, the models - trained by both pLn and mLn samples - continue to allow for iodine discrimination. However, the disparity in relative contrast between the 18-30 mg/mL iodine samples and the 27 mg/mL pLn and mLn samples results in large shifts in the dynamic ranges utilized by the reconstructed images. This can be seen by the "dimming" of the low-contrast signal relative to the iodine samples in several of the reported color space images.

5.4 Discussion and Conclusion

In this paper, the material-discriminatory ability achieved through PCDs is evaluated. Several phantoms which included various arrangements of iodinated-contrast as well as tantalum and lanthanide nanomaterials were scanned. The full power of the PCD-based material discrimination can be seen in images of low contrast as well as in phantoms containing multiple materials. Alone, the multivariate spectral data demonstrate larger numbers of statistically different contrast distributions between material volumes as calculated by T^2 test statistics. Furthermore, several FDA models built with various four-material combinations were shown to further enhance material separability. These models were also shown to be robust by mapping image data not used to build the models. Despite these results, the separability achieved by the FDA models are highly dependent on the materials used to build the model. For this reason, all possible combinations were analyzed, though only a subset showed enhanced material separation when compared to the spectral data set.

This paper also demonstrates how the inherent K-edge information of materials is utilized in material separability. As seen in Figure 5.2, Gd and Eu have K-edges which happen to fall in the 3rd energy bin while Yb, Lu, and Ta's K-edges occur near the threshold dividing the 4th and 5th energy bins. This natural K-edge grouping is reflected in all aspects of the data shown here,

i.e. both statistical separation and color representations demonstrate differences between (and not within) these two groups of materials. It should be noted that the FDA methods described in this paper have been shown to be very similar [144] to the MD methods that come equipped on the MARS micro-CT scanner which are based on linear least squares. These methods were disclosed as recently as February of this year [64], [65]. Future work will focus on developing algorithms for optimizing bin threshold placement for a given set of materials using complex multivariate statistical and machine learning techniques.

In conclusion, material separability measures are significantly enhanced in PCD-based spectral imaging relative to energy-discriminating detector-based imaging. Furthermore, material-based FDA models can be used to further enhance separation by producing robust LC models. These models can then be mapped into commonly used color spaces to achieve qualitative images which reflect the quantitative measures provided by the data. Lastly, this work consolidates the groundwork for further exploration and development of novel contrast materials as well as molecular CT through targeted contrast.

5.5 Acknowledgements

This work was partially supported by the Ministry of Science and Innovation (New Zealand) and the Clark & Crossan Endowment fund from Rensselaer Polytechnic Institute. The funders had no role in study design, data collection and analysis, decision to publish, or preparation of the manuscript.

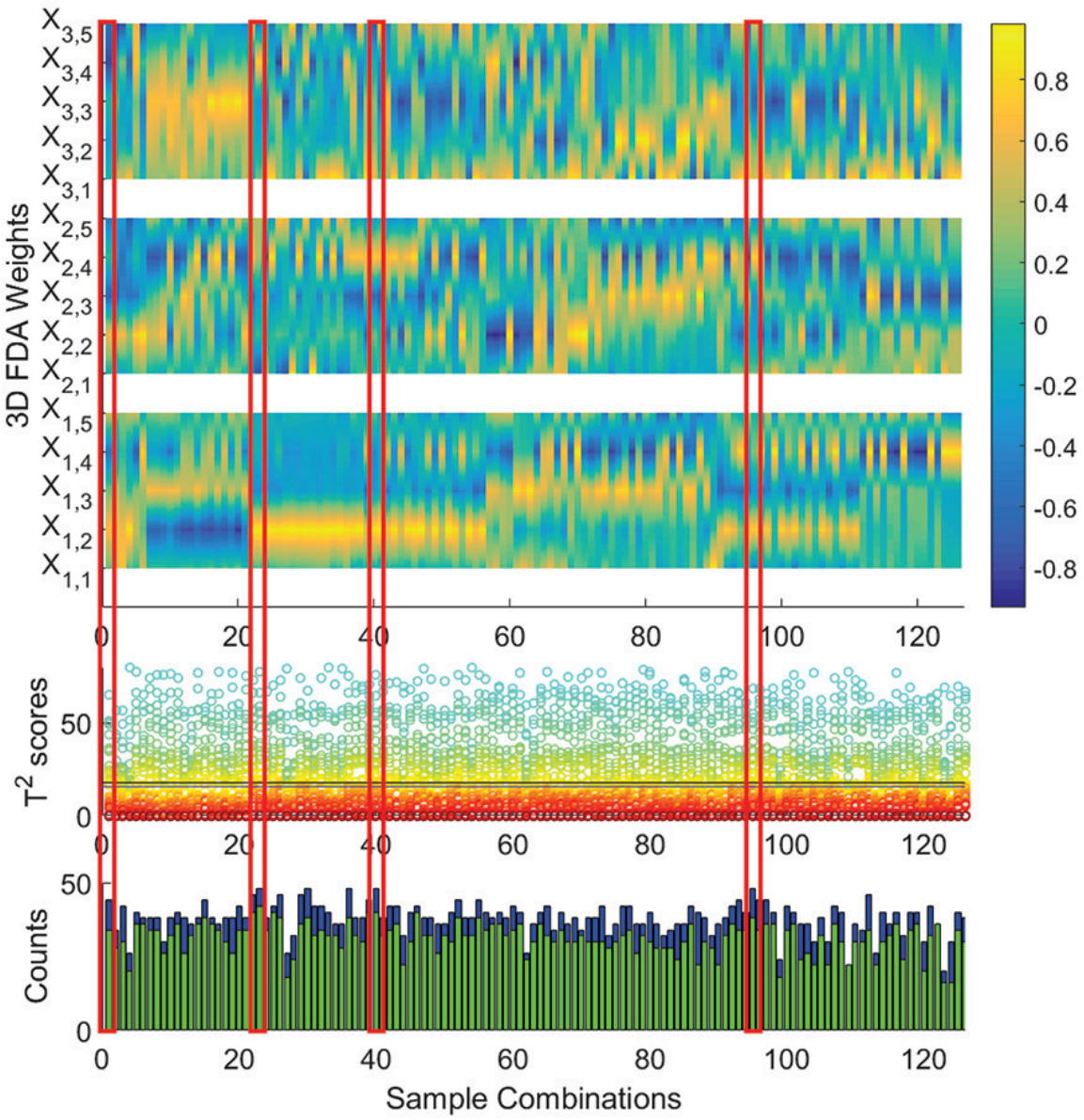

Fig. 5.9: The top row shows the weights for all the 126 four-sample combinations for the pLn phantom which were used to calculate 3 LC FDA models. The middle row shows a scatter plot of T^2 scores for each combination as well as the α* and α values which shown as blue and green horizontal lines, respectively. The bottom row is the total number of significant T^2 statistics as compared to α* and α** values.**

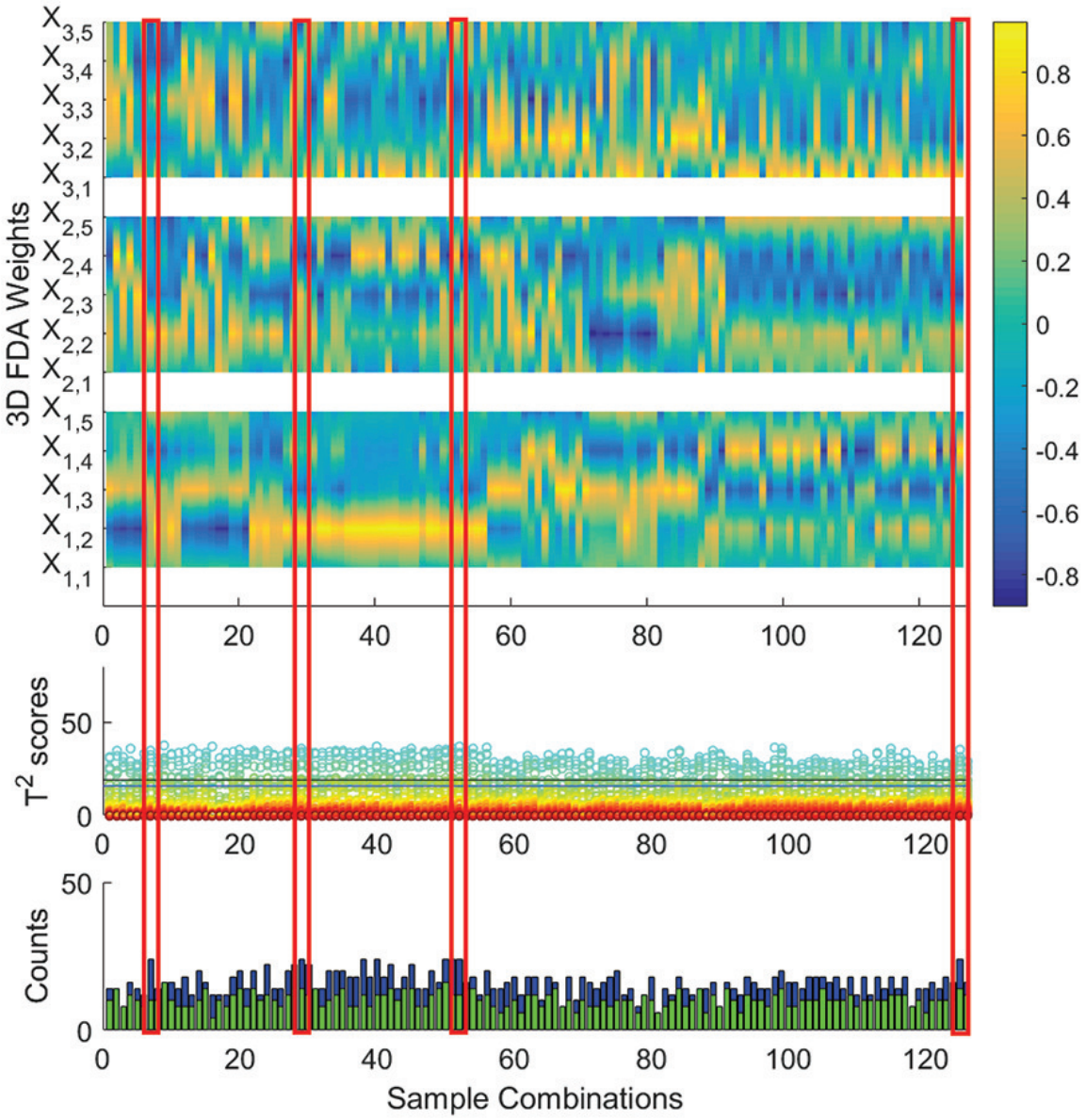

Fig. 5.10: The top row shows the weights for all the 126 four-sample combinations for the mLn phantom which were used to calculate 3 LC FDA models. The middle row shows a scatter plot of T^2 scores for each combination as well as the α* and α values which are shown as blue and green horizontal lines, respectively. The bottom row is the total number of significant T^2 statistics as compared to α* and α** values.**

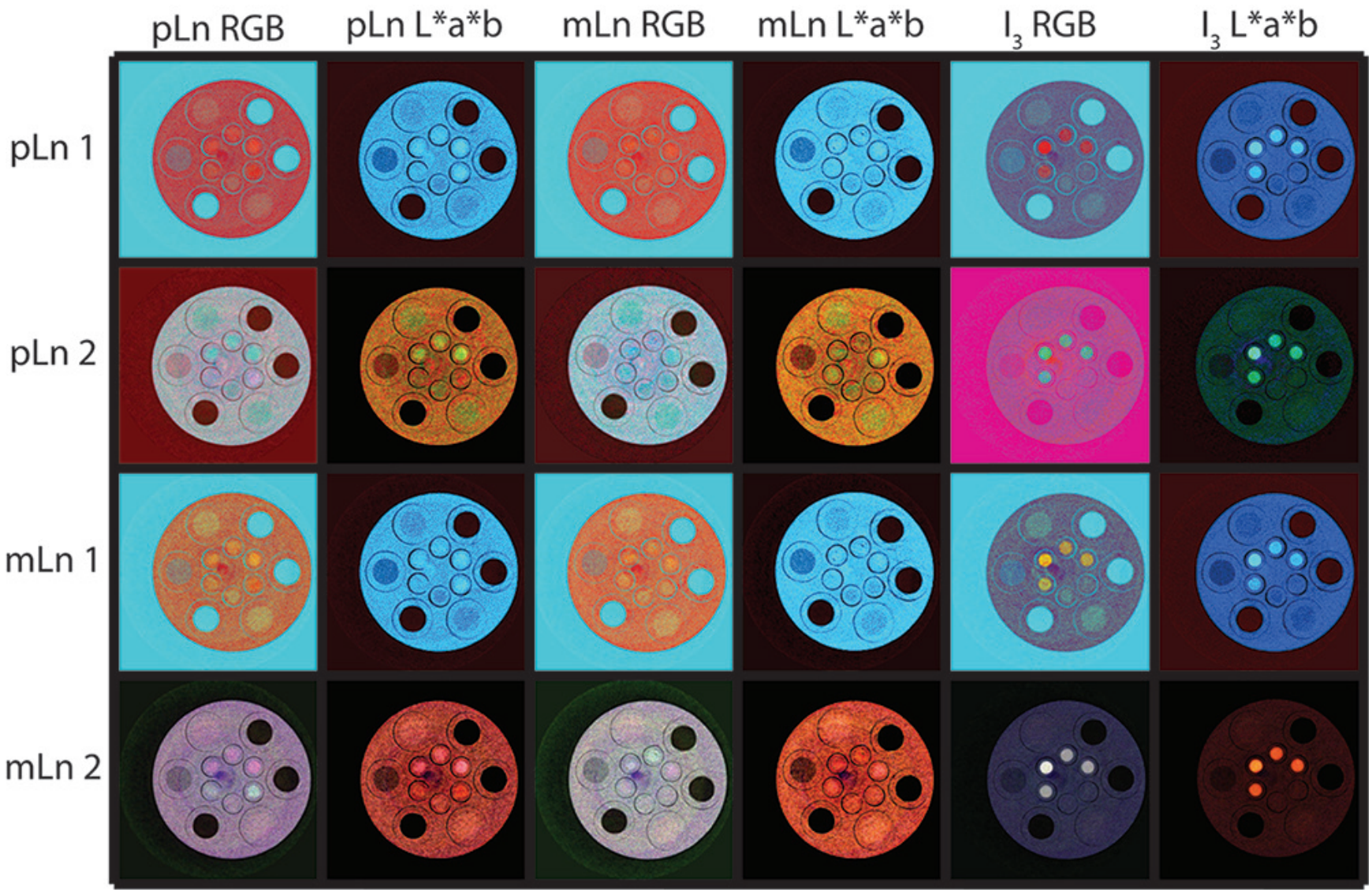

Fig. 5.11: FDA models mapped into multiple color spaces demonstrate the combination-dependence of the 3D FDA models that can be used to further separate different contrast materials.

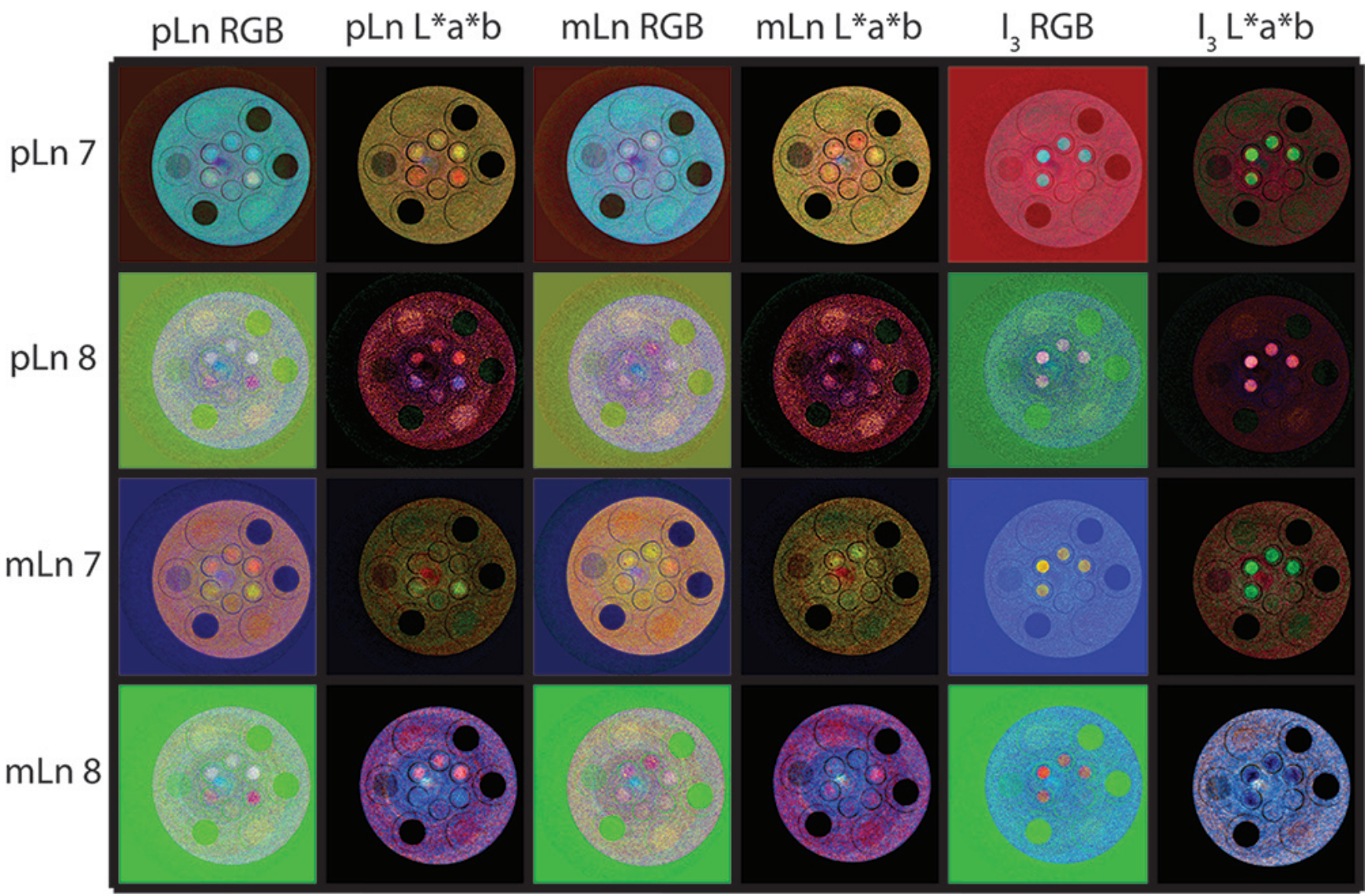

Fig. 5.12: FDA models mapped into multiple color spaces demonstrate the combination-dependence of the 3D FDA models that can be used to further separate different contrast materials. Some of these color combinations also seem to highlight the image artifacts introduced from system aspects that are outside the scope of this study (*i.e.* miscalibration, spatial non-uniformities, etc.). equally

Chapter 6
Non-linear Material Segmentation and Quantification

6.1 Introduction

The development of X-ray photon-counting detectors (PCDs) made from semiconducting materials such as silicon (Si), cadmium-telluride (CdTe), cadmium-zinc-telluride (CZT), and germanium (Ge) promises to hail in a new era of X-ray-based imaging. Some have called this new era "full-color" X-ray given that the expansion of the measured spectral information obtainable by PCDs is comparable to the expansion of black-and-white photography to color. With the Medipix 3RX detector, up to 8 energy thresholds can be defined and the resulting measurements will compose 8 separate energy-bin measurements which are subtly different yet provide important information regarding scanned materials. Indeed, several research examples have shown an increase in material separation in spectral photon-counting images [13], [17].

Identification and quantification of materials in an X-ray CT image is an important step in the image analysis pipelines, even today with conventional and dual energy CT [9], [145]. In the spectral photon-counting space, this task has been deemed material-decomposition (MD) and most of the methods discussed in the literature have adopted the inverse-problem framework for solving the problem [16], [58], [59], [62], [65]–[67], [133]. The common goal for each of these methods is to solve the linear system

$$\mathbf{A} \cdot \mathbf{x} = \mathbf{b} \tag{6.1}$$

where b is the pixel-wise, post-reconstruction measurement set, x is the pixel-wise term for which to solve, and A is a functional matrix which, depending on the decomposition model, can contain a set of physical interaction functions for a given material (*i.e.* photoelectric effect, Compton scatter, and K-edge terms) [58], [59] or energy-bin-specific mass attenuation coefficients [65]–[67]. The well-known limitation of these inversion techniques is that the system is often ill-posed (*i.e.* more unknowns than measurements), so there is no unique solution. The methods cited above each have their own unique methods for regularization and prior-information which can allow for quite accurate parameter estimations and material decompositions.

Some early work in the area, proposed simpler methods for identifying and quantifying ma-

terials in the spectral image sets through segmentation [64], [70]. Le and Molloi proposed a two-step *segmentation* and *quantification* method based on a least-squares minimization. Bateman *et al.* focuses on the identification of materials into one of three categories: air, soft-tissue, or dense tissue/contrast material. This method uses a multivariate Malhalanobis distance to determine a voxels likelihood of containing one of the three categories of materials. This method is used as the segmentation-based subproblem later described in the same-group's 2018 *MARS-MD* paper [65].

This paper belongs to the second group of material identification and quantificaton papers, as it proposes the use of segmentation (and subsequent quantification) for material identification purposes. Building on the Fishers discriminant analysis (FDA) described in our previous publication [17], a kernel expansion is proposed as a semisupervised material identification scheme. This type of method has been used with success in the field of hyperspectral satellite image segmentation [146]–[148] and is shown here to have similar power in identifying materials. The remainder of this paper will (1) describe the data sets (both real and simulated) which were used to demonstrate this method, (2) describe the kernelized expansion of the FDA methods previously reported, (3) provide model and segmentation results, and (4) discuss the implications and limitations of the proposed method.

6.2 Materials and Methods

6.2.1 Real Data

The Medipix All-Resolution Scanner (MARS; MARS Bioimaging Ltd., Christchurch, NZ) was used to scan and reconstruct two material phantoms. Both phantoms were made using a modular acrylic holder which allows for several combinations of known materials and concentrations to be scanned at any one time. Two configurations of such phantoms as well as two scanning protocols were used in this study.

- A 38mm iodine/calcium calibration phantom was scanned which contained four concentrations of iodine (I) mixtures (*i.e.* 2.25, 4.5, 6, and 9 mg/mL) and three solid concentrations of hydroxyapatite (HA) (*i.e.* 200, 800, and 1200 mg/mL). In addition, a pure water and oil sample were also included in the phantom.

- A 50mm K-edge material phantom was imaged which contained a single concentration ($\sim$27 mg/mL) of europium, gadolinium, ytterbium, lutetium, and tantalum-containing nanomaterials suspended in water. In addition to these samples, oil and water were also included in

the phantom. For more details about the phantom preparation of these materials see [17].

In addition to the standardized phantoms, a pair of excised carotid plaque samples underwent scans and subsequent pixelwise classification. The scanning protocol was the same for the plaques as that used to scan the HA-I phantom. To prepare the plaque samples, they were submerged in sodium diatrizoate solution with a concentration of 12.5 mgI/mL. The added contrast was meant to help differentiate the soft-tissue of the plaques from the surrounding solution allowing for accurate identification of the plaque lumen.

6.2.2 Simulated Data

All simulated data were produced in a customized graphical user-interface (GUI) made in MATLAB. The GUI itself was made to help organize and visualize the several necessary inputs of spectral CT simulation (*e.g.* source spectrum, material properties). In the GUI, the geometry of the system (*i.e.* source-to-object distance (SOD), object-to-detector distance (ODD), field of view (FOV), etc.) and the geometry of the detector (*i.e.* number of pixels, number of detector chips, spatial offsets) are customizable to allow for accurate mimicry of the MARS photon-counting scanner which was used to collect the real datasets. 3D phantoms were generated using the TomoPhantom package [77]. The simulated data were collected and reconstructed using the GPU-accelerated ASTRA Toolbox algorithms [78], [79]. Finally, the photon-counting detector modeling was achieved using the Photon-counting Toolkit (PcTK) [23], [26].

In this study, the simulation was performed using a single-chip camera located $110mm$ from the origin. The chip was 258×66 pixels and the pixel pitch was $.220mm$. The source was located $220mm$ from the origin and the center of the phantom was placed at the origin. The FOV of the scan was set to $360mm$. 360 equiangular projections were taken in a circular geometry around the phantom with a simulated count-rate of 20,000 photons per pixel per view (*i.e.* 10^7 photons/in^2/sec). The material properties were obtained from NIST tables and the source spectrum was a modeled tungsten source being operated at $120kVp$. The PcTK detector model was of a CdTe detector with lower thresholds set at 15, 28, 42, 55, and $65keV$. The PcTK was operated with default parameters as outlined in [23] except for electron cloud radius (r_0) and electronic noise standard deviation (σ_e) which were set to $12\mu m$ and $1keV$, respectively. The material calibration phantom was generated as a simplified brain-mimicking volume (*i.e.* water surrounded by bone) with subregions containing aqueous mixtures of K-edge materials (*e.g.* silver, gold, gadolinium, tantalum, and iodine). Each represented material had 4 mixture regions with the following concentrations (% by mass) - 2.5%,

Table 6.1: Imaging, energy binning, and reconstruction parameters.

	Iodine/Calcium Phantom	**K-edge Phantom**	**Simulated Phantom**
Tube Voltage (kVp)	80	120	120
Tube Current (μA)	35.0	085.0	*N/A*
Field-of-View (mm)	38.0	58.0	27.0
Source-to-Object (mm)	223.1	223.1	220.0
Object-to-Detector (mm)	50.0	60.0	110.0
Beam Filtration	*None*	1.96 mm Al	2 mm Glass + 1.96 mm Al
Projections/Rotation	1440	720	360
Integration Time (msec)	125	250	*N/A*
Energy Thresholds (keV)	23.5, 30.1, 38.9, 49.9	28.5, 41.0, 53.5, 65.0	32.0, 42.0, 55.0, 72.0
Reconstruction	MARS V1.1	MARS V1.2	ASTRA 3D FDK
Materials	H_2O, oil, air, I, Ca	H_2O, oil, air, Gd, Eu, Yb, Lu, Ta	H_2O, bone, Ag, Au, Gd, Ta, I
Concentration(s)	2.25, 4.5, 6, 9 mg I/mL 200, 800, 1200 mg Ca/mL	$\sim 27\ mg/mL$	2.5%, 3.33%, 5%, 10%

3.33%, 5%, and 10%. The four sets of collected sinogram data (*i.e.* material-basis, analytic ground-truth, mean detector model output, and detector model output with added Poisson noise) were

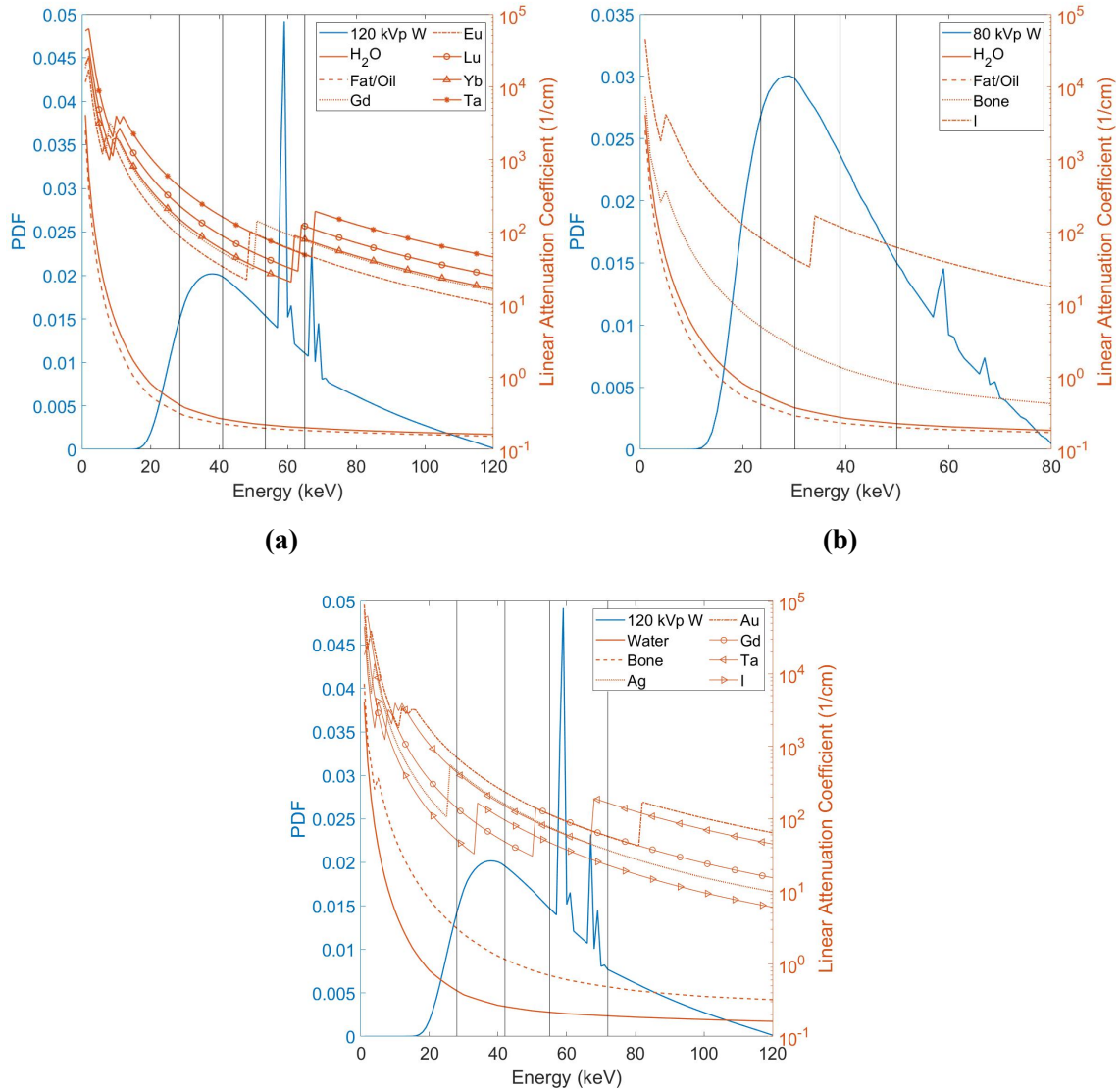

Fig. 6.1: (a) A model spectrum for a tungsten source operated at 120 kVp is depicted alongside NIST material attenuation profiles of those materials present in the MARS K-edge material phantom. The vertical lines represent the energy thresholds. (b) A model spectrum for a tungsten target operated at 80 kVp is depicted alongside the NIST material attenuation curves of those materials contained in the hydroxyapatite-iodine phantom. This phantom could be used to train a kFDA segmentation model for applications such as plaque characterization. (c) Again, the model 120 kVp tungsten source spectra is depicted alongside the K-edge material attenuation profiles of those materials contained in the simulated phantom.

reconstructed with the 3D FDK CUDA algorithm supplied by the ASTRA toolbox. All material classification was performed on the noisy data alone.

6.2.3 Data Handling

After reconstruction, the MARS data was manually segmented and labeled using a two-tier labeling scheme one for materials and one for concentrations. For each material (i), a subset of the segmented voxels ($N_i < 12{,}000$) were sequestered from the image volumes and arranged in an $\sum_i N_i = N \times 5$ data matrix where each column contained the estimated attenuation values ($1/cm$) for the measured energy bins (as output by the reconstruction algorithm). The simulated data were similarly handled, but rather than using manual segmentation to isolate the materials, the material-basis reconstructions were used as masks during the labeling process.

6.2.4 Data Polarization

Each voxel was represented as a vector v such that

$$\mathbf{v}^T = \begin{pmatrix} v_1 & v_2 & \cdots & v_n \end{pmatrix}, \quad \mathbf{v} \in \mathbb{R}^n. \tag{6.2}$$

In both our real data and simulated data, $n = 5$. By applying a geometric logic to the dataspace (previously suggested by [13]), a Cartesian to polar coordinate transformation was applied to our data based on the following relationships [149]:

$$v_r = \|\mathbf{v}\| \tag{6.3}$$

$$v_{\theta_1} = \cos^{-1}\left(\frac{v_1}{v_r}\right), \quad 0 \leq v_{\theta_j} < \pi \tag{6.4}$$

$$v_{\theta_{n-1}} = \cos^{-1}\left(\frac{v_{n-1}}{v_r \prod_1^{i-1} \sin(\theta_j)}\right) \tag{6.5}$$

$$\mathbf{v_p} = \begin{pmatrix} v_r & v_{\theta_1} & \cdots & v_{\theta_{n-1}} \end{pmatrix} \tag{6.6}$$

$\dot{v}$ and $\dot{v_p}$ are equivalent representations of the measured data, yet they are expressed in different coordinate systems. Both were used to classify the data.

6.2.5 Bin Gradient

Finally, to capture the non-monotonic nature of the K-edge containing materials, the gradient (*i.e.* difference) between energy bins is calculated such that:

$$\mathbf{v}_g = \begin{pmatrix} v_1 - v_2 & v_2 - v_3 & \cdots & v_n - v_{n-1} \end{pmatrix} \tag{6.7}$$

When put together, each voxel's data is represented by an extended vector which can be further arranged into a data matrix for N measurements as follows:

$$V = \begin{bmatrix} \mathbf{v}_1 & \mathbf{v}_{p,1} & \mathbf{v}_{g,1} \\ \vdots & \vdots & \vdots \\ \mathbf{v}_N & \mathbf{v}_{p,N} & \mathbf{v}_{g,N} \end{bmatrix} \tag{6.8}$$

6.2.6 Kernel Fisher Discriminat Analysis

Kernel FDA is a nonlinear extension of the traditional linear Fisher Discriminant Analysis [150], a popular classification tool that is used to classify a set of clusters and to associate, or label, a new observation to one of the clusters defined by reference data. This is accomplished by projecting the observations of the groups onto directions such that the individual cluster, one cluster per group, can be separated from one another. The objective function for determining the projection direction is given by:

$$J = \frac{\mathbf{p}^T \Big[\big(\overline{\mathbf{x}}_1 - \overline{\mathbf{x}}_0\big)\big(\overline{\mathbf{x}}_1 - \overline{\mathbf{x}}_0\big)^T + \cdots + \big(\overline{\mathbf{x}}_n - \overline{\mathbf{x}}_0\big)\big(\overline{\mathbf{x}}_n - \overline{\mathbf{x}}_0\big)^T \Big] \mathbf{p}}{\mathbf{p}^T \Big[\mathbf{S}_{x_1} + \cdots + \mathbf{S}_{x_n} \Big] \mathbf{p}} = \frac{\mathbf{p}^T \mathbf{S}_B \mathbf{p}}{\mathbf{p}^T \mathbf{S}_W \mathbf{p}} \tag{6.9}$$

Here, we assume that there are a total of n distinct clusters, or distinct groups of data, $\overline{\mathbf{x}}_0$ is the mean of the combined data set that includes the observations of all clusters, $\overline{\mathbf{x}}_i$, $1 \leq i \leq n$, is the mean vector (center) of the ith cluster and $\mathbf{p}$ is a unit length projection vector. The solution to this objective function is the eigenvector associated with the largest eigenvalue of the matrix product $\mathbf{S}_W^T \mathbf{S}_B$:

$$\lambda \mathbf{p} = \mathbf{S}_W^T \mathbf{S}_B \mathbf{p} \tag{6.10}$$

If the number of reference observations well exceeds the number of clusters, the rank of $\mathbf{S}_W^T \mathbf{S}_B$ is $n - 1$, which allows determining a total of $n - 1$ projection directions. A popular method

to do so is incorporating orthogonality constraints to ensure the projection vectors to by mutually orthogonal.

Kernel FDA first applies the nonlinear transformation $\phi(\cdot)$ to the reference observations, *i.e.* $\mathbf{f}_x = \phi(\mathbf{x})$. Next, kFDA determines projection vectors based on the nonlinearly transformed variables, *i.e.* the feature vector $\mathbf{f}_x$ by applying Eq. (6.9). To construct the matrices $\mathbf{S}_B$ and $\mathbf{S}_W$ yields scalar products of pairs of observations:

$$\mathbf{f}_x^T \mathbf{f}_y^T = \phi^T(\mathbf{x})\phi(\mathbf{y}) = \psi(\mathbf{x}, \mathbf{y}) \tag{6.11}$$

which can be described by kernel functions, among which the Gaussian kernel is popular:

$$\psi(\mathbf{x}, \mathbf{y}) = \exp\left(-\frac{\left\|\mathbf{x} - \mathbf{y}\right\|^2}{c} \right) \tag{6.12}$$

where c is a kernel parameter that can be adjusted improve performance of the classification performance of the kFDA model. A more detailed discussion of kFDA, including a cross-validatory selection of the kernel parameter and a regularization term for $\mathbf{S}_W$, based on the nonlinearly transformed data, is given in [151].

6.2.7 Parameter Selection with *k*-fold Cross-validation

For each dataset tested in this paper, the c parameter to be used in the respective kFDA classification model was chosen by varying c from 0.1 to 100 and quantifying the classification accuracy. 10-fold cross-validation was performed on subsets of V which contained 1000 randomly chosen points from each material group. In each fold, therefore, 900 points were used to generate the kFDA model and the remaining 100 points were used for testing. The best classification accuracy was achieved with $c = 3$ for the real K-edge phantom, $c = 1.5$ for the hydroxyapatite-iodine phantom, and $c = 0.9$ for the simulated K-edge dataset.

6.2.8 Image Segmentation and Material Quantification

After generating the kFDA model, each pixel of the original image (or naive image) is mapped using the eigenvector representation of the dataspace. The current implementation for this segmentation is strictly a pixelwise process, and therefore does not take spatial information into account. Pixel labels are chosen according to the minimum Euclidean distance between the pixel data and the mean of the known material regions from which the kFDA model was built. In the training models

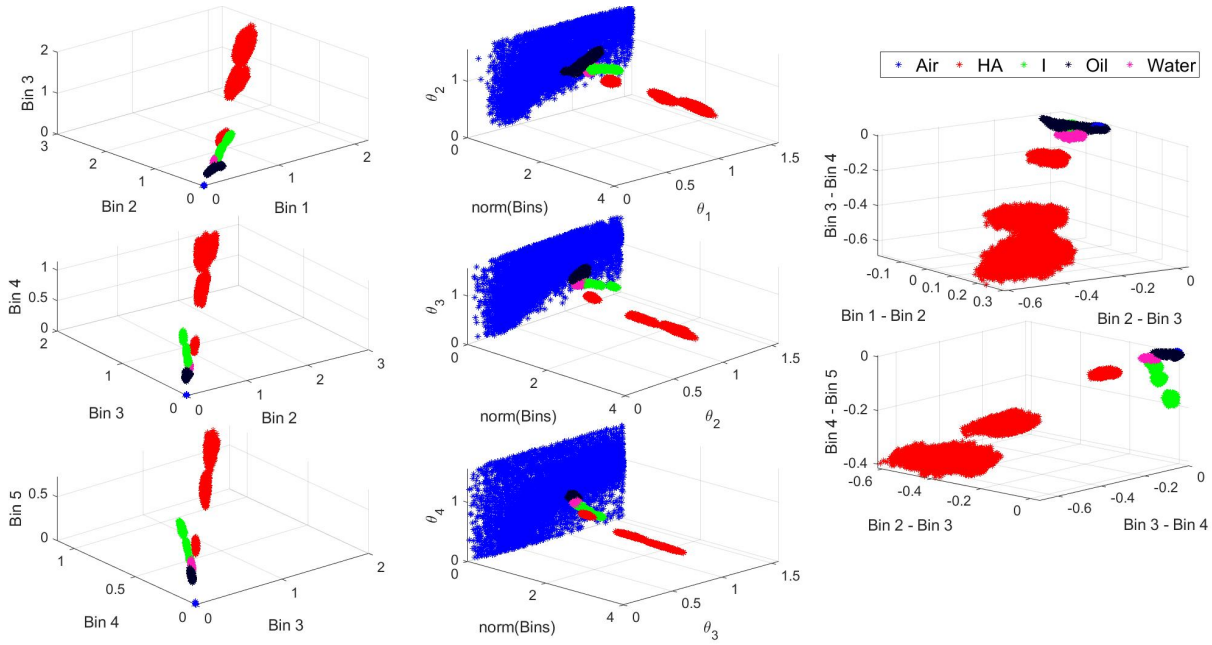

Fig. 6.2: Projecting each of the 14 V dimensions into a 3D subspace to allow for some basic understanding regarding relationship of mulitiple concentrations of HA, I, water, oil, and air in the expanded spectral dataspace.

which contained several concentrations of materials, labeled pixels were subsequently quantified according to the appropriate linear concentration curve which was fit individually for each material.

6.3 Results

6.3.1 Visualizing the Data Space

The high dimensionality of the data in the V matrix is intrinsically hard to visualize. The best one can do is to project the vector space into 3 (or less) dimensions to get a feel for the dataspace that each phantom provides. Figs. 6.2, 6.3, and 6.4 show each data point and vector dimension of the scanned and simulated phantoms projected into a 3D subspace. The relationships and similarities between materials and concentrations can be gleaned from these images, although this raw dataspace is subject to kernelization and transformation as per the kFDA methods for separation.

6.3.2 MARS HA-I Phantom

Given that data from five materials in the HA-I phantom are used to generate the kFDA model, the first four eigenvectors can be used in the subsequent classification/segmentation of the data. Fig. 6.5(a-d) show the training data mapped according to these four eigenvectors. Each of

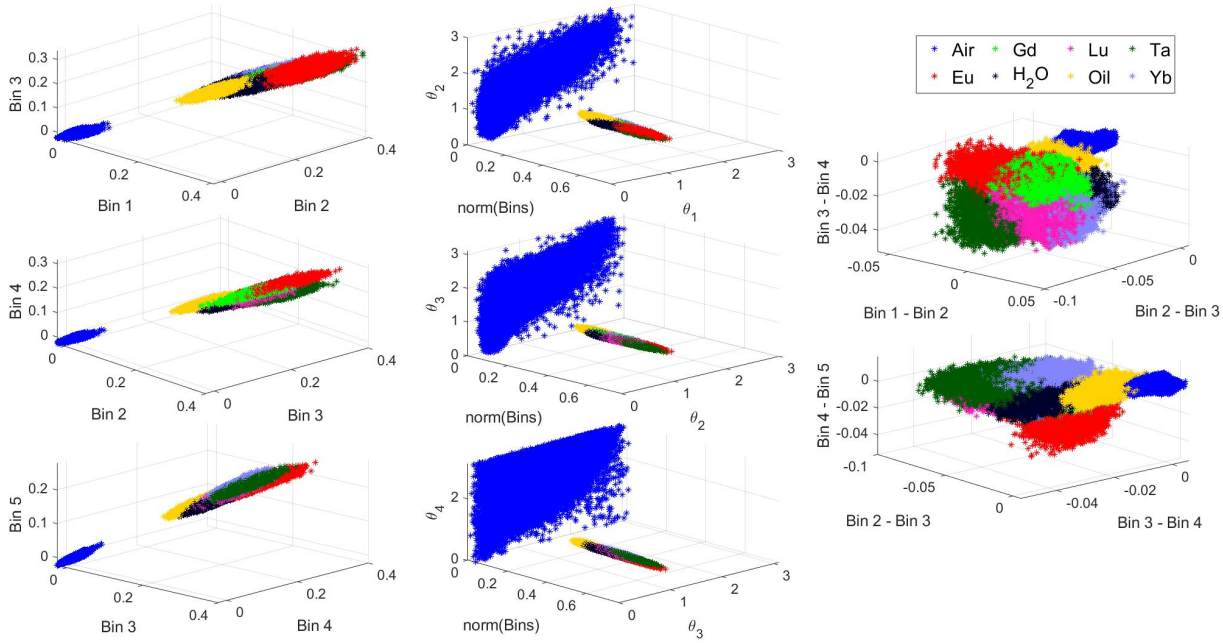

Fig. 6.3: Projecting each of the 14 V dimensions into a 3D subspace to allow for some basic understanding regarding relationship of the single concentrations of Gd, Lu, Ta, Eu, Yb, water, oil, and air in the expanded spectral dataspace.

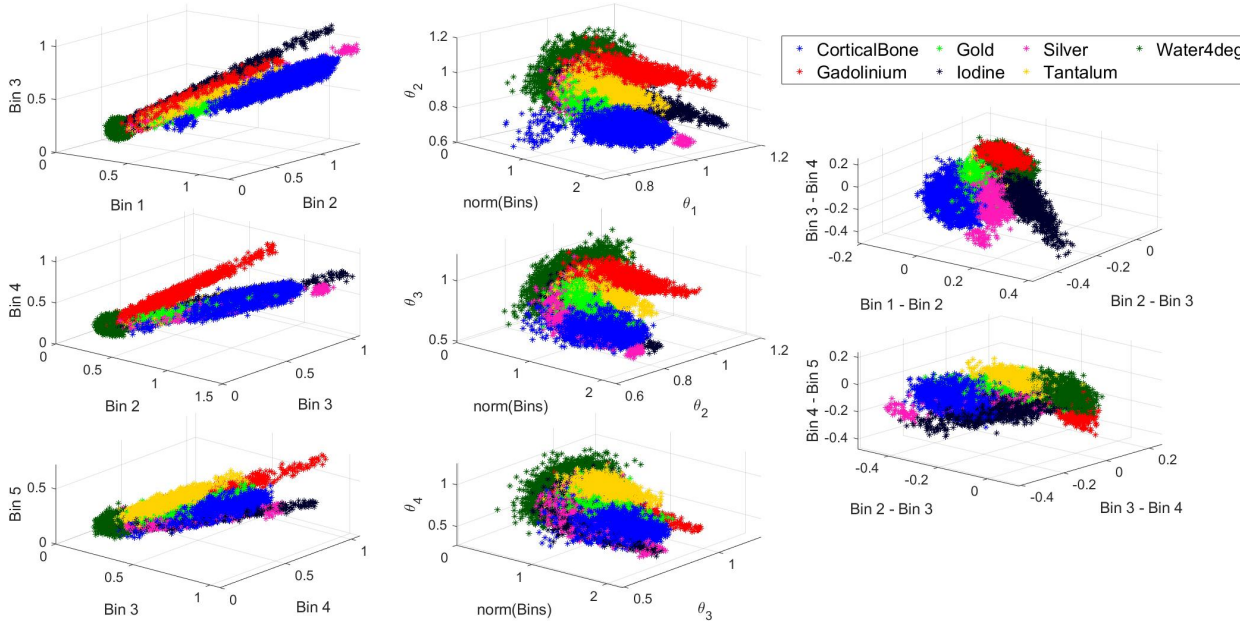

Fig. 6.4: Projecting each of the 14 V dimensions into a 3D subspace to allow for some basic understanding regarding relationship of multiple concentrations of cortical bone (HA), I, Au, Ag, Ta, Gd, and water in the expanded spectral dataspace.

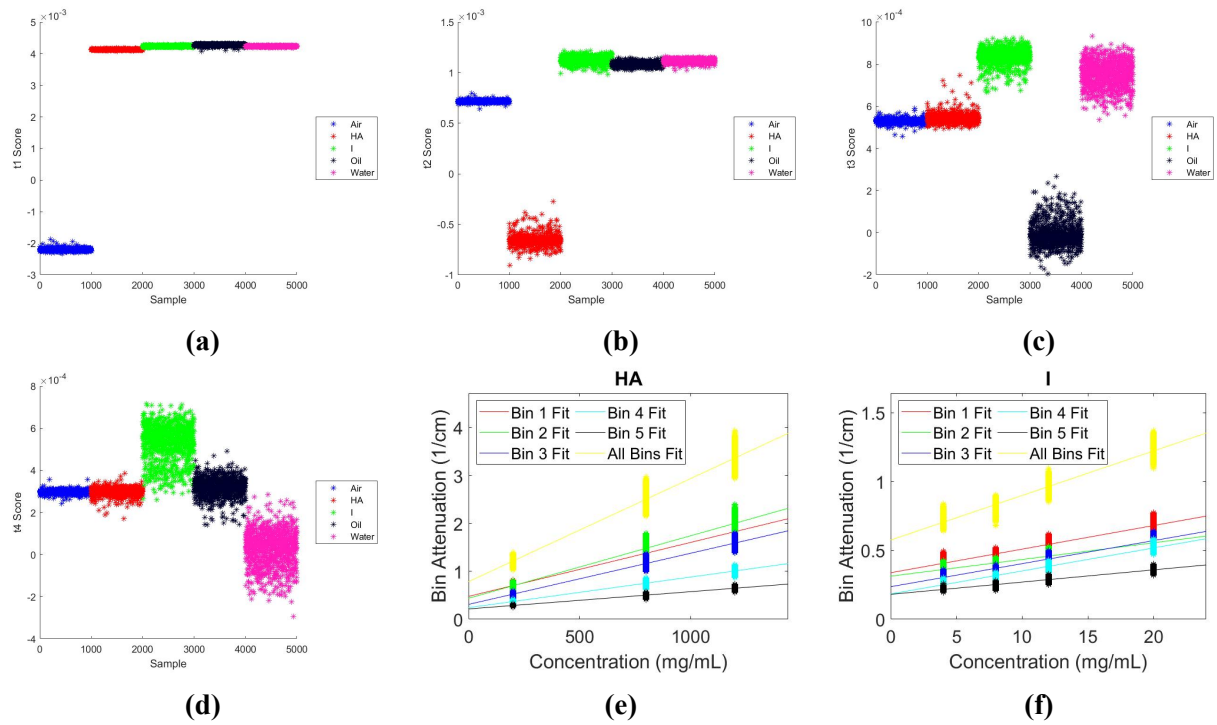

Fig. 6.5: (a-d) The first four eigenvectors of the kFDA mapped HA-I data show how the various materials are separated in the mapped dataspace. 2D plots of these eigenvector representations of the data are included in Appendix A. (e-f) Lines are fit to the two materials for which multiple concentrations are available in the phantom: (e) hydroxyapatite and (f) iodine. Each of fitted lines are used to quantify the material concentration in a labelled pixel and the final concentration is computed as the average of all computations.

these new data dimensions provide some discriminatory power as seen by the separation of the materials (identified by their different colors.) The five energy bin measurements as well as the sum of squares for these measured values follow a linear trend with concentration of HA and I, shown in Fig. 6.5(e-f). The lines calculated from the training data are later used to determine the pixelwise concentration for any pixel that labeled as HA or I.

Fig. 6.6 shows a labeled and quantified slice from the training phantom. Both the solid HA plugs as well as the iodine solutions are accurately classified and quantified. The plastic tubes in which the aqueous solutions and oil are placed are classified in the oil class. Several pixels in the open air are classified as contrast materials, though their concentration quantification is 0.

Of course, the utility of the kFDA model is not in its ability to classify materials in a training phantom, but rather in its translational capacity to naive samples. To demonstrate the ability for kFDA models to be applied for any sample which contains the trained materials, two excised, hu-

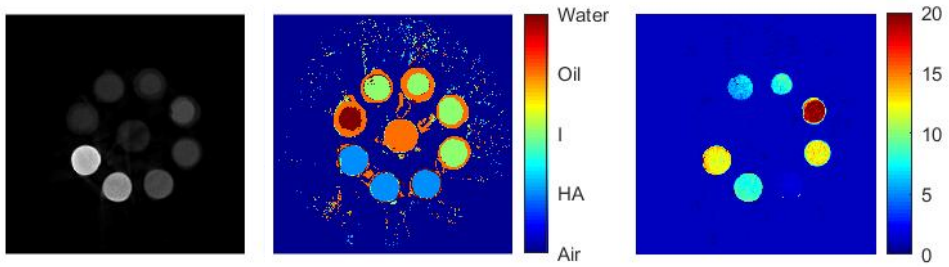

(a) (b) (c)

Fig. 6.6: (a) The reconstructed image from the first energy bin for the HA-I phantom. (b) The kFDA labeled image. (c) The linear fit concentration map for samples labeled as HA or as I. The HA sample concentrations should be multiplied by a factor of 100.

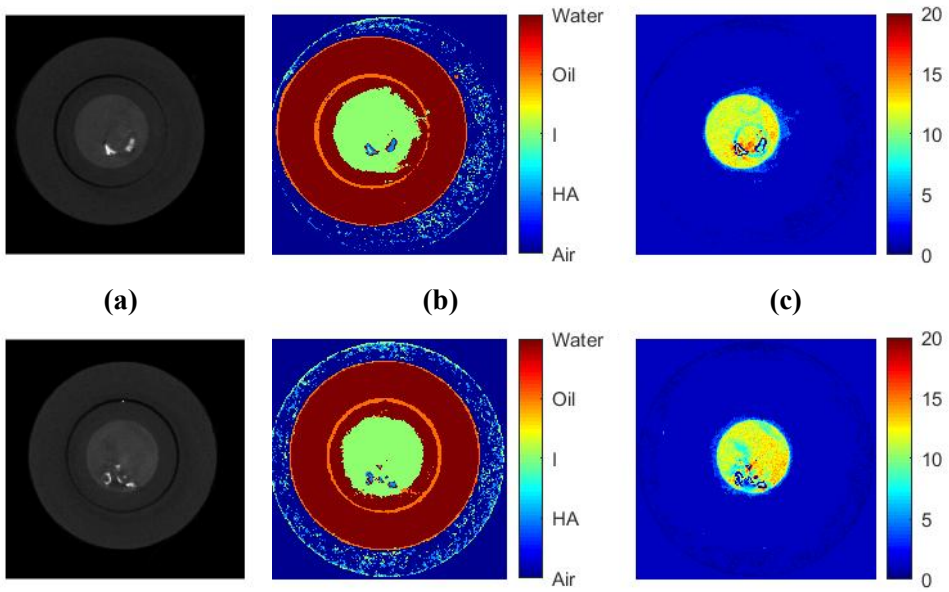

(a) (b) (c)

(d) (e) (f)

Fig. 6.7: (a) The reconstructed image from the first energy bin for plaque sample 1. (b) The kFDA labeled image (center). (c) The linear fit concentration map for samples labeled as HA or as I. The HA sample concentrations should be multiplied by a factor of 100. (d) The reconstructed image from the first energy bin for plaque sample 2. (e) The kFDA labeled image. (f) The linear fit concentration map for samples labeled as HA or as I. The HA sample concentrations should be multiplied by a factor of 100.

man carotid plaque images were classified using the above kFDA model. These tissues can be any combination of calcification, fibrous tissue (water-like), or fatty deposit (oil-like). Additionally, these plaques were submerged in iodine solution to help differentiate the soft-tissue plaque from an otherwise aqueous environment. The labeled images can be seen in Fig. 6.7. It is clearly observed in these images that iodine and calcification (HA) can be separated from each other with little error. Unfortunately, the process of submerging the plaque tissue in iodine seems to result in some diffusion of the iodine into the soft-tissue of the plaque. Therefore, all soft-tissue regions of the plaques are classified as iodine regions (with lower concentration than the surrounding solution). Despite this methodology limitation for analyzing the plaques, the 5 material kFDA model is transferrable to naive images.

6.3.3 MARS K-edge Phantom

The second set of real-data contain, in addition to water, oil, and air, 5 different K-edge nanoparticle suspensions made of Gadolinium, Europium, Ytterbium, Lutetium, and Tantalum. This data set is the same as seen in [17] where these materials where shown to be "separable" when compared to oil, water, and in some cases, each other. The previous methods only took the 5 energy bin attenuation estimates into account when calculating the multivariate T^2 metric used to determine separability. With the expanded data and the non-linear, kernel FDA method seven eigen vectors were calculated and used to classify the materials in this phantom. Fig. 6.8 shows each of these vector transformations with the training dataset. Unlike, those seen in Fig. 6.5 where each of the vectors provide considerable separation between the materials, only a handful of these vectors (*i.e.* a-e) create considerable separation amongst the material classes.

The lack of separation in the last 2 or 3 eigenvector dimensions is reflected in the resulting labeled image (Fig. 6.9). Clearly the segmentation of materials in this data set is not quite as definitive as compared with the HA-I phantom. This is especially true between the low signal samples (*e.g.* Yb and Lu). high accuracy classification is achieved for oil, water, Gd, Eu, and Ta. Even the majority of pixels in the Lu and Yb samples are correctly classified, though there are significantly more misclassifications for these materials. The acrylic holder has the largest number of misclassified pixels (should be classified as oil or water) with several being classified as Gd and Yb. These are likely due to reconstruction artifacts. The source of these artifacts may be traced back to ball-bearing unloading (*i.e.* geometric miscalibration) or detector shadows (a result of the stair-step configuration of the 3-chip detector which are exacerbated by large sample gantry

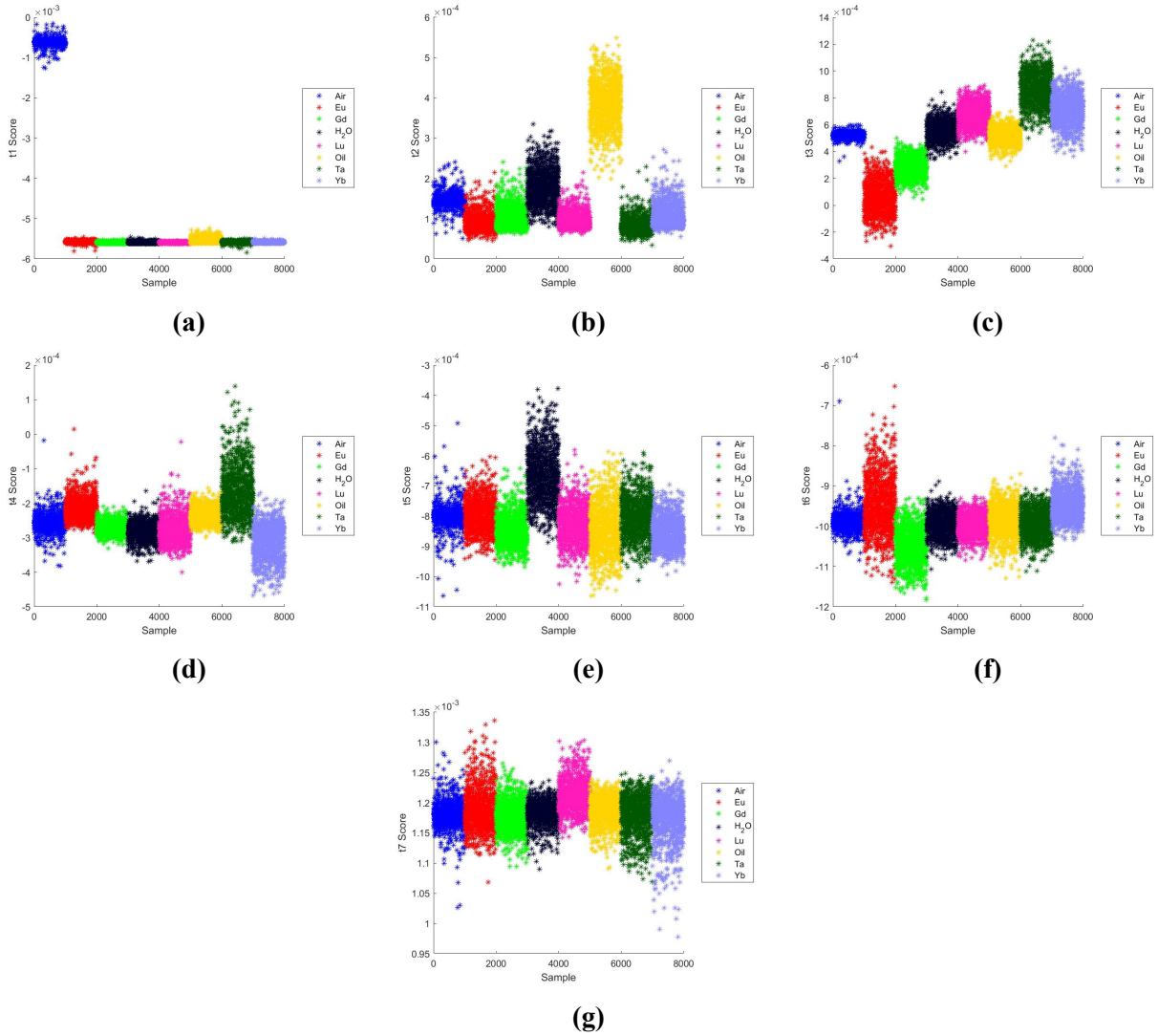

Fig. 6.8: (a-g) The first seven eigenvectors of the kFDA mapped MARS K-edge data show how the various materials are separated in the mapped dataspace. The first five eigenvectors do the most to distinguish the various materials. 2D plots of these eigenvector representations of the data are included in Appendix A.

configurations).

6.3.4 Simulated K-edge Phantom

While the real K-edge data set certainly provides some basis for using kFDA with K-edge materials, a simulated data set (also with 5 K-edge materials) was segmented and quantified using the methods outlined above. In this data set, the K-edge materials are much more spread out with respect to the energy bin placement than the real K-edge phantom. There is one material K-edge per energy bin and air is not considered as a separate class when computing the kFDA model.

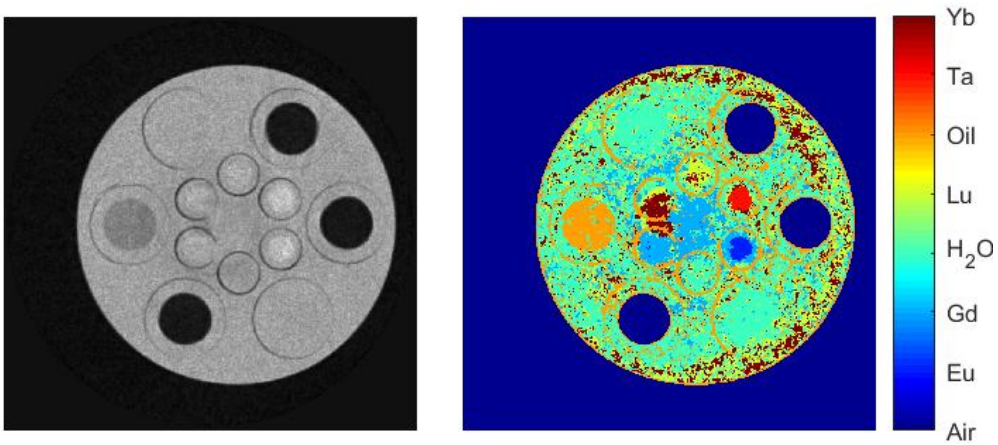

(a) **(b)**

Fig. 6.9: (a) The reconstructed image from the first energy bin for the real K-edge phantom. (b) The kFDA labeled image.

It was hypothesized that this strategic placement of the bins (vs. K-edges) would increase the classification accuracy afforded by the computed kFDA model. Fig. 6.10(a-f) show the 6 eigen vectors used in the classification model. The separation of the materials across the eigen vectors are not exceedingly high, although the labeling results seen in Fig. 6.11b demonstrate the model's ability to accurately classify each material. Simulations with more materials were also performed, however, misclassifications increased with the number of materials especially between materials whose K-edges share an energy bin.

6.4 Discussion and Conclusion

In this paper, two sets of real-world spectral CT data containing a variety of contrast inducing materials were shown to be effectively segmented and quantified using a two-step process. The novelty of this method lies in the first part of the method which uses the kernelized Fisher's Discriminant Analysis which is the non-linear extension of the linear FDA method presented in our previous work [17]. This method was shown to allow for more materials than measurements to be accurately classified/quantified which cannot be done by simply solving a linear system alone. It should be noted that in order to improve classification accuracy the original measurement set was augmented to include a polar representation of the measurement space as well as the bin-to-bin gradient. While these augmented values do in fact increase our number of "measurements" there is no linear system representation (at this time) that could be formulated to increase the theoretical

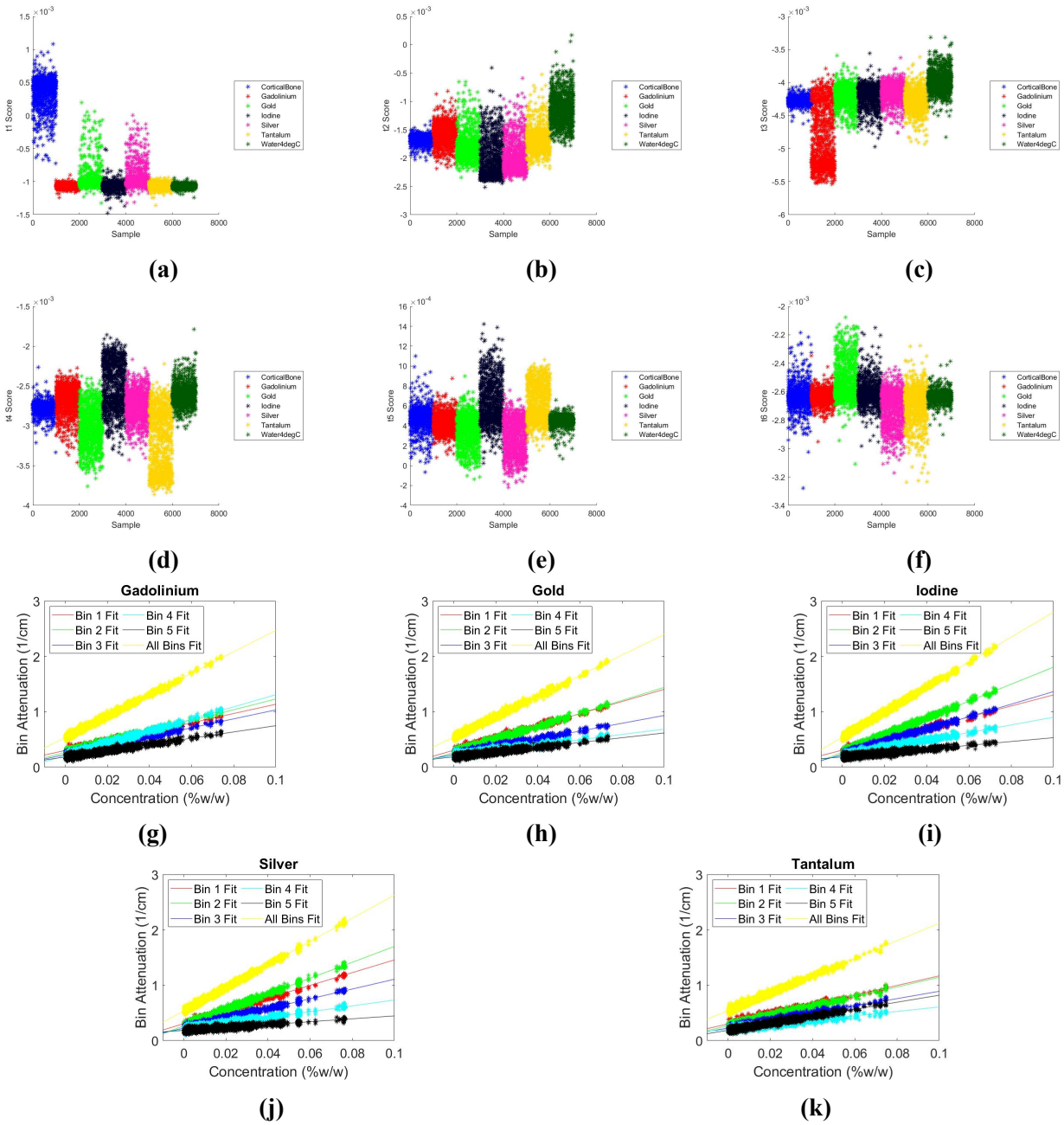

Fig. 6.10: (a-f) The first six eigenvectors of the kFDA mapped MARS K-edge data show how the various materials are separated in the mapped dataspace. 2D plots of these eigenvector representations of the data are included in Appendix A. (g-k) The linear fits for the concentrations found in the reconstructed material basis phantom produced by the simulation. The final concentration is an average of the calculated value from the 6 lines fit to the energy bin measurements.

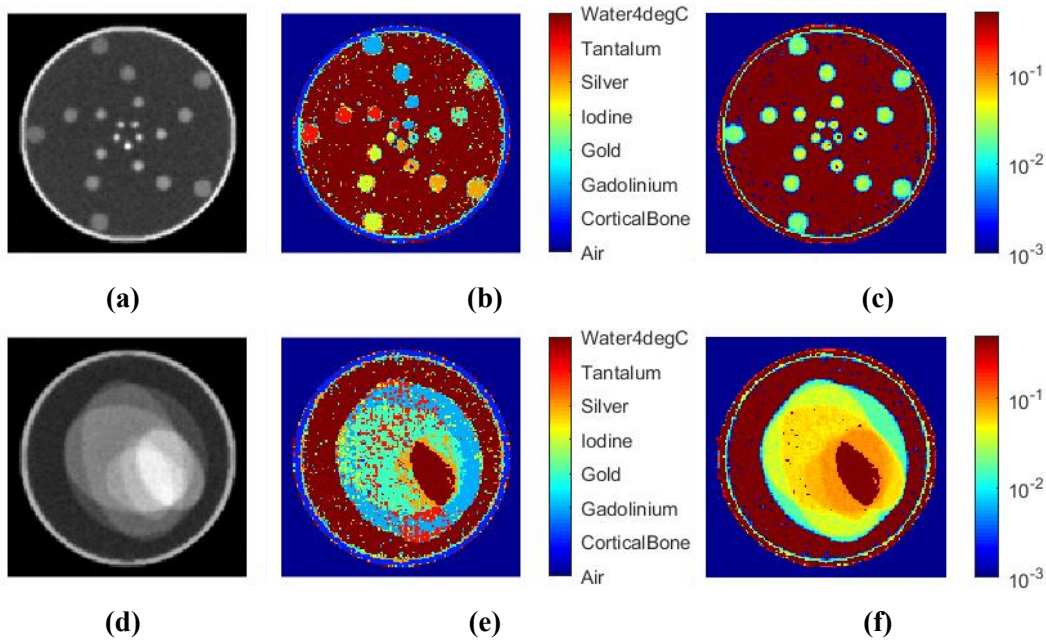

Fig. 6.11: (a) The reconstructed image from the first energy bin for simulated K-edge calibration phantom (left). The kFDA labeled image (center). The linear fit concentration map for samples labeled as a K-edge material (right). (b) The reconstructed image from the first energy bin for the mixed K-edge phantom (left). The kFDA labeled image (center). The linear fit concentration map for samples labeled as a K-edge material (right).

maximum number of materials which can be solved through inversion.

Of course, showing that the kFDA model can effectively segment the image which provided its training data is far from the end goal of such a method. Therefore, the translational potential of these models was demonstrated by segmenting altogether naive images of excised, human carotid plaques. Using the kFDA model trained with HA-I phantom, the plaque images were effectively classified (and quantified) into the major material regions - calcification as HA and the solution as iodine. The soft-tissue of the plaque, which may be expected to have a mixture of oil and water regions, was also identified as iodine. This is attributed to diffusion of the iodine salt solution into the tissue resulting in the low-contrast signatures to be overwhelmed by the iodine. Indeed, these regions do show lower concentration iodine than the surrounding solution. More work should be done to find an effective scanning protocol which can provide strong quantification of the plaques soft-tissue components; however, this is beyond the scope of this paper. The kFDA segmentation, therefore, was an effective tool for discovering the flaw in the iodine-submerged scanning protocol.

The same K-edge materials used to create the simulated phantom (see Fig. 6.11b) were ran-

domly selected to form ellipses of random concentrations and sizes in subsequent simulation. These ellipses could overlap, therefore mixing the materials in any given voxel. kFDA (and segmentation methods in general) do not do a good job in handling this scenario (as shown in Fig. 6.11e). Following the same logic as outlined by the MARS-MD [65] protocols, it may be possible to use kFDA as a starting segmentation to reduce the number of unknowns being solved for in the linear system introduced in Eq. 6.1. Regardless, regularization will likely be key in solving these problems.

Non-linear segmentation methods, such as kFDA, are shown here to be a powerful tool in spectral imaging scenarios with PCDs where the following assumptions can be made:

1. The sample consists of a known set of materials.
2. A calibration phantom can be made with a relevant dynamic range of concentrations for each sample.
3. The material regions do not overlap (*i.e.* single material class in each voxel).
4. Image noise can be effectively modeled and accounted for during the computation of the kFDA classification model.

This list, and specifically assumption 3, may seem too limiting. Indeed, for the "holy grail" applications that are being envisioned for spectral CT (*i.e.* multiplexed molecular imaging), it cannot be guaranteed that multiple materials won't occupy the same voxel. Already, partial volume effects can be seen at the edges of various regions in the labeled images presented here. Where air is certainly occupying the gaps between the phantom tubes, it is classified as oil due to the mix of acrylic and air within the voxels.

In conclusion, kFDA can be used a powerful multivariate segmentation tool in spectral CT applications that involve more materials than measurements. The method is most powerful for materials with high CNR, although moderate differences between even individual energy bins can provide sufficient separability to achieve accurate classification with this nonlinear method. A secondary linear regression (from known concentrations) can be used to quantify the labeled images with high accuracy. The method is limited, however, at edges and when materials start to mix into the same voxel. This method could be used to segment the image domain data in order to reduce the unknowns which need to be solved for in the linear system using more traditional material decomposition methods.

6.5 Acknowledgements

This work was partially supported by the Ministry of Science and Innovation (New Zealand) and the Clark & Crossan Endowment fund from Rensselaer Polytechnic Institute. The funders had no role in study design, data collection and analysis, decision to publish, or preparation of the manuscript.

Chapter 7
Material Decomposition with a Convolutional Neural Network (MD-CNN)

7.1 Introduction

In Chapters 5 and 6, the material decomposition problem was introduced. Briefly, the image-domain material decomposition problem is generally modeled as a linear system as shown in Eq. 6.1. More specifically, that model can contain terms for the major physical interactions of photons with matter which effect the measured attenuation coefficients (*i.e.* photoelectric absorption cross-section, Compton scatter cross-section, and K-edge discontinuities), as shown in Eqs. 5.1 – 5.4. This model was first introduced by Roessl and Proska in a 2007 paper in which they showed using simulation that by solving this inverse-problem using a feed-forward, maximum likelihood function, accurate material basis approximations could be made for gadolinium contrast containing images [58]. This work was experimentally supported a year later (2008) by the same group, specifically Schlomka *et al.* . The same physical interaction model was adopted (an iodine K-edge term) was added and real-world data was reconstructed and decomposed into the model representation of the model interactions. Regions containing gadolinium and iodine (separated in the phantom) are clearly separated by this decomposition model and the varying concentrations across regions are accurately reflected in the signal proportion attained in the respective K-edge images [59]. More recently this model has been adopted to demonstrate the technique's ability to tease out mixtures of materials [62] as well as its utility in images obtained from animal models (rather than phantoms) [63].

In addition to the physical interaction model, other groups have devised a voxel-wise density model where the linear attenuations approximated in reconstructed images for each energy bin are a linear combination of the mass attenuation coefficients for each of the materials and their relative density in the given voxel.

$$\underset{\mathbf{b}}{\begin{bmatrix} \mu_1 \\ \mu_2 \\ \vdots \\ \mu_n \end{bmatrix}} = \underset{\mathbf{A}}{\begin{bmatrix} \frac{\mu_{1,1}}{\rho_1} & \frac{\mu_{1,2}}{\rho_2} & \cdots & \frac{\mu_{1,m}}{\rho_m} \\ \frac{\mu_{2,1}}{\rho_1} & \frac{\mu_{2,2}}{\rho_2} & \cdots & \frac{\mu_{2,m}}{\rho_m} \\ \vdots & \vdots & \ddots &]\vdots \\ \frac{\mu_{n,1}}{\rho_1} & \frac{\mu_{n,2}}{\rho_2} & \cdots & \frac{\mu_{n,m}}{\rho_m} \end{bmatrix}} \underset{\mathbf{x}}{\begin{bmatrix} \rho_{v1} \\ \rho_{v2} \\ \vdots \\ \rho_{vm} \end{bmatrix}} \tag{7.1}$$

where μ_n is the measured linear attenuation in energy bin n, $\frac{\mu_{n,m}}{\rho_m}$ is the mass attenuation within energy bin n for material m, and ρ_{vm} is the voxel-wise density of material m (material basis). Several groups have adopted this model and are using a number of inverse-problem solving methods including linear least squares (LLS), non-negative linear least square (NNLLS), and LLS with regularizers [65]–[67]. Still other groups have approached the MD problem through the addition of spatial-spectral filters and subsequent sparse model-based decomposition for direct reconstruction of the material densities [152].

Outside the scope of solving these ill-posed inversion problems with traditional solver methods, other groups have turned toward the hot area of machine learning and neural networks to achieve an accurate material decomposition [69]. Chen *et al.* adopted two neural network frameworks based on simplified versions of convolutional neural networks (CNNs) that have been used for image classification: visual geometry group (VGG) and deep residual network (DRN). In both architectures, an image patch of size $X \times Y \times n$ is input to the network and a vector size $1 \times 1 \times m$ is output where n is the number of energy bins and m is the number of possible basis materials. With these networks, there is information loss in terms of image size due to the whole patches converging onto single vectors. The VGG and DRN networks performed significantly better than the compared extended direct inversion algorithm, especially when used to decompose real datasets containing iodine, gadolinium, and calcium bases.

This chapter looks to simplify the architecture proposed by Chen *et al.* through the elimination of max-pooling and batch-normalization layers. Additionally, more material basis, specifically more K-edge contrast materials, are tested with the proposed 8-layer CNN. Finally, two loss functions, both based on mean-squared error are tested for network training.

7.2 Methods

7.2.1 Simulation

One hundred (100), 8 material basis phantoms were generated and reconstructed using the simulation framework outlined in Chapter 2. Table 7.1 provides the details of the gantry, detector, and sample geometry as well as the detector-specific parameters. Each phantom was randomly generated and consisted of a cortical bone shell of random thickness filled with aqueous solution. The inner water portion could also contain a random number (up to 10) of randomly oriented 3D ellipsoids. Each ellipsoid could contain a random concentration within the range of (0.25-5% w/w) of either silver, iodine, gadolinium, tantalum, or gold. The total water weight percentage within

Table 7.1: Simulation geometry, energy binning, and reconstruction parameters.

Simulation Geometry		**PcTK Parameters**	
Tube Voltage	120 kVp	*nCh*	258
Photons/pixel/view	20,000	*nRow*	66
Field-of-View	36.0 mm	*Pixel Pitch*	220 μm
Source-to-Object Dist.	220.0 mm	*Cloud Radius*	24 μm
Object-to-Detector Dist.	110.0 mm	*Electronic Noise*	2 keV
Beam Filtration	1.96 mm Al	**Energy Thresholds**	
Projections/Rotation	360	*Energy1*	15.0 keV
ASTRA Reconstruction		*Energy2*	32.0 keV
Voxel Size	146.7 μm	*Energy3*	42.0 keV
Method	SIRT-CUDA	*Energy4*	55.0 keV
Phantom Size	141 x 141	*Energy5*	65.0 keV

voxels contained in these ellipsoids was adjusted according to the percentage of contrast material in each voxel. It should be noted that at the low end of the K-edge material concentration range, some of the materials do not actually produce measurable contrast differences between the baseline water contrast. Therefore, it is entirely possible that the ground-truth material basis set of images contain ellipsoids that are imperceptible in the reconstructed energy bin images. See Fig. 6.1c for the spectra and attenuation profiles used in these phantoms.

While it is briefly mentioned at the end of Section 2.2.7, the logic behind the generation of a material basis phantom which contains a mass percentage value is outlined here. When using the PcTK [23], [26], a set material basis sinograms are inputs to the detector model. The counts at the detector are modeled with the following discrete Beer-Lambert Law equation:

$$I_E = I_{E,0} \ \exp\left(- \sum_{m \in mats} \mu_{m,E} \ d_m \right) \tag{7.2}$$

where I_E and $I_{E,0}$ are the attenuated and open-beam counts within an energy range E. The material attenuation curves, according to the NIST tables, should be provided as prior information so that $\mu_{m,E}$ can be computed for each material (m) and energy range (E). The d_m term, therefore, is contained in the material basis sinograms, and is the distance traveled through material m from the source to the detector (*i.e.* line integral) and $mats$ refers the set of all materials contained in the phantom. Working in the distance units of pixels and with binary material masks, the forward projection results through any given material m will equal the distance (in pixels) traveled along the projection line through the material. This is a sufficient model for any material which fully

occupies a voxel; however, in the case of K-edge contrast materials, a small concentration of the material is co-located within voxels that contain water in much high concentrations. To account for this, Eq. 7.2 is adjusted to:

$$I_E = I_{E,0} \ \exp\left(- \sum_{m \in mats} \frac{\mu_{m,E}}{\rho_m} \ \tilde{d}_m \right) \tag{7.3}$$

where $\tilde{d}_m$ is a distance measure that is weighted by the mass percentage of the water-contrast material mixture, such that:

$$\tilde{d}_m = \rho_{water} \ \frac{mass_m}{mass_{water} + mass_m} \ d_m \tag{7.4}$$

An assumption is made in Eq. 7.4 that the resulting aqueous mixture has the same density as water ($\rho_{water} \approx 1$). This may not hold true in practice, but for the sake of the simulation it was considered a safe assumption which, at most, underestimates the contrast contributions for the K-edge material mixtures. The mixture regions' mass percentage is subtracted from the water binary mask such that:

$$\tilde{d}_{water} = \rho_{water} \left(d_{water} - \sum_{m \in C_{mats}} \tilde{d}_m \right) \tag{7.5}$$

C_{mats} refers to the set of contrast material mixtures. The result of this weighting term is an adjusted linear attenuation effect from the contrast material which lends itself well to the softmax activation function (*i.e.* single voxel across all channels add to 1). Fig. 7.1 shows three of the test phantoms that were generated using this method coupled with the PcTK. The energy bin outputs are shown on the left side of the images and the material basis images (reconstructed from the material basis sinograms) are shown on the right. These material basis images are used as the ground-truth for training the MD-CNN model.

7.2.2 Network Architecture

A simple 8-layer convolutional neural network is proposed for the task of material decomposition of the ill-posed inversion problem of spectral phantoms containing 8 materials including 5 K-edge contrast materials. The first seven layers each had 64, 3x3 filters and are activated with rectified linear unit (ReLU). The final layer outputs the number of materials basis that the network has been trained to identify and is activated by the softmax function. This final activation function is used based on the assumption that the sum of all channels is equal to 1 (*i.e.* the total mass percent

of all materials in a given voxel is 100%). Zero-padding is used in all layers to ensure that no spatial resolution is lost with respect to the input patch/image.

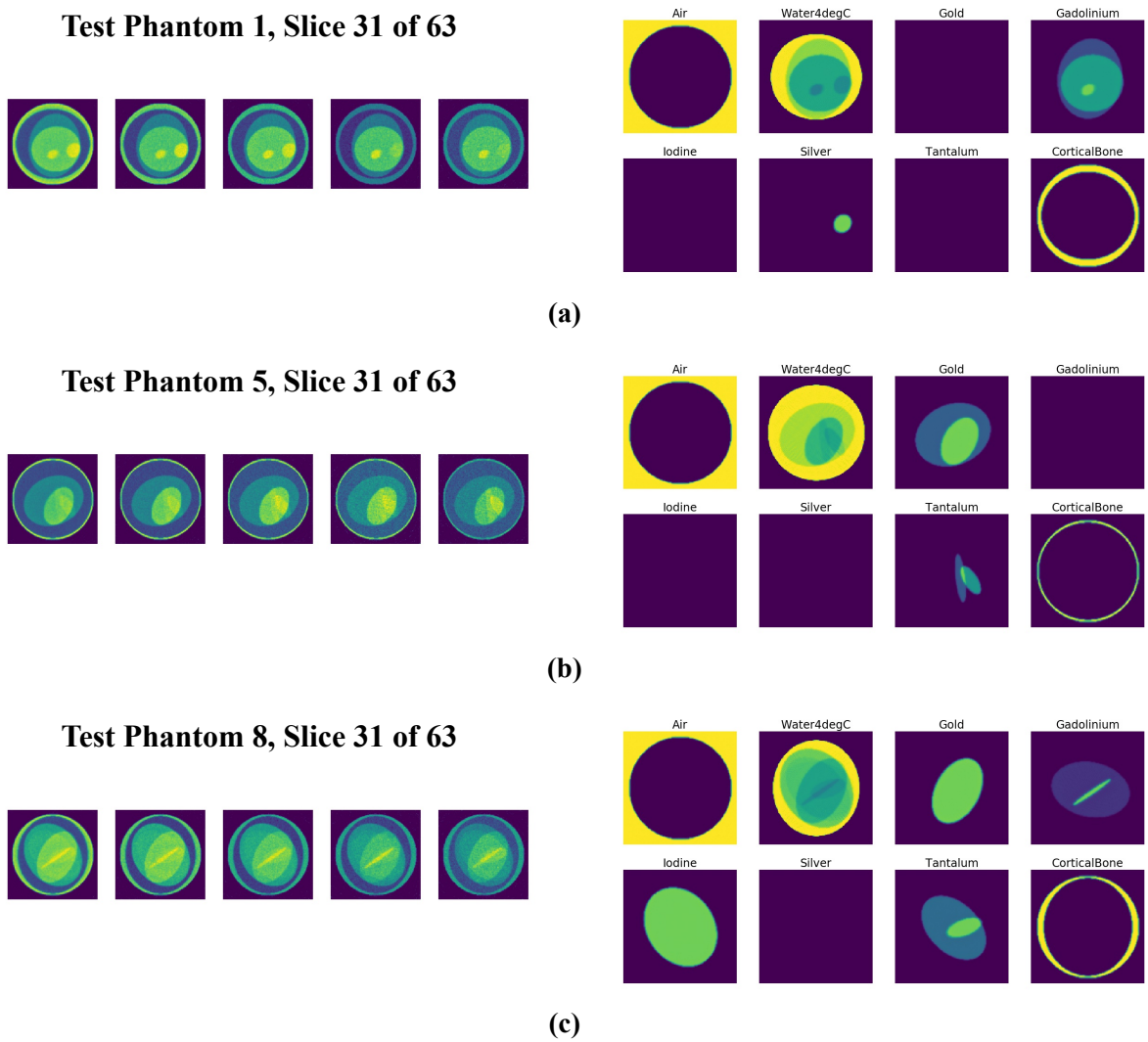

Fig. 7.1: The left image sets are one slice from the reconstructed simulation outputs for 3 of the test phantoms, and the right image sets are the material basis ground-truth (reconstructed from material basis sinograms during simulation). Each of the 100 simulated phantoms had 63 usable slices. The phantoms were randomly split into training (80), validation (10), and testing (10) sets. 49 patches of size (32x32) were extracted from the training and validation slices with a pixel stride of 16. Testing was done on full-size images.

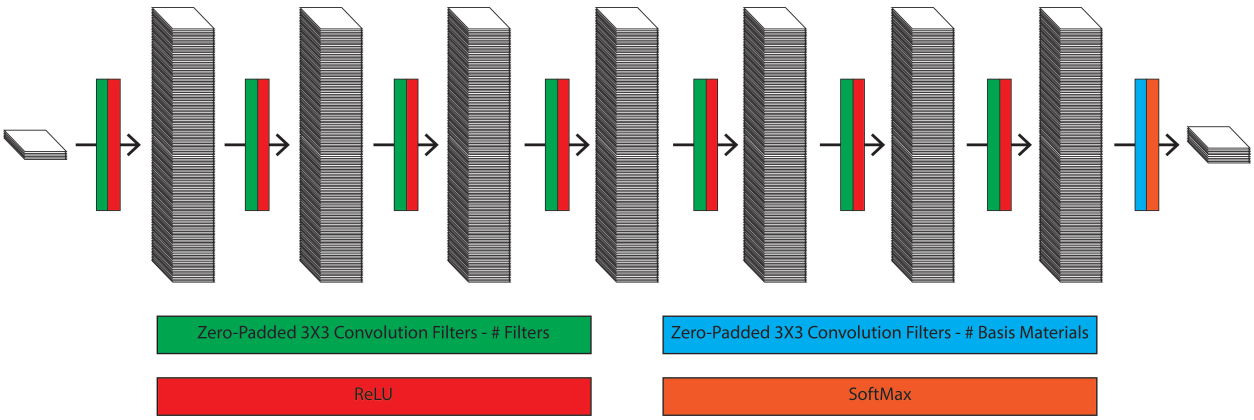

Fig. 7.2: The proposed CNN for material decomposition.

7.2.3 Loss Function, Hyperparameters, and Training

Two loss functions were tested in this study, both based on mean squared error (MSE). MSE was defined as

$$MSE = \frac{1}{n}\sum_{n}(\hat{y_n} - y_n)^2 \tag{7.6}$$

where n is the number of material bases channels in the ground-truth, $\hat{y_n}$ is the CNN output, and y_n is the ground truth. MSE alone was tested as a loss function for the network training.

$$Loss1 = MSE \tag{7.7}$$

The output from MSE will more heavily weight the channel values that are close to 1 (*i.e.* air, bone, and water). In order to achieve accurate metal concentrations, a second loss function which doubles down on Eq. 7.6 is introduced. This time MSE is computed only for the relatively low concentration K-edge materials and an additional weighting term υ included in the equation.

$$wMSE = \frac{\upsilon}{n}\sum_{n \in C_{mats}}(\hat{y_n} - y_n)^2 \tag{7.8}$$

With this new wMSE computation the second loss function is defined as a simple addition of MSE and wMSE:

$$Loss2 = MSE + wMSE \tag{7.9}$$

In all the models trained in this paper, the weighting term $\upsilon = 100$. Filter weights are updated using the TensorFlow Adam optimizer for stochastic gradient descent. Learning rate was set to $1e^{-4}$ and

the momentum hyperparameters $\beta 1$ and $\beta 2$ were set to 0.9 and 0.99, respectively. The training batch size was set at 32 patches per iteration, resulting in 7716 iterations per epoch. 100 epochs were used for training the networks and training was done a single Nvidia GTX 1080Ti. Both MSE and wMSE were logged during training and validation.

7.3 Results

7.3.1 Training

The same number of parameters are changed for both networks which are reported below, the difference between them being the loss function used during training. The training times for MD-CNN-Loss1 and MD-CNN-Loss2 were 5:03:36 and 5:11:10, respectively. The network trained with Loss1 minimizes MSE further than the one trained with Loss2; however, the Loss2 network minimized the wMSE further than the Loss1 trained network. The curves for Loss2 and wMSE are very similar since the magnitude of wMSE is $\sim 10^{-2}$ and MSE is two orders of magnitude smaller.

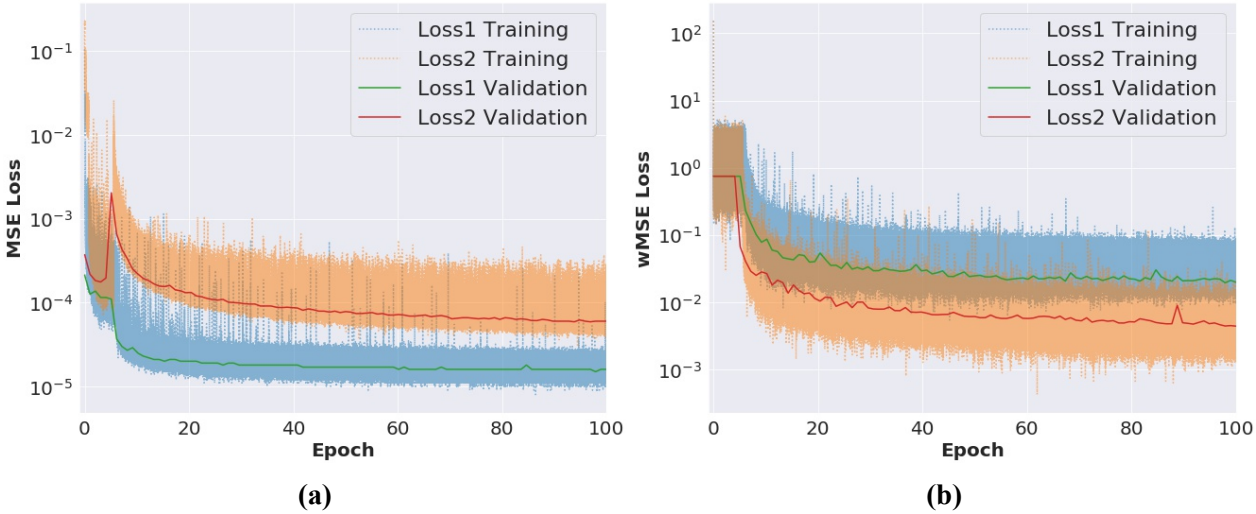

Fig. 7.3: The training and validation curves for (a) MSE and (b) wMSE over 100 epochs for the networks trained using Loss1 and Loss2 functions.

7.3.2 Decomposition

The two key contributors to the loss functions used in training of this CNN, MSE and wMSE, were quantified for each of the 10 test phantoms. The results are shown in Fig. 7.4. While the unweighted MSE function is reduced for all phantoms when the network is trained with Loss1, the Loss2 trained network results in a reduction of wMSE for 9 of the 10 test phantoms. Of those

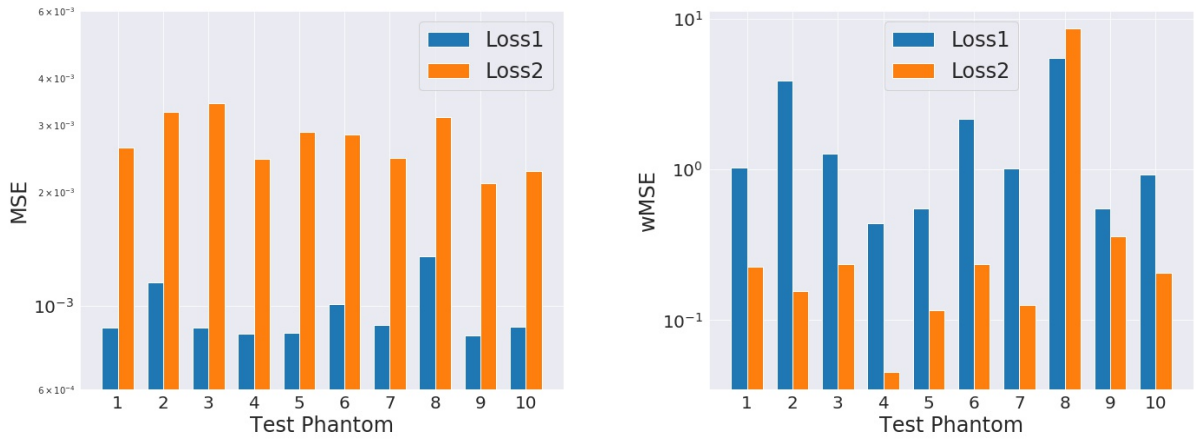

(a) **(b)**

Fig. 7.4: (a) MSE and (b) wMSE total cost across all 63 slices of the test phantoms. MSE levels differ by less than an order of magnitude between the network trained with Loss1 vs. Loss2. On the other hand, wMSE is reduced by over an order of magnitude for half of the phantoms when the network is trained with Loss2. Only phantom 8 shows a deviation from reduced wMSE when trained with Loss2.

9 phantoms, 5 have a reduction that is nearly an order of magnitude. The increase in phantom 8's wMSE is likely due to the presence of several low concentration ellipsoids, some of which overlap each other. As alone, these ellipsoids do little to change the contrast in the final image sets, the network has a particularly hard time determining with any accuracy from which materials the contrast comes. This can be seen in Fig. 7.7.

One might conclude that the MD-CNN-Loss1 network outperforms the MD-CNN-Loss2 network because MSE was minimized further by the former. However, since the contrast material channels have signals which are orders of magnitudes smaller than the air, water, and bone channels, errors in these channels have a very small effect on the overall MSE. The Loss1 columns of Figs. 7.5 – 7.7 demonstrate how MSE error alone can decompose the high concentration channels accurately, while performing increasingly poorly as the material concentrations decrease. Significant errors are shown in channels lack signal altogether. By adding the wMSE to the loss function (*i.e.* Loss2), increased accuracy is achieved in the low concentration contrast material channels (as seen in the Loss2 columns of Figs. 7.5 – 7.7). The MD-CNN-Loss2 network does not perform perfectly, as demonstrated in Fig. 7.7, where there is significant cross-talk between the true silver signal and the gold and iodine signals. This test phantom demonstrated decomposition errors which were largely absent from the other nine test phantoms. Fig. 7.8 provides the material basis

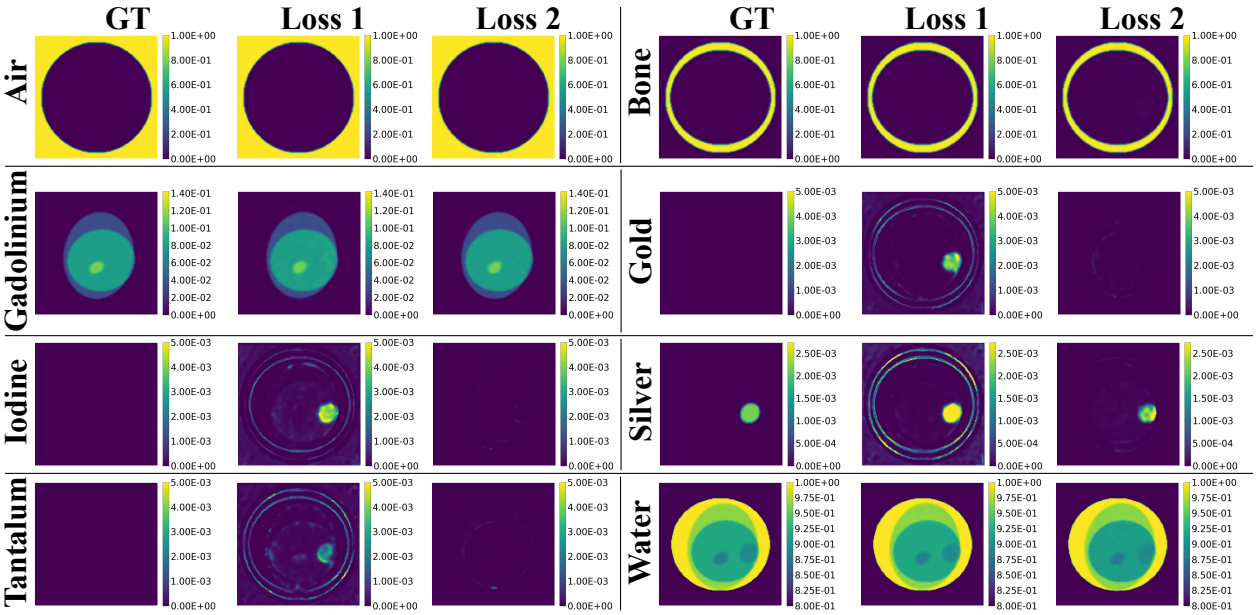

Fig. 7.5: The material basis ground-truth's for test phantom 4, slice 31 are shown next to the outputs from MD-CNN-Loss1 and MD-CNN-Loss2. Both loss functions do a good job at learning the high concentration material bases: air, water, and bone. MD-CNN-Loss2, however, is much better at distinguishing the K-edge material bases from the input image set.

plot profiles for further comparison of the decomposition results.

7.4 Discussion and Conclusion

As shown in this chapter, machine learning techniques such as CNNs may provide robust techniques for solving the highly ill-posed material decomposition problems of future photon-counting imaging applications. Due to their ability to measure several energy channels, the additional information should provide plenty of information about materials in an image to provide the basis for developing (1) novel K-edge material-based contrast and (2) molecular CT techniques which take advantage of the multiplexing opportunities that PCDs offer. Although, the MD-CNN was only demonstrated here with simulated datasets, further work to transfer the learning from simulation-trained networks to real-world data, where obtaining ground-truth measurements is extremely difficult, at best, and altogether impossible, at worst.

In addition to the transfer learning goals of future work, alternative loss functions and more complex architectures should be explored. Finding functions which can reduce random fluctuations in the MD result would provide better results for simulated data (and real-world data) which are

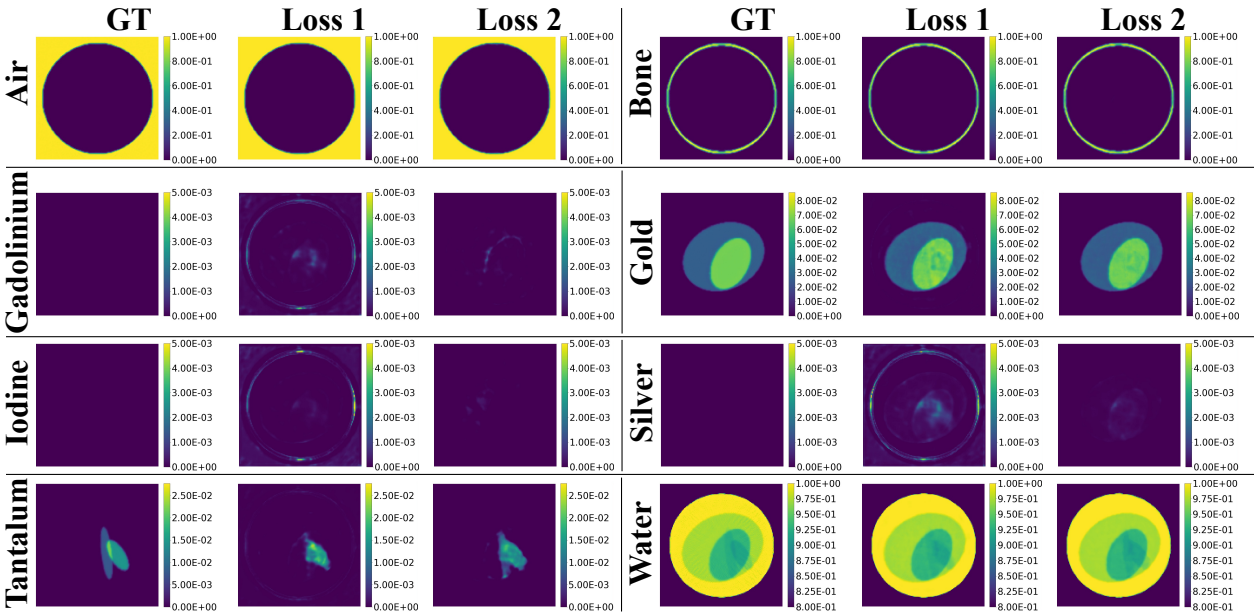

Fig. 7.6: The material basis ground-truth's for test phantom 5, slice 31 are shown next to the outputs from MD-CNN-Loss1 and MD-CNN-Loss2. Both loss functions do a good job at learning the high concentration material bases: air, water, and bone. MD-CNN-Loss2, however, is much better at distinguishing the K-edge material bases from the input image set.

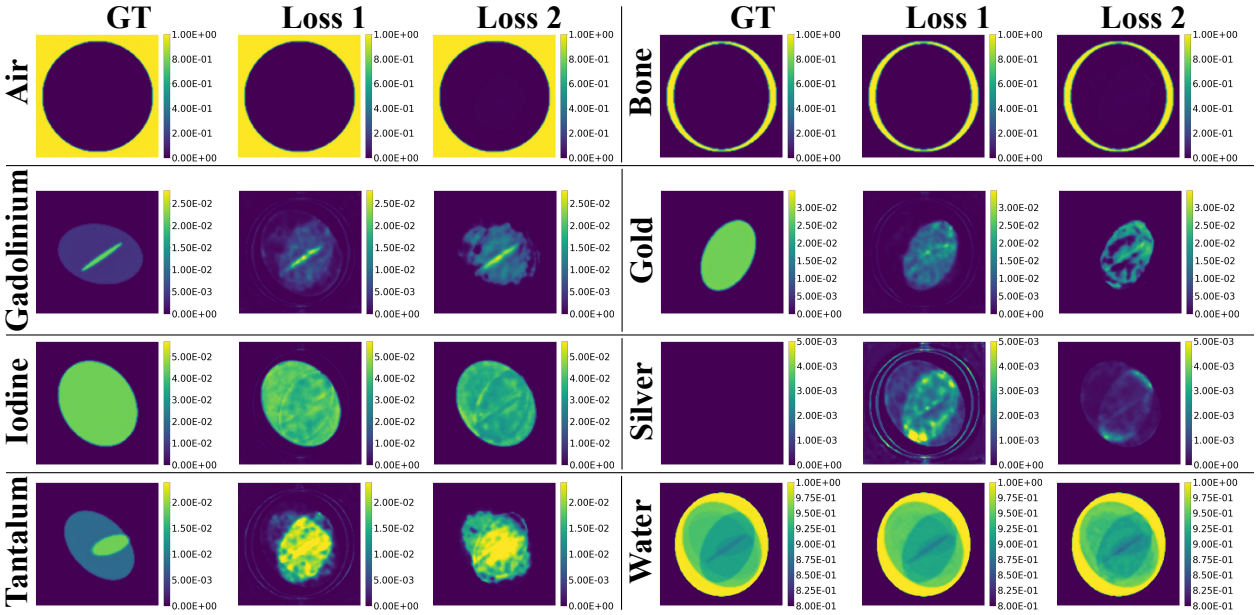

Fig. 7.7: The material basis ground-truth's for test phantom 8, slice 31 are shown next to the outputs from MD-CNN-Loss1 and MD-CNN-Loss2. Both loss functions do a good job at learning the high concentration material bases: air, water, and bone. The ground-truth concentrations for this phantom were particularly hard for the model to accurately predict.

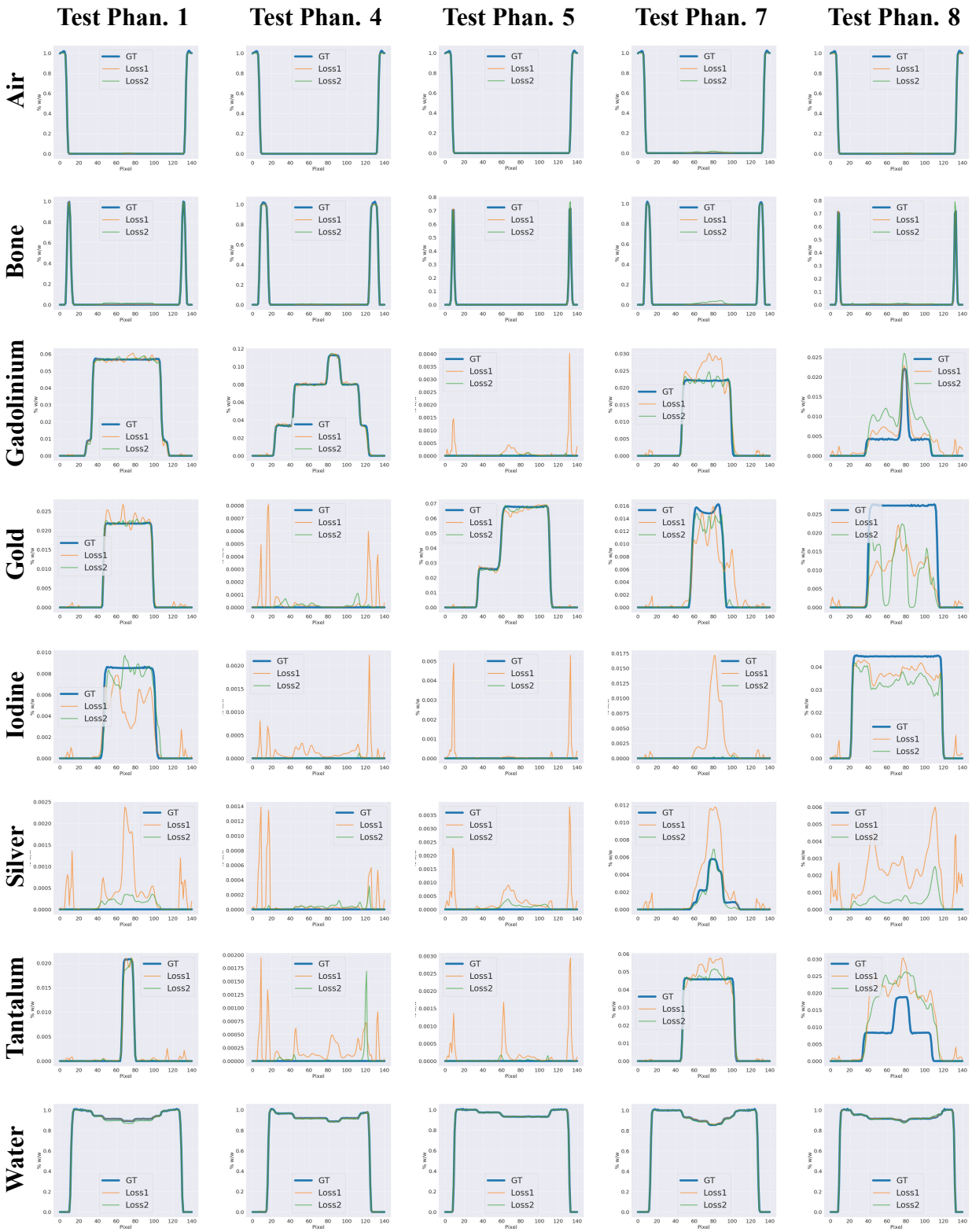

Fig. 7.8: Plot profiles across the central row of pixels of 5 of the 10 test phantoms (including those shown in previous figures) – ground-truth (blue), Loss1 (yellow), Loss2 (green).

piecewise-smooth (as in this study). Finally, better training data could conceivably be made where the ground-truth could never contain regions (and concentrations) which could not be distinguished in the energy bin reconstructions. It is hypothesized that because this dataset could have material concentrations below the perceivable limit present in the ground-truth, a greater effort is made by the network to find signal where there is none (*i.e.* making something out of nothing). This may be the cause of the ever-present signal fluctuations in zero-material channels seen in the results section. Despite these shortcomings, the network presented here provides a simple framework for accurately decomposing spectral data into separate material basis images with high accuracy.

Chapter 8
Summary

8.1 Contributions and Future Work

Each of the works presented in this thesis present a specific contribution toward deeper understanding, better model development, and better imaging outcomes from the MARS scanning pipeline (see Fig. 8.1). Specifically, interventions regarding the following workflow points are of interest to the lab, two of which were directly described in previous chapters (denoted by *):

1. Automatic system calibration (geometric)
2. *Pre-reconstruction data corrections
3. *Hardware configuration updates
4. Updated reconstruction methodology
5. *Post-reconstruction data analysis

In addition to the direct pipeline interventions, an overall system simulator was also developed. Chapter 2 describes the digital pipeline used to simulate the scanning geometry and physics provided by the MARS scanner. This software can be used as a teaching tool to help young imaging scientists better grasp the physics behind X-ray imaging in general as well as photon-counting detectors, specifically. In addition, the software tool can be used as a data generator for machine learning ground-truths during model development for network-based analysis and reconstruction methods. An updated detector model (*i.e.* CdTe to CZT, including of pulse pileup effects and charge-summing) could also provide similar enough data to enable transfer learning of the network models developed with simulation data to the real-world images. Finally, algorithms for automation of geometric calibration can be tested through the flexibility afforded when defining the detector configurations used in the simulation. To these ends, the simulation environment was used to generate test data for the methods described in several of the later chapters.

Chapter 3 describes pre-reconstruction data correction methods which, ideally, can be directly inserted into the existing MARS scanning pipeline. This intervention was shown to decrease

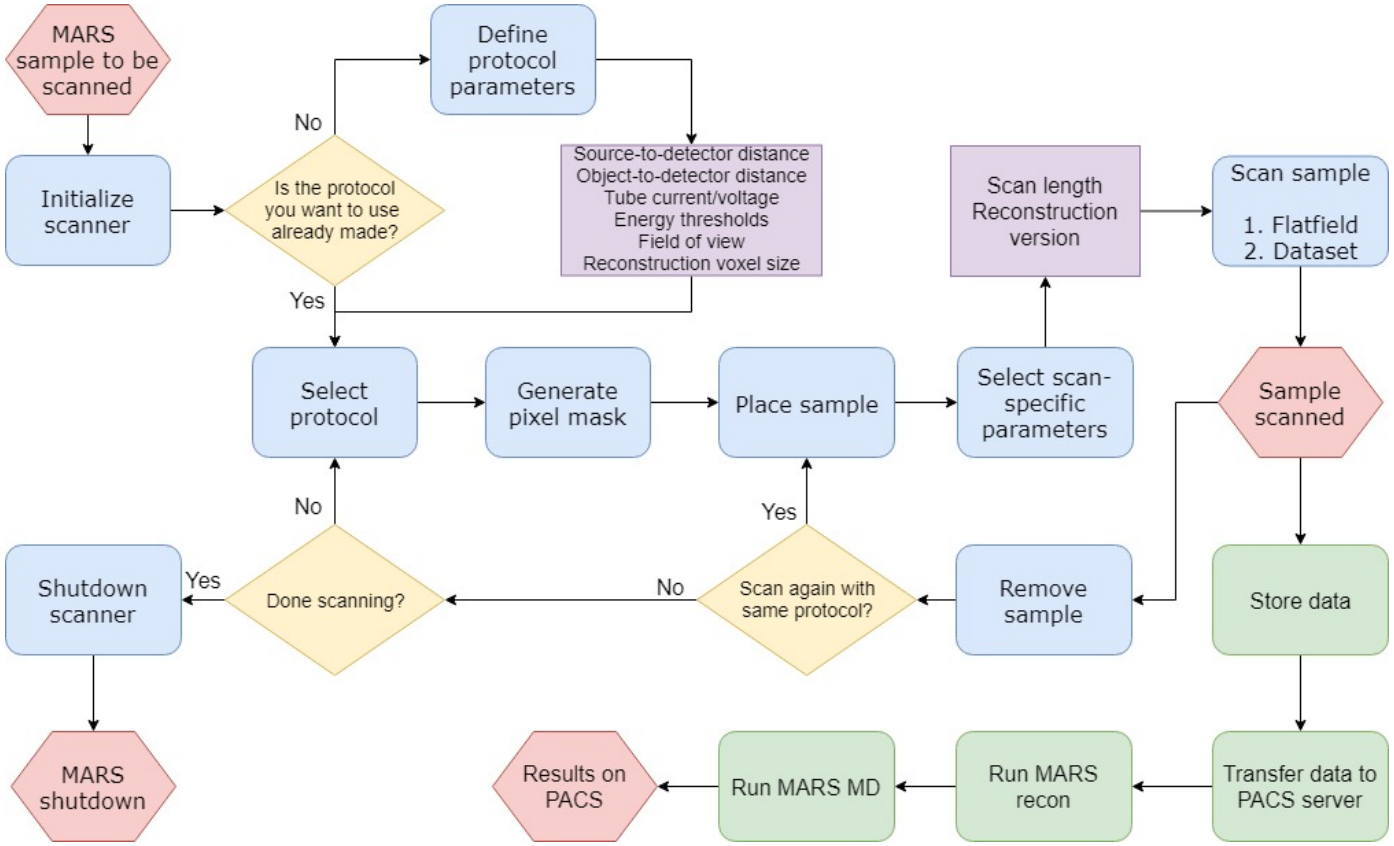

Fig. 8.1: The MARS scanning pipeline. The red hexagons represent start and endpoints in the user experience with the micro-CT scanner. The blue rectangles represent points along the pipeline which require human interaction, while the green rectangles are automated processes. The yellow diamonds are decision forks which dictate the workflow and the purple rectangles contain user-defined parameters.

the spatial non-uniformity seen in both the open-beam and single-frame projection data. The improvements shown should have a noticeable impact on the end reconstructions by reducing artifacts (*e.g.* ring artifacts) and ensuring accurate linear attenuation approximations. Efforts have been made to demonstrate the correction's effect on the reconstructions, but issues arise from the process of migrating the data from the PACS server to another PC where the MATLAB scripts are used to alter the data after which the data is migrated back to the PACS server. The MARS reconstruction software has troubles reading the header information of the altered images (even though they are largely unchanged) and the reconstructions cannot be completed. The solution to this problem is still under investigation.

The work Chapter 4 describes a relatively straightforward hardware update which could simultaneously act as a scatter guard and resolution-enhancing aperture. The scheme presented would require precise manufacturing of a heavy attenuating material, precision motors/placement of the aperture, and multiple scanning trajectories. The result from such a configuration would, in fact, be a higher resolution image. While the increased scan-time and dose needed for proposed aperture-encoding method may be of little consequence for studying phantoms or other inanimate objects, the use of such methods is unlikely to be incorporated into scanners/protocols for live organisms in either pre-clinical or clinical settings.

Despite the brief overview of reconstruction methods offered in Chapter 1, none of the work reported in this thesis was aimed at updating the MARS reconstruction methods. Very recent efforts toward a deep network-based, PRISM reconstruction method (2D) are premature and need much more work before they are discussed in any detail. Other lab members and collaborators have developed/are developing spectral reconstruction methods, however, most of these efforts still theoretical and have only been demonstrated for 2D datasets, not 3D conebeam data as output from the MARS scanner. A focused effort along this direction is needed to produce an alternative to the MARS reconstruction pipeline, not only as an effort to improve the technique, but also to allow for easy incorporation of the pre-processed projection data.

The last several chapters (Chapters 5 - 7) deal with post-processing of reconstructed images. Specifically, these chapters investigate the problem of material decomposition (MD) in the image domain. Chapters 5 and 6 use statistical methods and hypothesis testing to accurately separate, segment, and quantify materials. The methods require sets of known materials and known concentrations to pre-compute models for classification. Additionally, the segmentation method is limited to cases where the materials of interest do not mix and therefore the assumption that there is one

material in each image voxel is upheld. Despite these limitations, the methods presented show high classification and quantification accuracy even when there are several more material groups than measurements. The methods were demonstrated on both real and simulated datasets. Chapter 7 takes an altogether to the problem of MD through the application of a CNN. The simulated datasets are particularly useful for developing this network given that one of reconstruction the outputs is the materials basis images which can be used as ground-truth during the training. The network tested was shown to be accurate for most combinations of contrast materials (up to 8 material bases), although misclassifications were seen in image sets containing regions of very low contrast material. This shortcoming is especially important to consider in the clinical context. Since such high concentrations are needed (*e.g.* $> mg/mL$) to accurately identify and quantify the materials in these test phantoms, the translation of these methods to the clinic is limited until high efficiency detectors are developed to ensure accurate molecular imaging capabilities at lower, more clinically relevant concentrations.

A primary goal of future work in this area should be to develop an altogether separate data pipeline that parallels the MARS data pipeline. This is necessary to provide the framework and lab architecture which would allow for new researchers to provide improvements all along the analysis pipeline. Such a framework could allow for relatively easy incorporation of corrections algorithms, new reconstruction methods, and post-processing algorithms. The work presented in this thesis is fragmented largely as a result of the lack of such a "plug-and-play" framework. Despite the fragmented appearance, the methods and results described in the thesis, if unified, should improve overall image quality and post-processing outcomes. Of course, much work can still be conceived in areas such as automatic scanner calibration, long-distance fluorescence and pulse pileup corrections, and transfer learning with MD networks.

Besides improvements in the imaging chain, the PCD scanning technology lends itself to future research in areas such a material science, multiplexed contrast administration, disease targeting, etc. Many aspects of this type of research moves beyond the scope of the imaging physics and data analysis, at least during the development of new contrast materials, delivery mechanisms, and appropriate animal models. Spectral imaging with PCDs provide a unique and powerful tool to analyze such experiments and may one day be a powerful clinical tool for diagnosing disease states in humans as well as monitoring treatment options. The methods described in this thesis are modest contribution to that future vision.

References

[1] P. Ronan. (2007, Aug.) EM spectrum. [Online]. Available: https://en.wikipedia.org/wiki/File:EM_spectrum.svg (Accessed: Mar. 12, 2019).

[2] W. Röntgen. (1895, Dec.) Hand mit Ringen. [Online]. Available: https://commons.wikimedia.org/wiki/File:First_medical_X-ray_by_Wilhelm_R%C3%B6ntgen_of_his_wife_Anna_Bertha_Ludwig%27s_hand_-_18951222.gif (Accessed: Mar. 12, 2019).

[3] T. T. Truong, M. K. Nguyen, and H. Zaidi, "The mathematical foundations of 3D Compton scatter emission imaging," *Int. J. Biomed. Imaging*, vol. 2007, Feb. 2007. doi:10.1155/2007/92780. [Online]. Available: https://www.hindawi.com/journals/ijbi/2007/092780/cta/ (Accessed: Mar. 13, 2019).

[4] M. Nikl, "Scintillation detectors for X-rays," *Measu. Sci. and Technol.*, vol. 17, no. 4, pp. R37–R54, Feb. 2006. doi:10.1088/0957-0233/17/4/r01. [Online]. Available: http://iopscience.iop.org/article/10.1088/0957-0233/17/4/R01/pdf (Accessed: Mar. 13, 2019).

[5] M. Overdick *et al.*, "Status of direct conversion detectors for medical imaging with X-rays," *IEEE Trans. Nucl. Sci.*, vol. 56, no. 4, pp. 1800–1809, Aug. 2009. doi:10.1109/tns.2009.2025041

[6] R. Brooks and G. Di Chiro, "Beam hardening in X-ray reconstructive tomography," *Phys. Med. Biol.*, vol. 21, no. 3, pp. 390–398, May 1976.

[7] F. Boas and D. Fleischmann, "CT artifacts: Causes and reduction techniques," *Imaging in Medicine*, vol. 4, no. 2, pp. 229–240, Apr. 2012. [Online]. Available: https://www.openaccessjournals.com/articles/ct-artifacts-causes-and-reduction-techniques.pdf (Accessed: Mar. 13, 2019).

[8] L. Gjesteby *et al.*, "Metal artifact reduction in CT: Where are we after four decades?" *IEEE Access*, vol. 4, pp. 5826–5849, Sep. 2016. doi:10.1109/access.2016.2608621

[9] L. Ananthakrishnan *et al.*, “Dual-layer spectral detector CT: Non-inferiority assessment compared to dual-source dual-energy CT in discriminating uric acid from non-uric acid renal stones ex vivo,” *Abdominal Radiol.*, vol. 43, no. 11, pp. 3075–3081, Nov. 2018. doi:10.1007/s00261-018-1589-x. [Online]. Available: https://www.ncbi.nlm.nih.gov/pubmed/29626256 (Accessed: Mar. 12, 2019).

[10] Y. Zhao and M. Li, “Iterative beam hardening correction for multi-material objects,” *PLoS One*, vol. 10, no. 12, Dec. 2015. doi:10.1371/journal.pone.0144607. [Online]. Available: https://www.ncbi.nlm.nih.gov/pubmed/26659554 (Accessed: Mar. 13, 2019).

[11] P. M. Shikhaliev, T. Xu, and S. Molloi, “Photon counting computed tomography: Concept and initial results,” *Med. Phys.*, vol. 32, no. 2, pp. 427–436, Feb. 2005. doi:10.1118/1.1854779. [Online]. Available: https://www.ncbi.nlm.nih.gov/pubmed/15789589 (Accessed: Mar. 13, 2019).

[12] W. Barber *et al.*, “Characterization of a novel photon counting detector for clinical CT: Count rate, energy resolution, and noise performance.” in *Med. Imaging 2009: Phys. Med. Imaging*, vol. 7258, Mar. 2009. doi:10.1117/12.813915

[13] A. Wang, D. Harrison, V. Lobastov, and J. Tkaczyk, “Pulse pileup statistics for energy discriminating photon counting X-ray detectors,” *Med. Phys.*, vol. 38, no. 7, pp. 4265–4275, July 2011. doi:10.1118/1.3592932

[14] J. Silkwood, K. Matthews, and P. Shikhaliev, “Photon counting spectral breast CT: Effect of adaptive filtration on CT numbers, noise, and contrast to noise ratio,” *Med. Phys.*, vol. 40, no. 5, May 2013. doi:10.1118/1.4800504

[15] L. Boussel *et al.*, “Photon counting spectral CT component analysis of coronary artery atherosclerotic plaque samples,” *Br. J. Radiol.*, vol. 87, no. 1040, Aug. 2014. doi:10.1259/bjr.20130798. [Online]. Available: https://www.ncbi.nlm.nih.gov/pmc/articles/PMC4112393/pdf/bjr.20130798.pdf (Accessed: Mar. 13, 2019).

[16] D. P. Cormode *et al.*, “Multicolor spectral photon-counting computed tomography: In vivo dual contrast imaging with a high count rate scanner,” *Sci. Rep.*, vol. 7, no. 1, July 2017. doi:10.1038/s41598-017-04659-9. [Online]. Available: https:

//www.ncbi.nlm.nih.gov/pmc/articles/PMC5500581/pdf/41598_2017_Article_4659.pdf (Accessed: Mar. 13, 2019).

[17] M. Getzin *et al.*, “Increased separability of K-edge nanoparticles by photon-counting detectors for spectral micro-CT,” *J. Xray Sci. Technol.*, vol. 26, no. 5, pp. 707–726, Sep. 2018. doi:10.3233/XST-18382. [Online]. Available: https://content.iospress.com/articles/journal-of-X-ray-science-and-technology/xst18382 (Accessed: Mar. 13, 2019).

[18] P. L. Rajbhandary and N. J. Pelc, “Statistical bias in material decomposition in low photon statistics region,” in *Med. Imaging 2015: Phys. Med. Imaging*, C. Hoeschen, D. Kontos, and T. G. Flohr, Eds., vol. 9412, Mar. 2015. doi:10.1117/12.2081326

[19] M. Persson and F. Grönberg, “Bias–variance tradeoff in anticorrelated noise reduction for spectral CT,” *Med. Phys.*, vol. 44, no. 9, pp. e242–e254, Sep. 2017. doi:10.1002/mp.12322

[20] P. M. Shikhaliev, “Beam hardening artefacts in computed tomography with photon counting, charge integrating and energy weighting detectors: A simulation study,” *Phys. Med. Biol.*, vol. 50, no. 24, pp. 5813–5827, Nov. 2005. doi:10.1088/0031-9155/50/24/004

[21] R. Bellwied *et al.*, “Two dimensional studies of dynamics of electron clouds in silicon drift detectors,” in *1998 IEEE Nucl. Sci. Symp. Conf. Rec. 1998 IEEE Nucl. Sci. Symp. and Med. Imaging Conf.*, vol. 1, Nov. 1998, pp. 672–676. doi:10.1109/NSSMIC.1998.775227

[22] B. Donmez *et al.*, “Further studies of single-sided charge-sharing CZT strip detectors,” in *Hard X-ray and Gamma-Ray Detect. Phys. VII*, R. B. James, Ed., vol. 5922, Sep. 2005. doi:10.1117/12.617297

[23] K. Taguchi, K. Stierstorfer, C. Polster, O. Lee, and S. Kappler, “Spatio-energetic cross-talk in photon counting detectors: Numerical detector model (PcTK) and workflow for CT image quality assessment.” *Med. Phys.*, vol. 45, no. 5, pp. 1985–1998, Apr. 2018. doi:10.1002/mp.12863. [Online]. Available: https://aapm.onlinelibrary.wiley.com/doi/pdf/10.1002/mp.12863 (Accessed: Mar. 13, 2019).

[24] K. Taguchi and J. Iwanczyk, “Vision 20/20: Single photon counting X-ray detectors in medical imaging,” *Med. Phys.*, vol. 40, no. 10, 2013. doi:10.1118/1.4820371

[25] K. Taguchi, E. C. Frey, X. Wang, J. S. Iwanczyk, and W. C. Barber, "An analytical model of the effects of pulse pileup on the energy spectrum recorded by energy resolved photon counting X-ray detectors," *Med. Phys.*, vol. 37, no. 8, pp. 3957–3969, Aug. 2010. doi:10.1118/1.3429056. [Online]. Available: https://www.ncbi.nlm.nih.gov/pubmed/20879558 (Accessed: Mar. 13, 2019).

[26] K. Taguchi, C. Polster, O. Lee, K. Stierstorfer, and S. Kappler, "Spatio-energetic cross talk in photon counting detectors: Detector model and correlated Poisson data generator." *Med. Phys.*, vol. 43, no. 12, pp. 6386–6404, Nov. 2016. doi:10.1118/1.4966699. [Online]. Available: https://aapm.onlinelibrary.wiley.com/doi/pdf/10.1118/1.4966699 (Accessed: Mar. 13, 2019).

[27] T. R. Melzer *et al.*, "Spectroscopic biomedical imaging with the Medipix2 detector," *Australas. Phys. Eng. Sci. Med.*, vol. 31, no. 4, pp. 300–306, Dec. 2008. [Online]. Available: https://www.ncbi.nlm.nih.gov/pubmed/19239056 (Accessed: Mar. 13, 2019).

[28] M. F. Walsh *et al.*, "First CT using Medipix3 and the MARS-CT-3 spectral scanner," *J. Instrum.*, vol. 6, Jan. 2011. doi:10.1088/1748-0221/6/01/C01095

[29] H. Yu *et al.*, "Medipix-based spectral micro-CT," *CT Li Lun Yu Ying Yong Yan Jiu*, vol. 21, no. 4, pp. 583–600, Dec. 2012. [Online]. Available: https://www.ncbi.nlm.nih.gov/pmc/articles/PMC3815543/pdf/nihms509578.pdf (Accessed: Mar. 13, 2019).

[30] D. Pennicard, R. Ballabriga, X. Llopart, M. Campbell, and H. Graafsma, "Simulations of charge summing and threshold dispersion effects in Medipix3," *Nucl. Instrum. and Methods in Phys. Res. Sect. A: Accel., Spectrometers, Detect. and Associated Equip.*, vol. 636, no. 1, pp. 74–81, Apr. 2011. doi:10.1016/j.nima.2011.01.124

[31] A. Kak and M. Slaney, "Algorithms for reconstruction with non-diffracting sources," in *Principles of Computerized Tomographic Imaging*. Hoboken, NJ, USA: Wiley - IEEE Press, 1988, ch. 3, pp. 49–112.

[32] A. Rosenfeld and A. Kak, "Reconstruction," in *Digital Picture Processing*. Orlando, FL, USA: Academic Press Inc., 1982, ch. 8.

[33] M. McCann and M. Unser, “Algorithms for biomedical image reconstruction,” Jan. 2019, arXiv:1901.03565. [Online]. Available: https://arxiv.org/abs/1901.03565 (Accessed: Mar. 13, 2019).

[34] D. Kazantsev and V. Pickalov, “New iterative reconstruction methods for fan-beam tomography,” *Inverse Probl. in Sci. and Eng.*, vol. 26, no. 6, pp. 773–791, June 2017. doi:10.1080/17415977.2017.1340946

[35] B. Wang, H. Liu, S. Zhao, and G. Wang, “Feldkamp-type image reconstruction from equiangular data,” *J. of X-ray Sci. and Technol.*, vol. 9, no. 3,4, pp. 113–120, Jan. 2001.

[36] H. Yu and G. Wang, “Feldkamp-type VOI reconstruction from super-short-scan cone-beam data,” *Med. Phys.*, vol. 31, no. 6, pp. 1357–1362, June 2004. doi:10.1118/1.1739298. [Online]. Available: https://www.ncbi.nlm.nih.gov/pubmed/15259639 (Accessed: Mar. 13, 2019).

[37] B. Chen, K. Xiang, Z. Gong, J. Wang, and S. Tan, “Statistical iterative CBCT reconstruction based on neural network,” *IEEE Trans. Med. Imaging*, vol. 37, no. 6, pp. 1511–1521, June 2018. doi:10.1109/TMI.2018.2829896. [Online]. Available: https://www.ncbi.nlm.nih.gov/pubmed/29870378 (Accessed: Mar. 13, 2019).

[38] R. Gordon, R. Bender, and G. Herman, “Algebraic reconstruction techniques (ART) for three-dimensional electron microscopy and X-ray photography,” *J. Theor. Biol.*, vol. 29, no. 3, pp. 471–481, Dec. 1970.

[39] A. Andersen, “Simultaneous algebraic reconstruction technique (SART): A superior implementation of the ART algorithm,” *Ultrason. Imaging*, vol. 6, no. 1, pp. 81–94, Jan. 1984. doi:10.1016/0161-7346(84)90008-7

[40] R. E. Alvarez and A. Macovski, “Energy-selective reconstructions in X-ray computerized tomography,” *Phys. Med. Biol.*, vol. 21, no. 5, pp. 733–744, Sep. 1976.

[41] Q. Xu, H. Yu, X. Mou, L. Zhang, J. Hsieh, and G. Wang, “Low-dose X-ray CT reconstruction via dictionary learning,” *IEEE Trans. Med. Imaging*, vol. 31, no. 9, pp. 1682–1697, Sep. 2012. doi:10.1109/TMI.2012.2195669. [Online]. Available: https://www.ncbi.nlm.nih.gov/pubmed/22542666 (Accessed: Mar. 13, 2019).

[42] L. Xie *et al.*, “An effective CUDA parallelization of projection in iterative tomography reconstruction,” *PLoS One*, vol. 10, no. 11, Nov. 2015. doi:10.1371/journal.pone.0142184. [Online]. Available: https://www.ncbi.nlm.nih.gov/pmc/articles/PMC4664243/pdf/pone.0142184.pdf (Accessed: Mar. 13, 2019).

[43] B. Heismann and M. Balda, “Quantitative image-based spectral reconstruction for computed tomography,” *Med. Phys.*, vol. 36, no. 10, pp. 4471–4485, Oct. 2009. doi:10.1118/1.3213534. [Online]. Available: http://www.ncbi.nlm.nih.gov/pubmed/19928078 (Accessed: Mar. 13, 2019).

[44] Q. Xu *et al.*, “Image reconstruction for hybrid true-color micro-CT,” *IEEE Trans. on Biomed. Eng.*, vol. 59, no. 6, pp. 1711–1719, June 2012. doi:10.1109/Tbme.2012.2192119

[45] D. P. Clark and C. T. Badea, “Hybrid spectral CT reconstruction,” *PLoS One*, vol. 12, no. 7, July 2017. doi:10.1371/journal.pone.0180324. [Online]. Available: https://www.ncbi.nlm.nih.gov/pubmed/28683124 (Accessed: Mar. 13, 2019).

[46] S. Niu *et al.*, “Iterative reconstruction for photon-counting CT using prior image constrained total generalized variation,” *Comput. Biol. Med.*, vol. 103, pp. 167–182, Dec. 2018. doi:10.1016/j.compbiomed.2018.10.022. [Online]. Available: https://www.ncbi.nlm.nih.gov/pubmed/30384175 (Accessed: Mar. 13, 2019).

[47] M. Salehjahromi, Y. Zhang, and H. Yu, “Comparison study of regularizations in spectral computed tomography reconstruction,” *Sens. Imaging*, vol. 19, no. 1, Dec. 2018. doi:10.1007/s11220-018-0200-4

[48] W. Wu, Y. Zhang, Q. Wang, F. Liu, F. Luo, and H. Yu, “Spatial-spectral cube matching frame for spectral CT reconstruction,” *Inverse Probl.*, vol. 34, no. 10, Aug. 2018. doi:10.1088/1361-6420/aad67b

[49] W. Wu, Q. Wang, F. Liu, Y. Zhu, and Y. H., “Block matching frame based material reconstruction for spectral CT,” Oct. 2018, arXiv:1810:10346. [Online]. Available: https://arxiv.org/abs/1810.10346 (Accessed: Mar. 13, 2019).

[50] W. Wu, Y. Zhang, Q. Wang, F. Liu, P. Chen, and H. Yu, “Low-dose spectral CT reconstruction using image gradient ℓ0–norm and tensor dictionary,” *Appl. Math. Model.*, vol. 63, pp. 538–557, Nov. 2018.

[51] W. Wu, F. Liu, Y. Zhang, Q. Wang, and H. Yu, “Non-local low-rank cube-based tensor factorization for spectral CT reconstruction,” *IEEE Trans. on Med. Imaging*, vol. 38, no. 4, pp. 1079–1093, Oct. 2018. doi:10.1109/tmi.2018.2878226

[52] Z. Zhou, R. Xin, S. Guan, J. Li, and J. Tu, “Investigation of maximum a posteriori probability expectation-maximization for image-based weighting spectral X-ray CT image reconstruction,” *J. Xray Sci. Technol.*, vol. 26, no. 5, pp. 853–864, Sep. 2018. doi:10.3233/XST-180396. [Online]. Available: https://www.ncbi.nlm.nih.gov/pubmed/30124464 (Accessed: Mar. 13, 2019).

[53] S. Niu, Z. Bian, D. Zeng, G. Yu, J. Ma, and J. Wang, “Total image constrained diffusion tensor for spectral computed tomography reconstruction,” *Appl. Math. Model.*, vol. 68, pp. 487–508, Apr. 2019. doi:10.1016/j.apm.2018.11.020

[54] H. Lee, J. Lee, H. Kim, B. Cho, and S. Cho, “Deep-neural-network based sinogram synthesis for sparse-view CT image reconstruction,” Mar 2018, arXiv:1803.00694. [Online]. Available: https://arxiv.org/abs/1803.00694 (Accessed: Mar. 13, 2019).

[55] H. Zhang, J. Wang, D. Zeng, X. Tao, and J. Ma, “Regularization strategies in statistical image reconstruction of low-dose X-ray CT: A review,” *Med. Phys.*, vol. 45, no. 10, pp. e886–e907, Oct. 2018. doi:10.1002/mp.13123

[56] H. Chen *et al.*, “LEARN: Learned experts’ assessment-based reconstruction network for sparse-data CT,” *IEEE Trans. Med. Imaging*, vol. 37, no. 6, pp. 1333–1347, June 2018. doi:10.1109/TMI.2018.2805692. [Online]. Available: https://www.ncbi.nlm.nih.gov/pubmed/29870363 (Accessed: Mar. 14, 2019).

[57] H. Gao, H. Yu, S. Osher, and G. Wang, “Multi-energy CT based on a prior rank, intensity and sparsity model (PRISM),” *Inverse Probl.*, vol. 27, no. 11, Nov. 2011. doi:10.1088/0266-5611/27/11/115012. [Online]. Available: https://www.ncbi.nlm.nih.gov/pubmed/22223929 (Accessed: Mar. 14, 2019).

[58] E. Roessl and R. Proksa, “K-edge imaging in X-ray computed tomography using multi-bin photon counting detectors,” *Phys. Med. Biol.*, vol. 52, no. 15, pp. 4679–4696, Aug. 2007. doi:10.1088/0031-9155/52/15/020. [Online]. Available: http://iopscience.iop.org/article/10.1088/0031-9155/52/15/020/pdf (Accessed: Mar. 14, 2019).

[59] J. P. Schlomka *et al.*, “Experimental feasibility of multi-energy photon-counting K-edge imaging in pre-clinical computed tomography,” *Phys. Med. Biol.*, vol. 53, no. 15, pp. 4031–4047, Aug. 2008. doi:10.1088/0031-9155/53/15/002. [Online]. Available: http://iopscience.iop.org/article/10.1088/0031-9155/53/15/002/pdf (Accessed: Mar. 14, 2019).

[60] H. Q. Le and S. Molloi, “Least squares parameter estimation methods for material decomposition with energy discriminating detectors,” *Med. Phys.*, vol. 38, no. 1, pp. 245–255, Jan. 2011. doi:10.1118/1.3525840. [Online]. Available: https://www.ncbi.nlm.nih.gov/pubmed/21361193 (Accessed: Mar. 14, 2019).

[61] Y. Yamashita *et al.*, “Measurement of effective atomic numbers using energy-resolved computed tomography,” *J Nucl. Sci. Technol.*, vol. 51, no. 10, pp. 1256–1263, Oct. 2014. doi:10.1080/00223131.2014.919881

[62] S. Si-Mohamed *et al.*, “Multicolour imaging with spectral photon-counting CT: A phantom study,” *Eur. Radiol. Exp.*, vol. 2, no. 1, Oct. 2018. doi:10.1186/s41747-018-0063-4. [Online]. Available: https://www.ncbi.nlm.nih.gov/pubmed/30327898 (Accessed: Mar. 14, 2019).

[63] S. Si-Mohamed *et al.*, “Improved peritoneal cavity and abdominal organ imaging using a biphasic contrast agent protocol and spectral photon counting computed tomography K-edge imaging,” *Invest. Radiol.*, vol. 53, no. 10, pp. 629–639, Oct. 2018. doi:10.1097/RLI.0000000000000483. [Online]. Available: https://www.ncbi.nlm.nih.gov/pubmed/29794948 (Accessed: Mar. 14, 2019).

[64] C. Bateman *et al.*, “Segmentation enhances material analysis in multi-energy CT: A simulation study.” in *2013 28th Int. Conf. Image Vision Comput. New Zealand*, Nov. 2013, pp. 190–195.

[65] C. Bateman *et al.*, “MARS-MD: Rejection based image domain material decomposition.” *J. Instrum.*, vol. 13, no. 05, May 2018. doi:10.1088/1748-0221/13/05/P05020

[66] S. Tao, K. Rajendran, C. H. McCollough, and S. Leng, “Material decomposition with prior knowledge aware iterative denoising (MD-PKAID),” *Phys. Med. Biol.*, vol. 63, no. 19, Sep. 2018. doi:10.1088/1361-6560/aadc90. [Online]. Available: https://www.ncbi.nlm.nih.gov/pubmed/30136655 (Accessed: Mar. 14, 2018).

[67] B. Xie *et al.*, “Material decomposition in X-ray spectral CT using multiple constraints in image domain,” *J. Nondestruct. Eval.*, vol. 38, no. 1, Mar. 2019. doi:10.1007/s10921-018-0551-8

[68] W. Zhang *et al.*, “Image domain dual material decomposition for dual-energy CT using butterfly network,” Apr. 2018, arXiv:1804.01685

[69] Z. Chen and L. Li, “Robust multimaterial decomposition of spectral CT using convolutional neural networks,” *Opt. Eng.*, vol. 58, no. 1, Jan. 2019. doi:10.1117/1.oe.58.1.013104

[70] H. Q. Le and S. Molloi, “Segmentation and quantification of materials with energy discriminating computed tomography: A phantom study,” *Med. Phys.*, vol. 38, no. 1, pp. 228–237, Jan. 2011. doi:10.1118/1.3525835. [Online]. Available: https://www.ncbi.nlm.nih.gov/pubmed/21361191 (Accessed: Mar. 14, 2019).

[71] M. Persson, P. Rajbhandary, and N. Pelc, “A framework for performance characterization of energy-resolving photon-counting detectors,” *Med. Phys.*, vol. 45, no. 11, pp. 4897–4915, Nov. 2018.

[72] M. Persson, P. L. Rajbhandary, and N. J. Pelc, “Generalized linear-systems framework for performance assessment of energy-resolving photon-counting detectors,” in *Med. Imaging 2018: Phys. Med. Imaging*, T. Gilat Schmidt, J. Y. Lo, and G.-H. Chen, Eds., vol. 10573, Mar. 2018. doi:10.1117/12.2293402

[73] P. L. Rajbhandary and N. J. Pelc, “Effect of electronic noise and lowest energy threshold selection in photon counting detectors,” in *Med. Imaging 2018: Phys. Med. Imaging*, T. Gilat Schmidt, J. Y. Lo, and G.-H. Chen, Eds., vol. 10573, Mar. 2018. doi:10.1117/12.2293929

[74] S. Tabakov, “Digital radiography image parameters SNR, MTF, NPS, NEQ, DQE,” Sep. 13 - Oct. 1 2010, [PowerPoint Slides]. [Online]. Available: http://indico.ictp.it/event/a09166/session/23/contribution/15/material/0/0.pdf (Accessed: Mar. 14, 2019).

[75] J. M. Boone, “Image quality parameters and their measurement,” Sep. 2013, [PowerPoint Slides]. [Online]. Available: http://iupesm.ifmbe.org/wp-content/uploads/2014/08/03Boone_IQ.pdf (Accessed: Mar. 14, 2019).

[76] J. Baek and N. J. Pelc, “The noise power spectrum in CT with direct fan beam reconstruction,” *Med. Phys.*, vol. 37, no. 5, pp. 2074–2081, May 2010. doi:10.1118/1.3378673. [Online]. Available: https://www.ncbi.nlm.nih.gov/pubmed/20527540 (Accessed: Mar. 25, 2019).

[77] D. Kazantsev, V. Pickalov, S. Nagella, E. Pasca, and P. J. Withers, “TomoPhantom, a software package to generate 2D–4D analytical phantoms for CT image reconstruction algorithm benchmarks,” *SoftwareX*, vol. 7, pp. 150–155, June 2018. doi:10.1016/j.softx.2018.05.003

[78] W. van Aarle *et al.*, “The ASTRA toolbox: A platform for advanced algorithm development in electron tomography,” *Ultramicroscopy*, vol. 157, pp. 35–47, Oct. 2015. doi:10.1016/j.ultramic.2015.05.002

[79] W. van Aarle *et al.*, “Fast and flexible X-ray tomography using the ASTRA toolbox,” *Opt. Express*, vol. 24, no. 22, pp. 25 129–25 147, Oct. 2016. doi:10.1364/Oe.24.025129. [Online]. Available: https://www.osapublishing.org/oe/abstract.cfm?uri=oe-24-22-25129 (Accessed: Mar. 14, 2019).

[80] F. Jacobs, E. Sundermann, B. De Sutter, M. Christiaens, and I. Lemahieu, “A fast algorithm to calculate the exact radiological path through a pixel or voxel space,” *J. Comput. and Inf. Technol.*, vol. 6, no. 1, pp. 89–94, Mar. 1998.

[81] H. Q. Le, J. Ducote, and S. Molloi, “Radiation dose reduction using a CdZnTe-based computed tomography system: Comparison to flat-panel detectors,” *Med. Phys.*, vol. 37, no. 3, pp. 1225–1236, Mar. 2010.

[82] H. Ding and S. Molloi, “Image-based spectral distortion correction for photon-counting X-ray detectors,” *Med. Phys.*, vol. 39, no. 4, pp. 1864–1876, Apr. 2012. doi:10.1118/1.3693056

[83] D. Rundle, “Count correction in a photon counting imaging system.” US Patent 8 664 616B2, Mar. 4, 2014. [Online]. Available: https://patents.google.com/patent/US8664616B2/en?oq=8664616 (Accessed: Mar. 14, 2019).

[84] J. Jakubek, “Semiconductor pixel detectors and their applications in life sciences,” *J. Instrum.*, vol. 4, no. 03, Mar. 2009. doi:10.1088/1748-0221/4/03/P03013

[85] R. N. Cahn, B. Cederstrom, M. Danielsson, A. Hall, M. Lundqvist, and D. Nygren, “Detective quantum efficiency dependence on X-ray energy weighting in mammography,” *Med. Phys.*, vol. 26, no. 12, pp. 2680–2683, Dec. 1999. doi:doi 10.1118/1.598807

[86] J. Giersch, D. Niederlohner, and G. Anton, “The influence of energy weighting on X-ray imaging quality,” *Nucl. Instrum. and Methods in Phys. Res. Sect. A: Accel. Spect. Detect. and Assoc. Equip.*, vol. 531, no. 1-2, pp. 68–74, Sep. 2004. doi:10.1016/j.nima.2004.05.076

[87] R. K. Swank, “Calculation of modulation transfer-functions of X-ray fluorescent screens,” *Appl. Opt.*, vol. 12, no. 8, pp. 1865–1870, Aug. 1973. doi:doi 10.1364/Ao.12.001865

[88] N. G. Anderson *et al.*, “Spectroscopic (multi-energy) CT distinguishes iodine and barium contrast material in mice,” *Eur. Radiol.*, vol. 20, no. 9, pp. 2126–2134, Sep. 2010. doi:10.1007/s00330-010-1768-9. [Online]. Available: https://www.ncbi.nlm.nih.gov/pubmed/20309554 (Accessed: Mar. 14, 2019).

[89] J. F. Hainfeld, D. N. Slatkin, T. M. Focella, and H. M. Smilowitz, “Gold nanoparticles: A new X-ray contrast agent,” *Brit. J. Radiol.*, vol. 79, no. 939, pp. 248–253, Mar. 2006. doi:10.1259/bjr/13169882

[90] D. B. Akolekar, G. Foran, and S. K. Bhargava, “X-ray absorption spectroscopic studies on gold nanoparticles in mesoporous and microporous materials,” *J. Synchrotron Radiat.*, vol. 11, pp. 284–290, May 2004. doi:10.1107/S0909049504001694

[91] Z. J. Wang, L. N. Wu, and W. Cai, “Size-tunable synthesis of monodisperse water-soluble gold nanoparticles with high X-ray attenuation,” *Chem. Eur. J.*, vol. 16, no. 5, pp. 1459–1463, Feb. 2010. doi:10.1002/chem.200902463

[92] C. J. Xu, G. A. Tung, and S. H. Sun, “Size and concentration effect of gold nanoparticles on X-ray attenuation as measured on computed tomography,” *Chem. Mater.*, vol. 20, no. 13, pp. 4167–4169, June 2008. doi:10.1021/cm8008418

[93] P. M. Shikhaliev, “Energy-resolved computed tomography: First experimental results,” *Phys. Med. Biol.*, vol. 53, no. 20, pp. 5595–5613, Sep. 2008. doi:10.1088/0031-9155/53/20/002. [Online]. Available: http://www.ncbi.nlm.nih.gov/pubmed/18799830 (Accessed: Mar. 14, 2019).

[94] S. A. Leng, L. F. Yu, J. Wang, J. G. Fletcher, C. A. Mistretta, and C. H. McCollough, “Noise reduction in spectral CT: Reducing dose and breaking the trade-off between image noise and energy bin selection,” *Med. Phys.*, vol. 38, no. 9, pp. 4946–4957, Sep. 2011. doi:10.1118/1.3609097

[95] K. Rajendran *et al.*, “Reducing beam hardening effects and metal artefacts in spectral CT using Medipix3RX,” *J. Instrum.*, vol. 9, no. 03, Mar. 2014. doi:10.1088/1748-0221/9/03/P03015

[96] T. Koenig *et al.*, “Imaging properties of small-pixel spectroscopic X-ray detectors based on cadmium telluride sensors,” *Phys. Med. Biol.*, vol. 57, no. 21, pp. 6743–6759, Oct. 2012. doi:10.1088/0031-9155/57/21/6743

[97] T. G. Schmidt, “CT energy weighting in the presence of scatter and limited energy resolution,” *Med. Phys.*, vol. 37, no. 3, pp. 1056–1067, Mar. 2010. doi:10.1118/1.3301615. [Online]. Available: http://www.ncbi.nlm.nih.gov/pubmed/20384241 (Accessed: Mar. 14, 2019).

[98] C. C. Shaw, X. M. Liu, M. Lemacks, J. X. Rong, and G. J. Whitman, “Optimization of MTF and DQE in magnification radiography - a theoretical analysis,” in *Med. Imaging 2000: Phys. Med. Imaging*, vol. 3977, Apr. 2000, pp. 466–475. doi:10.1117/12.384522

[99] M. D. Tipton, J. E. Dowdey, F. J. Bonte, and H. J. Caulfiel, “Coded aperture imaging using on-axis fresnel zone plates and extended gamma-ray sources,” *Radiol.*, vol. 112, no. 1, pp. 155–158, July 1974.

[100] E. Klotz and H. Weiss, “X-ray 3-D coded aperture imaging: Displaying the heart,” *Appl. Opt.*, vol. 15, no. 8, pp. 1913–1918, Aug. 1976. doi:10.1364/AO.15.001913. [Online]. Available: http://www.ncbi.nlm.nih.gov/pubmed/20165298 (Accessed: Mar. 14, 2019).

[101] G. Groh, “Tomosynthesis and coded aperture imaging: New approaches to three-dimensional imaging in diagnostic radiography,” *Proc. Roy. Soc. London Ser. B. Biol. Sci.*, vol. 195, no. 1119, pp. 299–306, Jan. 1977. [Online]. Available: http://www.ncbi.nlm.nih.gov/pubmed/13398 (Accessed: Mar. 14, 2019).

[102] Y. Xi and J. Zhao, “Fast grating-based X-ray phase-contrast tomosynthesis,” in *2013 35th Annu. Int. Conf. IEEE Eng. Med. Biol. Soc. (EMBC)*, July 2013, pp. 2320–2323.

[103] Y. Xi and J. Zhao, “Inner-focusing reconstruction method for grating-based phase-contrast CT,” *Opt. Exp.*, vol. 21, no. 5, pp. 6224–6232, Mar. 2013. doi:10.1364/Oe.21.006224

[104] Y. Y. Sun, W. X. Cong, Y. Xi, G. Wang, and S. Pang, “Talbot interferometry with curved quasi-periodic gratings: Towards large field of view X-ray phase-contrast imaging,” *Opt. Express*, vol. 23, no. 20, pp. 26 576–26 585, Oct. 2015. doi:10.1364/Oe.23.026576

[105] M. N. Lakshmanan, J. A. Greenberg, E. Samei, and A. J. Kapadia, “Design and implementation of coded aperture coherent scatter spectral imaging of cancerous and healthy breast tissue samples,” *J. Med. Imaging*, vol. 3, no. 1, Feb. 2016. doi:10.1117/1.Jmi.3.1.013505

[106] A. Olivo and R. Speller, “Modelling of a novel X-ray phase contrast imaging technique based on coded apertures,” *Phys. Med. Biol.*, vol. 52, no. 22, pp. 6555–6573, Oct. 2007. doi:10.1088/0031-9155/52/22/001

[107] A. Olivo and R. Speller, “Image formation principles in coded-aperture based X-ray phase contrast imaging,” *Phys. Med. Biol.*, vol. 53, no. 22, pp. 6461–6474, Oct. 2008. doi:10.1088/0031-9155/53/22/012

[108] P. R. T. Munro, K. Ignatyev, R. D. Speller, and A. Olivo, "The relationship between wave and geometrical optics models of coded aperture type X-ray phase contrast imaging systems," *Opt. Express*, vol. 18, no. 5, pp. 4103–4117, Mar. 2010. doi:10.1364/Oe.18.004103

[109] G. H. Chen, J. Zambelli, N. Bevins, Z. H. Qi, and K. Li, "X-ray phase sensitive imaging methods: Basic physical principles and potential medical applications," *Current Med. Imaging Rev.*, vol. 6, no. 2, pp. 90–99, May 2010.

[110] P. R. T. Munro, K. Ignatyev, R. D. Speller, and A. Olivo, "Source size and temporal coherence requirements of coded aperture type X-ray phase contrast imaging systems," *Opt. Express*, vol. 18, no. 19, pp. 19 681–19 692, Sep. 2010. doi:10.1364/Oe.18.019681

[111] A. Olivo, K. Ignatyev, P. R. T. Munro, and R. D. Speller, "Noninterferometric phase-contrast images obtained with incoherent X-ray sources," *Appl. Opt.*, vol. 50, no. 12, pp. 1765–1769, Apr. 2011. doi:10.1364/Ao.50.001765

[112] K. Ignatyev, P. R. T. Munro, R. D. Speller, and A. Olivo, "Effects of signal diffusion on X-ray phase contrast images," *Rev. Sci. Instrum.*, vol. 82, no. 7, July 2011. doi:10.1063/1.3606442

[113] A. Olivo, P. C. Diemoz, and A. Bravin, "Amplification of the phase contrast signal at very high X-ray energies," *Opt. Lett.*, vol. 37, no. 5, pp. 915–917, Mar. 2012.

[114] M. Marenzana *et al.*, "Visualization of small lesions in rat cartilage by means of laboratory-based X-ray phase contrast imaging," *Phys. Med. Biol.*, vol. 57, no. 24, pp. 8173–8184, Nov. 2012. doi:10.1088/0031-9155/57/24/8173

[115] P. R. T. Munro, C. K. Hagen, M. B. Szafraniec, and A. Olivo, "A simplified approach to quantitative coded aperture X-ray phase imaging," *Opt. Express*, vol. 21, no. 9, pp. 11 187–11 201, May 2013. doi:10.1364/Oe.21.011187

[116] K. P. MacCabe, A. D. Holmgren, M. P. Tornai, and D. J. Brady, "Snapshot 2D tomography via coded aperture X-ray scatter imaging," *Appl. Opt.*, vol. 52, no. 19, pp. 4582–4589, July 2013. doi:10.1364/Ao.52.004582

[117] A. Kavanagh, A. Olivo, R. Speller, and B. Vojnovic, “Feasibility testing of a pre-clinical coded aperture phase contrast imaging configuration using a simple fast Monte Carlo simulator,” *Biomed. Opt. Express*, vol. 5, no. 1, pp. 93–105, Jan. 2014. doi:10.1364/Boe.5.5.000093

[118] P. R. T. Munro *et al.*, “Medicine, material science and security: The versatility of the coded-aperture approach,” *Philos. Trans. Roy. Soc. A Math. Physical Eng. Sci.*, vol. 372, no. 2010, Mar. 2014. doi:10.1098/rsta.2013.0029

[119] M. B. Szafraniec, T. P. Millard, K. Ignatyev, R. D. Speller, and A. Olivo, “Proof-of-concept demonstration of edge-illumination X-ray phase contrast imaging combined with tomosynthesis,” *Phys. Med. Biol.*, vol. 59, no. 5, pp. N1–N10, Feb. 2014. doi:10.1088/0031-9155/59/5/N1

[120] S. Pang, M. Hassan, J. Greenberg, A. Holmgren, K. Krishnamurthy, and D. Brady, “Complementary coded apertures for 4-dimensional X-ray coherent scatter imaging,” *Opt. Express*, vol. 22, no. 19, pp. 22 925–22 936, Sep. 2014. doi:10.1364/Oe.22.022925

[121] M. Das and Z. H. Liang, “Spectral X-ray phase contrast imaging for single-shot retrieval of absorption, phase, and differential-phase imagery,” *Opt. Lett.*, vol. 39, no. 21, pp. 6343–6346, Nov. 2014. doi:10.1364/Ol.39.006343

[122] P. Korecki, T. P. Roszczynialski, and K. M. Sowa, “Simulation of image formation in X-ray coded aperture microscopy with polycapillary optics,” *Opt. Express*, vol. 23, no. 7, pp. 8749–8761, Apr. 2015. doi:10.1364/Oe.23.008749

[123] M. Das and Z. H. Liang, “Approximated transport-of-intensity equation for coded-aperture X-ray phase-contrast imaging,” *Opt. Lett.*, vol. 39, no. 18, pp. 5395–5398, Sep. 2014. doi:10.1364/Ol.39.005395

[124] A. P. Cuadros, C. Peitsch, H. Arguello, and G. R. Arce, “Coded aperture optimization for compressive X-ray tomosynthesis,” *Opt. Express*, vol. 23, no. 25, pp. 32 788–32 802, Dec. 2015. doi:10.1364/Oe.23.032788

[125] D. J. Brady, D. L. Marks, K. P. MacCabe, and J. A. O’Sullivan, “Coded apertures for X-ray scatter imaging,” *Appl. Opt.*, vol. 52, no. 32, pp. 7745–7754, Nov. 2013. doi:10.1364/Ao.52.007745

[126] N. Tanaka *et al.*, “Investigation of optimum anti-scatter grid selection for digital radiography: Physical imaging properties and detectability of low-contrast signals,” *Radiol. Phys. Technol.*, vol. 6, no. 1, pp. 54–60, Jan. 2013. doi:10.1007/s12194-012-0169-y. [Online]. Available: http://www.ncbi.nlm.nih.gov/pubmed/22872419 (Accessed: Mar. 14, 2019).

[127] V. Singh, A. Jain, D. R. Bednarek, and S. Rudin, “Limitations of anti-scatter grids when used with high resolution image detectors,” in *Med. Imaging 2014: Phys. Med. Imaging*, vol. 9033, Mar. 2014. doi:10.1117/12.2043063

[128] R. Rana, V. Singh, A. Jain, D. R. Bednarek, and S. Rudin, “Anti-scatter grid artifact elimination for high resolution X-ray imaging CMOS detectors,” *Med. Imaging 2015: Phys. Med. Imaging*, vol. 9412, Mar. 2015. doi:Artn 941243 10.1117/12.2081430

[129] T. Goorley *et al.*, “Initial MCNP6 release overview,” *Nucl. Technol.*, vol. 180, no. 3, pp. 298–315, Dec. 2012.

[130] M. Chen, Y. Xi, W. Cong, B. Liu, B. Wei, and G. Wang, “X-ray CT geometrical calibration via locally linear embedding,” *J. Xray Sci. Technol.*, vol. 24, no. 2, pp. 241–256, Mar. 2016. doi:10.3233/XST-160548. [Online]. Available: https://content.iospress.com/articles/journal-of-X-ray-science-and-technology/xst548 (Accessed: Mar. 14, 2019).

[131] T. G. Flohr *et al.*, “First performance evaluation of a dual-source CT (DSCT) system,” *Eur. Radiol.*, vol. 16, no. 2, pp. 256–268, Dec. 2006. doi:10.1007/s00330-005-2919-2. [Online]. Available: https://www.ncbi.nlm.nih.gov/pubmed/16341833 (Accessed: Mar. 14, 2019).

[132] A. N. Primak, J. C. Ramirez Giraldo, X. Liu, L. Yu, and C. H. McCollough, “Improved dual-energy material discrimination for dual-source CT by means of additional spectral filtration,” *Med. Phys.*, vol. 36, no. 4, pp. 1359–1369, Mar. 2009. doi:10.1118/1.3083567. [Online]. Available: https: //www.ncbi.nlm.nih.gov/pmc/articles/PMC2719491/pdf/MPHYA6-000036-001359_1.pdf (Accessed: Mar. 14, 2019).

[133] D. P. Clark and C. T. Badea, “Spectral diffusion: An algorithm for robust material decomposition of spectral CT data,” *Phys. Med. Biol.*, vol. 59, no. 21, pp. 6445–6466, Nov.

2014. doi:10.1088/0031-9155/59/21/6445. [Online]. Available: https://www.ncbi.nlm.nih.gov/pubmed/25296173 (Accessed: Mar. 14, 2019).

[134] H. W. Li, X. W. Wu, B. Liu, W. D. Liu, and N. Gao, "Clinical values of of gemstone spectral CT in diagnosing thyroid disease," *J. Xray Sci. Technol.*, vol. 23, no. 1, pp. 45–56, Jan. 2015. doi:10.3233/XST-140469. [Online]. Available: https://www.ncbi.nlm.nih.gov/pubmed/25567406 (Accessed: Mar. 14, 2019).

[135] B. M. Yeh *et al.*, "Opportunities for new CT contrast agents to maximize the diagnostic potential of emerging spectral CT technologies," *Adv. Drug Del. Rev.*, vol. 113, pp. 201–222, Apr. 2017. doi:10.1016/j.addr.2016.09.001. [Online]. Available: https://www.ncbi.nlm.nih.gov/pubmed/27620496 (Accessed: Mar. 14, 2019).

[136] Y. Zhao *et al.*, "Application of low concentration contrast medium in spectral CT imaging for CT portal venography," *J. Xray Sci. Technol.*, vol. 25, no. 1, pp. 135–143, Jan. 2017. doi:10.3233/XST-16188. [Online]. Available: https://www.ncbi.nlm.nih.gov/pubmed/27768006 (Accessed: Mar. 14, 2019).

[137] O. Lee, S. Kappler, C. Polster, and K. Taguchi, "Estimation of basis line-integrals in a spectral distortion-modeled photon counting detector using low-rank approximation-based X-ray transmittance modeling: K-edge imaging application," *IEEE Trans. Med. Imaging*, vol. 36, no. 11, pp. 2389–2403, Nov. 2017. doi:10.1109/TMI.2017.2746269. [Online]. Available: https://www.ncbi.nlm.nih.gov/pubmed/28866486 (Accessed: Mar. 14, 2019).

[138] E. Samei *et al.*, "Characterization of a novel photon counting detector for clinical CT: Count rate, energy resolution, and noise performance," in *Med. Imaging 2009: Phys. Med. Imaging*, vol. 7258, Mar. 2009. doi:10.1117/12.813915. [Online]. Available: https://www.spiedigitallibrary.org/conference-proceedings-of-spie/7258/725824/Characterization-of-a-novel-photon-counting-detector-for-clinical-CT/10.1117/12.813915.pdf (Accessed: Mar. 14, 2019).

[139] P. He, B. Wei, W. Cong, and G. Wang, "Optimization of K-edge imaging with spectral CT." *Med. Phys.*, vol. 39, no. 11, pp. 6572–6579, Oct. 2012. doi:10.1118/1.4754587]. [Online]. Available: https://www.ncbi.nlm.nih.gov/pmc/articles/PMC3482256/pdf/MPHYA6-000039-006572_1.pdf (Accessed: Mar. 14, 2019).

[140] P. He *et al.*, “Energy-discriminative performance of a spectral micro-CT system,” *J. Xray Sci. Technol.*, vol. 21, no. 3, pp. 335–345, Nov. 2013. doi:10.3233/XST-130382. [Online]. Available: https://www.ncbi.nlm.nih.gov/pmc/articles/PMC3824963/pdf/nihms523891.pdf (Accessed: Mar. 14, 2019).

[141] R. Zainon *et al.*, “Spectral CT of carotid atherosclerotic plaque: Comparison with histology,” *Eur. Radiol.*, vol. 22, no. 12, pp. 2581–2588, May 2012. doi:10.1007/s00330-012-2538-7. [Online]. Available: https://link.springer.com/content/pdf/10.1007%2Fs00330-012-2538-7.pdf (Accessed: Mar. 14, 2019).

[142] R. Karunamuni and A. D. Maidment, “Search for novel contrast materials in dual-energy X-ray breast imaging using theoretical modeling of contrast-to-noise ratio,” *Phys. Med. Biol.*, vol. 59, no. 15, pp. 4311–4324, Aug. 2014. doi:10.1088/0031-9155/59/15/4311. [Online]. Available: https://www.ncbi.nlm.nih.gov/pubmed/25029534 (Accessed: Mar. 14, 2019).

[143] P. F. FitzGerald *et al.*, “CT image contrast of high-Z elements: Phantom imaging studies and clinical implications,” *Radiol.*, vol. 278, no. 3, pp. 723–733, 2015. [Online]. Available: https://www.ncbi.nlm.nih.gov/pmc/articles/PMC4770942/pdf/radiol.2015150577.pdf

[144] J. Ye, “Least squares linear discriminant analysis,” in *Proc. 24th Int. Conf. Mach. Learning*, June 2007, pp. 1087–1093.

[145] Z. Sedghi Gamechi *et al.*, “Automated 3D segmentation and diameter measurement of the thoracic aorta on non-contrast enhanced CT,” *Eur. Radiol.*, Jan. 2019. doi:10.1007/s00330-018-5931-z. [Online]. Available: https://www.ncbi.nlm.nih.gov/pubmed/30673817 (Accessed: Mar. 14, 2019).

[146] G. Yang, H. Liu, and X. Yu, “Hyperspectral remote sensing image classification based on kernel fisher discriminant analysis,” in *2007 Int. Conf. Wavelet Anal. Pattern Recognit.*, vol. 3, Nov. 2007, pp. 1139–1143.

[147] G. Yang *et al.*, “Hyperspectal RS image classification based on kernel methods,” in *MIPPR 2007: Pattern Recognit. Comput. Vision*, vol. 6788, Nov. 2007. doi:10.1117/12.750423

[148] X. Zhang, Y. He, N. Zhou, and Y. Zheng, “Semisupervised dimensionality reduction of hyperspectral images via local scaling cut criterion,” *IEEE Geosci. Remote Sens. Lett.*, vol. 10, no. 6, pp. 1547–1551, Nov. 2013. doi:10.1109/lgrs.2013.2261797

[149] W. Shih, “n-dimension spherical coordinates and the volumes of the n-ball in Rn.” [Online]. Available: http://www.ams.sunysb.edu/~wshih/mathnotes/n-D_Spherical_coordinates.pdf (Accessed: Mar. 14, 2019).

[150] R. A. Fisher, “The use of multiple measurements in taxonomic problems,” *Ann. of Eugenics*, vol. 7, no. 2, pp. 179–188, Sep. 1936.

[151] S. Mika, G. Rätsch, J. Weston, B. Schölkopf, and K. R. Müller, “Fisher discriminant analysis with kernels,” in *Neural Netw. Signal Process. IX: Proc. 1999 IEEE Signal Process. Soc. Workshop*, Aug 1999, pp. 41–48.

[152] J. Stayman and I. Steven Tilley, “Model-based multi-material decomposition using spatial-spectral CT filters,” in *Conf. Proc. Int. Conf. Image Form. X-ray Comput. Tomogr.*, May 2018, pp. 102–105.

Appendix A
Supplemental Figures: Material Segmentation

The following figures were not included in Chapter 6 in order to keep the discussion succint. However, the following images are eigenvector representations of different material groups after kFDA are plotted against each other in 2D. Besides being visually pleasing, the relationships seen between these vector representations of materials in simulation and real materials measured on the MARS are similar in shape and layout which may be a useful observation as this work progresses.

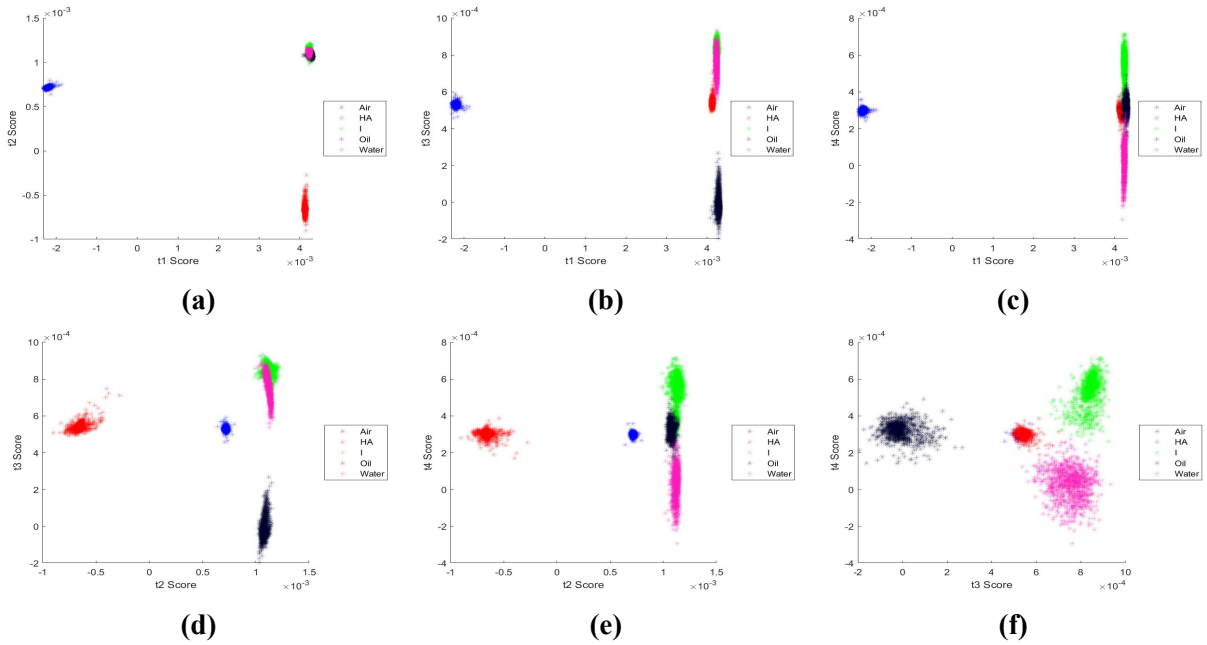

Fig. A.1: 2D plots of the materials in the eigenvector space made with the MARS HA I phantom.

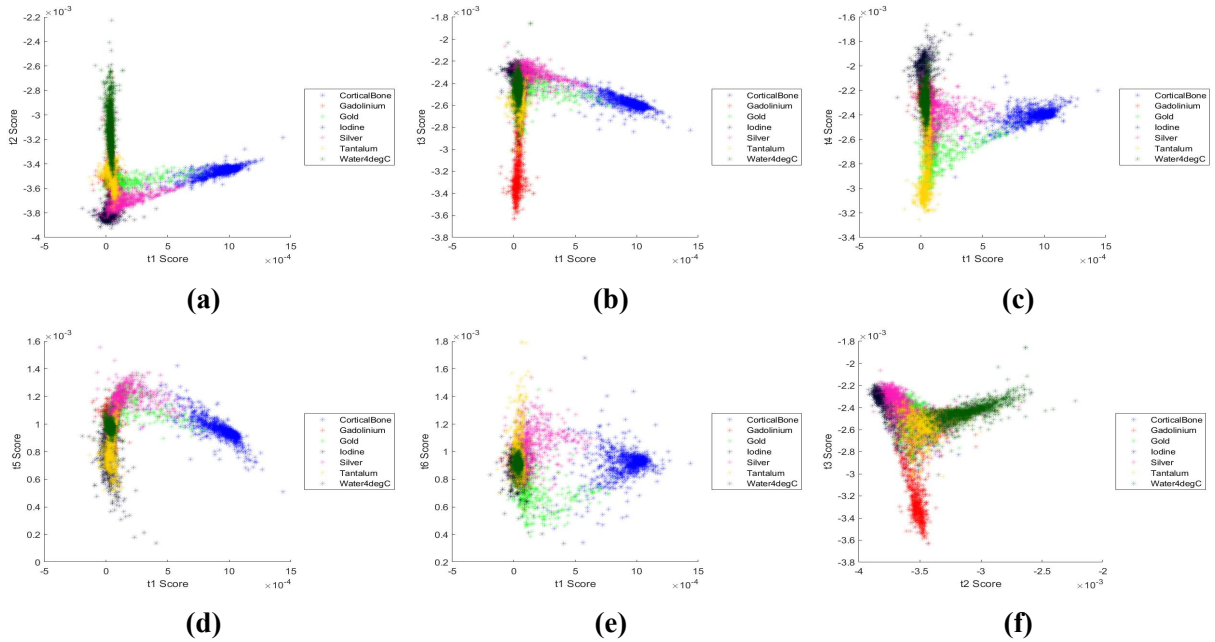

Fig. A.2: 2D plots of the materials in the eigenvector space made with the simulated 7 material phantom.

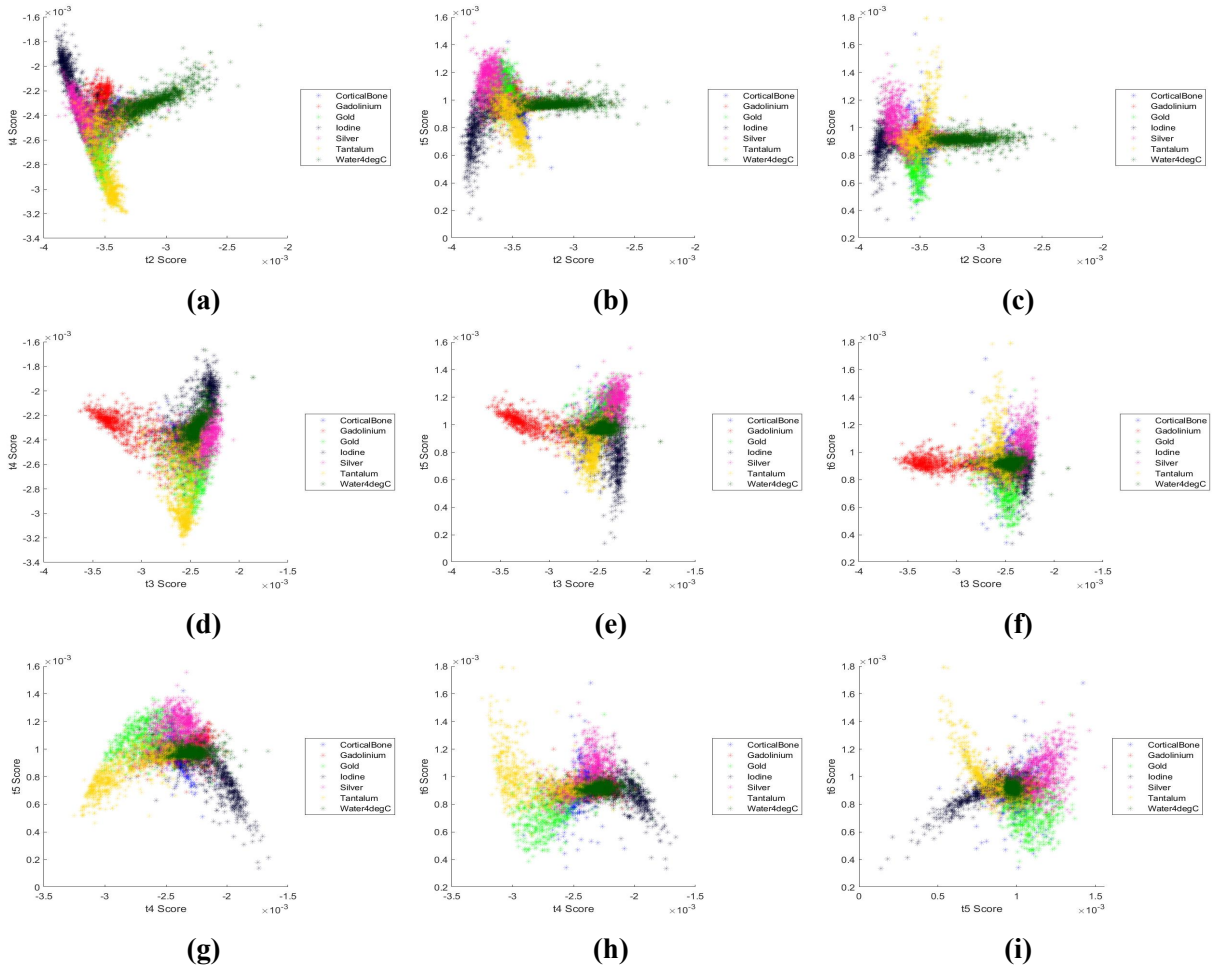

Fig. A.3: 2D plots of the materials in the eigenvector space made with the simulated 7 material phantom (continued).

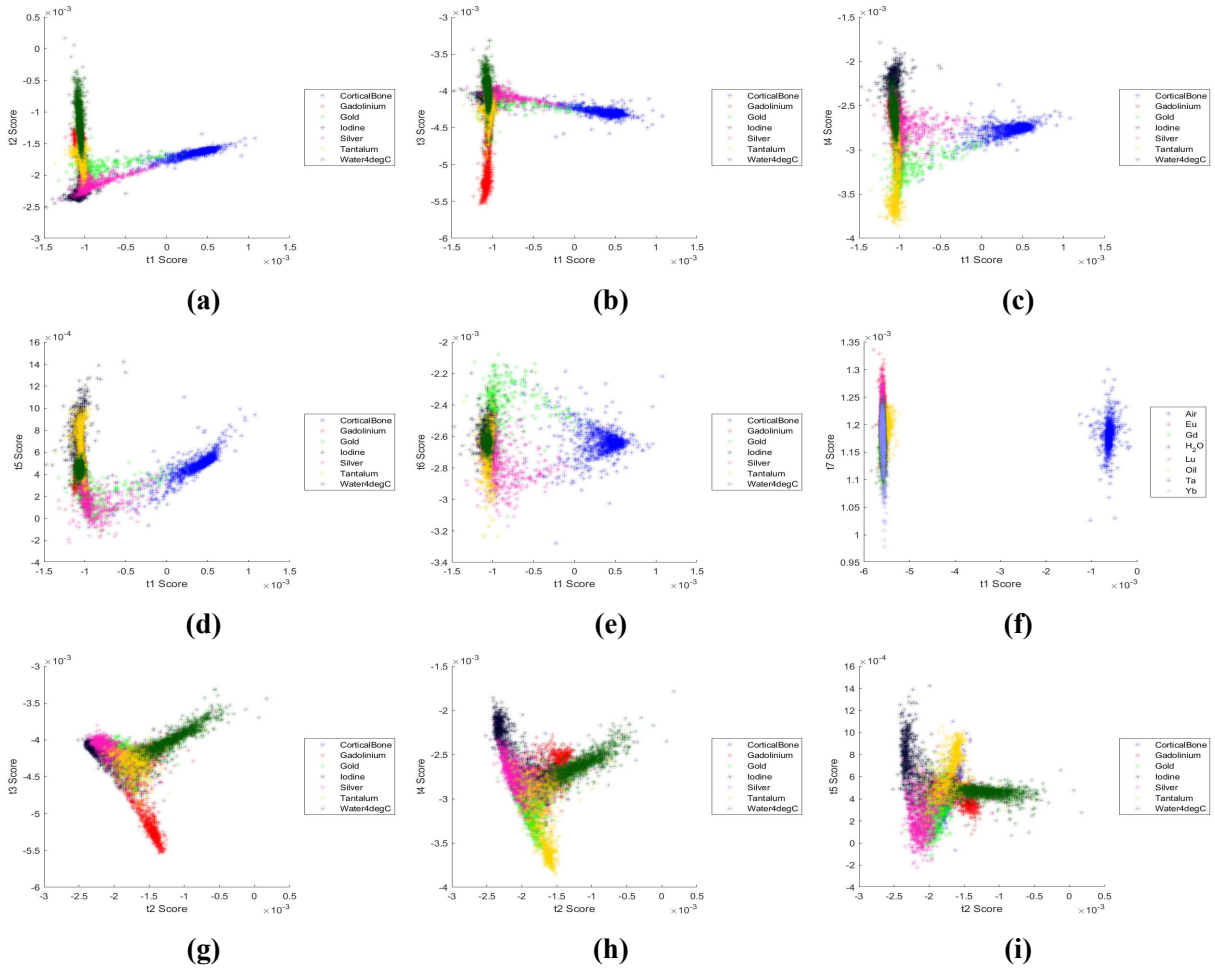

Fig. A.4: 2D plots of the materials in the eigenvector space made with the mars K-edge phantom.

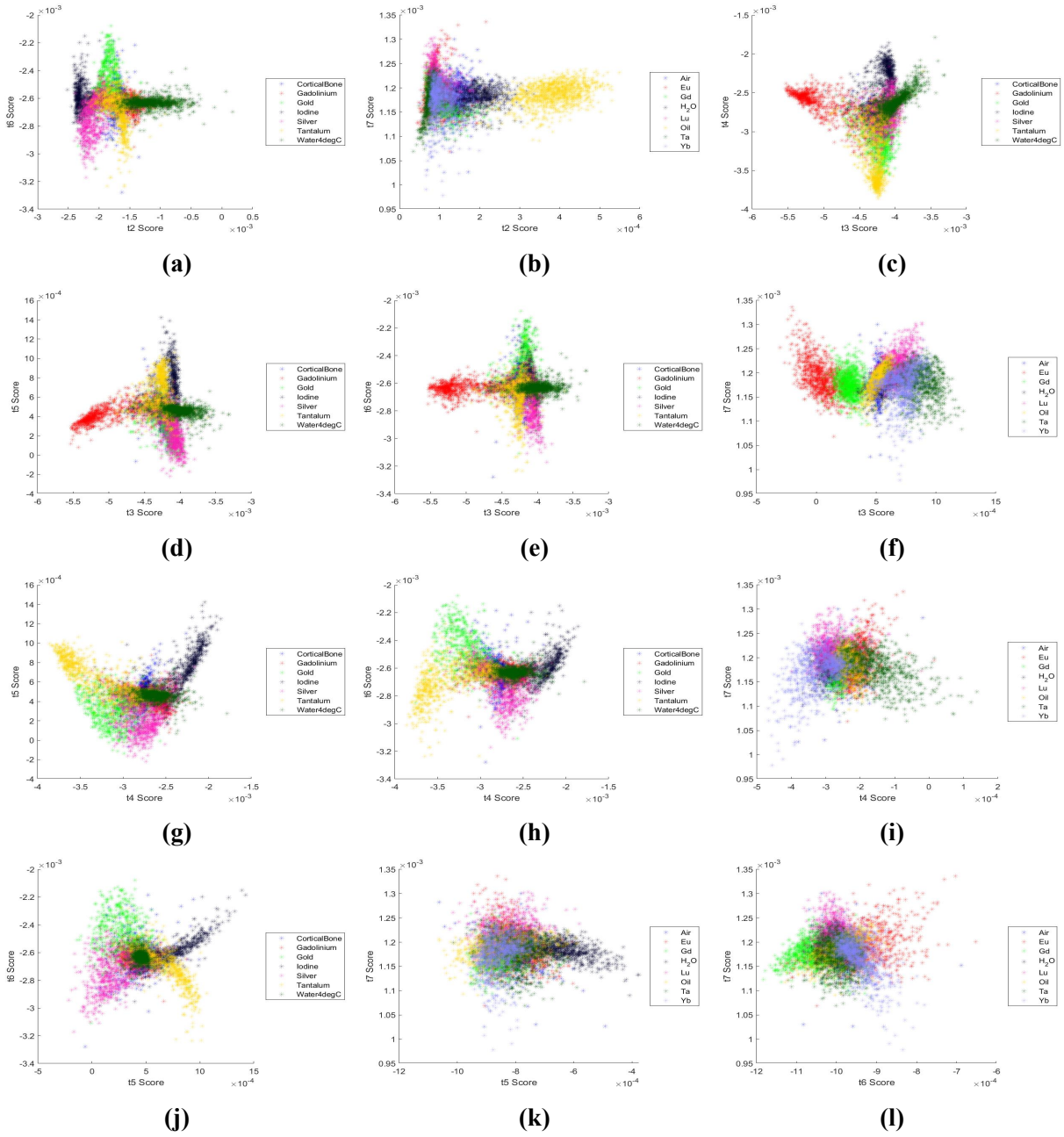

Fig. A.5: 2D plots of the materials in the eigenvector space made with the mars K-edge phantom (continued).